Characterizing the atomic structure in low concentrations of weakly ordered, weakly scattering materials using the pair distribution function

Maxwell W. Terban

Submitted in partial fulfillment of the
requirements for the degree of
Doctor of Philosophy
in the Graduate School of Arts and Sciences

COLUMBIA UNIVERSITY

2018

ABSTRACT

Characterizing the atomic structure in low concentrations of weakly ordered, weakly scattering materials using the pair distribution function

Maxwell W. Terban

Nanoscale structural characterization is critical to understanding the physical underpinnings of properties and behavior in materials with technological applications. The work herein shows how the pair distribution function technique can be applied to x-ray total scattering data for material systems which weakly scatter x-rays, a typically difficult task due to the poor signal-to-noise obtained from the structures of interest. Characterization and structural modeling are demonstrated for a variety of molecular and porous systems, along with the detection and characterization of disordered, minority phases and components. In particular, reliable detection and quantitative analysis are demonstrated for nanocrystals of an active pharmaceutical ingredient suspended in dilute solution down to a concentration of 0.25 wt. %, giving a practical limit of detection for ordered nanoscale phases within a disordered matrix. Further work shows that minority nanocrystalline phases can be detected, fingerprinted, and modeled for mixed crystalline and amorphous systems of small molecules and polymers. The crystallization of amorphous lactose is followed under accelerated aging conditions. Melt quenching is shown to produce a different local structure than spray drying or freeze drying, along with increased resistance to crystallization. The initial phases which form in the spray dried formulation are identified as a mixture of polymorphs different from the final α-lactose monohydrate form. Hard domain formation in thermoplastic

polyurethanes is also characterized as a function of methylene diphenyl diisocyanate and butanediol component ratio, showing that distinct and different hard phase structures can form and are solved by indexing with structures derived from molecular dynamics relaxation. In both cases, phase fractions can be quantified in the mixed crystalline and amorphous systems by fitting with both standards or structure models.

Later chapters, demonstrate pair distribution function characterization of particle incorporation, structure, and synthesis of nanoporous materials. Nanoparticle size distributions are extracted from platinum nanoparticles nucleating within a zeolite matrix through structural modeling, and validated by transmission electron microscope studies. The structure of zirconium phosphonate-phosphate unconventional metal organic framework is determined to consist of turbostratically disordered nanocrystalline layers of Zr-phenylphosphonate, and the local environment of terbium intercalated between the layers is found to resemble the local environment in scheelite-type terbium phosphate. Finally, the early stages of reaction between aqueous zinc dinitrate hexahydrate and methanolic 2-methylimidazole are characterized using *in situ* total scattering measurements, showing that secondary building units of tetrahedrally coordinated by 2-methylimidazole initially form upon reaction. Overall, the methodologies are developed and applied toward phase detection, identification, solution, and behavior in pharmaceuticals, polymers, and nanoporous materials. Advice is given for carrying out experiments and analysis on such materials so that these techniques can be applied to other similar systems.

Contents

List of figures **vi**

List of tables **xxiii**

Abbreviations and symbols **xxv**

Acknowledgements **xxx**

Preface **xxxiii**

1 Disorder and heterogeneity in weakly scattering materials **1**

1.1 Small molecules 4

1.2 Organic polymers 8

1.3 Microporous materials 10

1.3.1 Zeolites 11

1.3.2 Metal organic frameworks 12

1.3.3 Nanoporous framework formation 16

2 Pair distribution function analysis and modeling methods **19**

2.1 X-ray scattering 19

2.2 The pair distribution function . . . 21
2.3 Modeling the PDF . . . 23
2.3.1 Basics . . . 23
2.3.2 Intra- versus intermolecular correlations . . . 24
2.3.3 Benchmarking fit quality for molecular compounds . . . 25
2.3.4 Reduced structural coherence . . . 28
2.4 Differential pair distribution function . . . 29
2.5 Phase quantification . . . 31
2.6 Correlation analysis . . . 33

3 Experimental and data processing techniques 35

3.1 Rapid acquisition measurements . . . 35
3.2 Basic sample preparation . . . 38
3.2.1 Containers . . . 38
3.2.2 Sealing agents . . . 40
3.2.3 Powders . . . 40
3.3 Liquids . . . 43
3.4 Solid chunks . . . 45
3.5 Data processing with PDFGetX3 . . . 46
3.6 Q_{max} effects . . . 49

4 Signal sensitivity from dilute component concentrations 51

4.1 Detection and quantitation limits of the dPDF method . . . 51
4.2 Materials . . . 53

4.3 Results and discussion 55
4.4 Conclusions 61

5 Processing effects and crystallization of amorphous lactose 63

5.1 The interesting case of lactose 63
5.2 Materials 66
5.3 Supplemental experiments 67
5.4 Modeling amorphous and crystalline states 67
5.5 Results and discussion 69
5.5.1 Structural refinement of crystalline products 69
5.5.2 Unaged amorphous formulations 72
5.5.3 Crystallization behavior 76
5.5.4 Quantifying amorphous and crystalline phase content 79
5.6 Further analysis 86
5.7 Conclusions 88

6 Local ordering in thermoplastic hard phases 90

6.1 The structures of hard phases in thermoplastic polyurethanes 90
6.2 Sample preparation 91
6.3 Results and discussion 93
6.3.1 Form I 100
6.3.2 Form II 108
6.4 Conclusions 112

7 Nucleation of metal nanoparticles inside zeolitic frameworks 114

7.1 Log-normal spherical size distributions of supported nanoparticles 114

7.2 Sample preparation 116

7.3 Dark field scanning transmission electron microscopy (STEM) 117

7.4 Total scattering measurements 118

7.5 PDF refinement 118

7.6 Results 119

7.7 Conclusions 125

8 Structure and loading in unconventional framework materials 127

8.1 The structure of zirconium phosphonate-phosphate hybrid unconventional metal organic frameworks 127

8.2 Materials 131

8.3 Synthesis 131

8.4 Laboratory x-ray measurements 132

8.5 Total scattering measurements 132

8.6 Results and discussion 133

8.6.1 Intralayer structure 133

8.7 CIF coordinates for intralayer H-Zr model 139

8.7.1 Interlayer structure 141

8.7.2 Effects of the phosphonate:phosphate ratio 145

8.7.3 Local environment of Tb ions 147

8.8 Conclusions 152

9 Nucleation of metal organic frameworks from solution **154**

9.1 Room temperature solution synthesis of ZIF-8 154

9.2 Experiments 156

9.2.1 Synthesis of ZIF-8 156

9.2.2 Total scattering measurements 158

9.2.3 Static reaction cell 159

9.2.4 Flow cell 160

9.2.5 Supplemental experiments and simulations 161

9.3 Results and discussion 163

9.4 Conclusions 175

10 Concluding thoughts **177**

Bibliography **180**

List of figures

2.1 Visualization of the relationship between peaks in the PDF and the actual atom-pair distances in the sample structure. In molecular materials, there are two characteristic regions. The intramolecular region consists of sharp, well-defined peaks which correspond to the distances between directly bonded atom-pairs within a molecule. The intermolecular region consists of broadened peaks which come from distances between pairs of atoms located within separate molecules. 20

2.2 Benchmark goodness-of-fit, R_w values for known molecular crystalline compound structures (a-d) α-lactose monohydrate, where the fits correspond to (a) fitting with no low-r sharpening parameters, (b) using δ_2, (c) sratio using an r_{cut} value of 4.2, and (d) using separate intra- and intermolecular thermal parameters in Diffpy-CMI, all using a grid spacing of 0.01 which is the default from PDFGetX3. The same fit models are applied to the crystalline compound of L-tryptophan (e-h). An r_{cut} value of 3.8 was used for (g). 26

2.3 Molecular structures of (A) L-tryptophan and (B) α-lactose, where the atoms depicted are carbon (grey), nitrogen (blue), and oxygen (red). In (B), the extra detached oxygen atom represents the water molecule as in the crystalline monohydrate form. 27

3.1 Schematic diagram showing the relationship between the scattering angle, sample-to-detector distance, and the intensity measured in a certain pixel on the detector. 36

3.2 Photograph of the XPD beamline at NSLS-II. The dashed line indicates the path of the incident beam, while the transparent cones indicate the path of photons scattered from the sample at different degrees of momentum transfer, forming rings where they intersect with the detector. The letter labels indicate A. the detector, B. the beamstop which stops the transmitted beam from hitting and damaging the detector, and C. the collimator which is a metal tube, pushed close to the sample, which blocks any air scattering occurring along the incident beam path before hitting the sample. 38

3.3 (A) Kapton (or other material) capillary, (B) mortar and pestle for grinding, (C) quick dry epoxy, (D) sample spatula, (E) sample, (F) moldable clay, (G) filled and sealed sample, (I) labeled sample containers. 39

3.4 2D images collected from polycrystalline sulfur (S_8) with (a) a static capillary and (b) spinning the capillary about its center axis perpendicular to the beam. 41

3.5 Steps for loading a liquid into a Kapton capillary. 44

3.6 (A) bracket, (B) Kapton tape stretched over bracket (the sticky end on top will face the detector), (C) sample chunk, (D) calibration standard capillary. 45

3.7 Data processing steps 48

3.8 The Q_{max} used in the data reduction was varied depending on the region of scrutiny in order to optimize between real space resolution (high Q_{max}) versus noise reduction (low Q_{max}). We verified that the changes in this value did not degrade the signal of interest, particularly in the high-r region. Top left: HP1. Top right: HP3. Bottom left: HP4. Bottom right: TPU2. Low- and mid-r refinements used Q_{max}=13.20 Å^{-1} while high-r refinements used Q_{max}=11.3 Å^{-1} 49

4.1 Integration of measured intensity: 1D raw signal after integration of Debye-Scherrer rings for precipitated crystalline API (red), aqueous solvent (blue), and 0.25 wt. % API suspension (green). Curves are offset for clarity. 53

4.2 1D scattering intensities for the blank aqueous solvent (blue), and 0.25 wt. % API suspension (green), and difference (red). 54

4.3 Representative data sets from control samples: precipitated crystalline API (green) and aqueous solvent (blue). (a) $F(Q)$ (b) the PDF, $G(r)$. 54

4.4 Comparison of bulk versus precipitated crystalline samples: PDFs from the bulk crystalline API (blue) and the crystalline API that precipitated from solvent (green). The PDF signals are subtracted (red) and compared to that of the aqueous solvent (light blue) with very good agreement showing that the only difference between the signals is the presence of significant solvent scattering in the latter case. PDF is sensitive to the presence or absence of residual solvent in the crystalline API. 56

4.5 High-r comparison of bulk versus precipitated crystalline samples: scaled to highlight the signal from the intermediate-range molecular packing in the crystal, from the bulk crystalline API (blue) and the crystalline API that precipitated from solvent (green). The figure illustrates the level of reproducibility that may be obtained by measuring two different samples of the same material. 57

4.6 Comparison of precipitated and 5 wt. % suspension samples: PDFs from the 5 wt. % API (blue) and aqueous solvent (green). (a) Low-r region of the PDF. (b) wide r-range with the difference of the PDF signals shown offset below (red). 57

4.7 Determining the range of structural coherence for suspension particles: Reproducibility of the dPDF from the microfluidized 5 wt. % API obtained from reciprocal space subtraction of the suspension (green) and the crystalline precipitate corrected by a 16.9 nm domain size (blue). 58

4.8 Signal sensitivity: dPDFs from reciprocal space subtraction of the solvent for the 0.25 (blue), 0.66 (green) and 5 (red) wt. % API samples. Despite increased noise ripples in the low concentration samples, the signal from the API is clearly evident. 59

4.9 Peak fitting: PDF models are generated and compared by fitting Gaussian curves (light green) and a PDF baseline (black) at the extracted peak positions (black hash marks) to the data plotted on a Nyquist grid (blue) for (a) the crystalline standard, and (b) the 0.25 wt. % suspension. Differences are plotted in red. 60

5.1 Schematics of the α and β lactose molecules. Mutarotation occurs at the marked ($*$) site. 64

5.2 Calculated PDFs from lactose polymorph structures (anhydrous β (aqua), $\alpha\beta$ (lime), hygroscopic α (gold), stable α (orange), and monohydrate (red)) refined against the PDF of crystalline c-Flowlac (blue) with differences shown offset below (green). Visual comparison of the refined PDF of the monohydrate compared with that of the other models shows that it is clearly the correct structure. This is supported by the significantly lower R_w value. 70

5.3 Left: Calculated scattering intensities from Rietveld refinement of the α-lactose monohydrate structure (red) to the c-Flowlac and c-Spectrum scattering measured by XRPD (blue) with differences offset below (green). Right: Calculated PDF of the α-lactose monohydrate structure (red) refined to the other measured crystalline PDFs (c-Tablettose, a-Flowlac30 and a-lyoph15) (blue) with differences offset below (green). 71

5.4 Comparison of PDFs of amorphous samples at 0 aging, a-Flowlac0, a-lyoph0, and a-mq0. (a): Signals overlaid to demonstrate overall reproducibility of the primary structural features, and zoomed in the mid-r region to highlight nuanced signal differences. (b): Differences between the signals are taken and compared using Pearson values calculated over a range of r = 2.00–7.00 Å. It is clear that the initial states of lyophilized and Flowlac samples are substantially more similar than the melt quenched sample. 73

5.5 NMR spectra for (a) amorphous Flowlac100, (c) melt quenched lactose, (e) crystalline α-lactose monohydrate, and magnified plots of their peaks from α and β content (b), (d), (f) respectively. 74

5.6 (a): PDFs measured for a-Flowlac after aging for different lengths of time. (b): Signals from the Flowlac samples aged at room temperature for 1 month and at 3.5 minutes in the storage chamber are overlaid, showing a similar extent of transformation. Aging time is shown above each curve. (c): Signals from samples aged 1, 2.5, 3.5, and 5 minutes overlaid. The peak-to-peak amplitude of structural features in the mid-r region is observed to grow with increased aging time, showing an increasing concentration of crystalline phase. Differences can be seen between the precursor structure at 3.5 minutes and the final product at 5 minutes, which has been scaled for visual comparison. 75

5.7 (a): PDFs measured for a-mq after aging for different lengths of time. (b): Melt quenched and Flowlac samples are compared after aging for 0 minutes and for 1 month at ambient conditions. A crystalline component is observed in both, but less so for the melt quenched sample. Arrows indicate strong structural correlations growing in during aging over 1 month. 77

5.8 (a): PDFs measured for a-lyoph after aging for different lengths of time. (b). Crystalline signals from the sample aged for 3 and 15 minutes are overlaid with the a-Flowlac5 signal showing a higher degree of structural disorder for the lyophilized samples by the increase in signal attenuation. (c): Difference curves from the signals in panel (b) are overlaid to show that with increased aging time, the structure of the lyophilized samples approaches that observed in crystallized Flowlac. . . 78

5.9 (a) Refined coherence length from PDFgui and (b) least-squares crystalline phase fraction versus crystallization time for samples aged in the storage chamber. . . 80

5.10 (a): Amorphous Flowlac100 aged for 1 month at room temperature (blue) is compared to a mixed phase fit (red), and to the amorphous standard (lime), with improvement in signal reproduction with the mixed fit. (b): The difference (green) between the aged sample and the amorphous standard is compared to the scaled crystalline standard (purple). Features arising from the crystalline phase can be clearly seen in the difference. 81

5.11 Representative mixed phase (crystalline:amorphous) fits, G_{mix} (red) overlaid with measurement (blue) for (a): a-FlowlacRT (6.76:93.24), (b): a-lyoph3 (79.28:20.72), (c): a-mq55 (1.83:98.17). Differences plotted below (green). Phase concentrations chosen by least-squares refinement of a weighted linear sum of the amorphous and crystalline standard PDF signals (a-Flowlac1 and a-Flowlac30 respectively). The difference in (c) appears slightly noisier due to the amplification of high-r ripples in the amorphous standard which has a larger phase fraction in this case. 82

5.12 Calculated PDF of the mixed phase model (red) refined to the a-Flowlac1 and a-Flowlac2.5 PDFs (blue) with differences offset below (green). 87

5.13 Trends in phase fraction for the three phase model. The black dashed line indicates the first time point where the data was refined. There was not suitable signal-to-noise in the zero minute measurement to observe any peaks. Additionally, the 1.5 and 2.0 minute data points were switched for more consistent agreement. This was justified since the 1.5 minute sample was clearly more developed (it was from a different batch). 87

6.1 Schematics of (A) the hard segment monomer structures, 4,4'-methylene diphenyl diisocyanate, (B) the chain extender 1,4-butanediol, and (C) the soft segment monomer polytetrahydrofuran. 92

6.2 Best fit simulated PDFs (red) compared to measured PDFs (blue) of PTHF and MDI, with the difference curve offset below (green). Fit residuals are $R_w = 0.30$ and 0.39 respectively. (Q_{max}=16 Å^{-1}) 94

6.3 Depiction of process for fitting the model structures to the data, shown for the case of PTHF. (A) The crystal model is simulated and fit to the high-r region of the measured data to determine the intermolecular thermal parameter, U_{inter}. The PDF of a single molecule from the same structure is then calculated with the same thermal parameter and subtracted to obtain the intermolecular PDF. Another PDF of the molecule is then calculated with a much lower thermal parameter U_{intra} to produce the sharp peaks seen in the low-r region. (B) The full PDF produced from (A) is not able to describe the significant attenuation seen going from the low-r to high-r regions, indicating an additional disordered phase is present. This phase is modeled with the same local structure as the crystalline phase but calculated with a much smaller crystallite size. 95

6.4 Measured PDFs from the five hard phase samples (Q_{max}=16 Å^{-1}). 96

6.5 High-r signal in HP1 and TPU2. Left: The structuring in the PDFs of HP1 and TPU2 is compared to that of HP3 and HP5. It is clear that both samples show significant differences from the more crystalline phases. However, there is a small structural signal in TPU2 extending to higher-r given the distinct peak shapes. Right: HP1 shows several features at 9.77, 14.52, 18.53, and 27.65 Å. These features are much broader than the other sample PDFs indicating that there is far more structural disorder in samples HP1 and HP2. 97

6.6 Comparison of (A) model 9 (TPU-BDO-gauche-1) and (B) model 13 (TPU-BDO-trans-1) in the [100] direction, parallel to the hydrogen bonding direction. The difference between gauche and trans bonding in the butane-diol fragment is evident. The fragment forms a kink in the former, while it forms in a zig-zag fashion in the latter which remains fairly linear. Looking in the direction parallel to hydrogen bonding, all the models look similar to these examples depending on whether they are gauche or trans. 102

6.7 Comparison of models (A) 10 (TPU-BDO-gauche-2, type A1), (B) 9 (TPU-BDO-gauche-1, type B), and (C) 11 (TPU-BDO-gauche-3, type C) in the [010] direction, perpendicular to the hydrogen bonding direction. Of the new models developed and tested, these represent the essentially three different varieties of chain packing in this direction. In (A), the diphenyl-methane segments stack in the same orientation, while the butane-diol segment switches between two orientations from neighbor to neighbor. In (B), only every other diphenyl-methane segment stacks in the same orientation, while the others shift out of phase in the [100] direction. In (C), all segments are out of phase from layer to layer in this direction. 103

6.8 Measured PDFs of HP3 ($Q_{max} = 13.2$ Å) (blue) with fits of the 16 structural models (red) with the difference curve plotted below (green). (A) the fits in the low-r region ($1 < r < 10$ Å). (B) fits over the intermediate-r region ($5.5 < r < 17.0$ Å). 104

6.9 Comparison of measured PDFs of HP3 (blue) (Q_{max}=11.3 Å^{-1}), with models 1–16 superimposed (red) for direct comparison. Pearson coefficients listed for reference 105

6.10 PDF of the best-fit structural model (red) compared to the measured PDF (blue) of HP3 (Form I) with difference curve offset (green). Fitting is carried out over the range (1–50 Å) giving a fit residuals of $R_w = 0.23$. 106

6.11 (A) Molecular packing in the best fit structural model (#8) for Form I, viewed along the [001] direction. (B) The lateral aggregation of extended chains showing the associated hydrogen bonding cross-linkage. The hydrogen bonds are pointing in the [100] direction as in (A) while the figure is viewed along the [00$\bar{1}$] direction for direct comparison to (C) the lateral packing suggested by Blackwell and Gardner; figure adapted from Blackwell and Gardner [158]. (D) Packing of the non-hydrogen-bonded chains in the [001] direction shown with the (100) plane parallel to the page. The blue arrows highlight the rotation of the diphenylmethane units with respect to the neighboring chains. 107

6.12 Measured PDFs (blue symbols) of sample HP5 with fits of the 16 structural models (red lines) with the difference curve plotted below. (A) sixteen sub-panels show the fits to all models in the low-r region and (B) fits to the intermediate-r region. 108

6.13 Comparison of measured PDFs of HP5 (blue) (Q_{max}=11.3 Å^{-1}), with models 1–16 superimposed (red) for direct comparison. Pearson coefficients listed for reference. 109

6.14 Best fit PDF (red) to measured PDF (blue) of HP5 (Form II) with difference curve offset below (green). The fit is carried out over the range of 1–50 Å, resulting in fit residual of $R_w = 0.33$. 109

6.15 Molecular packing in the best fit structural model (#3) for Form II, along the (A) [010] direction and (B) [001] direction with hydrogen bonding linkages shown in the [010] direction. 110

7.1 Dark-field STEM images of Pt nanoparticles supported in zeolite Na13X and reduced ex situ at (a) 438 K, (b) 573 K and (c) 623 K, with their corresponding particle size diagrams. 119

7.2 Simulated PDFs from fcc structure refinement superimposed on the measured Pt PDFs at 518, 573 and 623 K for the (a) MM and (b) LNSD models. Differences are shown offset below the fits and black dashed lines show the size-dependent signal damping refined for the respective models. 120

7.3 Refined mean particle sizes during *in situ* reduction, using a spherical MM (D) and LNSD model (P size). 121

7.4 Histogram of the STEM results (bars), with the results of the lognormal size distribution (LNSD) and the mean diameter (D) obtained for the MM, for the samples reduced at (a) 573 and (b) 623 K. 123

7.5 Number-weighted lognormal distributions obtained through refinement of PDFs from samples reduced from 518 to 623 K. 125

8.1 The structures of α-ZrP and ZrPP are shown along the layers (a) and (c) and perpendicular to the layers (b) and (d) respectively. Light blue spheres and octahedra represent zirconium, orange spheres and tetrahedra are phosphorus, red spheres are oxygen, and gray is carbon. The disconnected oxygens in ZrP are the intercalated water molecules. 129

8.2 Laboratory XRD patterns for (a) bulk α-ZrP, (b) H–Zr hybrid, and (c) Na–Zr hybrid, respectively. 130

8.3 Reduced structure functions $F(Q)$ (a,c,e) processed from the x-ray scattering intensities collected from a synchrotron light source. It is clear that a significant amount of additional structure information is gained when considering the scattering at higher momentum transfers. The respective PDFs $G(r)$ (b,d,f) are shown on the right. 134

8.4 PDF fits (red) of the α-ZrP structure model to the measured data (blue): (a) fit of the bulk structure to the crystalline sample, and fit of the single layer model to (b) H–Zr and (c) Na–Zr. Difference curves (green) are offset for reference. 136

8.5 PDF fits (red) of the single layer ZrPP structure model to the measured data (blue): (left) (a) H–Zr and (b) Na–Zr and (right) (a) H–Zr unloaded and (b) H–Zr loaded. Difference curves (green) are offset for reference. 137

8.6 (a) The resulting PDF from the total scattering measurement of ZrPP over 0.1-7.0 Å^{-1} is shown with the resulting structural fit over 1–100 Å and difference offset below. A fit of the layer-layer stacking model is also shown to 150 Å. (b) The PDFs calculated from the reduced total scattering structure functions including the first Bragg peak Q_{min}=0.1, and omitting, Q_{min}=0.7, are overlaid. The difference is overlaid with the layer-layer model from (a) showing that the first Bragg peak in the diffraction data encodes this correlation in the PDF. 142

8.7 (a) The PDFs from the higher Q-resolution total scattering measurement and from the previous analysis overlaid for comparison. There are no obvious interlayer structure correlations in the H–Zr sample. (b) The PDFs obtained from the reduced total scattering structure functions including the first Bragg peak (Q_{min} = 0.4 Å^{-1}) and omitting it (Q_{min} = 0.7 Å^{-1}), are overlaid. (c) Zoomed plot of the difference to show that there is a small signal present. The interlayer model from ZrPP was fit to this signal to find that it gives a spacing of 10.26 Å which is close to the estimate from the Bragg position in the original lab XRD data. 144

8.8 (a) The reduced total scattering structure functions $F(Q)$ for the 1:0 and 1:2 phosphonate:phosphate H–Zr materials are overlaid for comparison. (b) The high-r region of the resulting PDFs are offset and compared. Of particular note is the more pronounced oscillation in the 1:0 sample. 145

8.9 (a) PDF fit (red) of the α-ZrP structure model to the measured data (blue) with difference below (green). (b) As in Figure 8.7, a difference was taken between PDFs processed with and without the first Bragg peak in order to extract the interlayer structure PDF signal (blue). The PDF from fitting the ZrPP interlayer model (red) and difference (green) are also shown. 146

8.10 (a) Comparison of the PDFs measured from the H–Zr hybrid unloaded and loaded with Tb^{3+}. Qualitatively, the PDF traces are nearly identical. The dPDF is shown offset below (magnified $\times 2$), showing that entirely new structural correlations emerge related to the Tb^{3+} environment after subtracting away the scattering contributions from the zirconium phosphonate-phosphate layers. (b) The first few peaks of the dPDF shown compared to all atom-pair distances containing a terbium atom for Tb–phosphate based structures from the ICSD database. 148

8.11 Fits of the Tb partial PDF for the best-fit Tb/phosphate based structures (red) to the measured H–Zr dPDF (blue). Difference curves (green) are offset for reference. Fits over a range of 1.0–12.0 Å are shown for the following structures (a) Potassium terbium tetrakis(phosphate(V)) (R_w=0.519), (b) Sodium terbium polytetraphosphate (R_w=0.517), (c) Potassium terbium diphosphate(V) dihydrate (R_w=0.471), and (d) scheelite-type terbium phosphate (R_w=0.449). Slices of the structures are shown respectively, viewed along the directions (e) [100], (f) [010], (g) [010], (h) [001]. The turquoise atom represents our origin Tb atom. O atoms are red, P atoms are orange, and all other Tb or other metal atoms are light blue. 150

8.12 (a) A (112) slice from the ZrPP structure with the layers offset, shifted so phosphorus atoms sit directly atop one another, and a Tb atom placed between the layers, compared to (b) a slice from the (001) plane of the scheelite-type terbium phosphate structure with neighboring Tb atoms in the center layer removed. . . 151

9.1 The crystal structure of ZIF-8 shown looking along the [001] direction (left) and along the [111] direction (right). 155

9.2 Static reaction cell. The pin on the right attaches to the goniometer to hold the cell in place. Precursor solutions are injected via syringe through the top ports, and x-rays penetrate the solution through the Kapton window in the center. . . 159

9.3 Flow cell used for *in situ* PDF measurements. Inlets mix (right side) then flow through an extended kapton capillary tube held in the beam path, before exiting the opposite end. 160

9.4 Time dependent *ex situ* transmission electron microscopy (TEM) data of ZIF-8 (a) 30 seconds (b) 10 minute (c) 1 hour. 163

9.5 (a) Low-r region of the PDFs measured for aqueous 2-MeIm, methanolic $Zn(NO_3)_2$ and crystalline ZIF-8. PDFs simulated from refined molecular or crystal (in the case of ZIF-8) structures are superimposed in black. (b) The experimental PDFs are then superimposed for direct comparison of the atom-pair distances associated with the respective molecular structures. The models used for the refinements in (a) are shown in (c): 1. 2-MeIm, 2. oxygen-coordinated zinc, 3. NO_3^-, 4. ZIF-8 crystal. The corresponding elements are carbon (brown), nitrogen (blue), zinc (silver), oxygen (red). 165

9.6 The PDF of the crystalline ZIF-8 standard (blue) is compared to that simulated from a refined structural model (red), with the difference curve plotted below (green). The long wavelength modulations are highlighted by the gray line, an approximate model of the density distribution between pore and framework, calculated as the Fourier transform of the first two Bragg reflections in a simulated powder pattern and damped by a Gaussian envelope corresponding to the experimental resolution. 166

9.7 (a) High-r comparison of the PDFs from the ZIF-8 standard and the product after nucleation. The standard is rescaled to fit the high-r signal in the nucleated product, showing that some long-range ordered crystalline phase has already formed. A zoomed plot of the region boxed by dotted lines is shown in the inset. (b) The difference between the product PDF and the rescaled standard shows that a significant signal persists, principally in the low-r region, which is substantially different from the final product. 168

9.8 (a) Low-r comparison of PDFs from the ZIF-8 standard (blue) and the ZIF-8 product directly after nucleation in MeOH:H2O (red). A PDF simulated from a single Zn(2-MeIm)$_4$ cluster (green) is offset below. Of particular note is the absence of a sharp peak at the Zn-Zn pair distance shown diagrammatically in (b) and indicated by the vertical dotted line in the Figure. This suggests the presence of a significant amount of Zn and 2-MeIm in the form of Zn(2-MeIm)$_4$ shown in (c), which does not have a distinct Zn-Zn pair contribution 169

9.9 ESI-MS spectra of mixtures 2-MeIm in methanol solution showing the presence of imidazole clusters in the solution (b) spectra depicting $Zn(NO_3)_2$ and 2-MeIm in 1:6 molar ratio. 171

9.10 Different configurations of Zn(2-MeIm)$_4$ optimized by DFT. 173

9.11 Examples of the different amorphous intermediate SROCs measured under similar reaction conditions (1:2 Zn:2-MeIm) are shown in green and purple, extracted from the measured data by fitting and subtracting the crystalline signal at high-r. The simulated Zn-Zn partial PDF from the ZIF-8 structure is given above for reference, and the partial PDF after fitting to intermediate 1 is shown. The black dashed line represents the spherical envelope applied to adjust the partial PDF for finite structural coherence of approximately ~15 Å. Additional dotted lines are given as reference markers for the approximate broad peak positions observed in the SROC and in the model. 175

List of tables

4.1 Peak positions extracted from the crystalline standard PDF with height A_i and width (standard deviation) σ_i obtained by fitting Gaussian functions, $G(r) = \sum_i A_i \exp\left(\frac{-(r-r_i)^2}{2\sigma_i^2}\right)$, onto the baseline for both the standard (stan.) and 0.25 wt. % suspension (susp.) PDFs. 61

5.3 Flowlac100, lyophilized, and melt quenched lactose aged for varying times at 40°C/75% RH. The crystalline component is estimated using least-squares and Pearson correlation methods (see text for details). d_c is the diameter of the coherent structural domain. 84

6.1 Samples measured. Casting T refers to the starting temperature of the hard cast. 92

7.1 Comparison of the mean particle sizes obtained from refinement of the PDF from the MM (D), the volume-weighted LNSD P_{size}, and the number-weighted LNSD D_{NWLNSD} with the values obtained from STEM D_{STEM} for the samples reduced at 573 and 623 K. 124

8.1 Summary of hybrid ZrP nanoparticles and control samples. 131

8.2 Refined models for the H-Zr and Na-Zr samples measured at X17A (NSLS), the H-Zr hybrid samples unloaded and loaded with Tb measured at F2 (CHESS), and the 1:0 phosphonate:phosphate H-Zr measured at 28-ID-2 (NSLS-II). Summary of PDF fit results using a single layer model. The c axis (originally 30.235 Å) was artificially modified to 400.0 Å to remove any interlayer correlations from the simulated PDF. The P atoms are refined in the original $C2/c$ symmetry, while Zr atoms are allowed to displace in z. Parameters for the previously reported bulk zirconium phenylphosphonate (ZrPP) structure are also listed for reference. . . 138

Abbreviations and symbols

Notation		Description
ADP	-	atomic displacement parameter
AFM	-	atomic force microscopy
API	-	active pharmaceutical ingredient
APS	-	Advanced Photon Source
BDO	-	1,4-butanediol
BNL	-	Brookhaven National Laboratory
CCD	-	Charge-coupled device
CHESS	-	Cornell High Energy Synchrotron Source
CRN	-	continuous random network
DFT	-	density functional theory
DLS	-	dynamic light scattering
DMSO	-	dimethyl sulfoxide
dPDF	-	difference pair distribution function

Continued on next page

Abbreviations and symbols – continued from previous page

Notation		Description
DSC	-	differential scanning calorimetry
ESI-MS	-	electrospray ionization mass spectrometry
ESRF	-	European Synchrotron Radiation Facility
EXAFS	-	extended x-ray absorption fine structure
fcc	-	face centered cubic
FSDP	-	first sharp diffraction peak
GMS	-	gravimetric moisture sorption
hcp	-	hexagonal close packed
ICP-MS	-	inductively coupled plasma mass spectrometry
ICSD	-	Inorganic Crystal Structure Database
IMC	-	isothermal microcalorimetry
LNSD	-	lognormal spherical distribution
MD	-	molecular dynamics
MDI	-	4,4'-methylene diphenyl diisocyanate
MOF	-	metal-organic framework
MM	-	monodisperse (spherical nanoparticle) model
NMR	-	nuclear magnetic resonance
NSLS	-	National Synchrotron Light Source
NSLS-II	-	National Synchrotron Light Source II

Continued on next page

Abbreviations and symbols – continued from previous page

Notation		Description
NTE	-	negative thermal expansion
PANI	-	polyaniline
PCC	-	Pearson product-moment correlation coefficient
PDF	-	pair distribution function
PSD	-	particle size distribution
PTHF	-	polytetrahydrofuran
RAPDF	-	rapid acquisition pair distribution function
RDF	-	radial distribution function
RMC	-	Reverse Monte-Carlo.
SAX	-	small angle x-ray scattering
SBU	-	secondary building unit
SC	-	solution calorimetry
SDA	-	structure directing agent
SROC	-	short range ordered component
SS-DSC	-	StepScan differential scanning calorimetry
STEM	-	scanning transmission electron microscopy
TEM	-	transmission electron microscopy
TR-SLS	-	time-resolved static light scattering
TPU	-	thermoplastic polyurethane

Continued on next page

Abbreviations and symbols – continued from previous page

Notation		Description
UMOF	-	unconventional metal-organic framework
WAX	-	wide angle x-ray scattering
WHO	-	World Health Organization
XRPD	-	x-ray powder diffraction
ZIF	-	zeolitic imidazolate framework

Math

Notation		Description
δ	-	peak sharpening coefficient for correlated motion
$\gamma_0(r)$	-	characteristic shape function
$\rho(r)$	-	the atom-pair density
ρ_0	-	average number density of the material
σ_{ij}	-	broadening term for PDF peaks
$A(\mathbf{Q})$	-	scattering amplitude function
$B(r)$	-	PDF dampening function coming from finite Q-resolution
c_α	-	concentration of atomic species α, or N_α/N.
$F(Q)$	-	reduced total scattering structure function.
$f(Q)$	-	x-ray atomic form factor or scattering length of an atom
$G(r)$	-	reduced atomic pair distribution function
$H(r)$	-	Heaviside step function

Continued on next page

Abbreviations and symbols – continued from previous page

Notation		Description
$I(Q)$	-	scattering intensity diffracted by a sample
N	-	total number of atoms or scatterers in a sample
$\mathbf{Q}$	-	magnitude and direction of the scattering momentum transfer
Q	-	magnitude of the diffraction vector
Q_{min}	-	minimum value of Q in a measurement
Q_{max}	-	maximum value of Q in a measurement
$R(r)$	-	radial distribution function.
R_w	-	residuals-function used as a measure of "goodness-of-fit"
r	-	distance
$\mathbf{r}_{ij}$	-	the vector joining the i^{th} and j^{th} atoms
$S(Q)$	-	total scattering structure function, normalized scattering intensity
Z	-	atomic number for a sample species

Acknowledgements

First of all, I would be nowhere in this endeavor without the support and guidance of my adviser Simon. Through discussions about physics and scientific reasoning, goal organization, writing proposals, collaborating with peers, mentoring students, and many others, he has taught me so much more than I could have ever expected. I am extremely grateful for his breadth of knowledge and experience, the great patience and trust he has shown me throughout this process, and the countless opportunities he has given me to work on interesting and important problems.

I thank my family, Mom, Dad, Steve, Will and Lane, for their love and support, and all that they have done to allow me to reach this point. They have taught me to be tenacious in work ethic, to always think critically, and have inspired me to persevere when the going is difficult.

I would like to acknowledge the many members and partners of the Billinge group, past and present, who have been there as friends, teammates, and mentors, including Soham Banerjee, Tim Liu, Chris Wright, Benjamin Frandsen, Xiaohao Yang, Chenyang Shi, Kirsten Jensen, Long Yang, Anton Kovyakh, Federica Bertolotti, Alex Beecher, Zach Norman, Zizhou Gong, Chris Gutierez, Neno Fuller, Joshua Choi, Milinda Abeykoon, Pavol Juhas, Emil Bozin, and Kevin Knox. I have also had the great privilege of working with many beamline scientists

and technicians with whom I have shared rich conversations and received substantial experimental support, including Sanjit Ghose, Eric Dooryhee, Milinda Abeykoon, John Trunk, and Jianming Bai at NSLS-II, J. Y. Peter Ko at CHESS, and Olaf Borkiewicz and Kevin Beyer at APS.

Finally, I would like to thank all of my collaborators and coauthors for their hard work and dedication. It has been a truly awesome experience to work with such a diverse group of individuals, to learn first-hand how science requires the collective efforts of a community, and to see the power of interdisciplinary collaboration. I would especially like to thank Abraham Clearfield and Luca Russo for their additional support.

To all who sacrifice sleepless nights at the beamline.

Preface

There are two separate events during my graduate studies that I believe give worthwhile context to the content of my dissertation. The first is that the United Nations declared 2014 as the International Year of Crystallography. [1] While previous years have been deemed for celebrating physics (2005) and chemistry (2011), I find this observance a particular testament to the importance that structure determination has played in shaping our understanding of many areas of physics, chemistry, and biology. 29 Nobel prizes have been awarded for achievements involving, directly or indirectly, crystallographic methodologies. [2] However, this dissertation is not about crystallography, though it does utilize the same underlying theories. It is actually about how to deal with materials where crystallographic ordering is significantly or entirely impaired, and I find it particularly exciting to participate in the efforts to build upon this rich foundation in characterizing structure at the scale of the atomic building blocks which make up the world around us.

The second event is that the 2016 Nobel prize in chemistry was awarded "for the design and synthesis of molecular machines", the works of synthetic chemistry by Sauvage, Stoddart, and Feringa which showed that the tailoring of molecular conformation and higher order organization can lead to interesting and useful functions on the nano-scale. [3] This dissertation is also not about synthetic chemistry, but it does study the structure and function of these

materials on a local scale. It is my opinion that this perfectly highlights the possibilities in designing materials of the future, in thinking about intermolecular and interparticle interactions, and how they might be built-in to provide novel properties to macroscopic functional materials.

Chapter 1

Disorder and heterogeneity in weakly scattering materials

This dissertation is concerned with the application of the pair distribution function (PDF) toward studying disorder in materials of technological interest. The PDF is a measure of the local structure in materials regardless of whether they are ordered or disordered, crystalline or amorphous, bulk or nanostructured. It is obtained from scattering measurements, and in this respect, I will focus on its application using x-rays. The methodology is well established in many instances [4, 5], but the focus herein will concern methodologies for studying weakly scattering materials where the advantages of this technique have not yet been fully realized. Further details of the PDF technique will be detailed in Chapters 2 and 3.

Classically speaking, the intensity of photons scattered by a single electron is proportional to the square of the electron radius $r_e = e^2/(m_e c^2)$ according to the Thomson scattering equation,

$$I_e = I_0 \frac{r_e^2}{r^2} \left(\frac{1 + \cos^2(\theta)}{2} \right), \tag{1.1}$$

at a scattering angle of 2θ and distance r. Due to the small cross section of the electron, this is a weak response at any appreciable distance relevant to an actual measurement. It is

tenable, however, given that the observed scattering intensities do not come from a single electron, but are summed from a collection of electrons within a macroscopic material. It is often sufficient to assume that scattered radiation does not interfere with the incident beam, and is overall a small proportion of the incident intensity (the kinematic approximation). The scattering of x-rays by electrons is in general *weak*.

The total intensities measured further depend intimately on the density and distribution of the constituent atomic species and packing thereof into macroscopic materials. It is here that the distinction is made for what I am considering *weakly scattering* materials in this thesis. This can manifest in several different ways, primarily dependent on the electron density of the constituent atoms and the density of the atoms within the total scattering volume.

The first case is in materials composed by elements with few electrons, or a low atomic number Z. The scattering amplitude from an atom can be given by its atomic form factor f which is related to the Fourier transformation of its electron density distribution $\rho(\mathbf{r})$. The integral of the density distribution over the effective volume of the atom $\int_0^\infty \rho(\mathbf{r}) dv_\mathbf{r} = Z$ and $f \to Z$ as the magnitude of the momentum transfer Q goes to 0. Therefore, the scattering intensity is proportional to Z^2, meaning that low-Z materials such as organics and hybrid organic-inorganics scatter substantially less than high-Z materials such as metals and many ceramics.

Another case of weak scattering from the sample can manifest due to a low atomic density. In terms of atomic packing, one might think of the idealized face-centered cubic (fcc) and hexagonal close-packed (hcp) models of close-packed spheres for many metallic compounds. In fact, many small molecule crystals have similar or even higher packing fractions [6]. This of course it not always the case. Size discrepancies in multi-element compounds and the

nature of the bonding can lead to a very broad range of atomic packing efficiencies observed in different materials. The extreme case can arise in microporous materials which contain significant void space within their structure. The nature of the porosity can be classed by the dimensionality: micropores ($d < 2$ nm, where d is the pore diameter), mesopores ($2 < d < 50$ nm), and macropores ($d > 50$ nm). For the sake of discussion, what actually matters is the the total void volume. This determines the reduction of electron density over the total scattering volume, which significantly reduces the amount of electrons available to scattering the incident radiation.

Weak scattering can occur in other ways. Many materials are composed of mixtures of separate phases: mixed polymorphs, crystalline and amorphous phases, particles in liquid suspension etc. If the component of interest represents a small fraction of the total system, then this too results in an overall lower signal intensity from that component over the total volume. The limits of detection and quantification for x-ray diffraction is typically quoted anywhere around 1–5 % by weight [7, 8], and even as high as 10 % for crystalline and amorphous pharmaceuticals [9]. However, the limit of detection also depends on the quality of the measurement and the modeling methodologies used to extract that quantity, and significant improvements in this value will be discussed in Chapter 4. As such, it is determined that it is possible to detect impurities phases and components with an order of magnitude better sensitivity.

A final form of weak scattering, can be thought of in terms of ordered versus disordered structures. Due to the nature of constructive interference in the scattering from highly crystalline materials, the majority of the scattering intensities are concentrated in sharp Bragg peaks which rise sharply above the background giving a high signal-to-noise. Technically,

the total integrated intensity for an amorphous material of the same composition, density, and volume, should give the same total integrated intensity. However, because the intensities are diffuse and spread out broadly against Q, the resolution of the signal over noise and background may be poorer. In practice, some intensity could also be lost to the regions of Q not measured, and structural deviations from this idealized case such as lower density.

All of these situations extend to the wide variety of organic and hybrid organic-inorganic materials which span the gamut in both structural complexity and technological applicability. These materials combine various aspects of order and disorder, which can significantly impact their macroscopic behavior. In the following subsections, I discuss several classes of such materials which will then be the focus of subsequent chapters. I will discuss current open problems in studying synthesis-structure-property relationships in these materials, and the state-of-the-art in local structural analysis using PDF methodology in each case.

1.1 Small molecules

Small molecules are broadly important across many areas of science and technology: as the building blocks or templating agents for many synthetic processes, *e.g.*, in industrial liquids and lubricants, and as active pharmaceutical ingredients (APIs) which will be the focus of the this section. The World Health Organization (WHO) model list of essential medicines includes a long list of anesthetic, analgesic, anti-epileptic, antiviral, immunosuppressant, and many more medicines which are considered critical to modern basic healthcare [10]. They are comprised almost entirely of small molecule compounds. The economic footprint of the pharmaceutical industry is enormous; it takes on average 10 to 15 years, and 2.6 billion dollars

(including the cost of failed drugs) to develop a new medicine [11]. It is clear that there should b.e a desire for high success rates to reduce those costs, yet between 70 and 90% of drug candidates in the pipeline are considered to have low solubility [12]. This is an enormous bottleneck in further development and has led to a vast movement in formulation engineering techniques to address these physical property limitations [13].

The physical form and formulation are fundamental to the development of successful solid dosage forms. They can determine solubility, release rate, and dosage, all critical to both efficacy and safety of the drug. A large area of study is centered around particle size reduction and amorphization to increase solubility [13]. However, the noncrystalline nature of the APIs creates problems both in uniquely identifying the form of the drug in the formulation, and in quantitatively analyzing their structure. These are areas where PDF analysis has been applied successfully. PDF traces have been shown to provide unique fingerprints for amorphous compounds even when the the standard diffraction halos may not be suitably differentiable [14]. The method further allows for quantitatively assessing the structural coherence and any differences or similarities of the nanostructured versions compared with bulk forms. Major interest has been in detecting variation in short range ordering in amorphous drugs that may develop due to different starting states or preparation routes such as milling [15], dehydration [16], compaction [17], or quench cooling [18]. However, there has been an issue with many of these studies in that low x-ray energies have been used which are not suitable for sufficient data quality in a PDF analysis, and this has led to a large body of ambiguous results when using PDF on pharmaceutical compounds [19].

During formulation development, it may be necessary to quantify the concentrations of separate phases. Amorphous and crystalline components can be intentionally mixed to

modify the physical properties of the formulation [20]. Subsequently, various steps during processing or aging can also lead to the development of undesired phases. There are a variety of ways to quantify amorphous and crystalline content [9], though there is currently no broadly applicable standard technique and current techniques lack quantitative accuracy which is crucial in a drug formulation since this affects the dose that a patient receives. Phase quantification for amorphous and crystalline pharmaceuticals has been demonstrated using the PDF method [21]. This was carried out by running a linear least-squares optimization which summed reference patterns for each phase weighted by its concentration. Due to the PDF method's sensitivity to structural coherence on the local scale, it should be broadly applicable to different compounds and useful even for formulations with multiple disordered phases. However, the accuracy and sensitivity of this method for pharmaceuticals have not yet been systematically studied. One reason may be that the artificial mixing of known phase concentrations can lead to highly inhomogeneous samples which can subsequently affect the measurement, depending on where the sample is probed [22].

Another issue with high energy formulations is that they tend to revert to lower energy forms. In other words, they crystallize. This leads to unstable formulations which may not have a suitable shelf life to make it to market. There are many methods which have been developed for formulation stabilization which focus on tailoring intramolecular versus intermolecular interactions in the formulation. By mixing the APIs with excipients, typically polymers or sugars, the combination of higher solubility and propensity to remain in a metastable state can be optimized. An important aspect of this process is in choosing the excipient material. The drug's solubility within the excipient can determine whether the formulation remains suitably mixed or phase segregates. All the while, this processing must

maintain (and sometimes enhance) the therapeutic action of the individual constituents, *i.e.* the intramolecular structural integrity of the drug. The understanding of component interactions is therefore pivotal in formulation design. Numerous studies in the literature have focused on determining the degree of mixing in multicomponent dispersions [23, 24]. Such analysis is similar to the method described for phase quantification. For phase separated systems, the PDF is assumed to be an incoherent sum of API-API and excipient-excipient interactions. It should be easily reproduced by a linear combination of reference patterns from the individual phases. In miscible systems, intimate mixing should yield a third significant component in the PDF signal related to API-excipient interactions. This should lead to poor fitting from the reference data or scale factors which deviate significantly from known weight percentages. These studies have also primarily used insufficient data quality [23–31], but this method has been demonstrated using high quality data more recently [32].

Another important area is in understanding phase transformation and disordering mechanisms. Such analyses can be useful for determining issues related to compound stability during processing and comparing the viability of different processing methods. Simple studies have been carried out by comparing the level of disordering occurring during the milling and compaction of different APIs [33], and in showing how disordering could occur from water loss and structural collapse of the dihydrated crystalline form upon both heating/drying and melt quenching [34]. More rigorous *in-situ* studies have started to emerge in studying the mechanisms of disordering [35] and crystallization from solution [36].

In Chapter 5, I will discuss the characterization of an important excipient material, lactose. The characterization will comprehensively assess the effects of different amorphization routes, the crystallization behavior, and phase quantification of amorphous/crystalline mix-

tures.

1.2 Organic polymers

Organic polymers are another class of weakly scattering materials due to their low atomic number and their low degree of structural order where various types of disorder manifest on multiple length-scales. This has major implications on the properties and applications, for example in areas of both synthetic polymers and biopolymers from proteins (*e.g.* silks fibers) and sugars (*e.g.* cellulose). There is a massive industry, e.g., in thermoplastic elastomers. They are highly versatile materials with wide ranging applications from construction, transportation and healthcare, to packaging and consumer goods [37]. Thermoplastic polyurethanes (TPUs) comprise a large subset that form the basis for many high-performance films, coatings, adhesives, fibers, and smart materials. The TPUs are block copolymers formed from soft segments of polyester or polyether chains, which give the material its plasticity, and hard segments formed by addition of a chain extending diol and a diisocyanate [38], which provide rigidity and elasticity through physical crosslinking. The nature of micro-phase segregation of these soft and hard domains dominates many of the bulk properties of these materials. They are not long range ordered, making studies of their structure extremely difficult. The structure and morphology of the hard phase has been a topic of particular interest since the x-ray investigations by Bonart *et al.* [39] in 1968 to study the nature of the cross-linking between molecules in the hard segments. Structures such as this have been described as semi-crystalline or paracrystalline due to the limited ordering of the chains. The crystallinity of the hard segments may be artificially increased through elongation and annealing treat-

ments used to promote chain alignment, but the resulting material is still often only weakly crystalline. Therefore there are two substantial issues that PDF analysis can address. How can all the aspects of conformation, chain persistence and packing, microdomain structure, phase content, and interphase mixing/segregation be studied with high quantitative accuracy? Also, how can this be done using the material in its native rather than modified state?

This does not just apply to elastomers. Aspects of structure phase segregation play a critical role in the properties of many polymer systems, for instance in synthetic conjugated polymer systems [40]. It has important implications on the charge transport processes in these materials for conductive polymer purposes, such as for polypyrrole and polyaniline systems [41]. An interesting case study has been the utilization of PDF analysis on polyanilines (PANI). PANI is a class of low density, easily processable, and relatively inexpensive conductive polymer which has potential applications in gas separations and organic electronic applications, despite neutral pH and high temperature instability [42, 43]. The backbone is built up from monomers in reduced (y) and oxidized ($1-y$) states, where $0 \leq y \leq 1$ and each oxidation state can exist in the base or salt form by doping with protonic acids [44]. Early PDF studies investigated the position of bromine sites on doping of dilute hydrogen bromide into the emeraldine base form of PANI [45, 46], and the local structural order in the amorphous polymers as a function of synthesis and processing (undoped-doped-dedoped samples) [47]. Further decomposition of intra- and interchain correlation contributions showed reversible changes in the intramolecular structure on doping/undoping from the as-cast base form, while the interchain structure depends on its processing history which correlates with enhanced selectivity in gas diffusion studies for the redoped PANI films [48], and provided insights into the molecular origins of charge transport in these systems [49]. There are a

handful of other PDF studies on synthetic polymer systems, but they are over a decade old and therefore have not yet taken advantage of the massive improvements in the experimental and data processing tools available.

In Chapter 6, I will discuss a comprehensive PDF analysis of a family of TPUs. Issues including hard phase structure solution, chain conformation, and phase quantification will be addressed in the context of state-of-the-art data analysis methods, showing the potential value of the PDF toolset in modern polymer research.

1.3 Microporous materials

Microporous materials typically consist of a framework constructed by linking or bridging units which envelop pores on the order of one nm. They are a natural extension of traditional polymers as the framework is constructed of monomer-type building blocks termed secondary building units (SBUs), commonly associated with zeolites and metal-organic frameworks (MOFs) [50, 51]. During synthesis, solvents or other secondary species are used as structure directing agents (SDAs) to template the framework, which may be followed by some removal process depending on the stability of the framework alone. The results are low density porous materials with high surface area and a broad range of functionality regarding gas adsorption and storage, catalysis, separations, and many other uses. A high degree of geometric flexibility has been found to result in interesting macroscopic properties which result from local structural distortions, for example negative thermal expansion (NTE) [52, 53]. In general, the appearance of studies using PDF methods to characterize these materials is fairly recent, since around 2005, and while rapidly increasing, still relatively lim-

ited in number. Therefore it is incredibly important to expand the methodologies used for characterizing these materials so that more powerful tools will be available.

1.3.1 Zeolites

Zeolites comprise a large family of nanoporous, aluminosilicate minerals, which are widely used as absorbents and catalysts in the petrochemical industry. Other types of microporous mineralogical materials display similar structural properties, such as aluminosilicate based geopolymers and hydrate gels which can be used for gas capture or as functional building materials. Despite their topological complexity, many zeolitic materials form very well-ordered long range structures amenable to crystallographic techniques. For example, there are 225 ordered zeolite framework types on the database of zeolite structures [54], but there are still prominent cases where where disordered-type structures can occur, *i.e.* the other seven 'partially disordered' frameworks cataloged. This has been noted for zeolite β which occurs through displaced layers on (001) planes, allowing for various polytypes including heavily faulted versions to form [55]. An early demonstration of PDF characterization on zeolites showed that it was possible to refine the local structure of different polytypes of highly faulted zeolite β by coupling neutron and x-ray PDF data [56]. Improved starting models were achieved through classical force field optimization of the reported crystal structures, and in fact, dealing with such complicated structures on a local scale typically requires both judicious limitation in the number of parameters being refined, and coupling with optimization methods to ensure that the resulting structures are energetically feasible. Success using this methodology has been further demonstrated through the characterization of a disor-

dered layered aluminosilicate clay, metakaolin, through iterative PDF refinement and DFT optimization [57].

Another target area of disorder in zeolitic materials is in determining the locations and interactions of guest-species within the framework. This can include the very SDA species used in templating the framework, the interaction with subsequent gas adsorbate species as in separations, or in the growth and containment of catalytic nanoparticle species. A general idea of guest species sites can be determined by mapping the residual electron density, but this requires accurate crystal structure refinements [58]. Plus, this additionally falls into the category of lower resolution characterization, and cannot typically resolve the specific structure, orientation, or sites of interaction in the host. Here also, the PDF technique has aided, for example in determining the local arrangement of Cs^+ ions within the zeolite ITQ-4 [59], or the structure of nanocrystalline Na clusters within silica gel pores [60]. Moving this a step forward, would be the quantitative structural analysis of guests as a function of some reaction input parameters. In Chapter 7, I will discuss the growth of metal nanocluster populations supported within a zeolitic framework, showing how the size distributions can be extracted and quantitatively determined using PDF analysis.

1.3.2 Metal organic frameworks

It is possible that MOFs may become the next technological iteration of zeolites for many applications. Instead of linking SiO_2 tetrahedra as in zeolites, MOFs are formed by combining metal ions or metallorganic clusters with organic ligands. They can form direct topological analogues to zeolites as in the case of zeolitic imidazolate frameworks (ZIFs) which consist

of divalent metal ion centers such as Zn^{+2} or Co^{+2} tetrahedrally coordinated by imidazolate-type linkages [61]. However, the choice of metal or node species, coordination preference, and ligand chemistry and size, can all be tailored, creating a vast landscape for designing the pore structure, surface area, and chemically active sites in the material. However, the full understanding and interplay of these effects is limited. The full-scale commercial realization of these materials has not truly been met, a fact exemplified by small number of companies who have actually taken such materials to market [62].

Like zeolitic materials, MOFs are considered metastable materials with respect to dense-phase assemblages [63], however they are softer and more flexible than zeolites [64]. Stemming from this, it seems to be the case that the chemists tend to produce a large number of disordered structures in the lab, which may be inherently nanocrystalline or amorphous, which then get thrown into a drawer for indefinite storage. It may truly be that they do not have desirable properties, *i.e.* lower porosity in certain cases, though I expect that many times it is simply to avoid a dark path of characterization difficulties. However, the use of PDF modeling has already been shown to be amenable to solving the structures of locally ordered nanoporous materials. This has typically been done using Reverse Monte Carlo (RMC) modeling methods [65–67], though given the right input information and choice of constraints, small box modeling methods can prevail as well [68].

It is plausible that the wide availability of ordered structures of the same MOF family or zeolitic analogues, and coupled with MD or DFT geometry optimization, might provide suitable starting points to model the disordered structures in these cases. In fact this has already been done for amorphous ZIFs which show complex structure landscapes. They tend to go through reconstructive transitions, as demonstrated in a recent paper detailing

mechanosynthesis-induced amorphization of ZIF-8, and further crystallization to reveal a novel topology [69]. As such, it has been a focus to characterize these amorphous phases to better understand the nature of the transitions. PDF analysis has been carried out on a variety of amorphous ZIFs prepared by heating the starting ZIF structures which then go through a reconstructive phase transition producing a continuous random network (CRN)-like topology, similar to that of amorphous SiO_2 [70]. Milling was shown to have a similar effect [71], though a recent comparison between the milling of Zn versus Cd based ZIFs showed that unlike Zn, the Cd based ZIFs experience a change in local structure on amorphization suggesting differences in the amorphization mechanisms of the two families [72]. While no long-range ordered porosity is maintained in these amorphous forms, there are still pores, or distributions of pore size/shape which are shown to change slightly with linker size. While not rigorously studied yet, this leaves an important area open in using PDF analysis for quantifying pore structure in disordered nanoporous materials. This could also aid as a constraint in implementing more small-box modeling type methodologies toward modeling the structures of nanocrystalline, nanoporous materials. The study of pore structure with PDF could be further extended to studying possible local symmetry breaking behavior of different pore structures in highly ordered nanoporous materials where an average structure is already known.

The study of local distortions in higher crystallographic symmetry nanoporous structures is not without precedent. Two prime examples are the studies of NTE referenced earlier for both zeolites and MOFs which respectively showed local tetrahedral distortions and the presence of transverse vibrational modes on bridging ligands as the local mechanisms for these materials macroscopic behavior. Other stimuli driven behavior in MOFs have also been

determined via PDF analysis. There are a handful recent studies including the hysteretic effects of gas sorption on ligand binding geometries [73], and the precise atomic mechanisms allowing temperature dependent structural transitions and relationship between hydration and gas sorption mechanisms [74]. A very recent study observed local distortions in M_6O_8 (M = Zr, Hf) nodes similar to the bulk MO_2, despite no effect on the long range symmetry of the MOF [75]. This was particularly interesting in that the transitions were inverted, symmetry-lowering with increasing temperature, and that they occurred at much lower temperatures than the bulk. Such behaviors could hold potential applications by influencing the electronic state of the active sites, allowing for tailoring of the activity at catalytic sites over particular ranges of operating conditions.

Both the site activity and pore size/geometry play an integral partnership in determining the sorption properties of the nanoporous materials. The topology of the channels can determine gas, solvent, or ion transport properties of the material. Pore size can imbue size-selectivity toward different guest species, and the presence and type of active sites can determine the type of binding, physisorption or chemisorption. While sorption behavior and capacity can be routinely probed, a quantitative atom-scale understanding of the interactions between guest and host remain difficult to obtain. In this respect, inelastic neutron scattering has been used to determine the nature of H_2 binding in both zeolites [76] and MOFs [77], which work particularly well due to both the considerable mobility of H_2 within these large frameworks and its large neutron scattering cross section, allowing for a high signal to be obtained even over the scattering from the host. A higher resolution picture of the binding could be achieve using single crystal x-ray diffraction [78], but this of course relies on both the framework being highly crystalline, and in this case having a large open-pore structure

which allows for more distinct adsorption sites. This is another area where PDF methods have been extremely useful in determining the binding properties of gas species such as N_2, H_2, and I_2 [53, 79, 80]. Alternatively, moving toward heavy metal sorbents, another effective technique can be to use x-ray absorption spectroscopy to determine the local environment of the sorbent [81], but again lose out on the structural details of the other components.

An interesting class of MOFs which do not meet the common prerequisite of crystallinity but display useful properties as ion exchangers are the unconventional metal organic frameworks (UMOFs), pioneered by the Clearfield group [82]. They are termed unconventional for the very reason that despite their lack of long range order, they are still highly porous. The UMOFs typically consist of layers of tri- or tetravalent metals including aluminum, zirconium, and tin, combined with phosphonate linkers, and they can display a high level of selectivity for ions of difference valence. The lack of a quantitative structural solution for these disordered materials, coupled with their interesting ion exchange behavior make them a good case study for a comprehensive PDF investigation. In Chapter 8, I will discuss a study that combines both local structure determination of a weakly ordered UMOF and determines the binding behavior. In this case, multi-scale analysis shows how the PDF methodology can be used to study simultaneously the atomic structure of a disordered material, the structure and local ordering of the pores, and the ion specific binding sites.

1.3.3 Nanoporous framework formation

For the sake of discussing framework formation, it is helpful to lump zeolites and MOFs back together. That is not to say that the processes which govern the development of the frame-

works from their precursor constituents are necessarily the same, but rather that they have so far been studied using similar techniques, and that the understanding on the level of the atomic-scale mechanisms controlling the formation of primary building units, aggregates, and other precursor phases is still limited. These reaction systems utilize hydro- or solvothermal conditions which are inherently 'dirty', meaning that the pot contains both metal and ligand precursors, dissociated species left over from the precursors, solvents, SDAs, and intermediates all at the same time. This makes it quite difficult to isolate the particular species of interest in the system.

Progress has been made in identifying the fundamental building blocks or SBUs which assemble to form the framework structures using several different methodologies. The combination of small and wide angle x-ray scattering (SAXS/WAXS) techniques have allowed the observation of precursor particle populations during synthesis [83]. Similar characterization has been performed using electrospray ionization mass spectrometry (ESI-MS) to measure the precursor cluster mass distribution in addition to dynamic light scattering (DLS) to observe the development of cluster size populations with time [84]. For zeolites, some success has been achieved in characterizing the formation of amorphous zeolitic gel precursors using PDF measurements and RMC modeling. The presence of ring structures forming in the gels was detected prior to crystallization [85]. This can be compared to analysis by NMR or EXAFS of element specific local environments in the materials, but gives more complete structural information about the entire precursor units [86, 87]. In fact, for MOFs, the SBUs have been identified to some extent using EXAFS [88], ESI-MS [89], and SAXS/WAXS [90]. Interestingly, the self assembly process does not necessarily derive from the expected SBUs from a structural standpoint, as evidence by an atomic force microscopy (AFM) study which

determined that the growth units could actually be simpler fragments of the precursors and solvent [91]. This leads to a further complication, that the identification of SBU units does not necessarily ensure a specific mechanism of assembly. Another possibility is the formation of medium range ordered intermediate phases or 'gels' [90, 92]. It is plausible that these phases might reconstructively assemble into a crystalline state given the evidence from the milling studies previously mentioned for ZIF-8. Such higher order structuring has been observed in using transmission electron microscopy (TEM). The growth of zeolitic single crystal species was observed from the gel-liquid interface between solution and amorphous gel aggregates [93]. There are limitations, particularly in the possibility of the analytic probe modifying the system. TEM beam damage for example can be significant for these soft materials, though is has been shown for ZIF-8 that similar kinetics, morphology, and crystal structure could be achieved under TEM and bulk synthetic conditions [94]. The usage of electrospray ionization leaves questions regarding the extent to which the ionized fragments measured truly represent the state of the system in its natural state. In Chapter 9, an *in situ* PDF method is employed to study the early stage structural development of ZIF-8. The PDF method has previously made vast advances in understanding nucleation of metal nanoparticles through direct *in situ* observation of their formation [95–101]. However, until now, it has never been employed for solution based synthesis of soft systems and therefore warrants investigation to see what information can be learned, and how it could be improved for these systems.

-

Chapter 2

Pair distribution function analysis and modeling methods

The pair distribution function gives a scaled histogram of atom-pair distances in the material. It is averaged over all atoms in the scattering volume and the total time of the experiment, giving a measure of the average radial structural environment of all the atoms. A qualitative depiction of the relationship between the atomic structure and PDF is shown in Fig. 2.1.

2.1 X-ray scattering

In depth accounts on the theory of x-ray scattering are widely available [102–104]. I reproduce here only a few main points to give context to the methods used in this thesis. By not assuming any periodic nature of the materials at hand, properties of order and disorder can be studied, in a real material, on the same footing.

Shining a beam of x-rays onto a collection of atoms, the amplitude function for the scattered wavefront $A(\mathbf{Q})$ can be described as the Fourier transform of the electron density $\rho(\mathbf{r})$ by

$$A(\mathbf{Q}) = \int \rho(\mathbf{r}) \exp\left(i\mathbf{Q}\cdot\mathbf{r}\right) dv_{\mathbf{r}}, \tag{2.1}$$

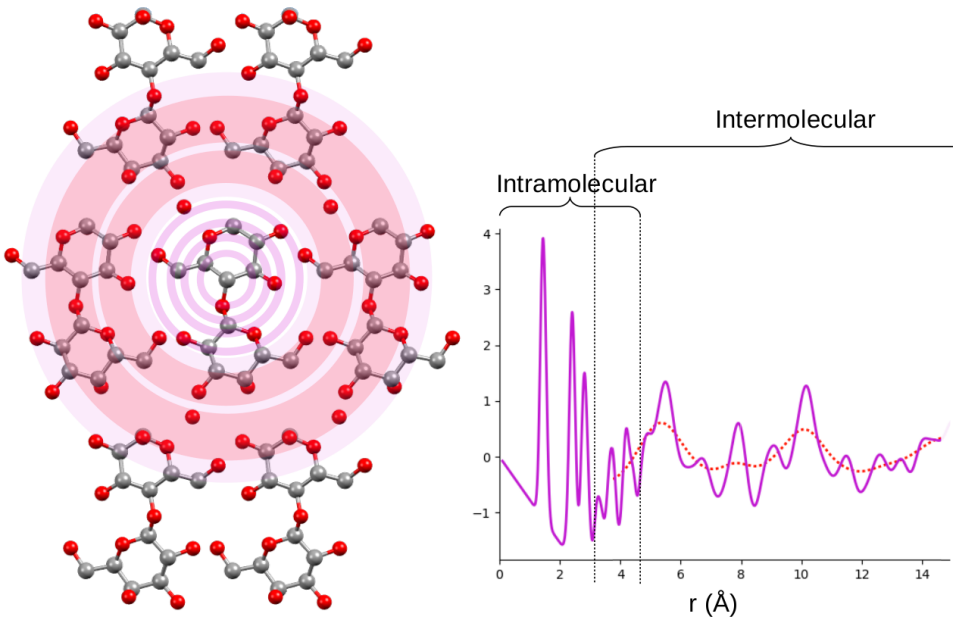

Figure 2.1: Visualization of the relationship between peaks in the PDF and the actual atom-pair distances in the sample structure. In molecular materials, there are two characteristic regions. The intramolecular region consists of sharp, well-defined peaks which correspond to the distances between directly bonded atom-pairs within a molecule. The intermolecular region consists of broadened peaks which come from distances between pairs of atoms located within separate molecules.

integrated over the total volume $v_{\mathbf{r}}$ of the scattering object. The quantity experimentally measured by the detector is the square of the amplitude function or the intensities, $I(\mathbf{Q})$, given as

$$I(\mathbf{Q}) = |A(\mathbf{Q})|^2 = \iint \rho(\mathbf{r})\rho(\mathbf{r}') \exp\left(i\mathbf{Q} \cdot (\mathbf{r}' - \mathbf{r})\right) dv_{\mathbf{r}} dv_{\mathbf{r}'} \tag{2.2}$$

where r' is denoted as the independent variable of the duplicate electron density distribution. It it shown that the intensities measured correspond to a Fourier transforming the autocorrelation function of the electron density. The electron density function for the scattering object can be described instead in terms of *atomic* density. The total density is redefined in terms of contributions from the individual atoms, replacing the density functions with the atomic scattering factors f for the respective atoms. The f factors are a function of magnitude and

direction of **Q**, however I consider only the dependence on magnitude for the purposes of this thesis, and write without the Q-dependence for brevity. The integrals are replaced by a sum over all pairs of atoms in the collection, as

$$I(\mathbf{Q}) = \sum_i \sum_j f_i f_j^* \exp\left(i\mathbf{Q} \cdot (\mathbf{r}_i - \mathbf{r}_j)\right). \tag{2.3}$$

In a powder diffraction experiment, the beam is shone through not one, but a large collection of these atomic groups arranged randomly, such that every orientation is sampled with equal probability. The orientational averaging means that the information from all directions are collapsed to one, reducing the vector **Q** to just the magnitude Q. An integration over all directions in spherical coordinates results in the well known Debye scattering equation,

$$I(Q) = \sum_i \sum_j f_i f_j^* \frac{sin(Qr_{ij})}{Qr_{ij}}. \tag{2.4}$$

By subtracting out the incoherent self-scattering terms, and normalizing by the average scattering per atom, Eq. 2.4 can be reformulated in terms of the reduced total scattering structure function given by

$$F(Q) = Q[S(Q) - 1] = \frac{1}{N} \sum_i \sum_{j \neq i} \frac{f_i^* f_j}{\langle f \rangle^2} \frac{\sin Qr_{ij}}{r_{ij}}. \tag{2.5}$$

2.2 The pair distribution function

Considering again the autocorrelation of the atomic density (or electron density) for an orientationally averaged scatterer, this is equivalent to a histogram of all the atom-pair distances

in the collection, averaged over all the atoms, and is called the radial distribution function, $R(r)$. It can be described as

$$R(r) = \frac{1}{N} \sum_{i} \sum_{j \neq i} \frac{f_i^* f_j}{\langle f \rangle^2} \delta(r - r_{ij}) \tag{2.6}$$

where δ functions, located at all the interatomic spacings and weighted by the scattering of the constituent atoms, have been summed and normalized by the total number of atoms and the mean scattering power. It is also described by $4\pi r^2 \rho(r)$ where $\rho(r)$ is the local atom-pair density and $4\pi r^2$ describes the increase in the size of the spherical shell at a distance r from the origin. $R(r)$ is typically considered in a modified form, the pair distribution function, $G(r)$, given as

$$G(r) = \frac{R(r)}{r} - 4\pi r \rho_0 \gamma_0(r) \tag{2.7}$$

where the second term results from the finite range of Q measured. The term $-4\pi r \rho_0$ creates a negatively sloping baseline related to the average atomic density of the material ρ_0. The additional $\gamma_0(r)$ is a characteristic function which further modifies the shape of the baseline. It results from the missing small angle scattering below Q_{min} in the measurement and is related to the size and shape of the domains. For bulk crystals, the small angle scattering is negligible and this term reduces to one. A rigorous derivation of this was shown by Farrow and Billinge [105]. $G(r)$ is obtained by direct Fourier inversion of $F(Q)$ by

$$G(r) = \frac{2}{\pi} \int_{Q_{min}}^{Q_{max}} Q[S(Q) - 1] \sin(Qr) dQ, \tag{2.8}$$

meaning it can be obtained directly from the experimental intensities after proper correction and normalization. Rigorous descriptions of all the corrections can be found in Egami and Billinge [4]. Furthermore, it has been shown that many of these corrections can be made using an *ad hoc* procedure [106], and the work in this thesis has utilized this method within the program PDFGetX3 [107].

2.3 Modeling the PDF

2.3.1 Basics

It is straightforward to simulate the PDF for an atomic model of a material. Excepting systems of a very large number of atoms, it is also a fast calculation with modern computers and algorithms. The programs PDFgui [108] and Diffpy-CMI [109] were used to perform these simulations for the work in this thesis, and following, I discuss the primary modeling parameters used. For crystalline materials, the PDF can be simulated using a crystal structure, similar to the case for a Rietveld refinement [110]. The PDF is calculated for the atoms of the unit cell, with periodic boundary conditions applied, by

$$G(r) = \frac{1}{Nr} \sum_i \sum_{j \neq i} \left[\frac{f_i^* f_j}{\langle f \rangle^2} \exp\left(\frac{-(r - r_{ij})^2}{\sigma_{ij}^2} \right) \right] - 4\pi r \rho_0 \tag{2.9}$$

where the δ functions of Eq. 2.6 are convolved with the broadening term $\exp\left(-(r - r_{ij})^2/\sigma_{ij}^2\right)$ where σ_{ij} is defined by

$$\sigma_{ij} = \sigma'_{ij} \sqrt{1 - \frac{\delta_1}{r_{ij}} - \frac{\delta_2}{r_{ij}^2} - Q_{broad}^2 r_{ij}^2}. \tag{2.10}$$

Here, $\sigma_{ij}^{'}$ is the root mean squared displacement coming from the atomic displacement parameters (ADP) tensors of the atom-pair. δ_1 and δ_2 are corrections that can be separately used to account for correlated atomic motion [111], and Q_{broad} is an instrumental broadening factor coming from the finite Q-resolution of the experiment. There is also a dampening of the PDF signal due to this finite resolution which is accounted for by multiplying the whole signal by $B(r) = e^{-(rQ_{damp})^2/2)}$. Both Q_{damp} and Q_{broad} can be determined by fitting to a calibration standard assumed to be perfectly crystalline. Other parameters can also be refined including lattice constants of the unit cell a, b, c, α, β, γ and the fractional coordinates of the atoms. The physical parameters can all be refined in order to achieve the best agreement between experimental G_{exp} and calculated G_{calc} PDFs by minimizing R_w,

$$R_w = \sqrt{\frac{\sum_{i=1}^{n}[G_{exp}(r_i) - G_{calc}(r_i, \mathbf{P})]^2}{\sum_{i=1}^{n} G_{exp}(r)^2}}, \tag{2.11}$$

given the set of refined parameters **P**, which indicates the goodness-of-fit.

2.3.2 Intra- versus intermolecular correlations

In the case of molecular materials, δ_1 and δ_2 are not suitable for describing the discrepancy in peak sharpening between the covalently bonding intramolecular pairs versus the more weakly interacting intermolecular pairs. PDFgui provides a third r-dependent sharpening term called $sratio$, which sharpens the peaks in the simulated PDF up to a defined cutoff distance r_{cut}. r_{cut} should be chosen based on the molecular species. For small rigid molecules, it should be chosen as the diameter of the molecule, while for larger more flexible molecules, it might be chosen as the average diameter of freely rotating groups. In layered molecular

materials, it should be chosen as the thickness of an individual layer. PDFgui cannot refine r_{cut}, though once the rest of the structure is refined, it can be varied manually to find the best fit, in which case, an effective size of the rigid units within the molecule can be determined.

Instead of the correlated motion parameters, a separate modeling procedure has been described [112, 113] in which separate ADPs are used to describe the mean squared displacements of intramolecular and intermolecular pairs. This can be performed using Diffpy-CMI by first calculating the PDF from a crystal $G_c(r)$ as described above, with ADPs U_{inter}. Then, the PDF is separately calculated for an individual molecule $G_{m1}(r)$ with U_{inter} and subtracted. Finally, the individual molecule PDF is calculated again $G_{m2}(r)$ but with separate ADPs U_{intra} and added, giving the total contribution

$$G_{total}(r) = G_c(r) - G_{m1}(r) + G_{m2}(r) \tag{2.12}$$

Prill *et al.* [113] suggest that δ sharpening parameters be turned off in this case, although for larger molecules, it is likely that atom-pairs located within the same rigid unit may experience a higher degree of correlated motion than atom-pairs located in separate units related by some or multiple free rotors.

2.3.3 Benchmarking fit quality for molecular compounds

In Figure 2.2, standard molecular material with a known structure are fit using the different low-r sharpening corrections to give a benchmark for the quality of fits that can typically be expected from molecular materials. The two compounds are α-lactose monohydrate measured at 300 K, and L-tryptophan measured at 100 K. The structure models used are CCDC

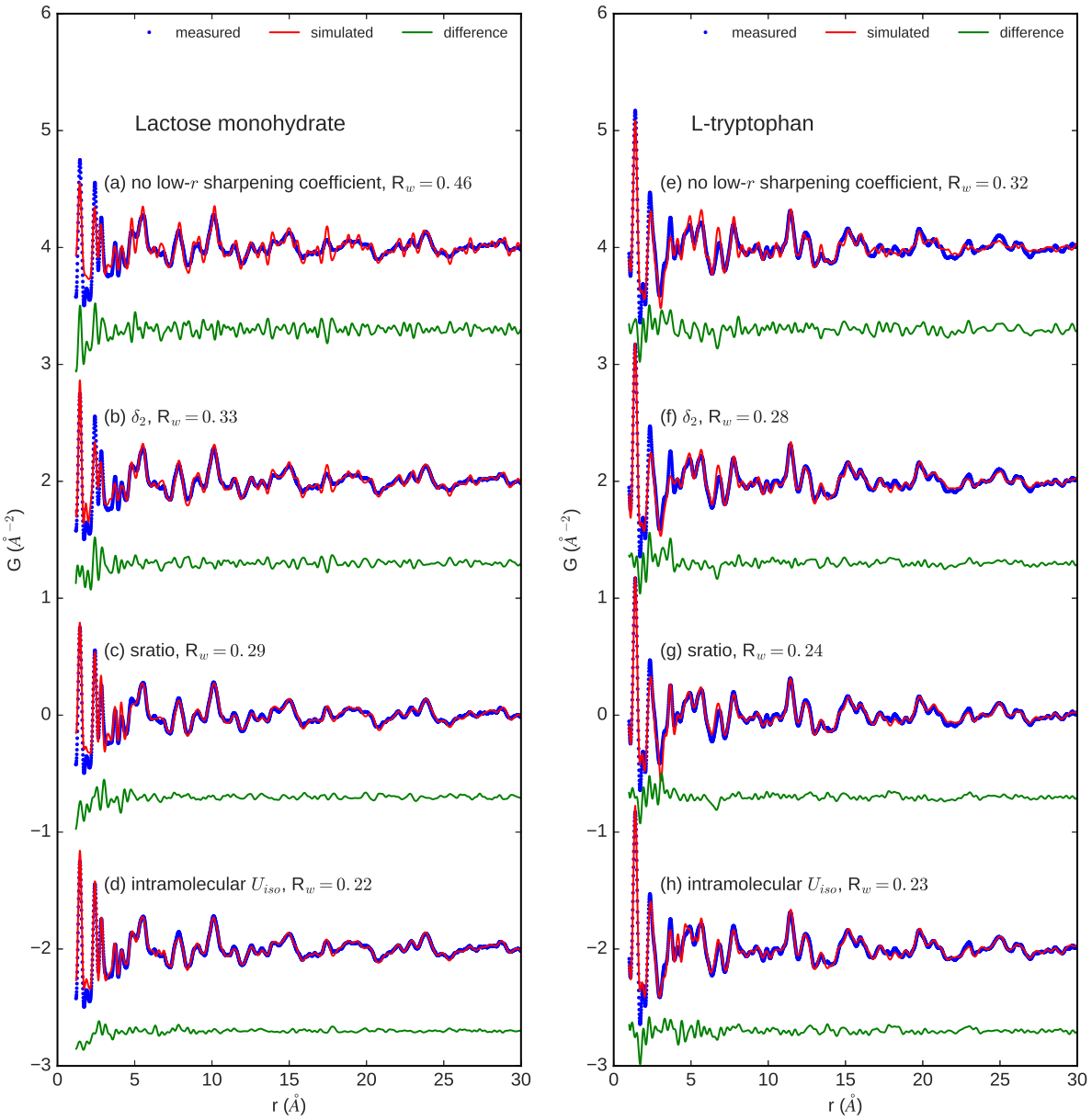

Figure 2.2: Benchmark goodness-of-fit, R_w values for known molecular crystalline compound structures (a-d) α-lactose monohydrate, where the fits correspond to (a) fitting with no low-r sharpening parameters, (b) using δ_2, (c) sratio using an r_{cut} value of 4.2, and (d) using separate intra- and intermolecular thermal parameters in Diffpy-CMI, all using a grid spacing of 0.01 which is the default from PDFGetX3. The same fit models are applied to the crystalline compound of L-tryptophan (e-h). An r_{cut} value of 3.8 was used for (g).

1202389 (LACTOS10) for lactose and CCDC 986568 (VIXQOK) for L-tryptophan, both from the Cambridge Crystallographic Data Centre, which have the space groups $P21$ (monoclinic) and $P1$ (triclinic) respectively. The molecular structures are shown in Figure 2.3. The refine-

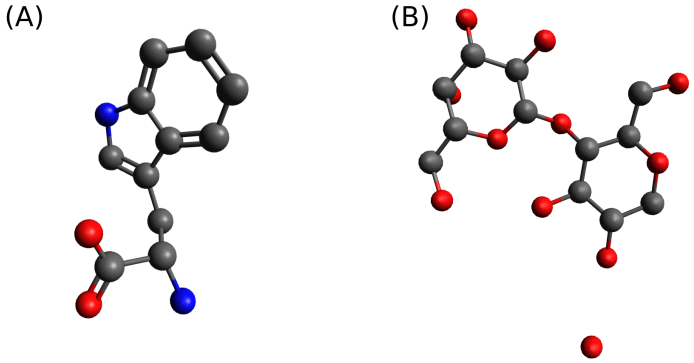

Figure 2.3: Molecular structures of (A) L-tryptophan and (B) α-lactose, where the atoms depicted are carbon (grey), nitrogen (blue), and oxygen (red). In (B), the extra detached oxygen atom represents the water molecule as in the crystalline monohydrate form.

ments include the lattice parameters by symmetry, a scale factor, a global isotropic thermal displacement parameter, and either no, or some, correction for the correlated motion which comes from the discrepancy between intra- versus intermolecular bonding in the material.

The starting lattice parameters for α-lactose monohydrate are $a = 7.982$, $b = 21.562$, $c = 4.824$, $\beta = 109.57$, which refine to $a = 7.937$, $b = 21.570$, $c = 4.812$, $\beta = 109.80$ with an intramolecular isotropic thermal displacement $U_{intra} = 0.0020$ and intermolecular isotropic thermal displacement $U_{inter} = 0.019$. For L-tryptophan the starting parameters are $a = 11.4305$, $b = 11.4645$, $c = 35.6057$, $\alpha = 84.421$, $\beta = 87.694$, $\gamma = 60.102$, which refine to $a = 11.399$, $b = 11.449$, $c = 35.378$, $\alpha = 84.755$, $\beta = 88.472$, $\gamma = 60.378$ with $U_{intra} = 0.00083$ and $U_{inter} = 0.011$. The goodness-of-fit values R_w show that values of around 0.2-0.3 are suitable for simple structural refinements of crystalline small molecule compounds. More detailed fitting could be used to improve the fit quality by including things

such as element specific and anisotropic thermal parameters, conformation distributions, or allowing slight displacive or rotational distortions in the orientations of the molecules.

2.3.4 Reduced structural coherence

For discrete crystallites, typically on the nanoscale or smaller, there is additional dampening of the PDF signal as related to the size and shape of the coherent structural domains, or crystallite size. In cases where the structure within the particle is still well described by the atomic packing of the bulk crystal model, this size effect can be quantitatively accounted for by additionally multiplying Eq. 2.9 by the characteristic function previously described, as in

$$G_{nano}(r) = \gamma(r)G_{\infty}(r), \tag{2.13}$$

which reflects the expected attenuation with increasing-r. Again, this characteristic function depends on the shape and size of the domains. When the peaks in the experimental PDF fall to zero before the resolution limited dampening factor does, then the point where they disappear gives a direct measure of the largest dimension of the coherent domain. The shape of the signal fall-off is then related to the shape of the domain. Theoretically, it is the autocorrelation function of the coherently scattering domains in the material. It can be determined experimentally by directly measuring the small angle scattering (SAXS), though analytical forms are solved for many basic geometries [114]. If the correct geometry is known, the respective size parameters can be refined to obtain useful information about the relative dimensions of the domains. In general however, the *shape* of the characteristic function is a very subtle effect. Usually, a similar R_w's and at least a semi-quantitative measure of the

average domain size can be achieved using the function for a spherical domain, given by

$$\gamma(r)_{sphere} = \left[1 - \frac{3r}{2d} + \frac{1}{2}\left(\frac{r}{d}\right)^3\right] H(d-r), \tag{2.14}$$

where d is the diameter of the domain. $H(r)$ is a step function with value 1 for $r \leq d$ and 0 beyond [115]. Other forms available for use with the Diffpy-CMI software.

In other cases, the atomic packing in a periodic crystal model is not suitable for describing the structure. In these cases, discrete atomic models can be built which describe both the atom positions and domain/particle shape explicitly. It is useful to simulate the PDF in such cases using the Debye equation, Eq. 2.5, directly, then Fourier transforming the result. In this case, the small angle scattering is also generated, and a suitable Q_{min} can be chosen for the transformation such that the characteristic function is incorporated directly by the explicit size and shape of the model particle.

2.4 Differential pair distribution function

The work also makes heavy use of analyzing separate constituents within multicomponent materials. In dealing with these cases, it is useful to reconsider the total scattering structure function in terms of the partial structure functions, which describe the scattering contribution between atoms of type α surrounded by atoms of type β. Then, the total structure function can be given by the sum of all partials as in

$$S(Q) = \sum_{\alpha}\sum_{\beta} \frac{c_\alpha c_\beta f_\alpha^* f_\beta}{\langle f \rangle^2} S_{\alpha\beta}(Q), \tag{2.15}$$

and it follows that the total PDF can similarly be described as a sum of all the partials as in

$$G_r = \sum_{\alpha} \sum_{\beta} \frac{c_\alpha c_\beta f_\alpha^* f_\beta}{\langle f \rangle^2} G_{\alpha\beta}(r), \tag{2.16}$$

or for example, in a system composed of two elements a and b (these could also represent two separate phases, molecular entities, or the components in a host-guest system)

$$G_{total} = G_{aa} + G_{bb} + G_{ab}. \tag{2.17}$$

In practice, rather than the partial contributions discussed above, it is much more straightforward to access the differential PDF (dPDF). This can be done experimentally by collecting two separate measurements of the same sample, varying the energy of the incident beam in the vicinity of the absorption edge of a particular element in the sample, and then subtracting the resulting signals. In the work of this thesis, a slightly simpler method is used in which the two measurements are instead of the material as-is and as-loaded with a secondary component of interest. The subtraction of the two signals in this case is valid when the structure of the *host* component does not change, which is a good assumption when loading levels of the component of interest are very low. In contrast to the partials described above, the dPDFs could be described for component a as $(G_{aa} + G_{ab})$ and for component b as $(G_{bb} + G_{ab})$. In other words the dPDF contains peaks pertaining the distances between the component of interest with itself and the component of interest with the host material, while the peaks between the host and itself will be removed. In addition, if there is no coherent structural relationship between component a and b, then the ab terms are considered negligible.

2.5 Phase quantification

As mentioned above, if a system composed of separate components is sufficiently phase segregated, then the interphase components are negligible and the total PDF can be considered as

$$G_{total} = G_{\alpha\alpha} + G_{\beta\beta} \tag{2.18}$$

or more generally the incoherent sum of all phases present,

$$G_{total} = \sum_{k} G_k, \tag{2.19}$$

where the sum runs over all separate phases k in the mixture. When this assumption is valid, it also allows the use of simple optimization methods to perform phase quantification in mixed phase systems with either measured standard for the separate phases, or simulated PDFs from models, without having to worry about inter-phase contributions muddling the result.

Often it is possible to measure standard datasets of the individual phases, with which an optimization routine can be run to determine the approximate phase fraction in the real system. In the following I give example models which can be used to fit a mixed phase system. In this case, consider a bulk starting material which has been micronized through a milling procedure. These simple models account for both generation of some amorphous phase fraction and additional effects from domain size reduction of the original phase. In practice, the datasets must be put onto an absolute scale, which in the most simple case can be done by normalizing the area under the first peak, assuming that the local structure is

identical in both samples. The models tested involve a summation of the amorphous G_a and crystalline G_c standards, along with the application of different domain size effects, where the spherical envelope function γ_{sphere} is used for domain size manipulation. The models are as follows:

1. A rescaling of the crystalline standard alone. This would imply the micronized sample has the same structural coherence (*i.e.* no domain size reduction).

$$G_{mix} = scale \times G_c(r) \tag{2.20}$$

2. A linear summation of the crystalline and amorphous standards. This would imply that the micronized sample is an incoherent summation of the perfect crystalline and perfect amorphous phases.

$$G_{mix} = scale \times [x \times G_c(r) + (1 - x) \times G_a(r)] \tag{2.21}$$

3. A rescaling of the crystalline standard and spherical domain size modification. Implies that the micronized sample contains only a reduction in domain size (no amorphous content).

$$G_{mix} = scale \times G_c(r) \times \gamma_{sphere} \tag{2.22}$$

4. A linear summation of the crystalline standard plus the crystalline standard modified by a reduced spherical domain size. Implies that there is a combination of perfectly

crystalline phase together with domains of reduced size (no amorphous content).

$$G_{mix} = scale \times [x \times G_c(r) + (1 - x) \times G_c(r) \times \gamma_{sphere}] \tag{2.23}$$

5. A linear summation of the crystalline and amorphous standards plus a spherical domain size modification of the crystalline phase. Implies that there is both crystalline content of reduced domain size and amorphous content generated.

$$G_{mix} = scale \times [x \times G_a(r) + (1 - x) \times G_c(r) \times \gamma_{sphere}] \tag{2.24}$$

2.6 Correlation analysis

Since the PDF measurement provides a robust structural fingerprint for a material, it is comparatively useful in many cases to use model-independent methods to analyze the measured signal. This can be valuable in comparing the measurements between synthesized and standard materials or new materials synthesized through competitive methods. Further, it is also helpful for determining the viability of potential structure models before wasting precious time trudging down the long path of optimization and verification for too many obviously wrong starting models. The work in this thesis makes heavy use of a particular tool, the Pearson product-moment correlation coefficient which determines the level of linear correlation between two datasets. It is calculated by

$$PCC = \frac{1}{1 - n} \sum_{i=0}^{n} \left(\frac{x_i - \bar{x}}{\sigma_x} \right) \left(\frac{y_i - \bar{y}}{\sigma_y} \right), \tag{2.25}$$

where $\bar{X}$ and $\bar{Y}$ are the means and σ_x and σ_y are the standard deviations of the respective datasets. The resulting coefficient is a value between -1 and 1 where -1 implies anticorrelation, 0 implies no correlation, and 1 implies perfect correlation. This is a good value to benchmark the likeness and therefore structural similarity between the PDF curves [19, 116].

Chapter 3

Experimental and data processing techniques

3.1 Rapid acquisition measurements

The rapid acquisition PDF (RAPDF) method is an experimental setup designed to collect a high flux of scattered x-rays, over a large Q-range, in a short period of time [117]. It is the best setup for most standard PDF experiments, despite the reduced Q-resolution of the measurement, and is generally the default setup at synchrotron light source, high energy, PDF beamlines. The method uses a large area flat panel detector which is able to measure the whole cross section of cones of scattered intensity. The Q values measured are determined by the detector setup. The scattering angle, denoted by convention as 2θ, of a pixel can be determined geometrically from the vectors between sample-to-detector d and incident-beam-center-to-pixel b, or

$$\tan(2\theta) = \frac{b}{d}, \tag{3.1}$$

with scattering angle 2θ, shown in Figure 3.1 For elastic scattering at a fixed wavelength, the momentum transfer between incident and scattered photons can be determined in terms of

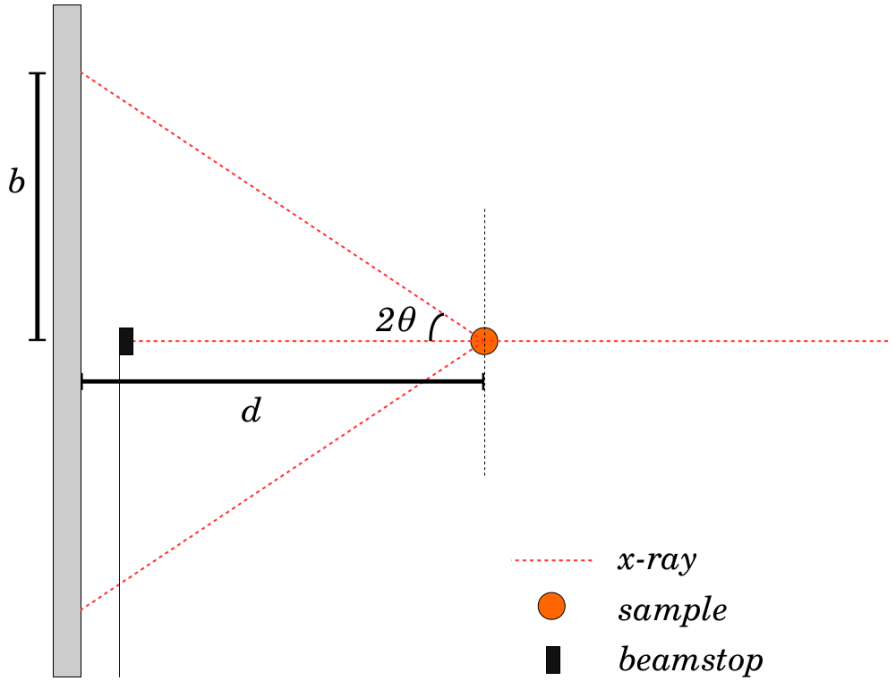

Figure 3.1: Schematic diagram showing the relationship between the scattering angle, sample-to-detector distance, and the intensity measured in a certain pixel on the detector.

the experimental scattering angle by

$$Q = \frac{4\pi sin\theta}{\lambda}. \tag{3.2}$$

For a constant incident energy, the measurable Q-range of the experiment is then primarily determined by the beamstop for Q_{min} and by the detector edge for Q_{max}. It can be tuned slightly by changing the sample-to-detector distance and by offsetting the detector relative to the incident beam, so that the direct beam hits near the edge or corner of the detector, or lies just off the edge of the detector. The Q_{min} can be lowered further by shifting the beamstop slightly off-center with respect to the incident beam. This allows a portion of the lower-Q scattering intensities to be measured on one side of the beamstop, which must later be masked to ensure the intensities from the partially measured low-Q arcs are normalized.

There are two additional important considerations when doing this. One, ensure that none of the incident beam escapes the beamstop and hits the detector. Two, air scattering intensities may increase on the side with less beamstop coverage (larger background subtraction).

The flat geometry of the detector means that incident photons scattered from the same position but at different degrees of momentum transfer actually travel slightly different distances from the scattering event to detection pixel. In practice, the distance, oblique incidence, and geometry of the detector are all calibrated and corrected for by measuring a standard material. A highly crystalline material such as nickel, silicon, lanthanum hexaboride, cerium dioxide etc. is measured and the positions of the Debye-Scherrer rings are matched to a known list of d-spacings for the respective material.

The work herein utilized measurements taken at the European Synchrotron Radiation Facility (ESRF) in Grenoble, France, and the National Synchrotron Light Source (NSLS), and NSLS-II, both located at Brookhaven National Laboratory (BNL) on Long Island, New York. Total scattering powder diffraction measurements were collected in rapid acquisition mode [117] where a typical x-ray energy and wavelength are on the order of 67.419 keV (λ=0.18390 Å) and using a Perkin Elmer 2D flat panel detector (2048×2048 pixels and 200×200 μm pixel size) mounted orthogonal to the beam path. The sample-to-detector distance was approximately 205 mm across experiments and was calibrated using a nickel standard with the program FIT2D [118]. The raw 2D intensity was corrected for experimental effects and azimuthally integrated and converted to 1D intensity versus Q plots using FIT2D, and then PDFgetX3 [107] was used to correct and normalize the diffraction data to obtain $F(Q)$ then Fourier transform $F(Q)$ to obtain the PDF, $G(r)$. The experimental setup for beamline 28-ID-2 (XPD) at NSLS-II is shown in Figure 3.2

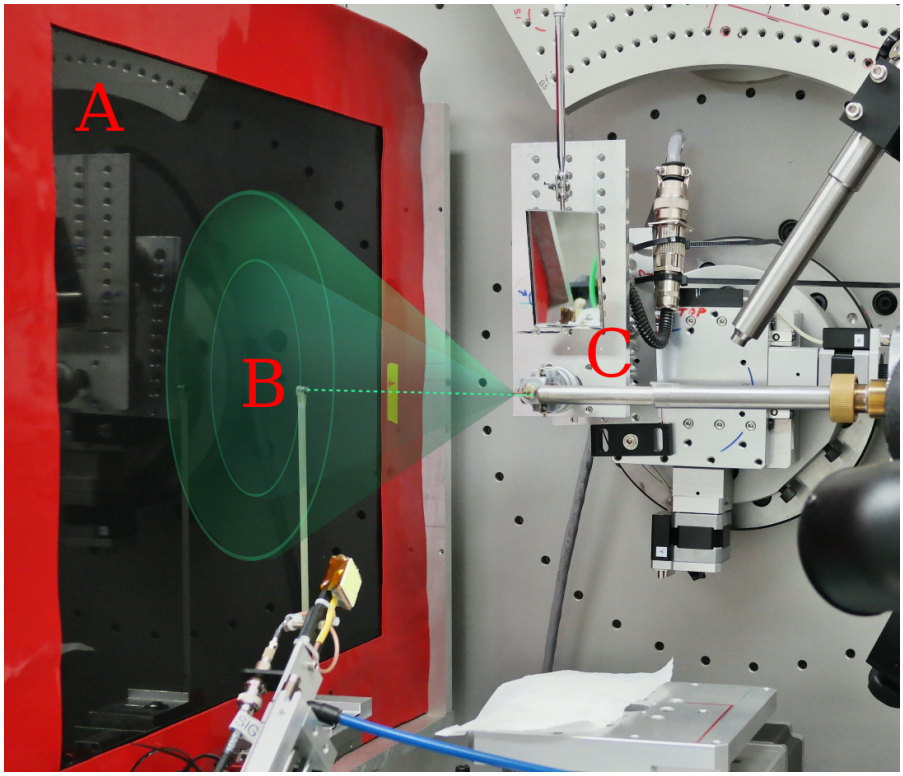

Figure 3.2: Photograph of the XPD beamline at NSLS-II. The dashed line indicates the path of the incident beam, while the transparent cones indicate the path of photons scattered from the sample at different degrees of momentum transfer, forming rings where they intersect with the detector. The letter labels indicate A. the detector, B. the beamstop which stops the transmitted beam from hitting and damaging the detector, and C. the collimator which is a metal tube, pushed close to the sample, which blocks any air scattering occurring along the incident beam path before hitting the sample.

3.2 Basic sample preparation

Following is a breakdown of basic sample types analyzed by the PDF method, and a few tricks for loading them into a vessel for measurement. The basic tools are shown in Figure 3.3.

3.2.1 Containers

Kapton tubing is the ideal capillary material because the Kapton polyimide material scatters very weakly and produces only broad diffraction features in the scattering pattern. Other materials include quartz or borosilicate glass which scatter x-rays a bit more strongly than

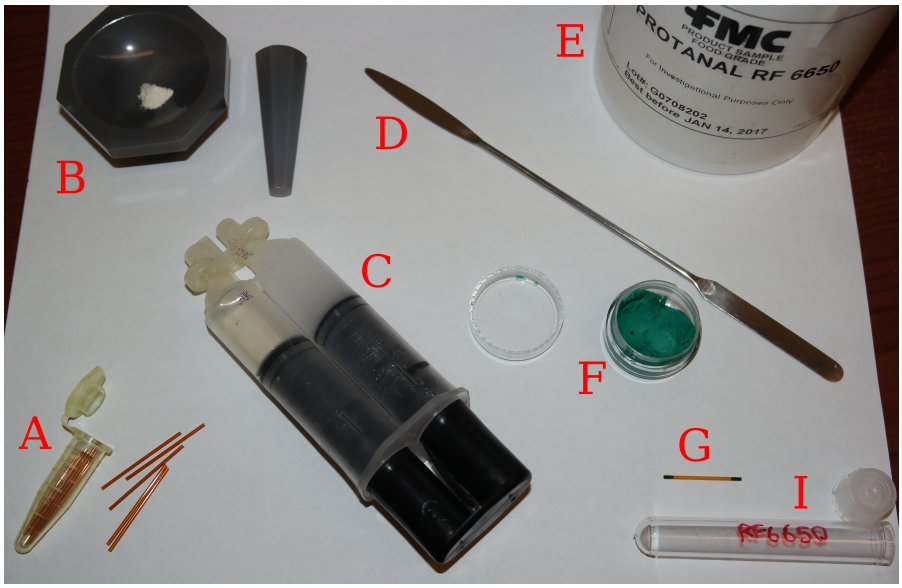

Figure 3.3: (A) Kapton (or other material) capillary, (B) mortar and pestle for grinding, (C) quick dry epoxy, (D) sample spatula, (E) sample, (F) moldable clay, (G) filled and sealed sample, (I) labeled sample containers.

Kapton, but still weakly compared to most other materials. Quartz and borosilicate glass can be better for air-sensitive samples. The glass capillaries can also typically work better for liquid samples requiring long-term storage or experiencing large changes in pressure such as during air travel, because they can be completely sealed by flame. However, if sealed within a glovebox, typically with epoxy or some other thermosetting agent, Kapton is also quite impermeable to oxygen or moisture over reasonable time scales as shown by the discussion of air sensitive samples on the APS 11-BM website (https://wiki-ext.aps.anl.gov/ug11bm/index.php/Air_Sensitive_Samples).

A section of Kapton tubing is cut using scissors to a length that depends on the length of the holder being used in the goniometer for the measurement. For example, this varies for room-temperature and cooling or heating under flowing nitrogen vs. loading in a cryostat. Typically, a length of approximately 3 cm will work well for flowing N2 measurements and

provide a good length for easy handling and not too much fuss during alignment. In cases where less sample is available (rare, valuable, or low yield product materials) shorter tube lengths and narrower diameter tubes may be used.

3.2.2 Sealing agents

To seal the tubes, a variety of basic clays and epoxies are suitable. For samples that are unstable to long term air or moisture exposure, epoxy should be used in order to seal the capillary as best as possible. It is comprised of two precursor agents which react when mixed to form stable crosslinks which set the polymer. For other cases, either hardening or nonhardening clay can be used. If their is no air sensitivity, nonhardening clay is easiest and will not crack or crumble over long term storage. When less sample is available, the more clay can be pressed into either end of the tube to center the sample in the capillary for easier alignment. However, it is critical that the clay does not get mixed into the sample, as it will diffract a strong crystalline pattern if in the path of the incident beam. For this reason it is also important not to contaminate the outside of the tube with clay while handling the tubes during filling.

3.2.3 Powders

Powders are the most common and basic sample form, and simultaneously the most easy to work with. However, powders themselves are a complicated material since they can simultaneously have physical properties of solids and liquids, as well as all the intrinsic chemical properties that come along with the material itself. In the basic case, a collaborator sends

bulk chunks or coarse grained powder sample. Using proper personal protective equipment (PPE) (*i.e.* goggles, gloves, lab-coat etc.), approximately 10-50 mg of the sample can be placed into a small agate mortar. Light grinding with a pestle can be applied in order to break up aggregate particles, to increase powder flowability, and to reduce the the size in the case of large bulk particles to avoid single crystal scattering peaks from anomalously large crystallites in the sample. Careful consideration should be made beforehand about whether or not grinding will degrade the sample chemically or mechanically and if this will ruin the experiment. In cases where the sample cannot be ground, or the crystallites are very hard and difficult to reach a homogeneous small particle distribution, the capillary can also be spun during the measurement to improve the level of orientational averaging of all crystallites in the scattering volume. The effects of the measurement by spinning are shown in Figure 3.4.

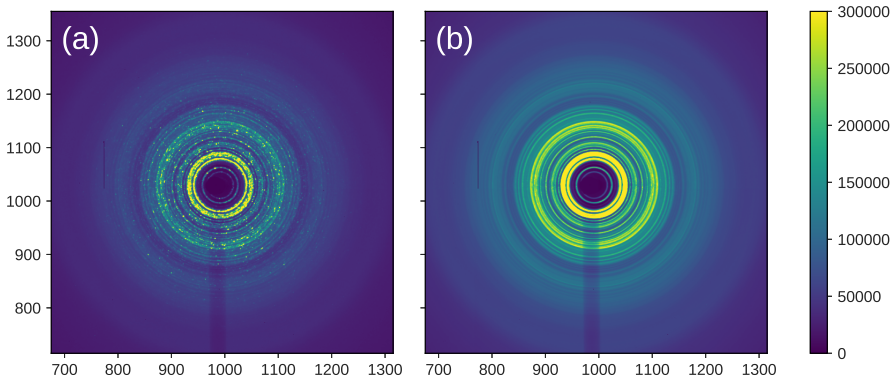

Figure 3.4: 2D images collected from polycrystalline sulfur (S_8) with (a) a static capillary and (b) spinning the capillary about its center axis perpendicular to the beam.

Clay or the mixed epoxy agents are then pressed into one end of the cut capillary. A few mm or so should be fine, though it can be pressed further in cases where a longer tube is necessary despite limited material to fill it. If epoxy, it should then be given time to dry (approx. 10-15 minutes for quick dry epoxies) though it does not need to fully cure (usually

approx. 24 hours). If clay, you can immediately move to loading the sample. The capillary should be held like a sewing needle, and then the other end can be scraped into the ground powder in the mortar. Two to three scrapes should be followed by holding the capillary open-end-up and tapping to get any larger powder aggregates to fall to the closed end. This process should be continuously repeated until the capillary is filled with only a few mm left at the open end. Then additional clay should be pressed in to close the tube and prevent the sample from falling out. As much clay as reasonably possible should be pressed in to compress the powder and maximize the packing fraction, which intensifies the scattering efficiency of the sample volume enabling shorter and higher quality measurements. Unfortunately, the epoxy cannot be pressed in this way. Instead, the capillary end must be scooped into the epoxy mixture and simultaneously rotated in order to achieve a sort of ball of epoxy on the end with partial entry into the open end, then let carefully dry without letting an holes or bubbles open. However, clay could be pressed in first to also improve the packing fraction. Otherwise, the capillary should again be gently tapped on one end prior to measurement to concentrate the sample.

It is my great regret that I never used a vacuum to suck powdered samples into the capillary. This could be done using the vacuum suction available in fume hoods, or by purchasing a low power vacuum motor. Plug a high density mesh, or something like cotton between one open end and the source of the suction, and do not get the wrist pain I have experienced through fully manual sample loading.

3.3 Liquids

Liquids can be treated similarly to powders as far as capillary measurements go. The loading and sealing procedure is a bit different and can be significantly quicker and easier with the right tools. In addition to the capillary and sealant materials, a syringe is also preferred. To start, the section of capillary tubing should be cut with a few extra centimeters of length to work more easily with the syringe pump. The capillary should then be fit into the opening of the syringe where the needle would otherwise go, and sealed around the edges of the fitting with clay create a seal. The liquid can then be drawn up into the capillary directly from the source by pulling the plunger up. The steps are shown in Figure 3.5. At least a centimeter or so should be left unfilled on both ends of the capillary. The liquid should hold by capillary forces alone in the center. When removing the filled capillary from the pump, ensure that the liquid does not continue to get sucked in by simultaneously pressing the plunger down such that the internal volume remains approximately the same. Once removed, the ends can be cut, if necessary, and then sealed with clay or epoxy.

A slightly better method can be used, by sucking a plug of some of the still-liquefied epoxy mixture up into one end prior to removing the liquid filled capillary. Then after removal, the capillary can be attached to the syringe from the opposite end, and an additional plug of epoxy sucked into the opposite opening, resulting in a nice, fully closed tube which should not have any of the issues with leakage that clay might, allowing it to also be stored.

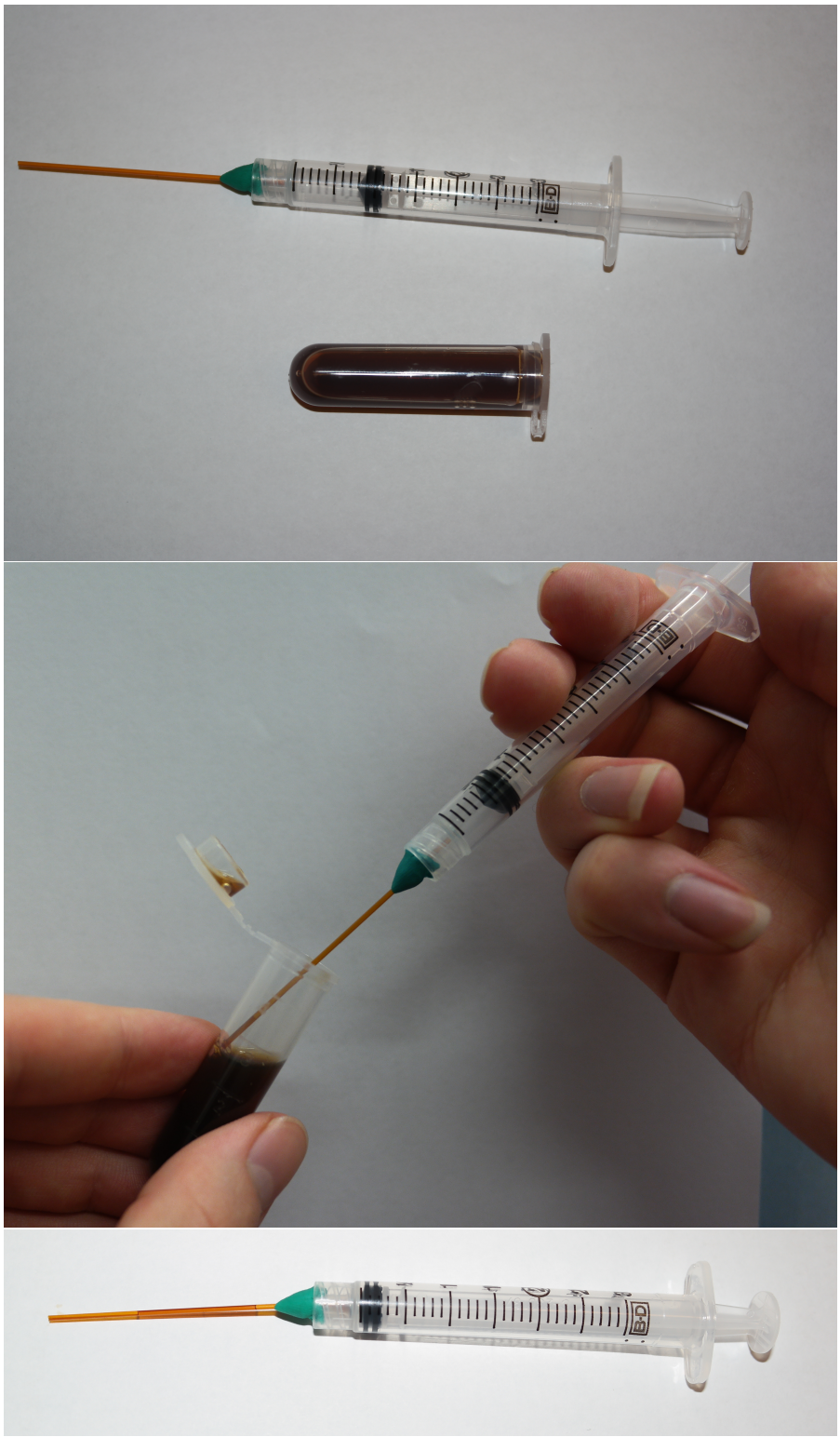

Figure 3.5: Steps for loading a liquid into a Kapton capillary.

3.4 Solid chunks

In some cases the physical form and properties of a material make it difficult to put into a capillary. For example, highly elastic polymers may not be amenable to powdering. In such a case, a chunk of the polymer should be cut with a thickness matching the diameter of the capillary used for the standard material. Then the chunk can be attached to a bracket using Kapton tape to hold it in the beam-path. The capillary with the standard can then be attached to the tape in the same way to obtain a proper calibration. The arrangement of the samples of the the bracket is shown in Figure 3.6

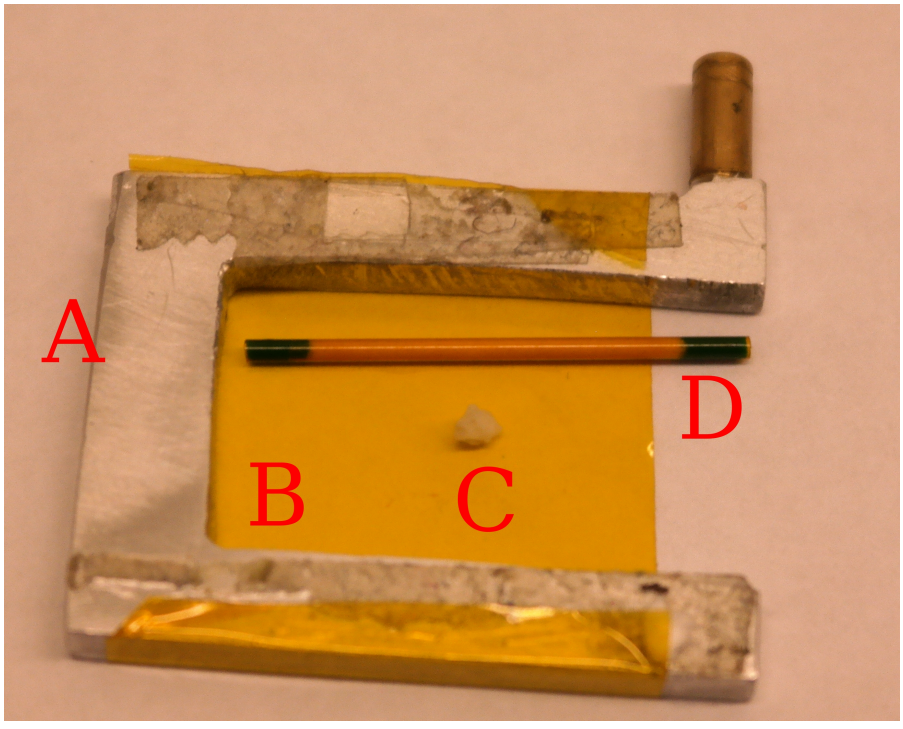

Figure 3.6: (A) bracket, (B) Kapton tape stretched over bracket (the sticky end on top will face the detector), (C) sample chunk, (D) calibration standard capillary.

3.5 Data processing with PDFGetX3

Following measurement, the images are calibrated for geometrical effects (sample-to-detector distance, oblique incidence), detector specific corrections (dark subtraction, flat field correction if available), and incident beam polarization; see Egami and Billinge for further details [4]. Prior to integration, the image should also be masked to eliminate malfunctioning bright and dark pixels, edges, and any significant shadowing from instrumental equipment (*e.g.* cryostream, sample holder, or beam stop). This is especially important for weakly scattering samples because the errors in the detector intensities will be more significant as compared to the much larger intensities measured from strongly scattering samples. Anomalous variations in the mean intensities along different azimuths in 2D can lead to sharp, nonphysical jumps or dips in the integrated 1D $I(Q)$, while bright/dark pixels will lead to sharp delta-type peaks which will eventually create intense, nonphysical, high frequency components in the PDF after Fourier transformation. Separate masking software is being developed that does a better job of masking based on a more rigorous statistical analysis of the scattering [119]. For charge-coupled device (CCD) detectors, it is also important to consider that the functioning of the pixels cannot be modified by prior exposure to high flux of photons, creating residual patterns in subsequent measurements which change slowly in time [120]. It is critical that this is not significant during the measurement of weakly scattering material and can be reasonably alleviated by allotting specific times for respective high and low scattering measurements, and never measuring high scattering materials directly before. After all corrections have been applied, the image is azimuthally integrated along arcs of constant momentum transfer, to obtain the 1D scattering intensities $I(Q)$.

Background intensities from all non-sample components must be subtracted including the container, air scattering, and sometimes even a component of the sample itself. Subtraction can also be performed directly on the raw images; they should be measured with the same exposure rate. This is easiest if the total summed acquisition image is averaged by the exposure time, and the background should typically be measured with suitable statistics so as not to harm the dataset-of-interest on subtraction. In cases where the utmost levels of data accuracy are required for the scientific question at hand, more detailed background considerations should be made [121].

Physical corrections to the scattering such as absorption and Compton scattering etc. can be made explicitly for instance in PDFGetX2 [122]. All PDF processing herein has used the program PDFGetX3 which performs the corrections in an *ad hoc* way [107]. It parameterizes corrections to the raw intensities as additive or multiplicative, and automates them based on the asymptotic behavior of the total scattering structure function. For more information see Billinge and Farrow [106] and Juhas *et al.* [107].

The three inputs are the two files for the 1D sample scattering intensities, the 1D background scattering intensities (if not already subtracted), and the sample composition. The scale factor for the background subtraction can be modified if necessary. Then next inputs include the instrumental Q_{max} ($Q_{max-inst}$) which should be set to a Q-value just below the most distant edge of the detector. Then the Q_max used in the Fourier transformation must be adjusted. It should be further lowered below any nonphysical kinks in the dataset which can come from other detector or masking edges, and possibly reduced further to eliminate noisy data from the PDF if the signal-to-noise ratio becomes unfavorable in the high-Q region. In general, it is good practice to process and analyze the PDFs over a range of Q_{max} values if the

signal is noisy at higher values. The Q_{min} should be set to cut off any stepping in intensity resulting from masking the beamstop in the images before integration. The last value R_{poly} can typically be left as-is at the default value of 0.9. Examples of the relevant functions are shown for crystalline and amorphous lactose in Figure 3.7.

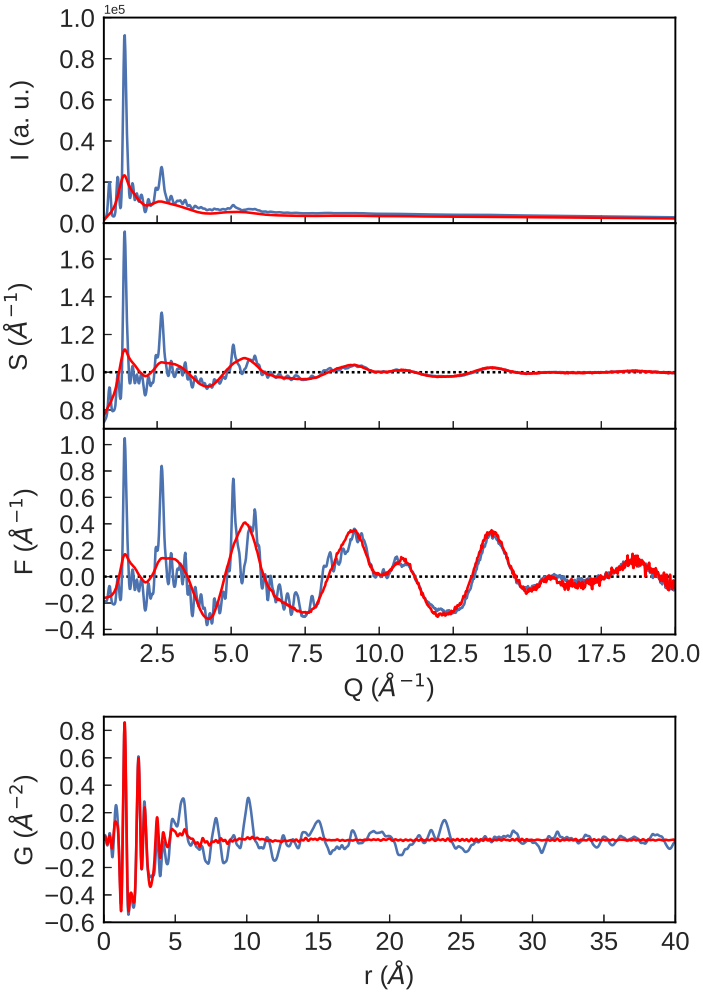

Figure 3.7: Data processing steps as applied to crystalline (blue) and amorphous (red) lactose, showing (a) the 1D, background subtracted scattering intensities $I(Q)$, (b) the total scattering structure function $S(Q)$, (c) reduced structure function $F(Q)$, and (d) the PDF, $G(r)$.

3.6 Q_{max} effects

Often, for weakly scattering samples and components, it is difficult to obtain sufficient scattering statistics in the high-Q region, approximately 20 Å^{-1} and above. In these case, it is possible to reduce the Q_{max} of the Fourier transform to gain enhanced signal to noise when the region of interest for analysis is primarily in the high-r region. In Figure 3.8, I show several examples of the effects of this reduction for several thermoplastic polyurethane samples.

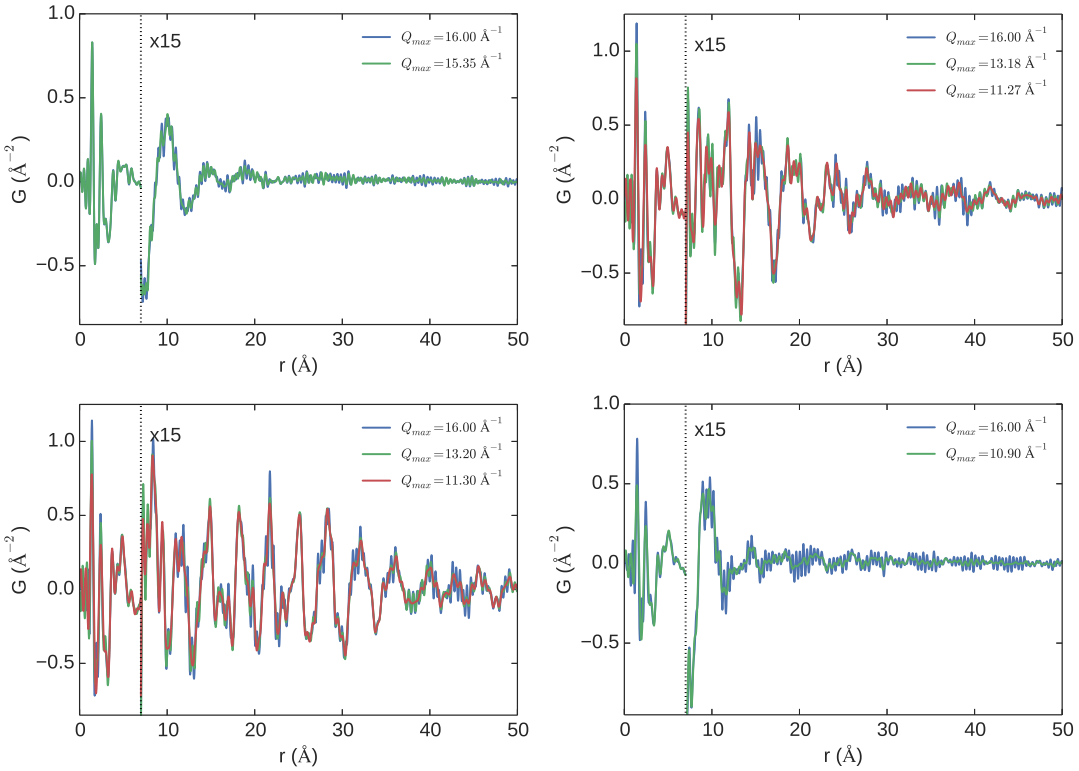

Figure 3.8: The Q_{max} used in the data reduction was varied depending on the region of scrutiny in order to optimize between real space resolution (high Q_{max}) versus noise reduction (low Q_{max}). We verified that the changes in this value did not degrade the signal of interest, particularly in the high-r region. Top left: HP1. Top right: HP3. Bottom left: HP4. Bottom right: TPU2. Low- and mid-r refinements used Q_{max}=13.20 Å^{-1} while high-r refinements used Q_{max}=11.3 Å^{-1}

The result is that the problematic noise frequencies at high-r are significantly reduced with smaller Q_{max}, though at the expense of also decreasing the real-space resolution of

the signal. Often, for molecular materials, intermolecular thermal and displacive disorder over long distances makes it so that the high-r signal is not significantly degraded with such lower resolutions, though it is important to test this before moving forward with analysis, such for the case shown. Even the peak resolution at low-r is still not completely destroyed, even down to approximately $Q_{max} = 10.90$ Å^{-1}. These samples will be further discussed in Chapter 6.

Chapter 4

Signal sensitivity from dilute component concentrations

In this chapter, I present the use of the difference PDF (dPDF) methodology in order to fingerprint and model component signals at high levels of dilution. This shows that the PDF method enables quantitative detection of components at much lower mass percentages than typically reported, as low as 0.25 wt. % in this case for weakly scattering drug nanoparticles. The work presented was published in the journal Nanoscale (2015) [123].

4.1 Detection and quantitation limits of the dPDF method

Determining the limits of an analytical probe are crucial for characterizing how well it can perform, and its reliability, under various conditions [9]. Two important characteristics are the limit of quantification and the limit of detection [124]. Respectively, these quantities give a measure of the lower limit for which a certain concentration of component or phase may be quantified with suitable accuracy and precision, and a measure of the concentration at which a signal is detectable above the noise limit. There are many complications arising with establishing these values. The most basic is that the values are highly dependent on the nature

of the material system and component of interest, and can change drastically from system to system, and component to component. Further, the determination of these values often requires designed experiments with specially prepared control samples, and these samples may not be truly representative of the system and its components in the real case. In other cases, it may even be difficult to prepare good control samples due to limitations in the sample preparation.

It is important to determine the sensitivity of the dPDF method to the concentration of constituents of interest, for example, studies of minute impurity phases in solids, or in this case, nanoparticles in solution. This value is dependent upon species scattering intensity, structural arrangement (*e.g.* whether the signal is crystalline or amorphous), and measured counting statistics, so defining a generic limit is imprecise. Concentrations at and above 1 wt. % are widely quoted, for example 2.5 wt. % amorphous in crystalline silica [8], and 1 wt. % platinum nanoparticles on alumina support [125]. Sensitivity down to 0.2 wt. % is reported for CdSe nanoparticles in toluene [126]. Here, the sensitivity is measured to 0.25 wt. %, but in this case for an organic sample which has a much weaker scattering power than the prior cases. The practicality of such measurements is improved by taking advantage of data reduction methods used by the software PDFgetX3 [107]. This is for a system of organic nanoparticles in an aqueous suspension, which is a challenging case due to the weaker scattering of the particles of interest. Samples consisted of small nanoparticles of a proprietary active pharmaceutical ingredient (API) under development by GlaxoSmithKline (GSK).

4.2 Materials

Samples were prepared at GSK, and included the API as a bulk crystalline powder and as precipitated from a non-microfluidized 5 wt. % suspension (2 % Polysorbate 80 (PS80), 0.2 % Sorbitan monolaurate (SML), 0.3 % Oleic Acid (OA) in water), three samples of API in the same solution at concentrations of 5, 0.66, and 0.25 wt. % which were size reduced by microfluidization, and a blank sample of the aqueous solution. The sample that precipitated out was measured still in the capillary with solution. Examples of the 1D integrated scattering patterns are shown in Fig. 4.1, before being normalized and reduced to the structure function $F(Q)$, and transformed to the PDFs. The difference in scattering intensities between the

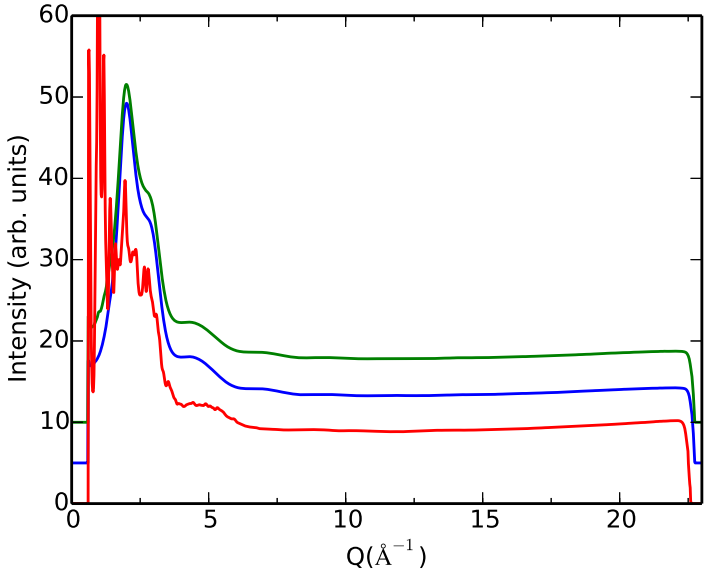

Figure 4.1: Integration of measured intensity: 1D raw signal after integration of Debye-Scherrer rings for precipitated crystalline API (red), aqueous solvent (blue), and 0.25 wt. % API suspension (green). Curves are offset for clarity.

0.25 wt. % sample and the blank solution is shown in Fig. 4.2, showing that the signal from the actual particles of interest is very small compared to the total signal. The $F(Q)$ and $G(r)$ are shown for both the precipitated crystalline API and the aqueous solution in Fig. 4.3. These

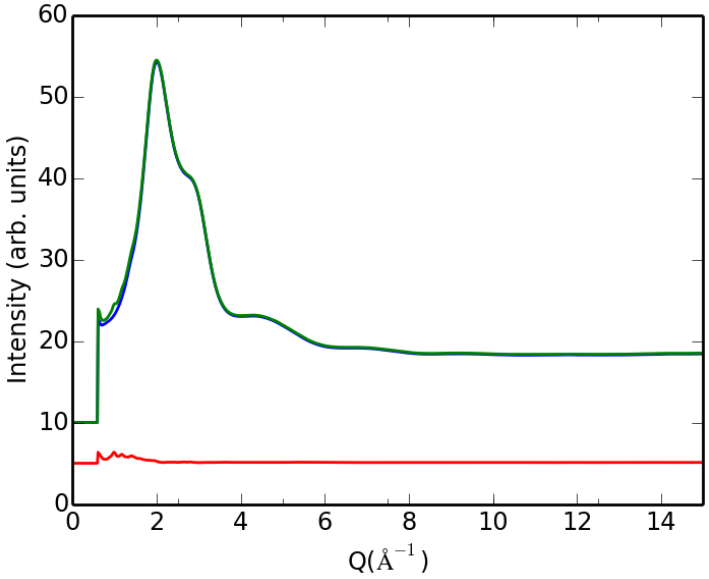

Figure 4.2: 1D scattering intensities for the blank aqueous solvent (blue), and 0.25 wt. % API suspension (green), and difference (red).

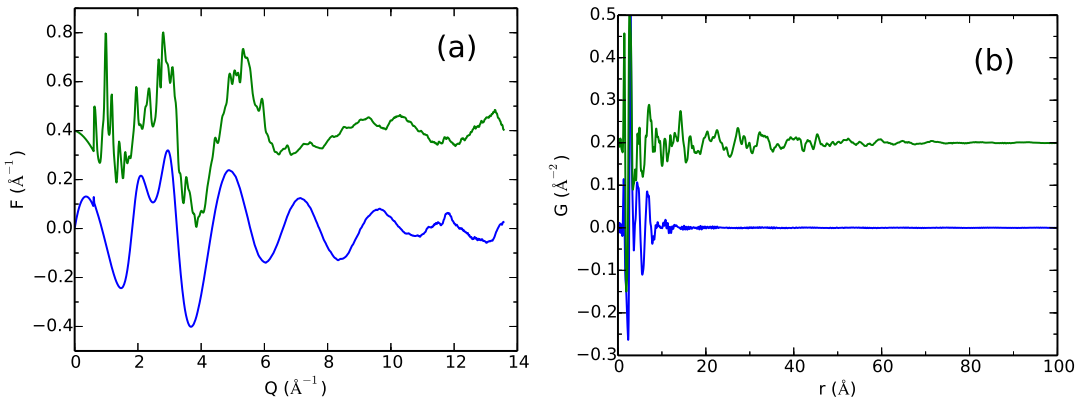

Figure 4.3: Representative data sets from control samples: precipitated crystalline API (green) and aqueous solvent (blue). (a) $F(Q)$ (b) the PDF, $G(r)$.

can be considered as controls which establish the nature of the PDF for these constituents. Persistence of the signal out to high-r (around 90 Å) for the crystalline control is due to its well ordered periodicity giving long-range coherence. The signal finally drops off due to the finite reciprocal-space resolution of the measurement. Meanwhile, the signal from the aqueous solvent disappears well before $r = 20$ Å, because there is no structural coherence beyond the intramolecular bonding of the solution molecules and some near neighbor packing. This signal was measured with good statistics, as evident by minimal noise in the $F(Q)$, allowing its use as a background subtraction to the sample data.

4.3 Results and discussion

Over the course of the experiment, the non-size reduced API settled out of suspension, precipitating out the crystalline form. Before being used as a control for the other suspension samples, this signal is scaled and superimposed over that of the bulk crystal for comparison in Fig. 4.4. It is clear that there is significant disparity between the two PDFs in the low-r region, up to about $r = 10$ Å. To explore the cause of this, the difference is taken between the scaled data sets, shown as the red line offset below the data curves. Plotted on top in light blue is the PDF of the aqueous solution which has been rescaled to have the same amplitude. The agreement is very good, in this case showing that the discrepancies between the two sample measurements do not come from irreproducibilities between data sets, but the fact that the precipitated API was still embedded in solution. Note that because the solvent signal is flat in the high-r region, there is excellent reproducibility in the signals beyond 10 Å, even before subtraction, as seen in Fig. 4.5. This illustrates the useful fact that a crystalline, or as

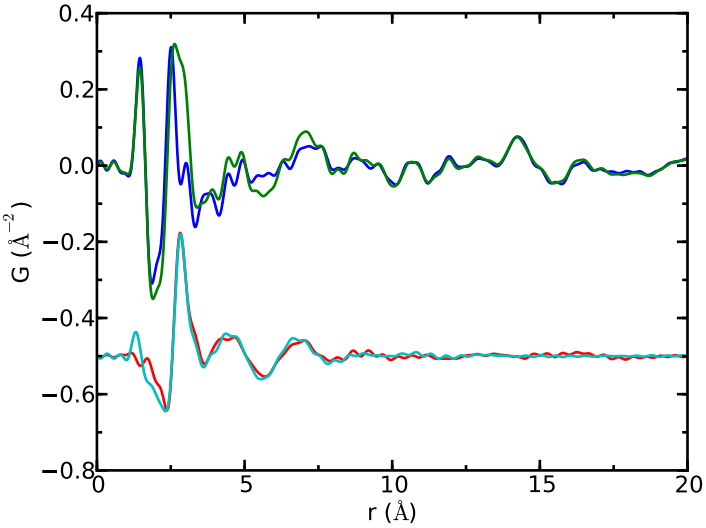

Figure 4.4: Comparison of bulk versus precipitated crystalline samples: PDFs from the bulk crystalline API (blue) and the crystalline API that precipitated from solvent (green). The PDF signals are subtracted (red) and compared to that of the aqueous solvent (light blue) with very good agreement showing that the only difference between the signals is the presence of significant solvent scattering in the latter case. PDF is sensitive to the presence or absence of residual solvent in the crystalline API.

will be shown later, a nanocrystalline component can be easily seen in the PDF, even in the presence of significant liquid or amorphous components.

While the non-size-reduced API fell out of suspension and recrystallized, the microfluidized API at 5 wt. % did not. In this sample, the signal is dominated by 95 wt. % solvent. This is shown in Fig. 4.6(a), where the PDF is plotted, overlaid by a scaled plot of the pure solvent. The curves are very similar, albeit with small deviations evident. A dPDF approach is taken to extract the signal coming from the micronized API in suspension by subtracting the scaled solvent background. Fig. 4.6(b) shows the PDFs, where signals from both 5 wt. % micronized suspension and the pure solvent are plotted over a wide range of r, with the difference curve plotted below in red. A signal is clearly visible extending to around 70–80 Å which presumably comes from the API in suspension. In order to confirm that the signal in the dPDF

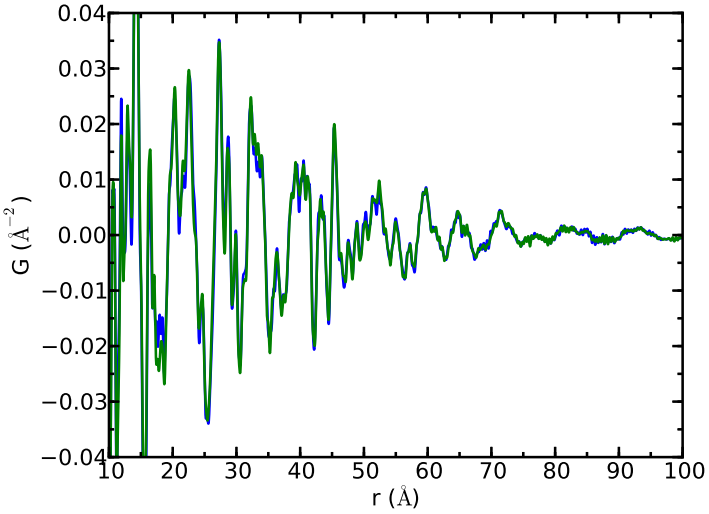

Figure 4.5: High-r comparison of bulk versus precipitated crystalline samples: scaled to highlight the signal from the intermediate-range molecular packing in the crystal, from the bulk crystalline API (blue) and the crystalline API that precipitated from solvent (green). The figure illustrates the level of reproducibility that may be obtained by measuring two different samples of the same material.

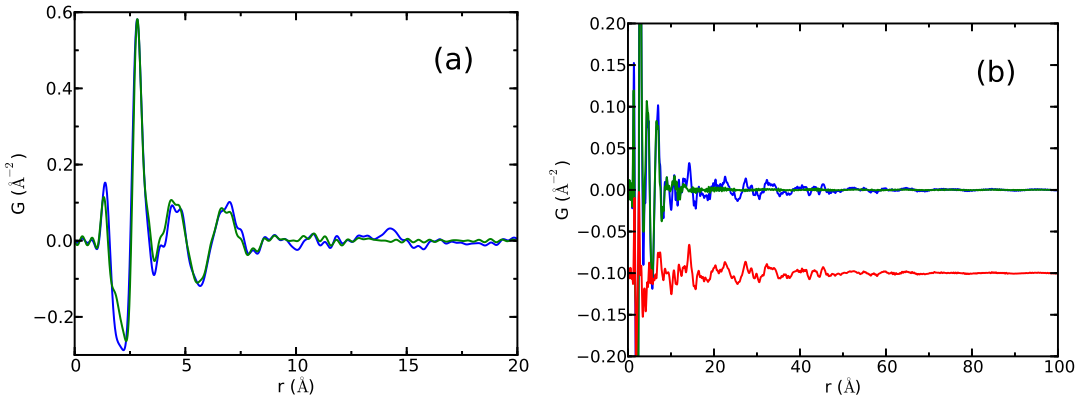

Figure 4.6: Comparison of precipitated and 5 wt. % suspension samples: PDFs from the 5 wt. % API (blue) and aqueous solvent (green). (a) Low-r region of the PDF. (b) wide r-range with the difference of the PDF signals shown offset below (red).

originates from the API, it is compared to the PDF of the precipitate recrystallized from solution with the same concentration in Fig. 4.7, with solution subtracted as shown necessary in Fig. 4.4. It is clear that the dPDF signal from the size-reduced suspension is the same as that

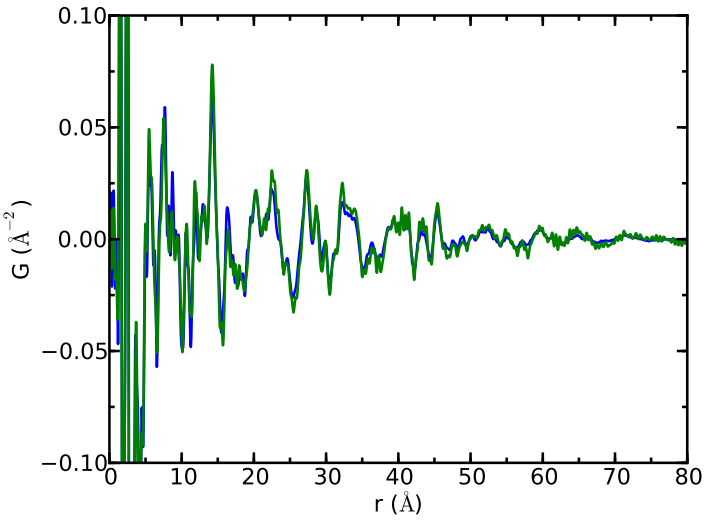

Figure 4.7: Determining the range of structural coherence for suspension particles: Reproducibility of the dPDF from the microfluidized 5 wt. % API obtained from reciprocal space subtraction of the suspension (green) and the crystalline precipitate corrected by a 16.9 nm domain size (blue).

from the crystalline API giving clear confirmation that this dPDF method is able to detect the presence of the API signal in suspension, even at 5 wt. % concentrations. In order to achieve this level of agreement, the signal from the crystalline precipitate was corrected for finite domain size effects. It was multiplied by the characteristic function for a sphere (Eq. 2.14) of diameter 16.9 nm. The diameter was estimated by carrying out a least-squares fit such that d was allowed to vary until the PDFs of the nanoparticles and size-corrected crystalline data gave the best agreement.

Sensitivity analysis is carried out to see how dilute the API can be while still remaining visible in the measured PDF. To do this, further diluted concentrations of 0.66 and 0.25 wt. %

are considered. As concentrations become more dilute, it is increasingly challenging to detect a contribution that is statistically different from the blank with PDF methods. As seen in Fig. 4.1, the raw intensity from the solvent and 0.25 wt. % suspension are nearly indistinguishable. However, the question is whether any signal can be detected in the data after processing to obtain the fully corrected $F(Q)$ and PDF, $G(r)$, functions. The resulting dPDFs are compared in Fig. 4.8. With decreasing API concentrations, there is an increasing pres-

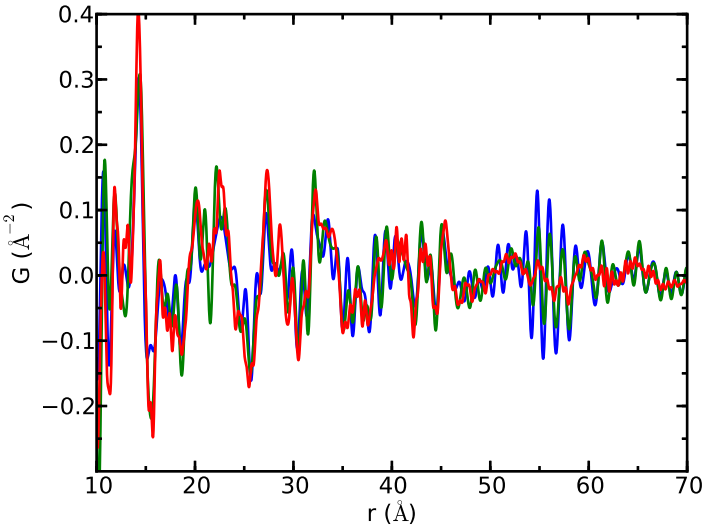

Figure 4.8: Signal sensitivity: dPDFs from reciprocal space subtraction of the solvent for the 0.25 (blue), 0.66 (green) and 5 (red) wt. % API samples. Despite increased noise ripples in the low concentration samples, the signal from the API is clearly evident.

ence of noise in the dPDF, as the API now accounts for less than one percent of the total signal. However, it is clear that as the concentration is reduced down to 0.25 wt. %, the structural signal from the API is still highly reproducible out to high-r. While no structural model is available for the API, agreement with the crystalline form shows that quantitative analyses of the dPDF data from the dilute API is possible. To further explore this, a peak fitting algorithm [127] was used to extract peak positions and a baseline from the PDF of the domain-size corrected crystalline standard PDF. Gaussian functions were then fit to the

crystalline and 0.25 wt. % PDFs at these positions, see Fig. 4.9. This constitutes a less highly

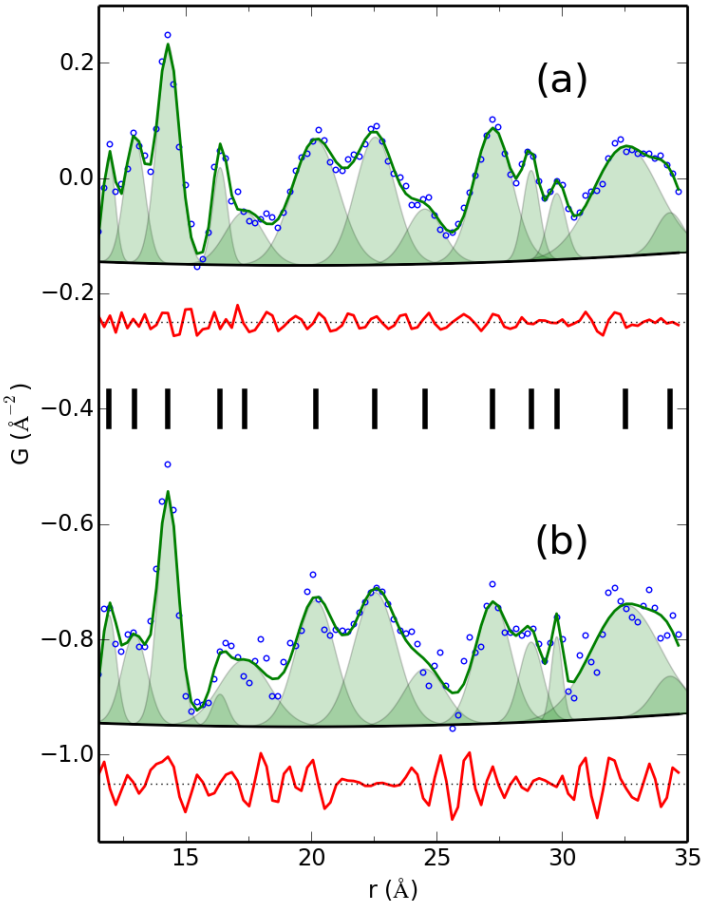

Figure 4.9: Peak fitting: PDF models are generated and compared by fitting Gaussian curves (light green) and a PDF baseline (black) at the extracted peak positions (black hash marks) to the data plotted on a Nyquist grid (blue) for (a) the crystalline standard, and (b) the 0.25 wt. % suspension. Differences are plotted in red.

constrained fit than would be the case in a real PDF structural refinement carried out with PDFgui [108] and so is a strict test of the reliability of extracting quantities from the PDF of the dilute sample. Though there is higher uncertainty associated with the dilute suspension PDF due to the small signal, the peak positions from the crystal adequately account for all signal arising from the structure in the dilute PDF (Fig. 4.9) and values for peak widths and intensities match well, see Table 4.1.

Table 4.1: Peak positions extracted from the crystalline standard PDF with height A_i and width (standard deviation) σ_i obtained by fitting Gaussian functions, $G(r) = \sum_i A_i \exp\left(\frac{-(r-r_i)^2}{2\sigma_i^2}\right)$, onto the baseline for both the standard (stan.) and 0.25 wt. % suspension (susp.) PDFs.

Position (Å)	height ($Å^{-2}$)		width (Å)	
	stan.	susp.	stan.	susp.
11.92	0.18(1)	0.19(3)	0.25(2)	0.30(5)
12.94	0.22(1)	0.16(2)	0.40(3)	0.50(7)
14.28	0.38(1)	0.40(1)	0.44(1)	0.40(3)
16.36	0.17(1)	0.06(3)	0.29(3)	0.31(18)
17.34	0.092(7)	0.12(1)	0.77(13)	1.01(22)
20.17	0.22(1)	0.22(2)	0.93(6)	0.79(10)
22.55	0.22(1)	0.23(2)	0.79(4)	0.86(10)
24.53	0.095(8)	0.10(2)	0.72(10)	0.82(23)
27.25	0.23(1)	0.21(2)	0.76(5)	0.70(10)
28.77	0.16(1)	0.14(2)	0.33(3)	0.47(11)
29.80	0.11(1)	0.15(3)	0.36(5)	0.22(6)
32.54	0.190(7)	0.19(2)	1.31(8)	1.39(17)
34.31	0.07(1)	0.07(2)	0.55(11)	0.65(33)

4.4 Conclusions

Though PDFs from a wide variety of materials and at a varying range of diluted concentrations have been measured, few have reported on the actual sensitivity limits of the technique for their respective systems. One systematic study by Peterson *et al.* [8]. reported phase determination with PDF to be accurate down to at least 2.5 wt. % and lower with single data set standards available. In the present case, single data set standards are utilized, and much lower component concentrations are analyzed, in our case with components which scatter far more weakly than do typical inorganic materials. As previously discussed, the limit of detection will depend on the particular situation in a dPDF study. For example, it is easier to detect the signal from a nanoparticle on the background of a liquid or amorphous host than it would be to detect a minority crystalline component in another crystalline material.

This work reports the sensitivity of the PDF to the presence of small quantities of crystalline or nanocrystalline components in a disordered matrix for a weakly scattering carbonacious material. PDFs from quantities of nanocrystalline material as small as 0.25 wt. % could be extracted using difference methods from high quality synchrotron data that are suitable for quantitative analysis such as fingerprinting and structural modeling, even when the coherent domain size is only on the order of 10 nm. In terms of wt. % it is comparable to the reported state of the art for inorganic materials [126], though much improved in terms of scattering power of the component of interest. The practicality of such a measurement is also improved using the latest data reduction methods. This will open doors to a multitude of studies such as crystalline and nanocrystalline APIs in amorphous matrix formulations (*e.g.* dispersion in polymer excipients), or inorganic nanoparticles embedded in a glass matrix, or in liquid suspensions as studied here.

Detection at very dilute concentrations with PDF means that more components can be studied in their native environments, *i.e. in situ*, rather than in contrived situations with exaggerated concentrations. This is important, for example where aggregation of higher concentrations is an issue. Also, dilute samples can benefit time and cost when the primary component is rare or expensive. Better resolution can be expected in identifying consumption and production of components in reactive systems so that kinetic behavior can be studied. In the present case, the API can be studied at the actual concentration of the marketed drug product. In later chapters, the implications of this sensitivity will be shown for various cases involving other systems with dilute component concentrations, intrinsically, or as they form *in situ*.

Chapter 5

Processing effects and crystallization of amorphous lactose

This chapter presents a case study of PDF methods for small molecule compounds, using a popular excipient in the food and pharmaceutical industries, lactose. I show how to distinguish differences in local ordering and quantify mixed phases, then follow these properties as the compound crystallizes. The work was published in the journal Crystal Growth Design (2015) [128].

5.1 The interesting case of lactose

Lactose, $C_{12}H_{22}O_{11}$, is an important material due to its widespread application as a pharmaceutical excipient, filler, binder, flavor enhancer, and sweetener. It is a disaccharide of galactose and glucose with two anomeric forms, α and β, characterized by isomerization of the C_1 hydroxyl group on glucose (see Fig. 5.1) [129]. Many different factors play a role in the crystallization behavior of lactose. Anomeric concentration has marked effects on the physical properties of lactose solids [130], and can play a determining role in which forms nucleate from the amorphous state. Other factors include the presence of nucleation precur-

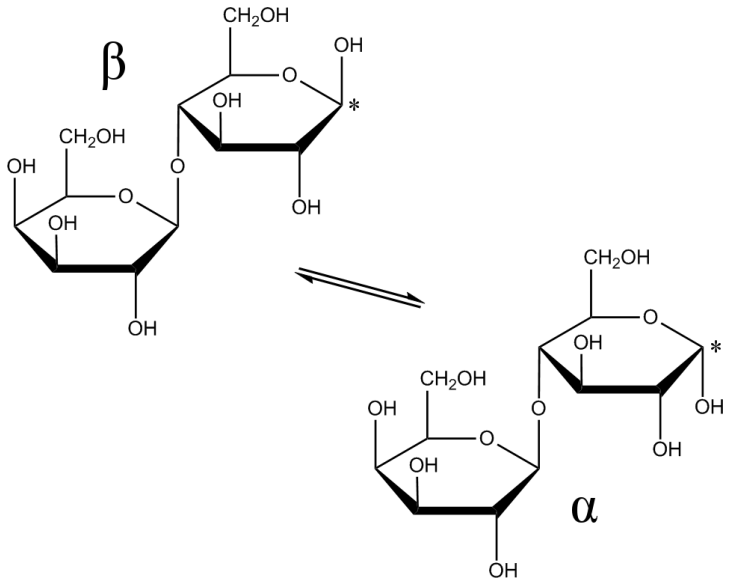

Figure 5.1: Schematics of the α and β lactose molecules. Mutarotation occurs at the marked ($*$) site.

sors or nucleation sites [131] or moisture content [132]. Storage environment also directly influences the crystallization behavior [133, 134]. For example, water can be held within the amorphous phase in different ways depending on RH and exposure time, affecting the mobility and diffusion rates [135]. Isolating the effects on the crystallization kinetics, and products, of any one parameter is difficult leading to a range of results in the literature that are difficult to compare directly. Here, a structural characterization is carried out for a series of differently amorphized lactose samples undergoing crystallization.

Lactose displays rich polymorphic phase behavior. There are at least four validated polymorphs [136] including α-lactose monohydrate [137], hygroscopic [138] and stable [139] anhydrous α-lactose, and anhydrous β-lactose [140]. Other studies report mixed molecular compounds with varying stoichiometric ratios of α:β [141–143] depending on the crystallization conditions. Amorphous lactose can be prepared from the crystalline phase through various techniques including freeze drying [132], ball milling [144], and spray drying. [145]

In commercial products, intentional mixing of amorphous and crystalline content can be used to modify physical properties such as caking, hardness, flowability, compaction, solubility, and stability [20]. However, in many cases compositional variation can unintentionally develop during thermal and mechanical processing steps or aging. Therefore, to assess product stability and perform quality control for product regulation, it is extremely important to be able to quantify the concentrations of amorphous and crystalline phase content, particularly in cases where there is either very little, or nearly total crystalline content in the sample. A variety of techniques are available with varying test requirements and sensitivities [9]. Differential scanning calorimetry (DSC), x-ray powder diffraction (XRPD), StepScan DSC (SS-DSC), isothermal microcalorimetry (IMC), solution calorimetry (SC), Raman, and gravimetric moisture sorption (GMS) have been compared for quantifying nonfabricated amorphous lactose content [22], giving good agreement with the exception of DSC. For the cases of very low concentrations of amorphous content, sensitivity down to about 1 % for isothermal microcalorimetry [130], and less than 1 % [146], or better [147] has been demonstrated for GMS techniques. For lactose in particular, Gustafsson *et al.* showed that amorphous content down to 0.5 wt % could be detected [148], and work by Lubach *et al.* showed that relaxation time from solid–state NMR is a potential predictor for amorphous content and stability [149]. Unfortunately, there is no standard method for determining the degree of amorphous content across materials systems and tests must often be carefully designed for specific cases. [150] The community would therefore benefit from the development of a more broadly applicable method, such as PDF, for this purpose. We assess the capabilities for studying crystallization from the amorphous state and to quantify the amorphous and crystalline components using PDF analysis.

5.2 Materials

The samples studied are summarized in Table 5.1. Samples included three commercially produced forms of lactose: crystalline Flowlac 100 (Lot 001), amorphous Flowlac 100 (Lot 2027A4952), and crystalline Tablettose 90 (Lot 0945A4003) manufactured by MEGGLE. Two additional amorphous samples were prepared at AMGEN through melt quenching and lyophilization of lactose monohydrate (LA105, Lot 2AC1103) produced by Spectrum Chemical. Separate samples of the three different amorphous formulations were aged at 40°C/75% RH for varying lengths of time, then quenched, loaded, and sent for ex situ measurements.

Table 5.1: Samples.

Sample	Preparation	Starting Material
c[a]-Flowlac	as-received	crystalline Flowlac 100
c-Tablettose	as-received	crystalline Tablettose 90
c-Spectrum	as-received	crystalline Spectrum
a[b]-Flowlac0	as-received	amorphous Flowlac 100
a-Flowlac1	aged 1 min	
a-Flowlac1.5	aged 1.5 min	
a-Flowlac2	aged 2 min	
a-Flowlac2.5	aged 2.5 min	
a-Flowlac3.5	aged 3.5 min	
a-Flowlac5	aged 5 min	
a-Flowlac10	aged 10 min	
a-Flowlac20	aged 20 min	
a-Flowlac30	aged 30 min	
a-FlowlacRT	aged 1 month RT[c]	
a-lyoph0	not aged	lyophilized Spectrum
a-lyoph3	aged 3 min	
a-lyoph15	aged 15 min	
a-mq0	not aged	melt quenched Spectrum
a-mq55	aged 55 min	
a-mqRT	aged 1 month RT	

[a] (c) stands for crystalline starting product;
[b] (a) stands for amorphous starting product;
[c] (RT) stands for room temperature.

5.3 Supplemental experiments

Additional experiments were performed by the collaborators Eugene Cheung and Paul Krolikowski at Amgen. Powder diffraction experiments were performed separately using Cu Kα1/Kα2 radiation on crystalline Flowlac and Spectum lactose. Samples were measured from 2θ = 5–45°. An amorphous sample measured in this case gave a diffuse halo which could not be indexed by Rietveld. Samples were also tested by nuclear magnetic resonance (NMR) using the 1H-NMR technique as described by Jawad *et al.* [151], using Dimethyl Sulfoxide (DMSO) to prevent mutarotation. In our case, a 10 s recycle delay was used. Increased relaxation delay typically results in reduced differences in relaxation and is therefore better for quantitative results. Chemical shifts were taken as 6.31 ppm for α and 6.65 ppm for β.

5.4 Modeling amorphous and crystalline states

The PDF signal from the amorphous samples quickly flattens out because the molecular packing is highly disordered, and the probability of finding a neighboring atom quickly reduces to the average number density of the material. Because of the particular definition of the function $G(r)$ the function [4] has a value zero when this happens. We can define a size of the coherent structural domain which is the range of r where there are peaks and valleys in the PDF. This is reduced roughly to the size of the molecule itself, or less if the molecule has many internal degrees of freedom, in the amorphous state. In the amorphous state the packing of neighboring molecules may be specific or non-specific (i.e., there may be a preferred way of packing neighbors). In the former case, there will be a signal in the PDF that indicates the preferred packing, for example, if the low–energy configuration is a dimer. Some broad fea-

tures at higher-r may also arise that are related to the coordination of neighboring molecules. These latter two cases may be thought of as local structuring within the amorphous phase.

In this study structures for lactose polymorphs were obtained from the Cambridge Structural Database including β-lactose 'BLACTO02' [140], $\alpha\beta$-D-lactose 'LAKKEO01' [152], hygroscopic α 'EYOCUQ' [138] and stable α 'EYOCUQ01' [139] lactose, and α-lactose monohydrate 'LACTOS10' [137]. These were refined against the crystalline c-Flowlac signal to establish the sensitivity of the measured PDFs to differences in the polymorphic structures. Refined parameters included the lattice parameters by space group (a, b, c, and β in the case of the α monohydrate), isotropic displacement parameters U_{iso} for carbon C and oxygen O atoms. A PDF peak broadening term related to correlated atomic motions of the molecules, was also used [111]. The atom positions were not allowed to vary. These refinements were carried out over a range of 4.5 to 50 Å in real space to focus on the intermolecular peaks resulting from crystalline packing, though methods for simultaneously fitting intra- and intermolecular signals have been recently developed [113]. PDF broadening Q_{broad} and damping Q_{damp} terms which arise from experimental resolution effects were calculated as 0.017 Å^{-1} and 0.042 Å^{-1} respectively by refinement to a Ni standard and then set constant for subsequent refinements. The Q_{max} was set to 17.5 Å^{-1} which was used in the data transformation.

In order to study the extent of disorder in the crystalline samples, the characteristic function for spherical domains was used to determine relative changes in coherence length. A wider range including the low-r peaks which result from nearest-neighbor atomic correlations was used to better compare relative changes between the low- and high-r peak heights, 1.2–30 Å for amorphous samples and 1.2–50 Å for crystalline samples. Rietveld refinement of the lab source data was performed using the program GSAS-II [153]. The crystalline Flowlac

and Spectrum samples were fit with the α monohydrate structure over a range of 7.5–48.0 degrees 2θ. The same structural parameters as in the PDF case were used for comparison.

5.5 Results and discussion

5.5.1 Structural refinement of crystalline products

PDFs of the crystalline samples were compared with models of the various polymorphic structures. Local molecular ordering, particularly for the anhydrous α, $\alpha\beta$, and α monohydrate phases is similar, so it was important to establish confidence in the capability of the measurement to distinguish between them. It is shown in Fig. 5.2 that the c-Flowlac signal does not match well with any of the anhydrous polymorph structures. Each of the models failed to reproduce many of the structural features observed in the measurement, for example the peak at 17.4 Å. This can be seen in the difference curves plotted in green below the main curves, which show discrepancies over the entire range. The refinements led to substantial peak broadening to compensate for mismatched peaks, particularly in the cases of the β and $\alpha\beta$ structures. Although the fits improved slightly for the anhydrous α structures, the R_w values for all four structures were much higher than the values of $\lesssim 0.2$ that signify a good fit. The α monohydrate structure was then refined, and as shown, reproduced the c-Flowlac signal much better. In this case, all peaks were reproduced over the fit range, and the R_w value was reduced by more than half to 0.24. Additional refinements were carried out for the other commercial product, c-Tablettose, and for the PDFs of the crystallization products, a-Flowlac30 and a-lyoph15. These PDFs also gave good fits to the α monohydrate structure,

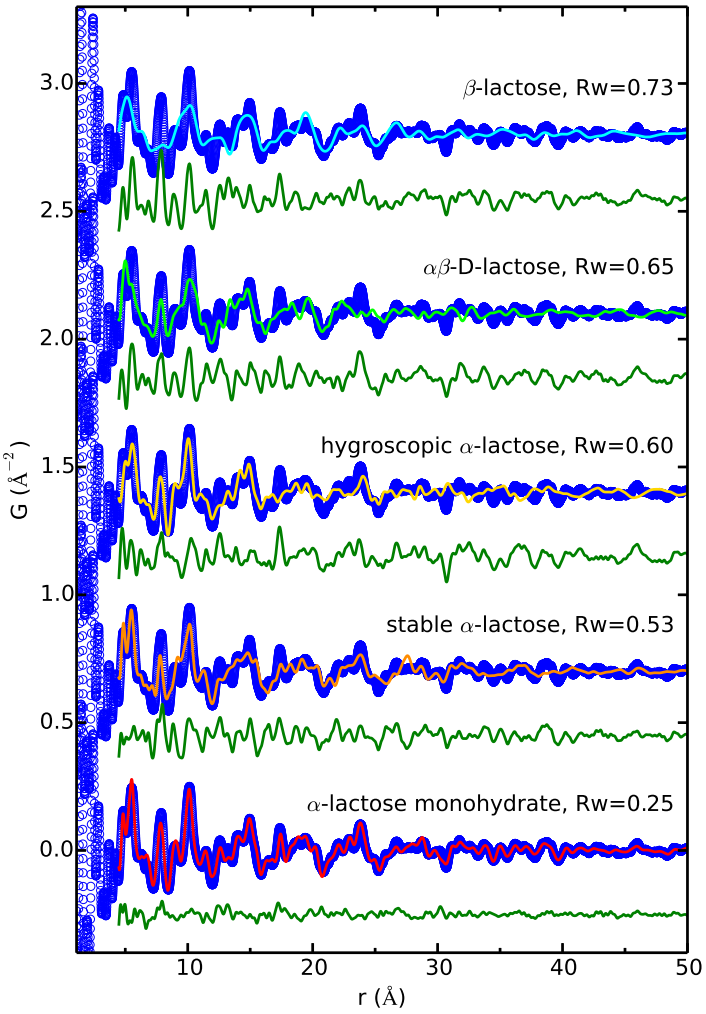

Figure 5.2: Calculated PDFs from lactose polymorph structures (anhydrous β (aqua), $\alpha\beta$ (lime), hygroscopic α (gold), stable α (orange), and monohydrate (red)) refined against the PDF of crystalline c-Flowlac (blue) with differences shown offset below (green). Visual comparison of the refined PDF of the monohydrate compared with that of the other models shows that it is clearly the correct structure. This is supported by the significantly lower R_w value.

indicating that both crystallized to this form under the given aging conditions. The crystalline Flowlac 100 and Spectrum lactose were additionally measured using Cu Kα radiation for reciprocal space comparison of the starting structure. Rietveld refinement of the α monohydrate structure is shown (see Fig. 5.3). Parameter values for all refinements are given in

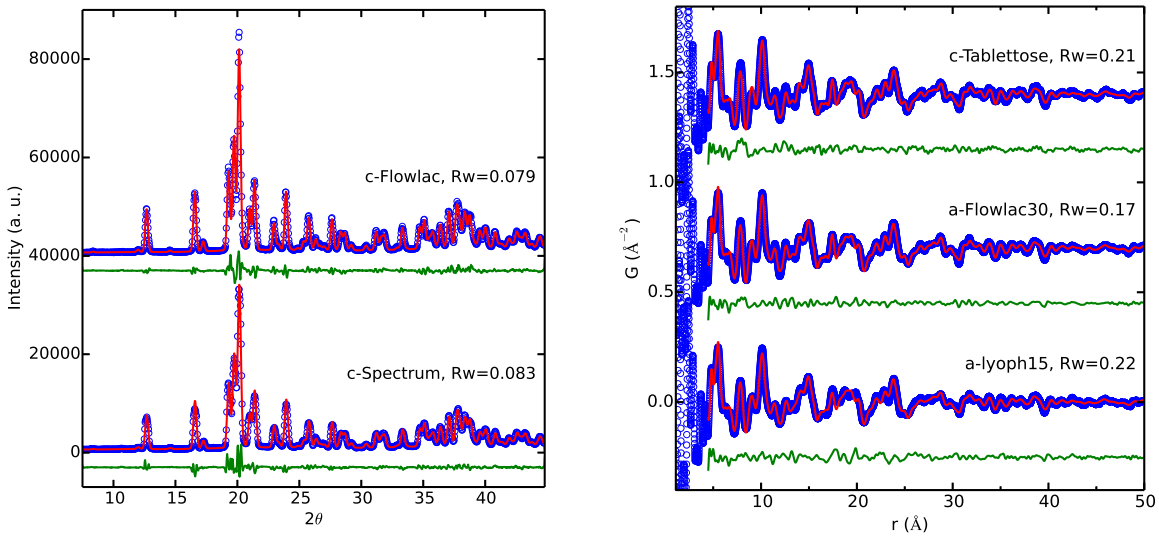

Figure 5.3: Left: Calculated scattering intensities from Rietveld refinement of the α-lactose monohydrate structure (red) to the c-Flowlac and c-Spectrum scattering measured by XRPD (blue) with differences offset below (green). Right: Calculated PDF of the α-lactose monohydrate structure (red) refined to the other measured crystalline PDFs (c-Tablettose, a-Flowlac30 and a-lyoph15) (blue) with differences offset below (green).

Table 5.2.

Table 5.2: Refined values for structural parameters from fitting the α-lactose monohydrate structure to the crystalline samples.

	Rietveld		PDF			
	c-Spectrum	c-Flowlac	c-Flowlac	c-Tablettose	a-Flowlac30	a-lyoph15
a (Å)	7.950(3)	7.950(2)	7.931(7)	7.939(7)	7.939(7)	7.951(7)
b (Å)	21.598(3)	21.606(2)	21.61(2)	21.60(2)	21.58(2)	21.57(2)
c (Å)	4.821(3)	4.823(2)	4.808(5)	4.822(5)	4.814(5)	4.808(5)
β (deg)	109.76(2)	109.77(14)	109.82(9)	109.94(9)	109.92(9)	110.06(9)
$U_{iso}(C)$ (Å^2)	0.032(6)	0.012(6)	0.021(3)	0.020(3)	0.021(3)	0.027(3)
$U_{iso}(O)$ (Å^2)	0.037(5)	0.017(5)	0.0192(2)	0.021(2)	0.020(2)	0.024(2)
R_w	0.083	0.079	0.24	0.21	0.16	0.22

Regarding the PDF refinements, differences between the standard samples and the crystallized samples are negligible. Due to the lower R_w value achieved for a-Flowlac30, it is used for the standard monohydrate signal for phase quantification.

5.5.2 Unaged amorphous formulations

The three non-aged PDFs, a-Flowlac0, a-lyoph0, and a-mq0, are compared in Fig. 5.4(a). The general structural features are reproducible, showing that amorphous formulations give a similar enough signal for fingerprinting purposes and that significant chemical degradation in the melt quenched sample is unlikely. However, there are slight differences, particularly between the melt quenched versus the Flowlac and lyophilized samples. Fig. 5.4(b) highlights this by comparing difference curves, taken to amplify the visibility of the discrepancies in the signals. In each case, two samples are compared with respect to how different they are from the third. This analysis suggests that the local structures of a-lyoph0 and a-Flowlac0 are very similar to each other but subtly different from the a-mq0 melt-quenched sample. Subtracting a-mq0 from either a-lyoph0 or a-Flowlac0, there are small but distinct features in the difference curve peaked at 2.75 Å and 4.0 Å (green and blue curves in Fig. 5.4(b)). A Pearson correlation analysis [19, 116] of these two difference curves gives 0.8, where 1.0 would be perfect correlation between the two curves, indicating that they are highly correlated over the whole range from 2 to 7 Å. On the other hand, when a-lyoph0 and a-Flowlac0 are subtracted from each other the resulting difference curves (red and orange in Fig. 5.4(b)) do not show features that suggest more than experimental noise. The appearance of peaks, small as they are, in the a-lyoph0 and a-Flowlac0 minus a-mq0 difference curves suggests a slightly

higher degree of intermolecular packing order in the former samples.

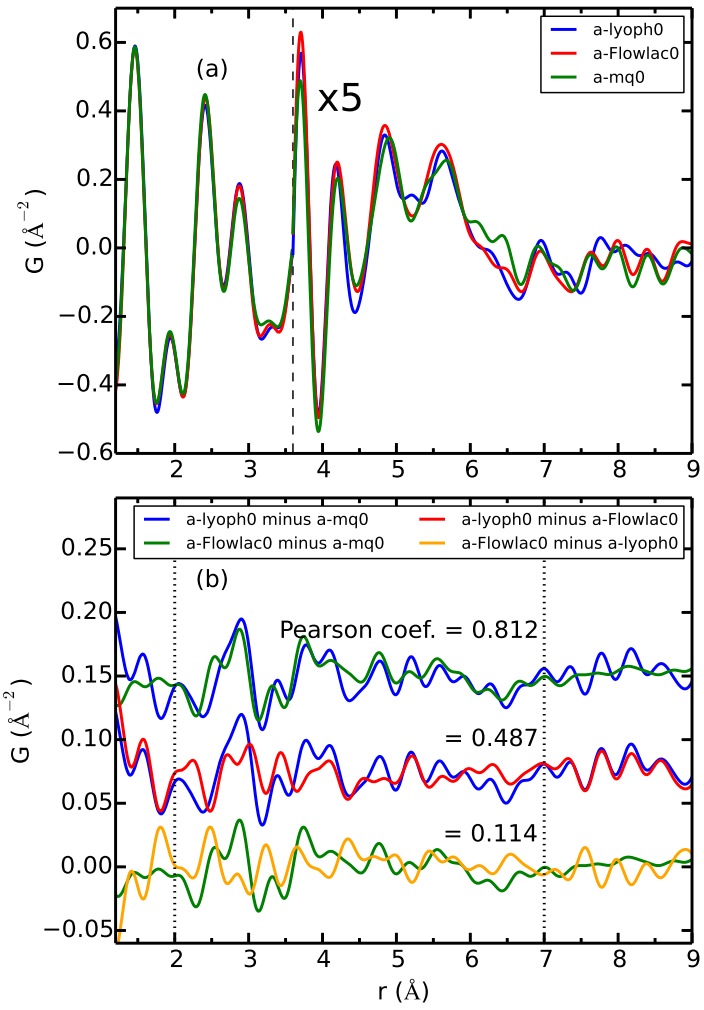

Figure 5.4: Comparison of PDFs of amorphous samples at 0 aging, a-Flowlac0, a-lyoph0, and a-mq0. (a): Signals overlaid to demonstrate overall reproducibility of the primary structural features, and zoomed in the mid-r region to highlight nuanced signal differences. (b): Differences between the signals are taken and compared using Pearson values calculated over a range of r = 2.00–7.00 Å. It is clear that the initial states of lyophilized and Flowlac samples are substantially more similar than the melt quenched sample.

The anomeric concentrations in the amorphous Flowlac100, melt quenched, and crystalline α monohydrate samples were measured using NMR. The chemical shifts for the α- and β-anomers are $\delta 6.31$ ppm and $\delta 6.65$ ppm respectively as seen in Fig. 5.5.

The resulting α anomer concentration, C_α, determined from the NMR data were 44(1)%

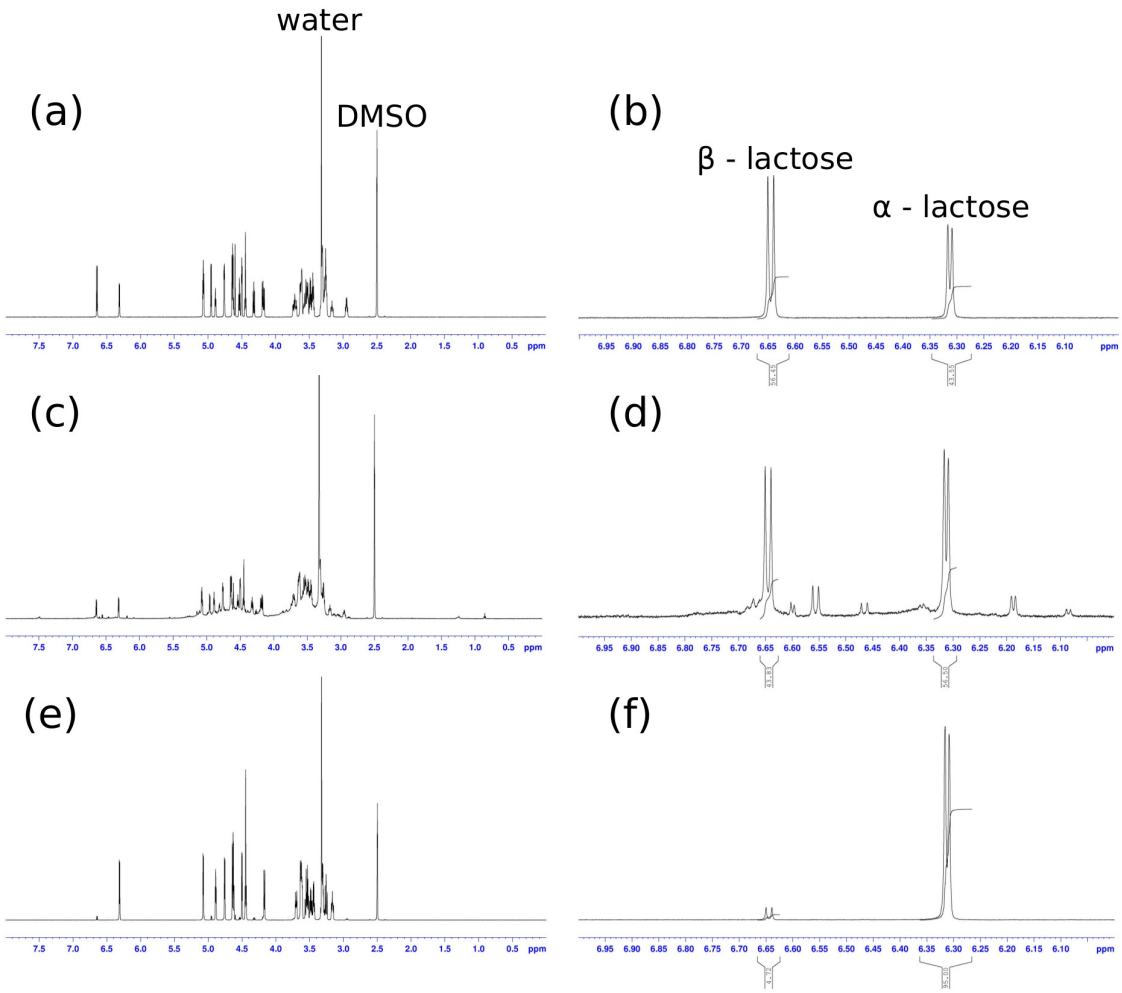

Figure 5.5: NMR spectra for (a) amorphous Flowlac100, (c) melt quenched lactose, (e) crystalline α-lactose monohydrate, and magnified plots of their peaks from α and β content (b), (d), (f) respectively.

for a-Flowlac0, 56(1)% for a-mq0, and 95(1)% for c-Flowlac, where the β concentration is equivalent to 100-C_α %. For reference, the C_α for an equilibrium solution is 37.3% [129]. The measured concentrations of the α and β anomers vary slightly, with α slightly higher in the melt quenched formulation. However, they are close to 50:50.

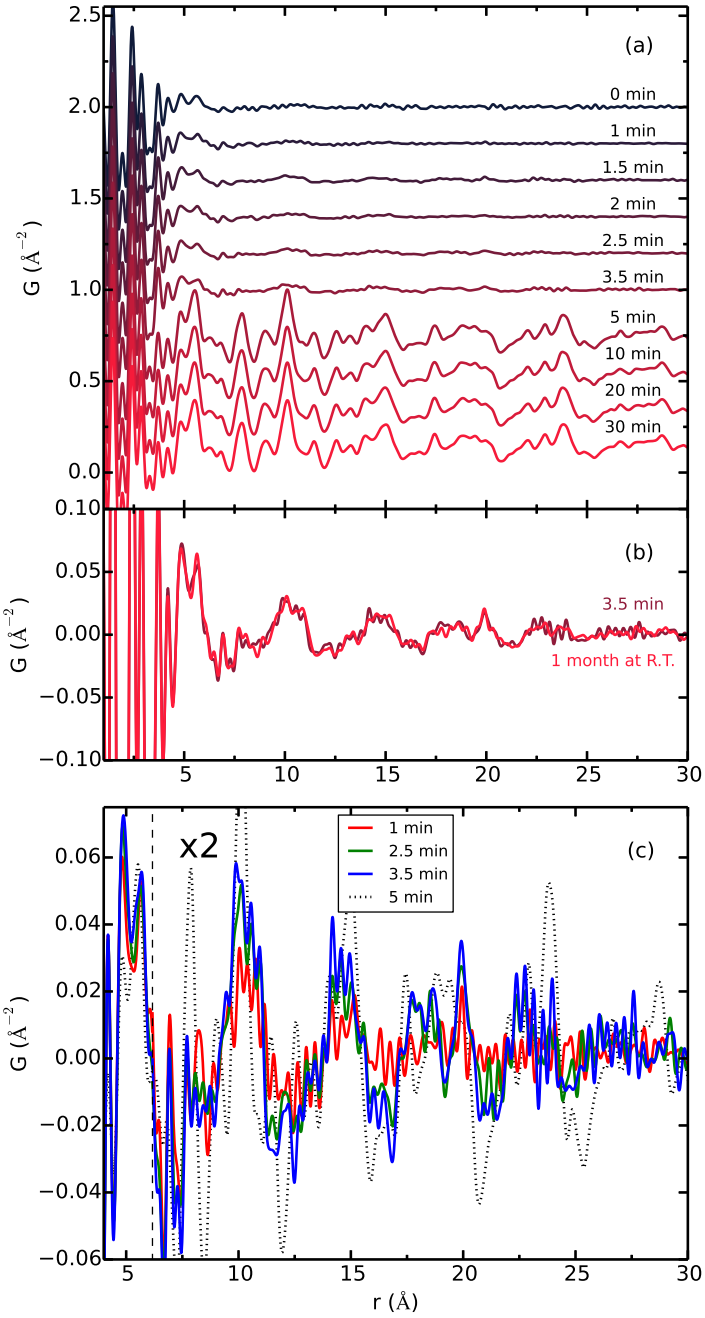

Figure 5.6: (a): PDFs measured for a-Flowlac after aging for different lengths of time. (b): Signals from the Flowlac samples aged at room temperature for 1 month and at 3.5 minutes in the storage chamber are overlaid, showing a similar extent of transformation. Aging time is shown above each curve. (c): Signals from samples aged 1, 2.5, 3.5, and 5 minutes overlaid. The peak-to-peak amplitude of structural features in the mid-r region is observed to grow with increased aging time, showing an increasing concentration of crystalline phase. Differences can be seen between the precursor structure at 3.5 minutes and the final product at 5 minutes, which has been scaled for visual comparison.

5.5.3 Crystallization behavior

Turning to the crystallization behavior of the amorphous samples under aging, the appearance in the PDF of the crystallization process is illustrated in Fig. 5.6(a) for a-Flowlac. There appears to be a latent period where changes in the PDF are subtle, followed by a rapid crystallization event between 3.5 and 5 minutes where strong features appear in the mid-r region of the PDF. The sample then evolves rather slowly after that. Zooming in on the low-time, mid-r region of the PDF (Fig. 5.6(c)) PDF features are weakly present and weakly growing. In other words, there are precursor signals in the PDF of the subsequent crystallization. The crystallization event between 3.5 and 5 minutes appears to be a complete transformation to the crystalline state, because the signals from samples aged further show little variation.

Interestingly, the signals in the PDF of the precursor clusters partially but not fully correlate with features in the resulting crystalline product (Fig. 5.6(c)). For example, strong PDF peaks will appear in the crystal at 10 and 15 Å which are present in the precursor. However, other strong crystalline peaks, for example at 7.8 and 23.9 Å are not present in the precursor PDF, and peaks in the precursor PDF, for example at 6.9 and 20 Å are not present in the resulting crystalline product. The reproducibility of the precursor PDF signals between different samples lends confidence that they are a robust signal of real structural features, suggesting that the precursor species actually have a different structure from the ultimate product.

It is interesting to try and compare the local structure of the samples where aging was accelerated to samples aged under ambient conditions. This is shown in Fig. 5.6(b) where it is shown that the amount and nature of the transformation that has occurred over one month in ambient conditions is very similar to that of the sample aged in the storage chamber for

3.5 minutes.

The samples prepared via melt quenching did not crystallize over a period of accelerated aging from 0 to 55 minutes, as evident by the similarity of the PDFs for the 0 and 55 minute samples in Fig. 5.7(a), compared with the crystallization that took place by 5 minutes under the same conditions for the Flowlac and lyophilized samples. Although some PDF features

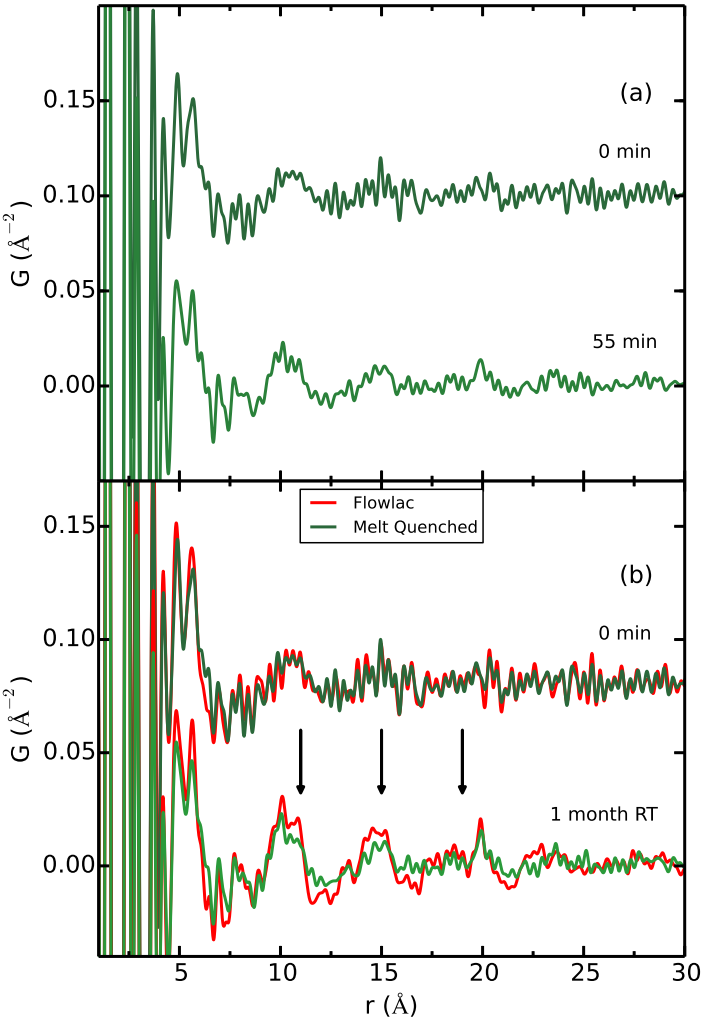

Figure 5.7: (a): PDFs measured for a-mq after aging for different lengths of time. (b): Melt quenched and Flowlac samples are compared after aging for 0 minutes and for 1 month at ambient conditions. A crystalline component is observed in both, but less so for the melt quenched sample. Arrows indicate strong structural correlations growing in during aging over 1 month.

did appear in the mid-r region, a major crystallization event was not observed for the melt-

quenched sample.

The melt quenched sample was also more stable than Flowlac under ambient conditions, as shown in Fig. 5.7(b), with a lesser degree of transformation occurring over 1 month.

The third set of samples, prepared by lyophilization (Fig. 5.8) display a crystallization

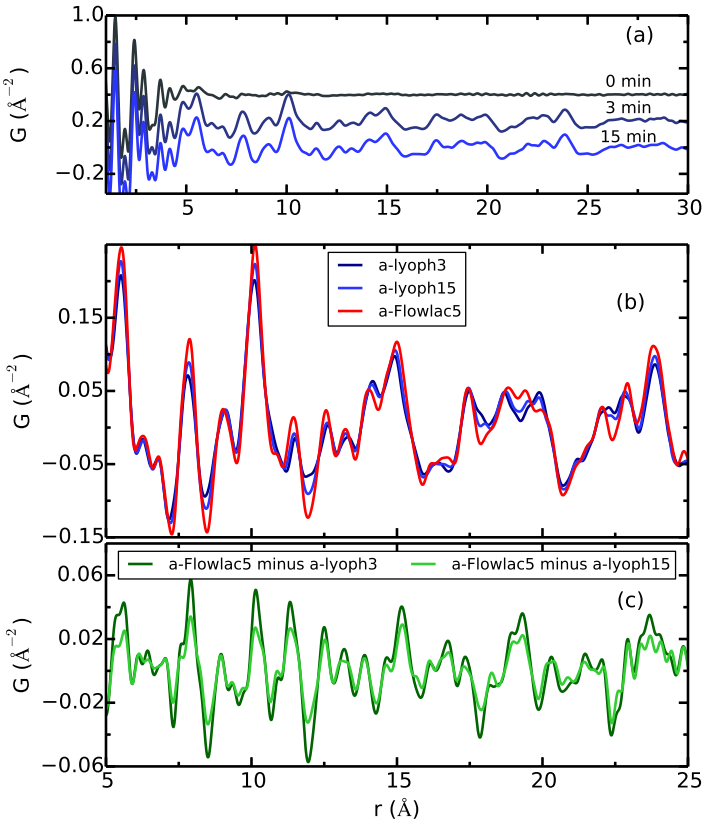

Figure 5.8: (a): PDFs measured for a-lyoph after aging for different lengths of time. (b). Crystalline signals from the sample aged for 3 and 15 minutes are overlaid with the a-Flowlac5 signal showing a higher degree of structural disorder for the lyophilized samples by the increase in signal attenuation. (c): Difference curves from the signals in panel (b) are overlaid to show that with increased aging time, the structure of the lyophilized samples approaches that observed in crystallized Flowlac.

transition similar to the Flowlac case, but it happens more quickly: between aging times of 0 and 3 minutes. In this case, although the sample begins to crystallize more quickly, the crystalline signal continues to evolve over a longer aging time than in Flowlac. This is more easily seen in Fig. 5.8(b), where the signals are overlaid with that of the Flowlac sample aged for 5

minutes. By direct comparison, the PDF features become successively more distinct moving from the lyophilized samples aged at 3 and 15 minutes to the Flowlac sample, respectively. This is evident by looking, for example, at the positive correlations at 7.8 and 10.1 Å, the negative correlation at 12.0 Å, and the splitting of the two peaks at 22.5 Å. Additionally, the signal in the lyophilized sample is slightly more damped with increasing r than Flowlac, indicating a slightly smaller crystallite size, or domain of structural coherence. In Fig. 5.8(c), the difference signals show that at higher aging time, the structure in the lyophilized sample approaches that of Flowlac, as the disorder gradually anneals away.

The coherence length of the structural order was determined for each sample using the α-lactose monohydrate structure model. Refined values of this domain size are plotted in Fig. 5.9. This again shows that crystallization of the lyophilized lactose displays gradual growth while the Flowlac 100 effectively does not change after the majority crystallization event occurs. Although the coherence length refined for the unaged samples is approximately the size of the molecule, a very minute structural signal can be seen beyond this.

5.5.4 Quantifying amorphous and crystalline phase content

It is possible to show that features arising in the PDFs with increasing sample aging are directly related to an increased crystalline component as evident in Fig. 5.10, First, a composite signal of both amorphous and crystalline standards fits the 1 month aged a-FlowlacRT PDF much better than an amorphous standard alone. This is shown in Fig. 5.10(a). Components were allowed to refine to find the best fit with approximately 7% crystalline content. Similarly, the difference curve obtained by subtracting the amorphous model from the 1 month

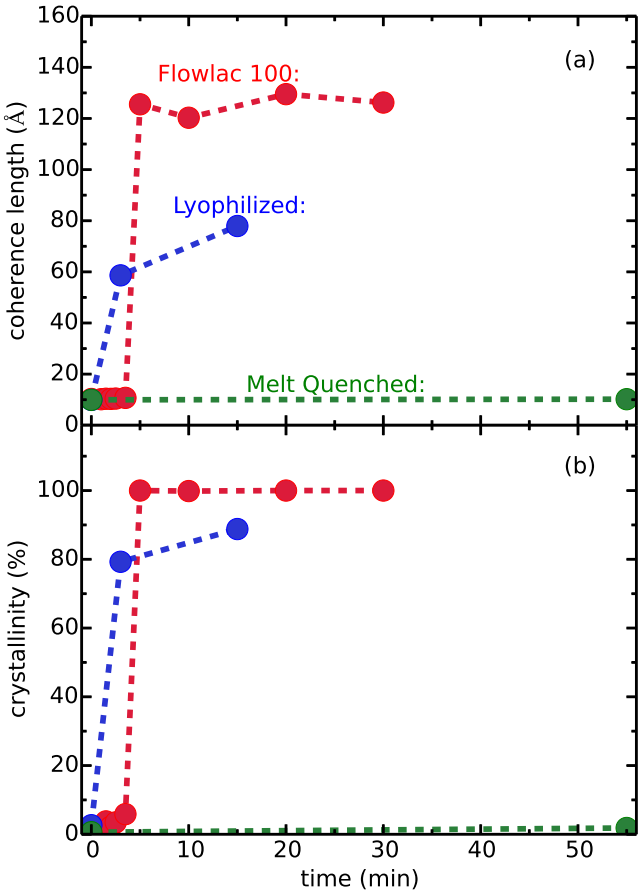

Figure 5.9: (a) Refined coherence length from PDFgui and (b) least-squares crystalline phase fraction versus crystallization time for samples aged in the storage chamber.

aged data is well explained by the measured PDF of the crystalline control sample, which we know to be the α monohydrate polymorph (Fig. 5.10(b)). Thus we use the approach to extract the quantity of crystalline and amorphous components as a function of aging time by measuring PDFs from the end-member (100% crystalline and 100% amorphous) samples, taking a linear combination of them, and varying the mixing fraction until the best fit to the measured data is obtained. Prior to refinement, the data were scaled so that the first carbon-carbon peak had the same integrated intensity, which is justified since the coordina-

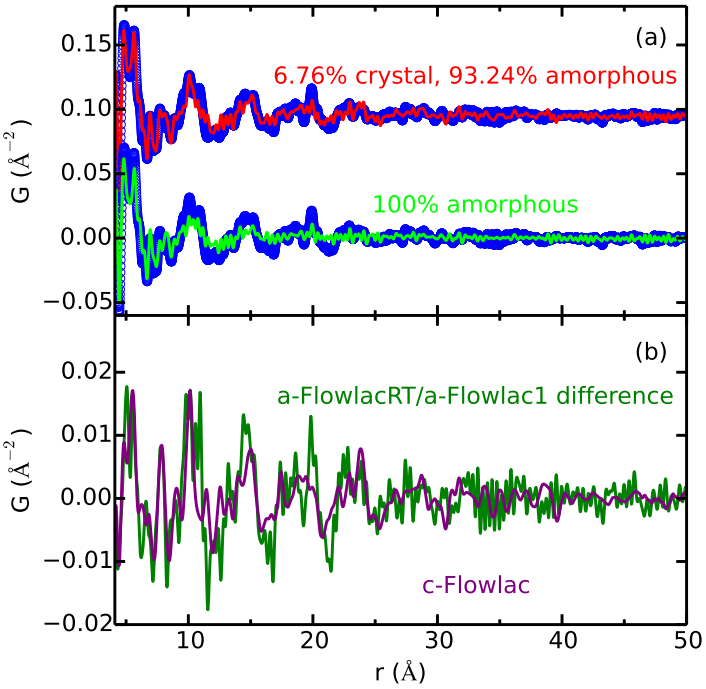

Figure 5.10: (a): Amorphous Flowlac100 aged for 1 month at room temperature (blue) is compared to a mixed phase fit (red), and to the amorphous standard (lime), with improvement in signal reproduction with the mixed fit. (b): The difference (green) between the aged sample and the amorphous standard is compared to the scaled crystalline standard (purple). Features arising from the crystalline phase can be clearly seen in the difference.

tion of carbon should be the same for samples comprised of the same molecules. In this case, sample densities were assumed to be approximately the same. Some representative agreements can be seen in Fig. 5.11 and the resulting proportions of amorphous and crystalline components are shown in Table 5.3. The reference crystalline and amorphous PDF curves used in the fitting were a-Flowlac30 and a-Flowlac1, respectively. It is clear from Fig. 5.6 that both the a-Flowlac0 and a-Flowlac1 samples display the least significant structuring in the mid-r region, though a-Flowlac1 is chosen as the standard since there is less noise in the signal. Meanwhile, there are negligible differences between the Flowlac samples which have achieved crystallization and the as-received c-Flowlac sample.

To check for reproducibility I tried two different measures of the agreement between the

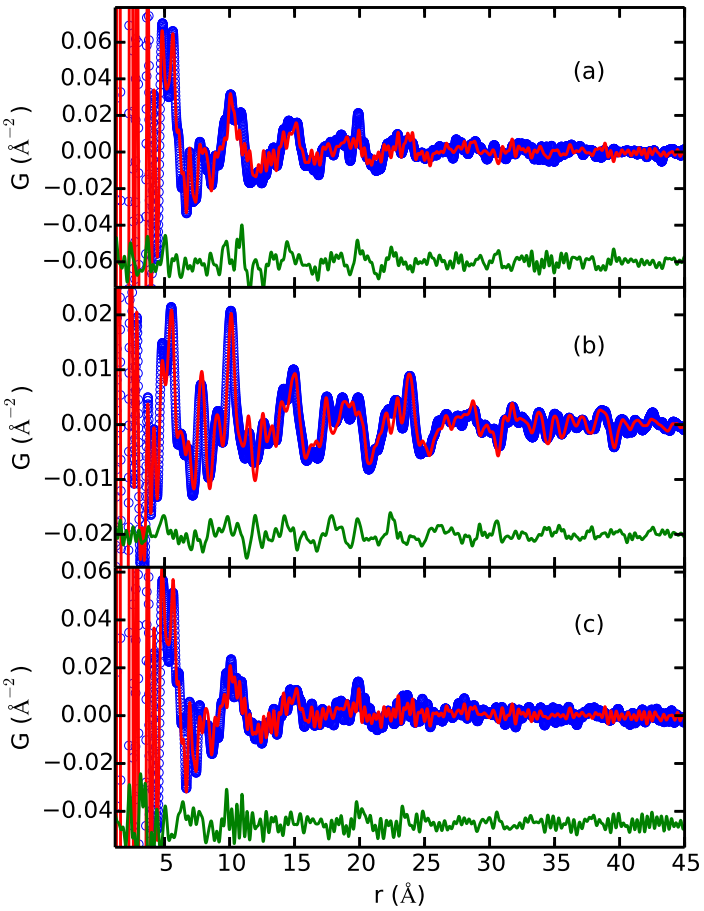

Figure 5.11: Representative mixed phase (crystalline:amorphous) fits, G_{mix} (red) overlaid with measurement (blue) for (a): a-FlowlacRT (6.76:93.24), (b): a-lyoph3 (79.28:20.72), (c): a-mq55 (1.83:98.17). Differences plotted below (green). Phase concentrations chosen by least-squares refinement of a weighted linear sum of the amorphous and crystalline standard PDF signals (a-Flowlac1 and a-Flowlac30 respectively). The difference in (c) appears slightly noisier due to the amplification of high-r ripples in the amorphous standard which has a larger phase fraction in this case.

linear combination and the measured data. In the first procedure, a linear addition of the standards is calculated as

$$G_{mix} = xG_c(r) + (1-x)G_a(r) \tag{5.1}$$

and the concentration, x, is varied such as to minimize the least-squares residual, $R = \sum_i (G_{exp}(r_i) - G_{mix}(r_i, x))^2$ with each measurement. In the second procedure, the concentration is varied such as to maximize the Pearson product-momentum correlation coefficient [21] between G_{mix} and the measurement. In the third column of Table 5.3 are the sizes of the coherent structural domain as refined from PDFgui, also shown in Fig. 5.9.

The variation between the phase concentrations calculated from the least squares minimization and from maximizing the Pearson coefficient gives some measure of the sensitivity and precision of this approach for estimating the phase fractions. For the samples with small crystalline components, all of them agree at the level of around 0.2%. The precision is still good, but less good, for the more highly crystalline components, being around the 1% level. This method thus appears to have rather good sensitivity to small changes in crystalline:amorphous ratio at all concentrations, but especially for the samples with low crystallinity.

There is a general monotonic trend of increasing crystalline component with time, as expected, with one exception, the a-Flowlac1.5 sample. This could reflect an uncertainty on the absolute accuracy (rather than the precision) of our measurement. However, I believe that it originates from the fact that the measurements were performed ex situ, and small changes in quenching rates and sample handling could potentially affect the actual crystalline

Table 5.3: Flowlac100, lyophilized, and melt quenched lactose aged for varying times at 40°C/75% RH. The crystalline component is estimated using least-squares and Pearson correlation methods (see text for details). d_c is the diameter of the coherent structural domain.

aging time (min)	cryst. comp. (%)		$\boldsymbol{d_c}$ (Å)
	least sq.	Pearson	
Flowlac 100			
1.0	0.00	0.00	10.18
1.5	3.75	3.52	10.37
2.0	2.21	2.27	10.32
2.5	3.47	3.24	10.44
3.5	5.87	5.78	10.71
5.0	100.00	99.72	125.54
10.0	99.85	99.90	120.29
20.0	100.00	100.00	129.51
30.0	100.00	100.00	126.23
Crystal AR	100.00	100.00	104.67
1 month RT	6.76	6.61	11.12
lyophilized lactose			
0.0	2.64	2.65	9.44
3.0	79.28	78.25	61.48
15.0	88.80	88.67	81.65
melt quenched lactose			
0.0	0.61	0.78	9.19
55.0	1.83	1.90	9.52
1 month RT	1.92	2.03	9.46

component, especially at these low levels of crystallinity. Looking at the data, it is clear that these calculated fractions are actually consistent with the signal and therefore more likely to be the result of some additional crystallization which occurred between removal from the storage chamber and the measurement.

The PDF can simultaneously provide quantitative information on the average and local structures of pharmaceutical materials, adding another complimentary tool for solid-state characterization of pharmaceuticals. As seen by the identification of α-lactose monohydrate as the product of the crystallization, this method yielded comparable information to reciprocal space techniques such as Rietveld refinement of x-ray powder diffraction data for

identifying and analyzing the crystalline samples. However, in contrast to such methods which give ambiguous data for amorphous materials or more complex mixtures, the PDF is capable of discerning subtle structural differences in such formulations. For example, this showed a reproducible fingerprint for amorphous lactose [14]. Even in the amorphous state, the data reproducibility and information content is sufficient to allow us to see the structural similarity between the lyophilized and amorphous Flowlac samples and dissimilarities when compared to the melt quenched form. Crystallization of the lyophilized and Flowlac samples was rapid when aged under elevated temperature and humidity, but negligible for the melt quenched sample up to 55 minutes under accelerated conditions. When aged at ambient conditions, both Flowlac and the melt quenched form experienced minimal crystallization over one month. This is expected since increases in both temperature and humidity reduce sample stability in the amorphous state [154], and we observe that the melt quenched form was more stable in both cases. Phase concentrations of aged samples were estimated using a linear combination of weighted amorphous and crystalline signals. These were optimized by both least-squares and Pearson correlation methods, and both were shown to give consistent results.

Proton NMR measurements were performed as described by Jawad *et al.* [151] to prevent mutarotation during measurement. These showed that the α:β anomer ratio in the amorphous Flowlac and melt quenched formulations are similar, but that the α concentration was higher in the more stable formulation. This is interesting since the final product requires mutarotation to α to form the monohydrate, and may be related to the formation of a precursor structure. An explanation for differences in crystallization may be differences in residual moisture content left over from the amorphization process. Crystallization can be postponed

when the moisture content is below 5% [155]. It is reasonable to expect that with a melting temperature above 200°C, melt quenching could more efficiently eliminate residual moisture than either spray drying or lyophilization leading to higher stability, but further investigation is needed to support this effect.

5.6 Further analysis

Further analysis of the medium range ordering was carried out after publication of the previous results to shed more light on the nature of the disordered phase development during crystallization. I attempted to index any nanocrystalline seeds which nucleated during the first few minutes of aging to see if they shared a resemblance to and other known structures. To do this, I fit the known polymorphic structures to the high-r region of the spray dried Flowlac sample after aging for 3.5 minutes, a-Flowlac3.5. This was done for the PDFs processed with a Q_{max} of 17.5 Å^{-1} and fits of the α monohydrate, stable α anhydrous, hygroscopic α anhydrous, $beta$ anhydrous and mixed $\alpha\beta$ forms. Qualitatively, the $\alpha\beta$ and β forms were better matches to the signal than the monohydrate form and α forms. This indicates that the monohydrate form is actually not the form which predominates prior to the bulk transformation event which agrees with the previous qualitative observation of differences in the signal between the nucleating and final forms. I tested multiphase fits of the monohydrate, β, and $\alpha\beta$ forms to see if there were any trends in phase development during crystallization. The multiphase fits reproduce all main features in the region of 8.0-40.0 Å well. Fits to a-Flowlac1 and a-Flowlac2.5 are shown in Figure 5.12 The trend in phase fractions for the three different phases is shown from 0 to 3.5 minutes in Figure 5.13 Searching the

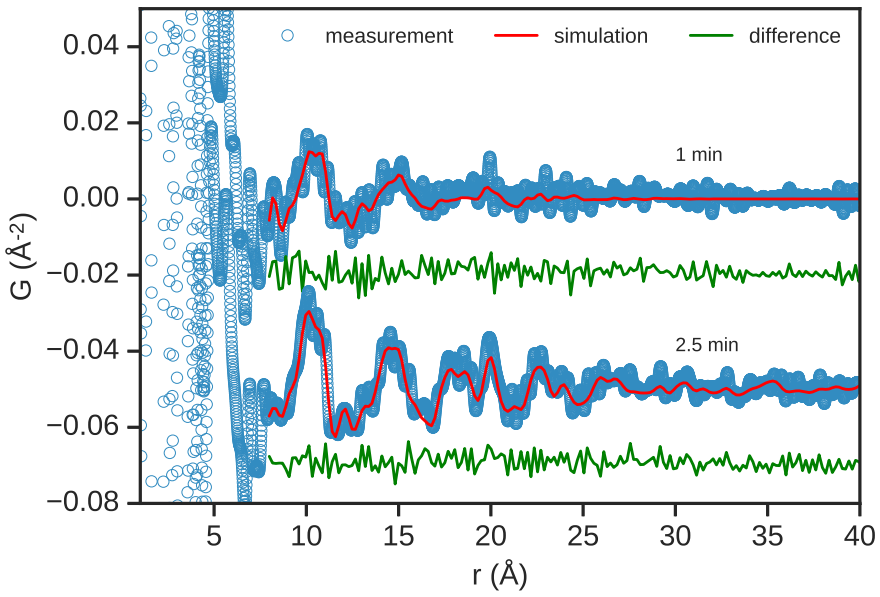

Figure 5.12: Calculated PDF of the mixed phase model (red) refined to the a-Flowlac1 and a-Flowlac2.5 PDFs (blue) with differences offset below (green).

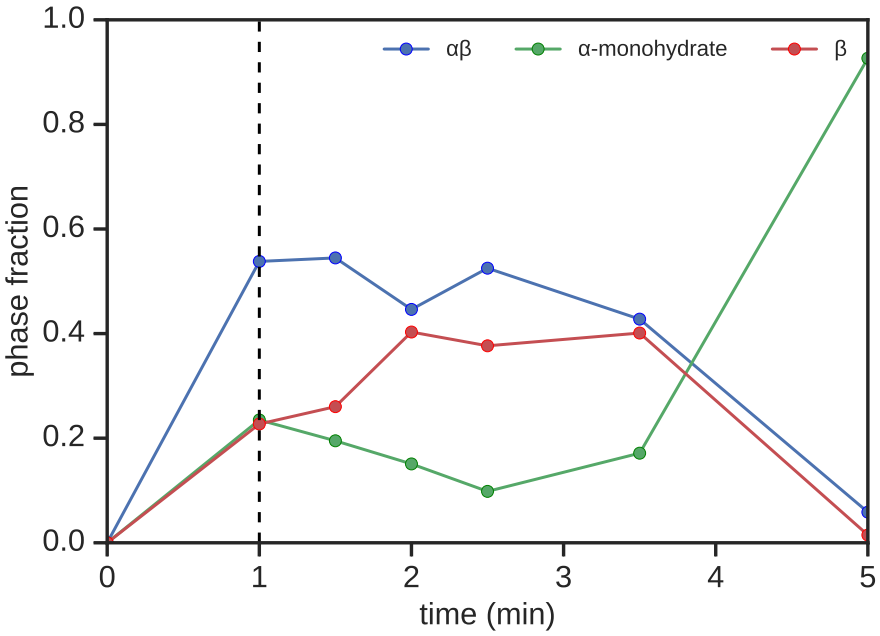

Figure 5.13: Trends in phase fraction for the three phase model. The black dashed line indicates the first time point where the data was refined. There was not suitable signal-to-noise in the zero minute measurement to observe any peaks. Additionally, the 1.5 and 2.0 minute data points were switched for more consistent agreement. This was justified since the 1.5 minute sample was clearly more developed (it was from a different batch).

literature I found that these results are highly consistent with previous reports of phase development in lactose crystallizing from a spray dried amorphous state [156]. Mixed anomer phases form first, along with β and α-monohydrate. Then there is a rapid transformation where the monohydrate takes over. At longer times, the β has been shown to eventually win out, but the conditions in this study were different (higher temperature and lower RH), so it is not easy to directly compare.

5.7 Conclusions

In this report, PDF analysis was used to interrogate the crystallization behavior and products of different samples of amorphous lactose prepared by spray-drying, lyophilization, and melt quenching. This is a powerful approach for following the crystallization process, from initial stages where small nuclei form to the final products. Different methods for amorphizing the samples produced material of different stability against crystallization. Subtle changes could be detected in the PDFs from samples with different stabilities, opening the door to the possibility that PDF may be able to predict the stability against crystallization of a sample in a system that has been well characterized, by observing pre-crystallization species. However, much more work is needed to establish if this is indeed the case.

The PDF unambiguously identified the crystallization product as α-lactose monohydrate. The pre-crystallization species was detected reproducibly between samples with features that are not seen in the PDF of α-lactose monohydrate. This indicates that the first objects to form and grow from the amorphous state have a different structure than the final product. These features were shown to come from nanocrystalline β and mixed anomer phases which nu-

cleate prior to the monohydrate form. This preliminary study on the use of PDF methods on a system of commercial interest, in this case an excipient, is very promising, suggesting that further advances in this method could lead to important practical applications in amorphous and nanocrystalline pharmaceuticals, and organic systems in general.

Chapter 6

Local ordering in thermoplastic hard phases

This chapter presents the use of PDF analysis to determine the structure of nanocrystalline hard segment domains in thermoplastic polyurethanes. The possibility to do this was inspired by the work in the previous Chapter 5. I observed that very small signals at medium-to-high-r were highly reproducible in lactose, and therefore must contain valuable structural information. I successfully tested this hypothesis on the very small signals observed in paracrystalline polymers. This work was published in the journal Macromolecules (2016) [157].

6.1 The structures of hard phases in thermoplastic polyurethanes

The importance of thermoplastic polyurethanes (TPUs) was noted in Chapter 1. It is therefore surprising that no fully quantitative models had been verified for the hard phase structure since studies of the structure began in the 1960s. Blackwell and Gardner [158] first proposed a model for the chain conformation based upon the previous solution of the crystal structure of methanol-capped MDI. However, it was determined that a detailed understand-

ing of the stereochemistry was needed to give insight into the packing [159]. Wide-angle x-ray scattering studies confirmed linearity of the hard segment chains, ruling out any appreciable folding, and identified the possibility of different polymorphic forms through differences in diffraction patterns [160]. Polymorphism was further studied through electron diffraction [161, 162], though quantitatively reliable structures were not obtained. Infrared spectroscopy measurements determined that MDI-based polyurethanes could form in various modifications depending on the types of hydrogen bonds present [163]. The hydrogen bonding interactions have been investigated more recently using density functional theory (DFT) [164].

Unit cells have been proposed from x-ray and electron diffraction [158, 165], and several structural refinements have been reported [166, 167]. However, there is ambiguity in these results due to the poor diffraction data and quality of the structural refinement. Beyond this, standard diffraction methods are challenged when studying structures such as these where crystallites are on the order of tens of nanometers or less [168] and, to date, significant questions remain about the structure of the hard phase crystallites in these materials.

6.2 Sample preparation

The samples studied were produced by the BASF corporation. They contained 4,4'-methylene diphenyl diisocyanate (MDI) and 1,4-butanediol (BDO) as a chain extender in the model hard phases. The final products also contain a polytetrahydrofuran (PTHF) soft segment, Figure 6.1. TPU samples consisting of MDI, BDO, and PTHF with a molar mass Mn $\sim$ 1000 g/mol, were produced using a band casting process [169]. The resulting pellets were

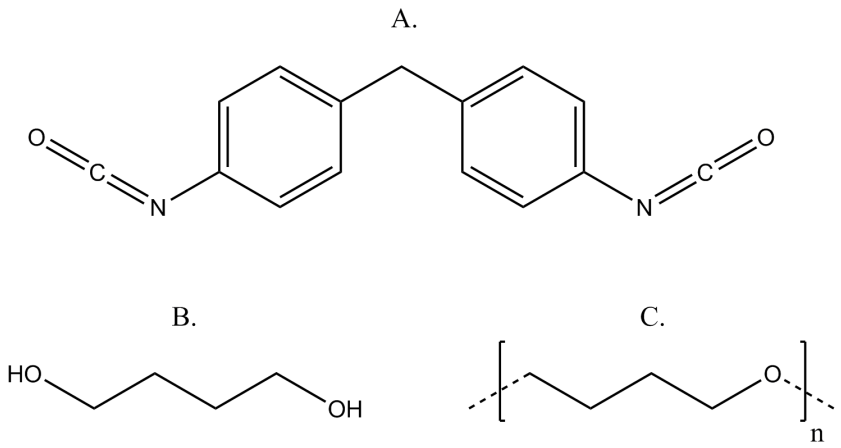

Figure 6.1: Schematics of (A) the hard segment monomer structures, 4,4'-methylene diphenyl diisocyanate, (B) the chain extender 1,4-butanediol, and (C) the soft segment monomer polytetrahydrofuran.

injection molded to sheets of 2 mm thickness. The model hard phases of MDI and BDO were synthesized by hand-casting in a one-shot process. The milled model hard phases and the TPU sheets were annealed at 100 °C for 20 hours. During sample preparation, the milled hard phases became increasingly brittle going from HP1 to HP5 while the TPU sheets were very flexible. Table 6.1, lists all of the samples studied.

Table 6.1: Samples measured. Casting T refers to the starting temperature of the hard cast.

#	ref.	sample	composition	ratio	cast T (C)
1	MDI	MDI	MDI	-	
2	PTHF	PTHF1000	PTHF	-	
3	HP1	TPU hard phase 1	MDI:BDO	(1:1)	80
4	HP2	TPU hard phase 2	MDI:BDO	(1:1)	40
5	HP3	TPU hard phase 3	MDI:BDO	(1:1.2)	80
6	HP4	TPU hard phase 4	MDI:BDO	(1:1.5)	80
7	HP5	TPU hard phase 5	MDI:BDO	(1:2)	80
8	TPU1	TPU Shore 60D	MDI:BDO:PTHF	(1:0.79:0.21)	
9	TPU2	TPU Shore 98A	MDI:BDO:PTHF	(1:0.73:0.27)	

6.3 Results and discussion

For molecular materials, the PDF can be categorized into three ranges. The low-r region ($0 < r < 10$ Å) is dominated by intramolecular correlations and has very sharp peaks resulting from strong covalent bonds. The mid-r region ($5.5 < r < 17$ Å) has broader peaks coming from a mixture of longer-range intramolecular and nearest neighbor intermolecular interactions, and the high-r region ($8 < r < 50$ Å) has broader PDF peaks exclusively from the molecular packing. These ranges can change based upon molecule size, conformation, and the degree of nearest neighbor interactions. As a local probe, the PDF is extremely sensitive to molecular conformation and packing which directly affect the position and shape of any ordered intermolecular peaks in the medium and high-r regions.

In order to benchmark the quality of high-r structural fits that can be expected for the relevant components, samples of crystalline MDI (SUPELCO Lot:LB98858V) and PTHF (Sigma Aldrich Lot MKBK9564V) were measured and fit with known structures: reference codes BUBVEZ [170] and LILVEH [171] in the Cambridge Structural Database, Figure 6.2. In order to model both intra- and intermolecular regions of the PDF, I used the fitting scheme described by Prill *et al.* [113] and discussed in Chapter 2. I refined the lattice parameters allowed by symmetry and a scale factor. Separate thermal parameters are refined to account for thermal motion between atoms on the same molecule (intra-molecular pairs) and between atoms on different molecules (inter-molecular pairs). This is required because of the very different intra-molecular (covalent) and inter-molecular (hydrogen bonding and van der Waals) bonding in molecular materials. For the case of PTHF, there is more significant attenuation in signal intensity moving from the intramolecular region to the intermolecular region, how-

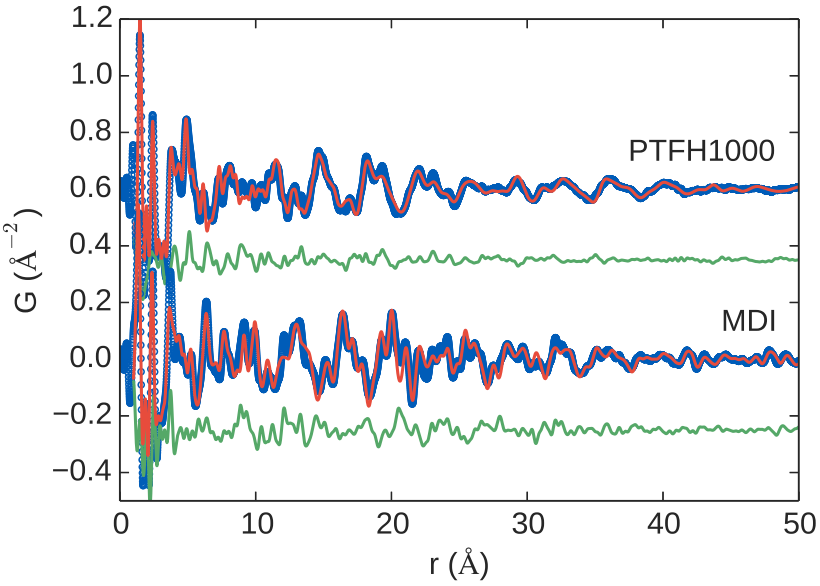

Figure 6.2: Best fit simulated PDFs (red) compared to measured PDFs (blue) of PTHF and MDI, with the difference curve offset below (green). Fit residuals are $R_w = 0.30$ and 0.39 respectively. (Q_{max}=16 Å^{-1})

ever the crystalline signal in itself still extends quite far. This is typical of materials whose structure consists of a mixture of crystalline and amorphous components. I therefore include a second disordered phase in the model. The signals from the crystalline and amorphous phases are also multiplied by a characteristic function for finite spherical domains to adjust for changes in coherence. The result is that 57% of the PTHF sample is disordered, lacking any spatial coherence beyond approximately 21 Å. A step-wise construction of this model is shown in Figure 6.3.

The resulting fits are good, though the R_w residuals that quantify the goodness-of-fit, are larger than is typically expected for a fit to a well ordered inorganic material. However, given the simplicity of the fits (no atoms were allowed to move), visual inspection of the curves which reveals that all of the main peaks are well reproduced, Figure 6.2, gives confidence that the structure of the samples is well represented by these models. It also places a scale

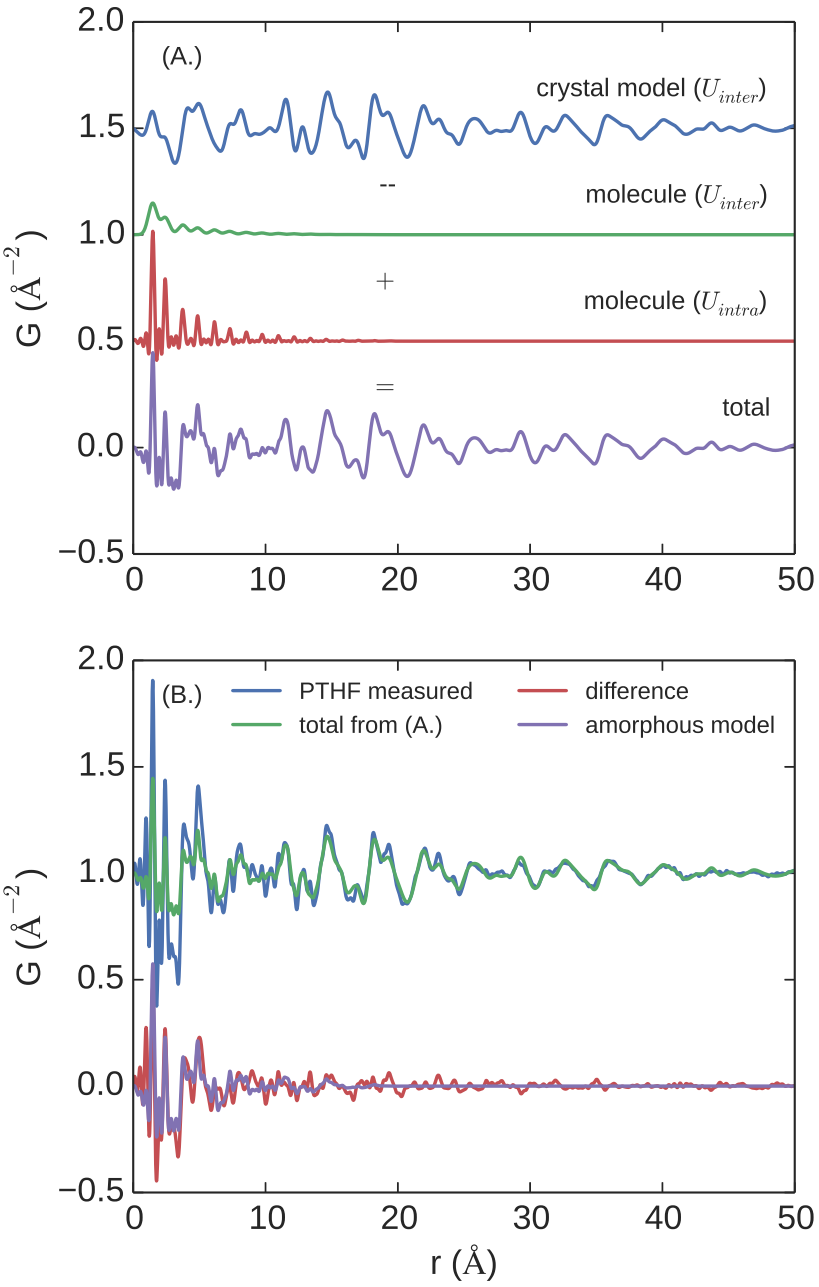

Figure 6.3: Depiction of process for fitting the model structures to the data, shown for the case of PTHF. (A) The crystal model is simulated and fit to the high-r region of the measured data to determine the intermolecular thermal parameter, U_{inter}. The PDF of a single molecule from the same structure is then calculated with the same thermal parameter and subtracted to obtain the intermolecular PDF. Another PDF of the molecule is then calculated with a much lower thermal parameter U_{intra} to produce the sharp peaks seen in the low-r region. (B) The full PDF produced from (A) is not able to describe the significant attenuation seen going from the low-r to high-r regions, indicating an additional disordered phase is present. This phase is modeled with the same local structure as the crystalline phase but calculated with a much smaller crystallite size.

on what may be considered as the R_w of a reliable fit for these systems.

The measured PDFs of the five prepared hard phase samples and two TPU products are displayed in Figure 6.4. Inspection of the figure indicates that HP1 and HP2 (plotted on top

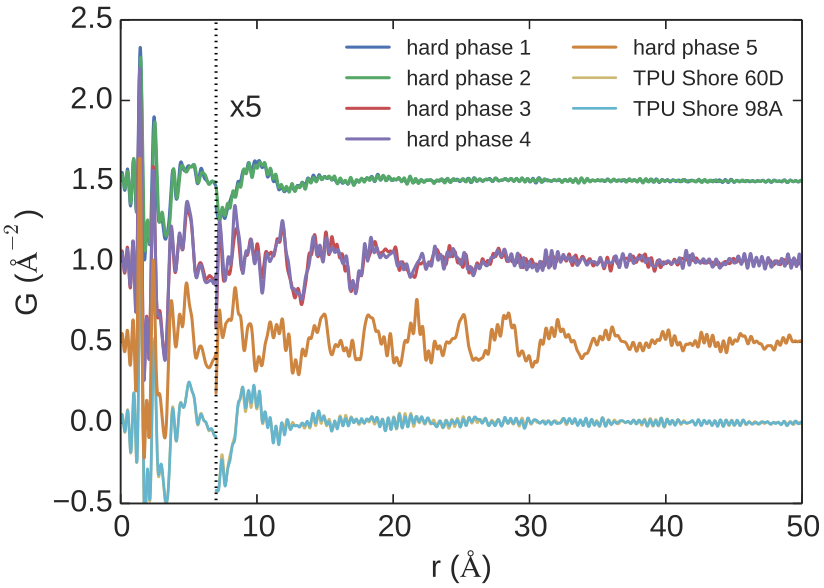

Figure 6.4: Measured PDFs from the five hard phase samples (Q_{max}=16 Å^{-1}).

of each other), which have the same MDI:BDO ratio but were cast with different starting temperatures, have a structure that is identical to one another but very different from the hard phase samples containing higher BDO contents, establishing the reproducibility of the measurements, and the fact that varying the casting temperature in this range does not affect the atomic-scale molecular packing in these materials. These two hard-phase samples are less crystalline, having a largely disordered or amorphous structure. This is evident by the rapid attenuation of the structural signal with increasing-r. Beyond about 7.0 Å, the PDF quickly damps to zero. There are still structural features present at about 9.8, 14.5, 18.5, and 27.6 Å. This information may give clues as to the nature of the polymerization and the local packing of the molecules, but is not indicative of any well-ordered (*i.e.* nanocrys-

talline/paracrystalline) structuring in these samples. Differences in the intermediate range structure, compared to the other samples, suggest that the molecular packing is not the same. Less crystallinity and more disordering of this structure corresponds well with the higher elasticity observed during sample preparation. A closer view of these details are shown in Figure 6.5 Samples HP3 and HP4 have slightly different MDI:BDO ratios to each other, but

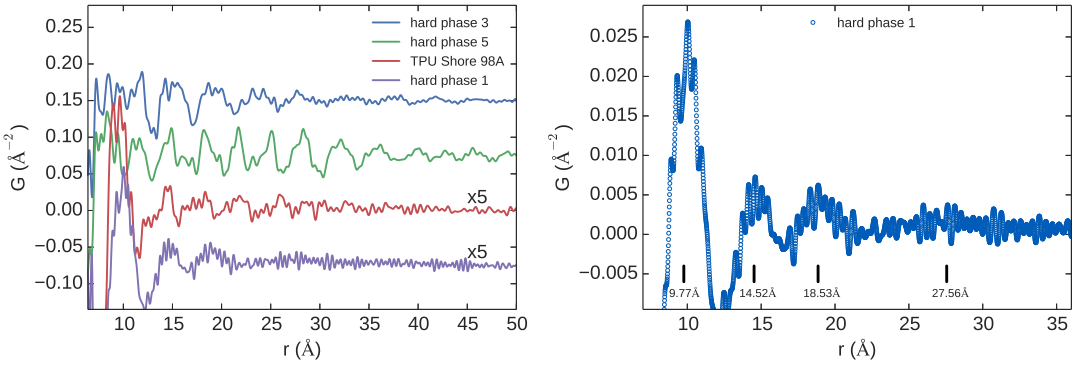

Figure 6.5: High-r signal in HP1 and TPU2. Left: The structuring in the PDFs of HP1 and TPU2 is compared to that of HP3 and HP5. It is clear that both samples show significant differences from the more crystalline phases. However, there is a small structural signal in TPU2 extending to higher-r given the distinct peak shapes. Right: HP1 shows several features at 9.77, 14.52, 18.53, and 27.65 Å. These features are much broader than the other sample PDFs indicating that there is far more structural disorder in samples HP1 and HP2.

are very similar to each other structurally, and are more ordered than the former samples as evidenced by the observation of peaks in $G(r)$ which extend to higher distances. Sample HP5, with a yet higher BDO component, is even more ordered, but has significant structural differences. The molecular packing between HP3/HP4 versus HP5 is distinctly different in the high-r region of the PDF. The two distinct structures (between the three samples) were termed Form I and Form II. The similarity of the low-r ($0 < r < 4$ Å) and intermediate range-r ($4 < r < 12$ Å) regions of these two structures suggests that the polymer form (*i.e.* the bonds that form during polymerization) is very similar. However, the different features in the high-r region suggest a different molecular packing between Form I and Form II:

there is a structural transition as a function of MDI:BDO ratio. More subtle differences in the intermediate-r region are not completely surprising since the samples have different compositions. There are similarities in the low-r region which are approximately the same in all the samples since it captures the basic structure of the smallest units such as linear carbon chains and rings. No differences in the low-r region were observed, which indicates no decomposition and degradation of the monomer units.

TPU1 and TPU2 have very similar atomic-scale structures to one another but are quite disordered, showing less crystallinity than hard-phase compounds HP3–HP5. From 4-7 Å their structure more closely resembles that of HP3–HP5, but in the region from 7-12 Å the local structure is much more like HP1–HP2. The similarity to the amorphous samples is primarily due to the absence of structural components at a distance of $r = 7.2$ Å, strong structure correlation at 9.8 Å, and significant signal attenuation going to higher-r. However, there are some features in the higher-r range which indicate the presence of a small degree of structural ordering. The similarities and dissimilarities for all samples were quantified by calculating the Pearson product-momentum correlation (PCC) between the PDFs [19, 116], Table 6.2. In summary, HP1 & HP2 are largely disordered, HP3 & HP4 have the same nanocrystalline structure, Form I, and HP5 has a different nanocrystalline structure, Form II. The similarity in the structures is shown semi-quantitatively using the PCC product-moment correlation coefficient. The values are shown in Table 6.2

The problem of identifying the structuring present in the MDI:BDO hard phases was approached by using an iterable structure assay to test various models against experimental PDFs. Model structures were obtained from the literature [166, 167]. Several plausible isocyanate based structures expected to show similarities in molecular packing were also tested,

Table 6.2: PCC values between $G(r)$ signals of the TPU hard phases (HP) and products calculated over a range of 7.5–50.0 Å. Values of 0.8 or higher are in bold to highlight datasets with a high degree of similarity.

Samples	h.p. 1	h.p. 2	h.p. 3	h.p. 4	h.p. 5	TPU60D	TPU98A
HP1	1.0000	**0.9617**	0.2129	0.026	-0.1681	**0.8285**	**0.8438**
HP2	-	1.0000	0.2148	0.0127	-0.1811	0.7511	0.7669
HP3	-	-	1.0000	**0.8661**	0.3841	0.1002	0.1042
HP4	-	-	-	1.0000	0.553	0.0461	0.0369
HP5	-	-	-	-	1.0000	-0.1196	-0.1171
TPU60D	-	-	-	-	-	1.0000	**0.9850**
tpu98A	-	-	-	-	-	-	1.0000

including crystal structures for MDI capped by butanol BUPHCB [172], and MDI capped by methanol MEPHCB [173] and MEPHCB01 [174].

Eleven additional structural models were built by Anthony Debellis at BASF, starting from the structure given by Born et. al [166] in which relevant dihedral angles along the chain were varied. As the previously reported structures were those of a model compound, the bisurethane of diphenylmethane-4-monoisocyanate and 1,4-butanediol, the individual molecular units were "polymerized" by bonding atoms along the newly formed backbone bonds through the appropriate functional groups. This provided a fully periodic polymeric model of the hard phase. Variants of the base structure were then prepared by systematically modifying the dihedral angles of the central C-C bond of the diol fragment, the orientation of the urethane linkage relative to the diol and phenyl segments, and the dihedrals about the methylene-phenyl bond. As the unit cell contains two chains (Z=2), the dihedrals of each chain were varied independently, only removing configurations that resulted in severe atomic overlaps. The resulting structures were then relaxed using the DREIDING force-field [175] with qEq charge equilibration [176]. See Table 6.3 for the list of structures

used. In general, the new structures display hydrogen bonding only in the [100] direction but vary significantly in the way that the polymer chains pack perpendicular to the hydrogen bonding direction. The structure models are labeled in terms of the way they pack together in this regard. The labeling is as follows:

1. (A0) Butane-diol and diphenyl-methane segments are in the same orientation from neighbor to neighbor. Chains stack vertically,
2. (A1) Diphenyl-methane segments are in the same orientation from neighbor to neighbor, but butane-diol segments alternate. Chains stack vertically.
3. (A2) Butane-diol segments are in the same orientation from neighbor to neighbor. Diphenyl-methane segments stack vertically but with the orientations of the phenyl rings rotated from neighbor to neighbor.
4. (B) Every other diphenyl-methane segment is oriented similar to the neighboring chain but the rest stack out of phase with different phenyl orientations.
5. (C) Chains stack completely out of phase. All phenyl groups are rotated with respect to those on the neighboring chain.

The primary differences between the models are then shown in Figures 6.6 and 6.7.

6.3.1 Form I

Form I was observed in HP3 and HP4. All models in the assay were refined to the low-r and mid-r regions in order to test the likeness of the molecular structure and local molecular packing. Low-r and mid-r refinements are shown in Figure 6.8(a), and (b), respectively. All the structural models fit the low-r region quite well as expected. However, even here slight

Table 6.3: 3D structure models used in the PDF analysis. Gauche and trans refer to the state of the central bond of the butanediol fragment and the difference is shown in Fig. 6.6. 'Type' describes distinct differences in the chain packing perpendicular to the hydrogen bonding direction and is broken down into four types which are described below (examples shown in Fig. 6.7). Models 3, 4, and 5 are not polymerized models.

#	model	S. G.	a	b	c	α	β	γ	Type
1	MDI/BDO ([166])	$P2_1/b$	5.103	39.628	6.735	85.948	90.0	90.0	A0
2	MDI/BDO ([167])	P1	5.33	5.26	38.68	113.6	116.0	94.4	A0
3	BuOH-capped MDI[1]	$P2_12_12$	16.511	13.970	4.778	90.0	90.0	90.0.0	
4	MeOH-capped MDI 1[2]	$P112_1/b$	5.157	9.800	31.472	90.0	90.0	93.90	
5	MeOH-capped MDI 2[3]	Aba2	8.167	16.54	11.56	90.0	90.0	90.0	
6	TPU-BDO-gauche[4]	P1	4.990	9.459	34.660	91.106	92.304	88.310	B
7	TPU-BDO-trans	P1	4.860	10.070	33.617	89.109	91.777	90.377	B
8	TPU-BDO-trans-3	$P2_1/c$	4.985	34.202	11.088	90.0	120.513	90.0	A2
9	TPU-BDO-gauche-1	P1	5.066	9.952	34.246	91.178	92.062	89.398	B
10	TPU-BDO-gauche-2	P1	5.094	9.907	34.465	90.282	91.989	90.409	A1
11	TPU-BDO-gauche-3	P1	5.062	10.042	33.833	91.753	91.319	89.639	C
12	TPU-BDO-gauche-4	P1	5.060	10.056	33.827	91.706	91.488	89.910	C
13	TPU-BDO-trans-1	P1	4.999	10.344	33.310	89.618	91.092	89.884	B
14	TPU-BDO-trans-2	P1	5.004	10.169	34.305	89.929	92.075	90.097	A1
15	TPU-BDO-trans-3-2	$P2_1/c$	5.051	34.493	11.167	90.0	117.140	90.0	A2
16	TPU-BDO-trans-4	P1	4.968	10.602	32.294	89.947	90.099	90.015	C

WebCSD codes [1]BUPHCB [172], [2]MEPHCB [173], [3]MEPHCB01 [174]. [4]Structures 6–16 developed by A. Debellis

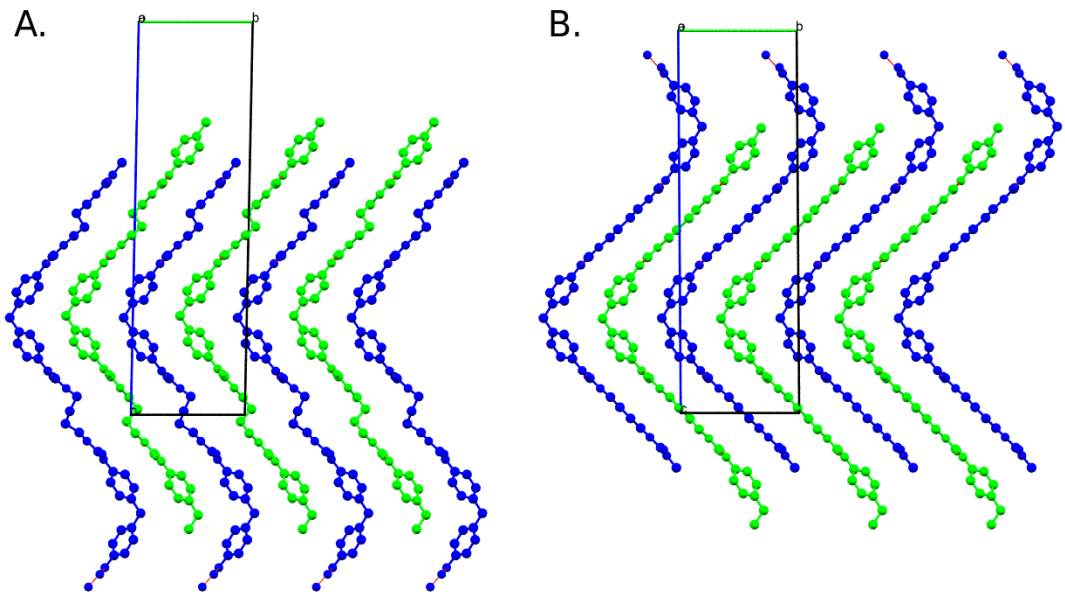

Figure 6.6: Comparison of (A) model 9 (TPU-BDO-gauche-1) and (B) model 13 (TPU-BDO-trans-1) in the [100] direction, parallel to the hydrogen bonding direction. The difference between gauche and trans bonding in the butane-diol fragment is evident. The fragment forms a kink in the former, while it forms in a zig-zag fashion in the latter which remains fairly linear. Looking in the direction parallel to hydrogen bonding, all the models look similar to these examples depending on whether they are gauche or trans.

conformational and molecular packing differences between the models show up resulting in some models giving better fits (less signal in the difference curve and lower agreement factor, R_w) than others. However, the models really begin to differentiate themselves on the intermediate range where different intermolecular packing arrangements result in dramatic differences in the positions and intensities of PDF peaks. Here, some models do so poorly that the fitting program converges to a flat line, which gives a better agreement than placing definite peaks in the wrong positions (models 1, 5, 6, 10, 11, 12, 14, 15 and 16). Other models do better, with model 8 being clearly preferred, though a few other models (*e.g.* models 3 and 4) still do well at describing the primary features.

If a model is capturing the correct packing, the calculated PDF, when extended into the high-r region should continue to pick up the features of the PDF correctly. Rather than

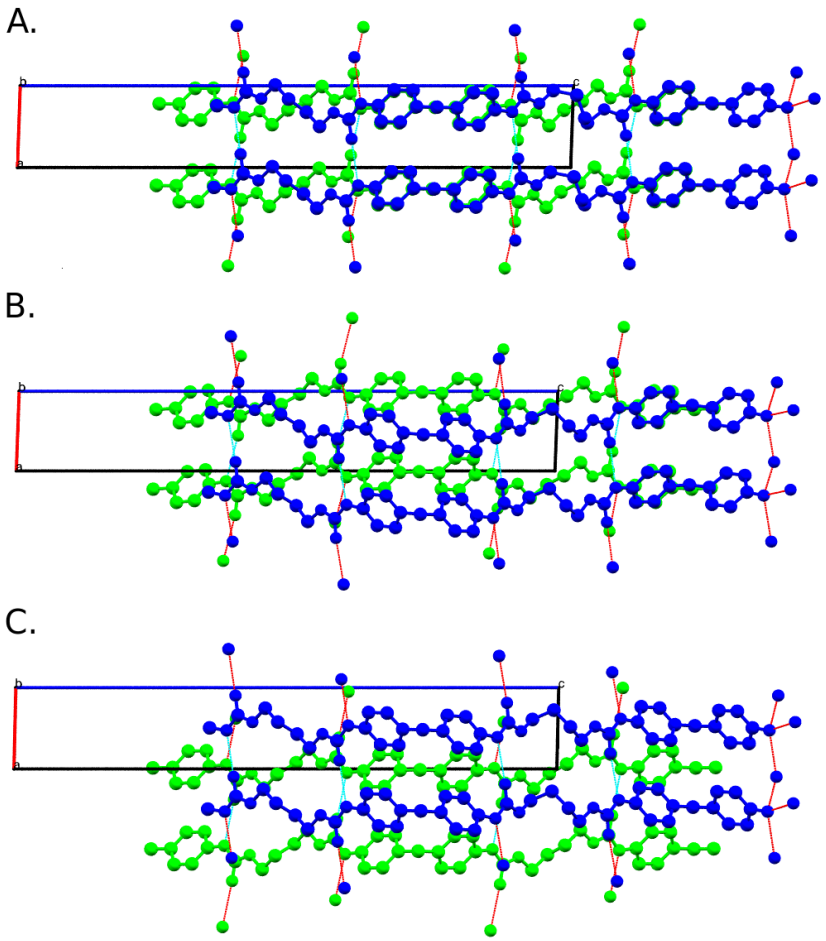

Figure 6.7: Comparison of models (A) 10 (TPU-BDO-gauche-2, type A1), (B) 9 (TPU-BDO-gauche-1, type B), and (C) 11 (TPU-BDO-gauche-3, type C) in the [010] direction, perpendicular to the hydrogen bonding direction. Of the new models developed and tested, these represent the essentially three different varieties of chain packing in this direction. In (A), the diphenyl-methane segments stack in the same orientation, while the butane-diol segment switches between two orientations from neighbor to neighbor. In (B), only every other diphenyl-methane segment stacks in the same orientation, while the others shift out of phase in the [100] direction. In (C), all segments are out of phase from layer to layer in this direction.

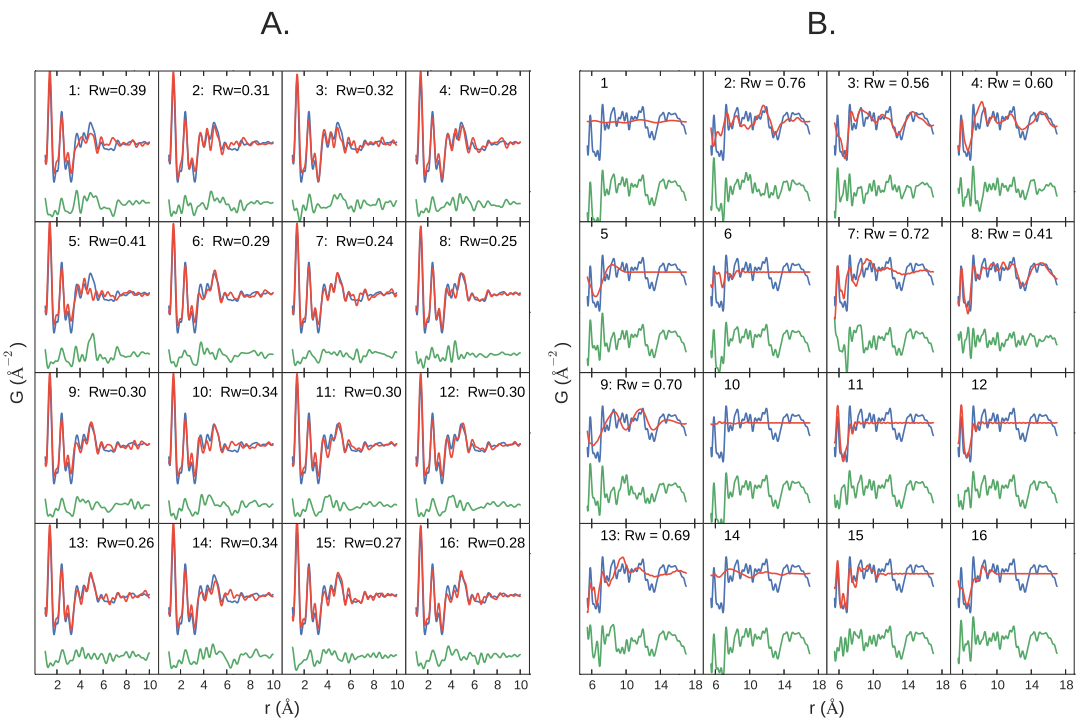

Figure 6.8: Measured PDFs of HP3 ($Q_{max} = 13.2$ Å) (blue) with fits of the 16 structural models (red) with the difference curve plotted below (green). (A) the fits in the low-r region ($1 < r < 10$ Å). (B) fits over the intermediate-r region ($5.5 < r < 17.0$ Å).

fitting the models over this wide range, I calculated PDFs for each model structure, with peak broadening and damping parameters determined from experiment, and these are shown in Figure 6.9. The PCC was calculated, and this is reproduced in the figure. A PCC of value close to 1 means the curves being compared are highly similar (correlated), a value of zero means they are uncorrelated (there is no specific relationship), and a value close to -1 indicates that the curves are anticorrelated. The PCC is a model independent, scale-independent measure of the similarity between two curves. Both visually and in terms of the PCC, it is clear that model 8 is definitely preferred. None of the other structural models are close in comparison.

A structural refinement of this model was therefore carried out over the full range of 1–50 Å where lattice parameters, a global atomic displacement parameter, but no atomic positions, were allowed to vary. As in the case of PTHF, an additional phase was included

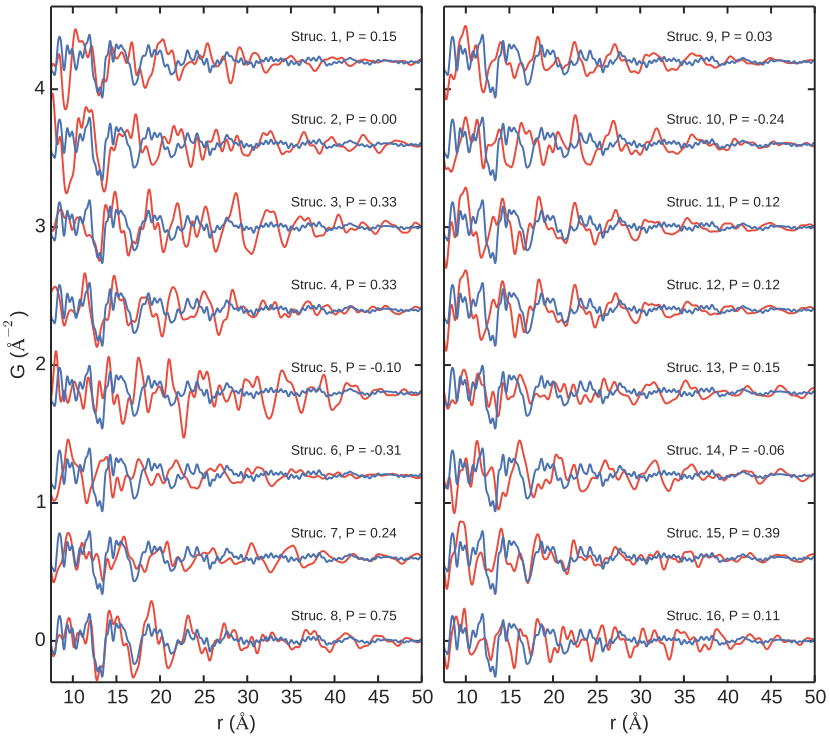

Figure 6.9: Comparison of measured PDFs of HP3 (blue) (Q_{max}=11.3 Å^{-1}), with models 1–16 superimposed (red) for direct comparison. Pearson coefficients listed for reference

in the modeling to account for a disordered component in the PDF signal, presumably from amorphous phase in the sample. The result is shown in Figure 6.10. The result is a very good fit over the whole range, with an $R_w = 0.23$ much better than that of the PTHF and MDI fits shown in Figure 6.2. The PDF is best described by a model consisting of an ordered component (22%) with a domain of structural coherence of 8.5 nm. This suggests that Form I contains nanocrystalline hard segments with a domain size of approximately 8.5 nm, together with an additional amorphous phase lacking order beyond approximately 18 Å, but accounting for a majority 78% of the PDF signal. A molecular unit of length 33.544 Å was cut out of the structure model to account for the intramolecular correlations in the signal. The absence of any sharp features beyond about 30 Å in the measured PDF suggests that there is unlikely to be any intrachain coherence beyond this distance, suggesting a persistence length in the

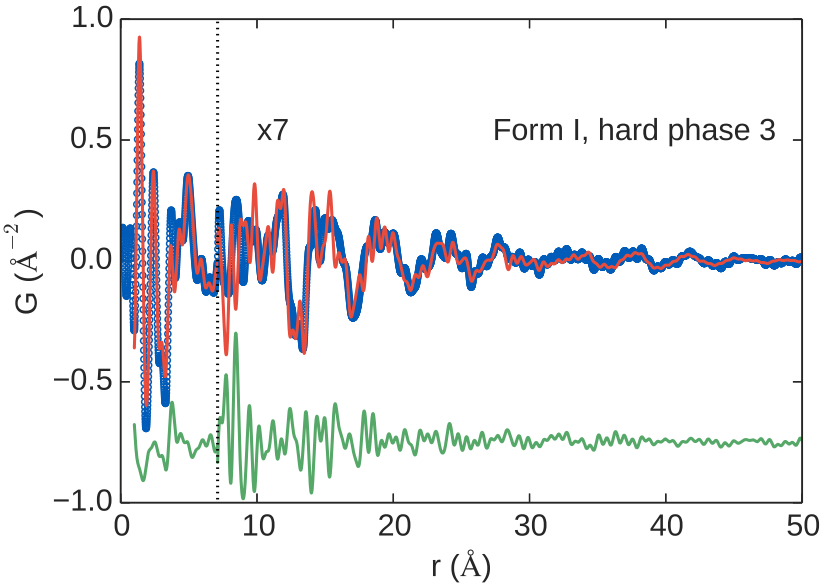

Figure 6.10: PDF of the best-fit structural model (red) compared to the measured PDF (blue) of HP3 (Form I) with difference curve offset (green). Fitting is carried out over the range (1–50 Å) giving a fit residuals of $R_w = 0.23$.

vicinity of 3 nm for this polymer.

The structure resulting from refinement of Form I agrees well with many of the general features reported in previous studies. For example, our structure is compared to that proposed by Blackwell and Gardner [158] in Figure 6.11. The gross features of the two models are similar. The crystallite domains result from a lateral aggregation of linear hard segments without any appreciable folding [160, 165] stabilized by hydrogen bonding crosslinks that form roughly perpendicular to the drawing plane [38]. Also, the butanediol segments are found to be in a planar zig-zag conformation in both. Hydrogen bonding distances in the model form between nitrogen and the carbonyl oxygen (N–H$\cdots$O=C) are 2.854 and 2.858 Å which agree fairly well with the range 2.90–3.02 Å measured by infrared spectroscopy [163]. However, in detail, the new model differs significantly. Hydrogen bonding occurs in only the [100] direction in the new model, whereas the hydrogen bonding direction alternates

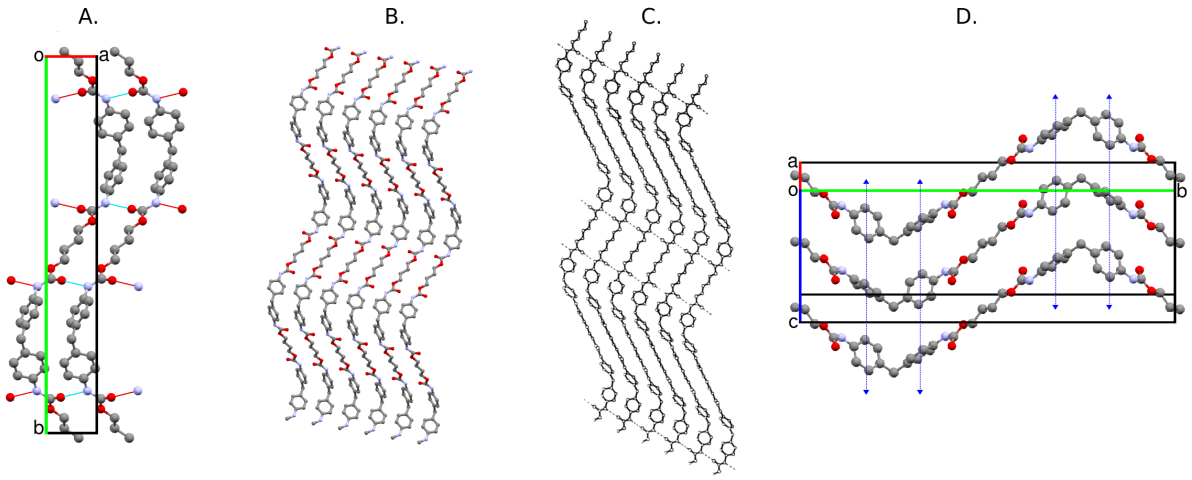

Figure 6.11: (A) Molecular packing in the best fit structural model (#8) for Form I, viewed along the [001] direction. (B) The lateral aggregation of extended chains showing the associated hydrogen bonding cross-linkage. The hydrogen bonds are pointing in the [100] direction as in (A) while the figure is viewed along the [001] direction for direct comparison to (C) the lateral packing suggested by Blackwell and Gardner; figure adapted from Blackwell and Gardner [158]. (D) Packing of the non-hydrogen-bonded chains in the [001] direction shown with the (100) plane parallel to the page. The blue arrows highlight the rotation of the diphenyl-methane units with respect to the neighboring chains.

between [100] and [010] directions from segment to segment in the Blackwell and Gardner model. Moving from chain to chain in the [010] direction, the planes of the phenyl rings in each diphenyl-methane unit are rotated by about 67° with respect to those in the neighboring chain. The packing of the diphenyl-methane unit adopts a similar structure to that of $P2_1/c$ crystalline benzene in that a T-shaped structural motif is evident. This T-shaped or "edge-to-face" structure manifests a stabilizing interaction in which the C-H dipoles at the edge of one phenyl ring are oriented towards the negatively charged carbons of a second ring on a neighboring chain.

6.3.2 Form II

I repeated the structural assay for the Form II structure observed in HP5, Figures 6.12, and 6.13. As before, all the models perform well in the low-r region. The intermediate-

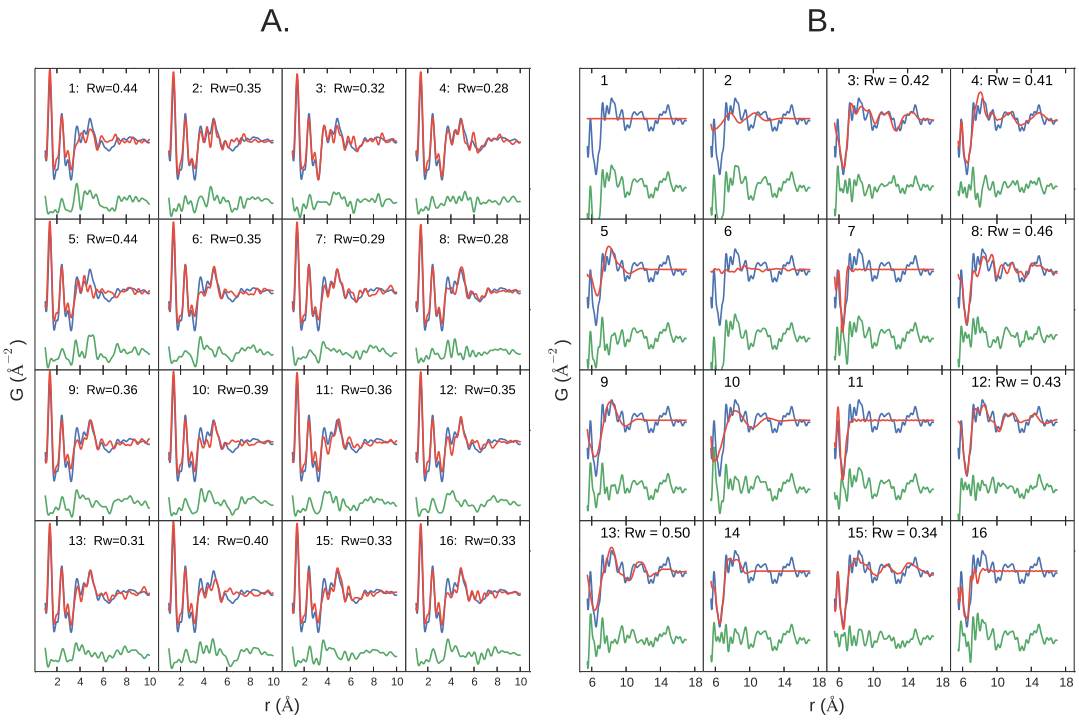

Figure 6.12: Measured PDFs (blue symbols) of sample HP5 with fits of the 16 structural models (red lines) with the difference curve plotted below. (A) sixteen sub-panels show the fits to all models in the low-r region and (B) fits to the intermediate-r region.

range-r is more discriminating with only models 3, 4, 8, 12, 13 and 15 performing reasonably. The high-r region is the most discriminating, where it is clear that only models 3 and 4 can explain the observed PDF signatures at all well. Model 3 represents the crystal structure of nonpolymerized MDI capped by butanol, while model 4 is the crystal structure for MDI capped by methanol. Clearly the local packing is similar between the structures, evidenced by the phase relationship with the peaks in the PDF, however model 4 can be eliminated since it is the wrong compound.

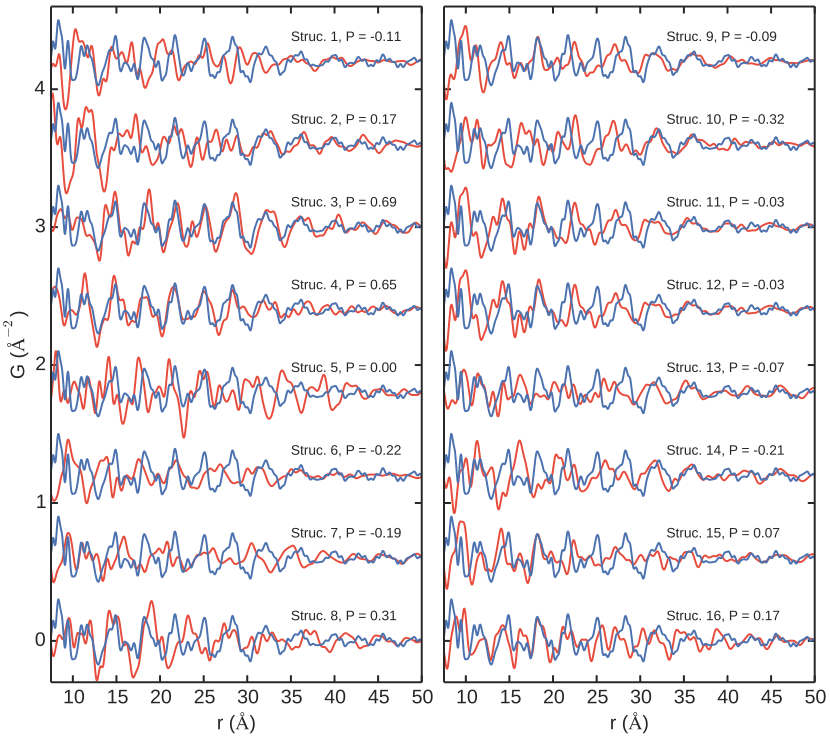

Figure 6.13: Comparison of measured PDFs of HP5 (blue) (Q_{max}=11.3 Å^{-1}), with models 1–16 superimposed (red) for direct comparison. Pearson coefficients listed for reference.

The resulting fit of model 3 over the entire range of the PDF is shown in Figure 6.14. The

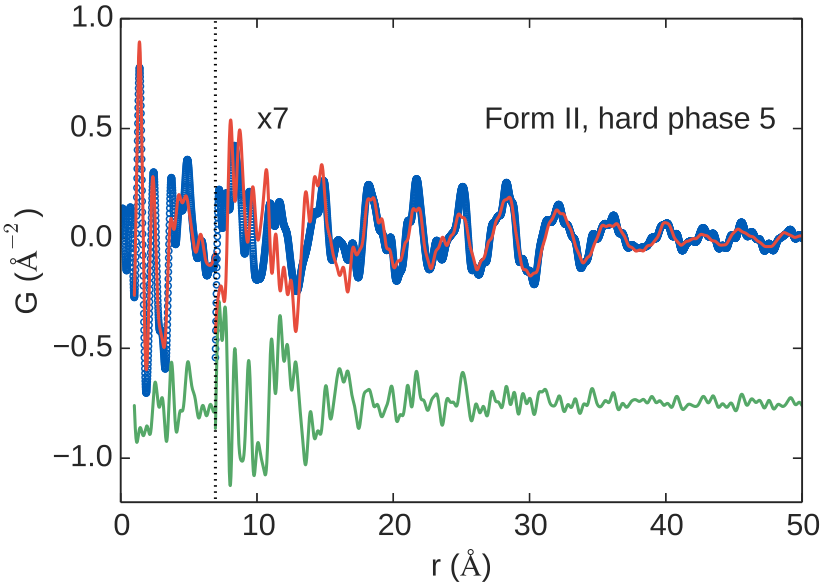

Figure 6.14: Best fit PDF (red) to measured PDF (blue) of HP5 (Form II) with difference curve offset below (green). The fit is carried out over the range of 1–50 Å, resulting in fit residual of $R_w = 0.33$.

refined model consists of an 85% disordered component with a domain size of 20 Å and a 15% crystalline component. The fit is good, with $R_w = 0.33$, suggesting that, although the structural model for the crystalline component is not from a polymerized molecule, the actual molecular packing in the sample is well captured by the packing in model 3. The packing is shown in Figure 6.15. Along the [110] projection there are stacks of bent chains, similar to the structure of Form I. However, the [100] projection is quite different, with a different hydrogen bonding network.

Despite the good overall fit, there are features in the PDF that are not explained by this model in the intermediate range between approximately 5 and 15 Å. This is an indication that an additional structural component may be present which is unaccounted for by the model, although this will contribute a rather small percentage of the total signal. Regardless, the long-range packing of Form II is well-described by structure for butanol-capped MDI, shown in Figure 6.15.

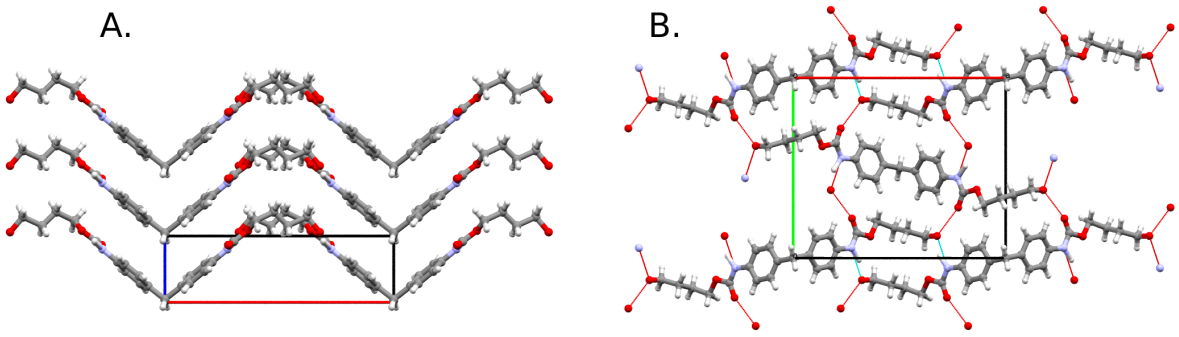

Figure 6.15: Molecular packing in the best fit structural model (#3) for Form II, along the (A) [010] direction and (B) [001] direction with hydrogen bonding linkages shown in the [010] direction.

This result may imply that the degree of polymerization is lower than in samples with a lower BDO concentration, which was confirmed by measuring the molecular weight by GPC.

The Mw's measured at BASF for HP3, HP4 and HP5 were 9,031, 3,540 and 2,232 g/mol, respectively. However, it is likely that some degree of polymerization is present since the sharp peaks at low-r are the same as in Form I. It is possible that a well-polymerized sample could assume a similar packing motif by forming crosslinks at the chain ends, but this is unlikely, given the consistent phase relationship between experiment and model even to very high distances. Perhaps the disordered component contains a different degree of polymerization, with crystalline domains of nonpolymerized BDO dominating the signal in the high-r region of the PDF. The signal from the crystalline component is only 15% of the total signal. This may also account for the unexplained signal in the intermediate-r range, as coming from nanocrystalline regions of the polymerized material. the fit parameters resulting from the structural refinements of HP3 and HP5 are shown in Table 6.4.

Table 6.4: Refined values for structural parameters from hard phase refinements.

	Model I	Form I	Model II	Form II
Space group	P21C		P21212	
a (Å)	4.9845	5.022	16.511	16.253
b (Å)	34.2020	32.707	13.970	13.871
c (Å)	11.0880	11.508	4.778	4.749
β (deg)	120.5128	119.137	–	–
U_{intra} (Å^2)	–	0.005	–	0.010
U_{inter} (Å^2)	–	0.043	–	0.053
crystalline phase (%)	–	22	–	15
crystalline phase d_c (Å)	–	85	–	–
disordered phase d_c (Å)	–	18	–	20
R_w	–	0.23	–	0.33

Turning now to the TPU samples, there are not any large features in the high-r region, indicating that these samples are structurally quite amorphous, and crystallinity of the hard-phase molecules is not visible, possibly a result of interactions with the PTHF. This is not completely unexpected. A thorough discussion of the considerations to be made in analyzing bulk elastomers versus model hard phases is provided by Koberstein and Stein [177].

Primarily, the hard-segment sequence length distribution is expected to have major implications on molecular packing. Chains could be expected to coil or fold back into the hard domains to accommodate shorter sequences while still maintaining their hydrogen bonding linkages [177]. Also, significant mixing of hard and soft microdomains [178] could contribute to the signal measured by PDF. It is clear that even in the hard phases studied here, composition likely plays a role in determining the miscibility between short and longer hard segment sequences. Further investigation will be needed to make these determinations, and may require proper handling of any disorder in the material and considering the possible presence and interplay between multiple phases.

6.4 Conclusions

In this study, the PDF technique unambiguously differentiated between different structural models in polymeric, macromolecular materials. Further, molecular packing patterns can be fingerprinted through iterative structure search and refined to identify the structure of crosslinked nanocrystalline domains. By comparing to known structures for similar materials or models generated by computational techniques, valuable information can be discerned about even very complicated structures. Such a brute force technique can be particularly useful, as in the present case, when a suite of other structural probes is not suitable for structural verification. Materials science is presently in an age where research is auspiciously supported by the wide availability of high performance computing, and the ease and accuracy with which model structures can be generated through electronic structure [179] and molecular dynamics calculations [180]. Molecular dynamics (MD) simulations, and to a lesser

extent DFT calculations, involve approximations, but a combination of these computational techniques with PDF data to validate the results, is a powerful methodology for studying macromolecular materials.

Chapter 7

Nucleation of metal nanoparticles inside zeolitic frameworks

This chapter presents a case study for extracting temperature dependent particle size distributions as they grow within a guest-host system. This was performed for Pt nanoparticles growing inside of a zeolite matrix. This was published in a study including comparative analysis of TEM data with my collaborators Liliana Gamez-Mendoza and Maria Martinez-Inesta from the University of Puerto Rico, in the Journal of Applied Crystallography (2017) [181]. Here I will present the PDF results and how they compare to the distributions measured by TEM.

7.1 Log-normal spherical size distributions of supported nanoparticles

As discussed in Chapter 1, zeolites are extremely important in the field of catalysis, including as supports for catalytic nanoparticles confined within the pores, ranging in diameter between 1-2 nm, which are typically not detected by conventional x-ray diffraction [182]. My collaborators provided an optimal case study for determining quantitative physical proper-

ties of guest particles in a host framework. I was able to show that it is possible to obtain accurate mean particle sizes and particle size distributions (PSDs) when studying the growth of Pt catalysts supported on zeolite X. The particle size and shape manifests in the PDF as the degree to which the signal dampens and the shape of the envelope. The first model tested was a spherical monodisperse model (MM) which uses the spherical characteristic function described in Chapter 2. The second model tested was a log-normal size distribution (LNSD) which was found suitable to describe the major PSD observed in the Scanning Transmission Electron Microscopy (STEM) images for the catalysts reduced up to 300°C and 350°C. For this distribution, the form factor $\gamma(r)$ is defined as:

$$\gamma_0(r)_{LNSD} = 0.5\left(\frac{-\mu - 3s^2 + \ln(r)}{\sqrt{2}s}\right) + 0.25r^3\left(\frac{-\mu + \ln r}{(\sqrt{2}s}\right)e^{(-3\mu - 4.5s^2)} - 0.75r\left(\frac{-\mu - 2s^2 + \ln r}{\sqrt{2}s}\right)e^{(-\mu - 2.5s^2)} \quad (7.1)$$

Where μ and s are the location parameter and the scale parameter of the LNSD, respectively, which are related to the mean particle diameter, P_{size}, and the standard deviation, P_{sig}, by:

$$s^2 = \ln\left(\frac{{P_{sig}}^2}{P_{size}} + 1\right), \quad (7.2)$$

$$\mu = \ln\left(P_{size}\right) - s^2/2. \quad (7.3)$$

The LNSD refined from the PDF is then generated using

$$F(r) = \frac{1}{rs\sqrt{2\pi}} \exp \frac{-(\ln r - \mu)^2}{2s^2}. \tag{7.4}$$

Although both the MM and LNSD yield similar particle size trends in the samples, the results obtained by the normalization of the LNSD describe more accurately the experimental particle size distribution observed in STEM. The particle sizes obtained by x-ray scattering describe the volume-weighted size of the crystallite domain. Microscopy techniques, on the other hand, are used to obtain number-weighted particle sizes that may contain multiple crystallites. Thus, the agreement between the PDF and STEM results suggests that many particles are monocrystalline and well-ordered. Moreover, this work shows that this technique is suitable to study the structure and size distribution of supported nanoparticles.

In this project, I performed the PDF data processing and modeling analysis. Sample preparation, all measurements, and TEM analysis for this project were performed by Liliana Gamez-Mendoza. Her procedures are referenced below.

7.2 Sample preparation

As bought zeolite Na13X (Sigma-Aldrich - 283592 with Si/Al=1.23) was calcined in air to burn off any remaining organic impurities for 5 h at 823 K and cooled to room temperature. The Pt was incorporated via incipient wetness impregnation with an aqueous solution of 0.1 M Pt $(NH_3)_4(NO_3)_2$ to obtain a 1.25% wt Pt loading. This solution was added drop wise to the calcined Na13X and dispersed to promote its homogeneous distribution; it was then dried at

RT overnight. This precatalyst was calcined in a quartz horizontal furnace reactor (609.6 mm long and 22 mm ID $\times$ 25mm OD), in pure oxygen at a heating rate of 1 K/min from room temperature to 573 K using an oxygen flow of 120 cm^3/min. The reduction of this sample was studied *in situ* with the synchrotron scattering experiments, as described below. This sample was also reduced ex situ using the same quartz horizontal furnace reactor in a flow of 70 cm^3/min of 10% H2/ N2 at a heating rate of 5 K/min up to 438 K, 573 K and 623 K and these samples were studied with electron microscopy as described below. Elemental compositions were obtained from Galbraith Laboratories, Inc. in Knoxville, TN and corroborated that the Pt loading was 1.23% and the zeolite Si/Al ratio was 1.26.

7.3 Dark field scanning transmission electron microscopy (STEM)

High Angle Annular Dark Field Scanning Transmission Electron Microscopy (HAADF-STEM) images were obtained at room temperature with a spherical aberration corrected JEM-2200 Scanning Transmission Electron Microscope (STEM) operating at 200 kV of samples reduced ex situ. To diminish the nanoparticle damage due to the electron beam, a maximum exposure time of 2 min was used while obtaining the images. The STEM distributions of the samples reduced ex situ at 573 K and 623 K were separated using the Mixtools package from the R-project.

7.4 Total scattering measurements

The x-ray scattering experiments were carried out at the 11-ID-B beamline of the Advanced Photon source at Argonne National Laboratory. Diffraction data were collected using a two-dimensional amorphous silicon flat panel detector from Perkin-Elmer. A sample to detector distance of 20 cm and a maximum 2-theta scan angle of 50 ° were used. The powder samples were analyzed in transmission geometry, with an x-ray wavelength of λ=0.2128 Å. The two-dimensional data were integrated and converted to one-dimensional intensity versus 2-theta using the FIT2D program [118]. Scattering data were obtained for the calcined NaX and Pt/NaX samples individually packed inside a polyimide capillary (Cole-Parmer, 1.1 mm OD and 1 mm ID, part number 95820-09 manufactured by Microlumen,Inc). The calcined NaX sample was heated *in situ* from 323 K to 623 K under a flux of pure oxygen at a heating rate of 10 K/min. The sample Pt/NaX was reduced *in situ* in 5% H2/Ar with a heating rate of 5 K/min from 323 K to 623 K and a hold time of 10 min at 623 K. The scattering data from an empty polyimide capillary at room temperature was also obtained for background subtraction. For all samples, each scattering pattern was obtained every minute to allow proper subtraction.

7.5 PDF refinement

To obtain the dPDF of the Pt nanoparticles, the scattering of the NaX support was subtracted from the scattering of the reduced Pt/NaX sample at the same temperature using the PDFgetX3 program [107]. The scale of the scattering data of the support was chosen to optimize the quality of the resulting PDF. Refinements with the monodisperse spherical nanoparticle model (MM) and those using the log-normal spherical distribution model (LNSD) were

done with Diffpy-CMI. In both models the same parameters were refined up to an interatomic distance of 40 Å starting with a scale factor, isotropic thermal factor, an r-dependent sharpening term, and the crystallite size parameters. Refinement with the monodisperse particle model yields only a mean size (D), while refinement with a log-normal distribution model yields a mean particle size (P_{size}) and the standard deviation of the distribution (P_{sig}).

7.6 Results

The dark field STEM images and particle size histograms in Figure 7.1 show how the Pt particles grow with temperature and the increased fraction of particles that are in the surface of

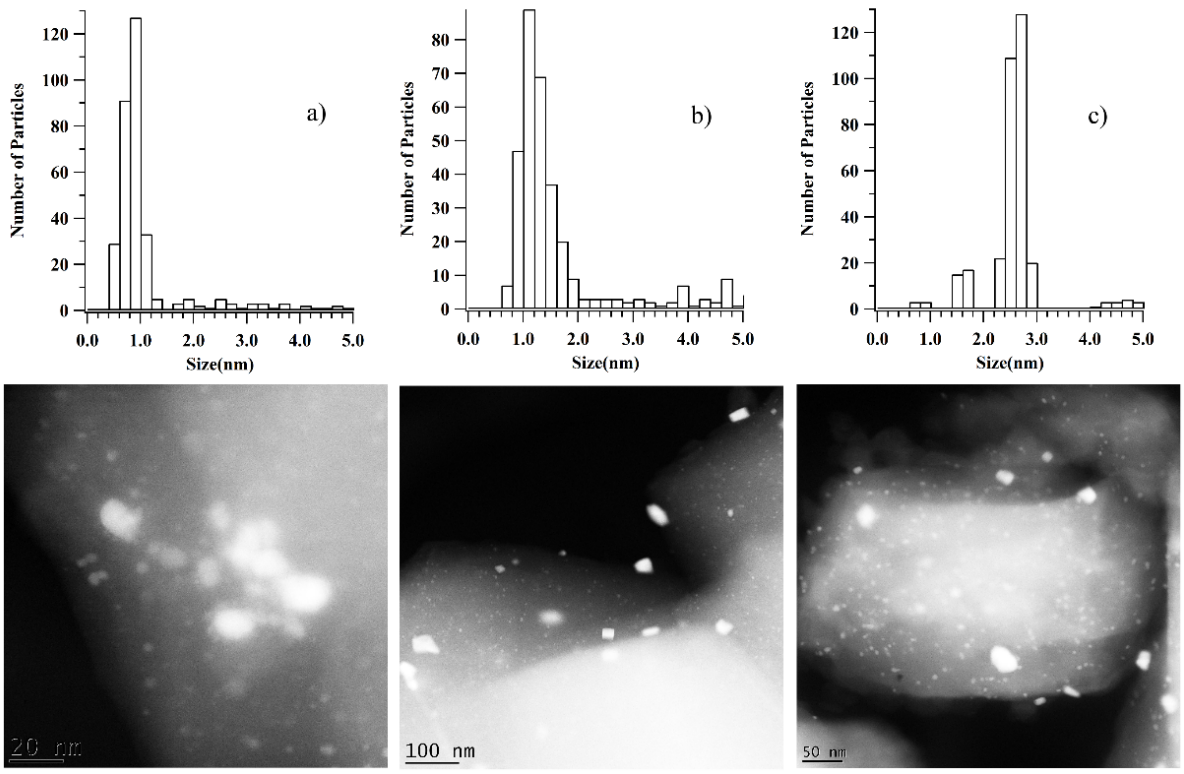

Figure 7.1: Dark-field STEM images of Pt nanoparticles supported in zeolite Na13X and reduced ex situ at (a) 438 K, (b) 573 K and (c) 623 K, with their corresponding particle size diagrams.

the zeolite.

Structure refinements for the Pt dPDFs using the MM resulted in R_w values that ranged from 0.185–0.318 for all the reduction temperature, Figure 7.2. The residuals improved with

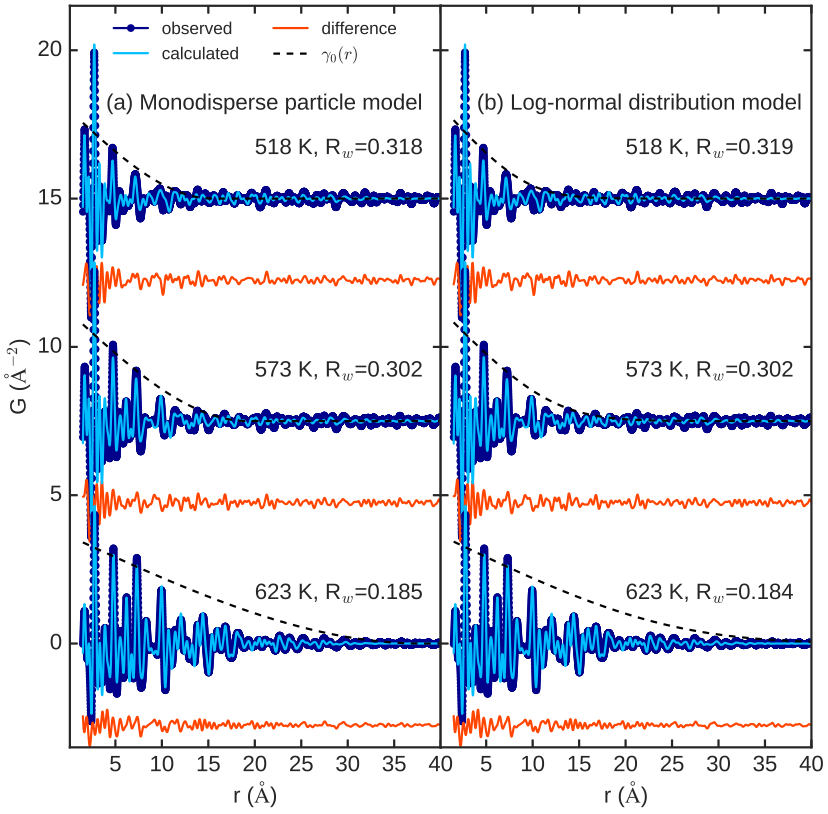

Figure 7.2: Simulated PDFs from fcc structure refinement superimposed on the measured Pt PDFs at 518, 573 and 623 K for the (a) MM and (b) LNSD models. Differences are shown offset below the fits and black dashed lines show the size-dependent signal damping refined for the respective models.

increasing temperature as the scattering signal from the growing Pt nanoparticles increased. The higher values of R_w at low temperatures are due to errors in the subtraction of the zeolite support scattering. This is caused by a modification of the cage structure due to the presence of the nanoparticles, manifesting extra components in the PDF (for example the positive peak at 1.69 Å and negative peak at 2.38 Å) which were accounted for in the model using the PDF of the support alone, which was accounted for after the structure refinement. Some

residual signal from the support will result in larger R_w values for the fits, but is unlikely to introduce significant bias since there are no peaks in the nanoparticle models at exactly those locations. This argument is further supported by the observation that the zeolite subtraction works better at higher temperatures (623 K) where the nanoparticles have been forced out of the pores and reside on the surface of the zeolite, as suggested by the STEM images.

The refinement using the LNSD resulted in similar R_w values to the MM, so both particle size models can fit the dPDF with similar accuracy. The mean sizes obtained with the two models follow a similar trend at all the reduction temperatures, which suggests a jump in growth between 573 and 623 K, Figure 7.3. However, the refined values of the mean crystallite

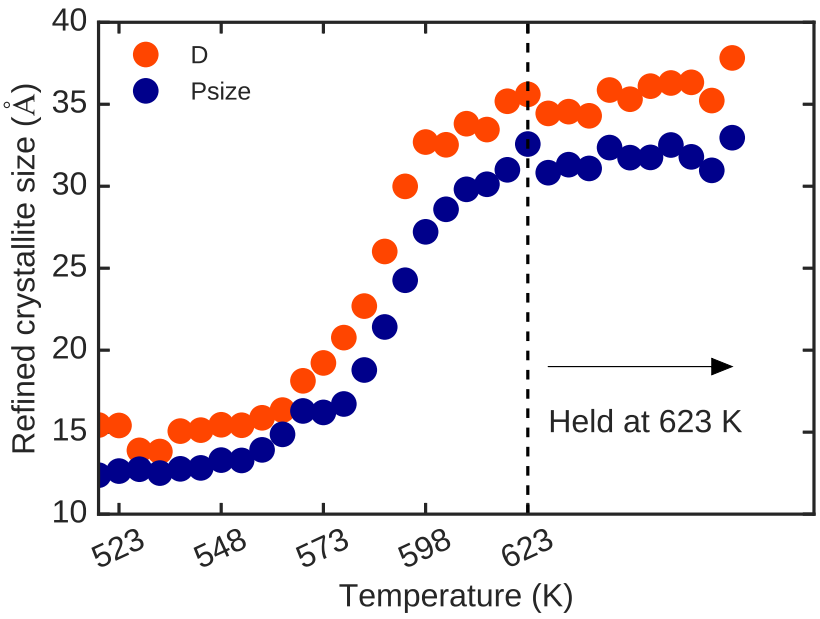

Figure 7.3: Refined mean particle sizes during *in situ* reduction, using a spherical MM (D) and LNSD model (P size).

diameter in the MM are 8.2–12.9% larger than the mean of the LNSD. This is not surprising because the lognormal distribution is asymmetric. This result shows that, for these particles, the PDF cannot be used by itself to differentiate between the presence of monodisperse

spherical nanoparticles and a lognormal size distribution of spherical nanoparticles. This is expected when most of the scattering signal comes from the particles of the dominant size.

The limitation in sensitivity of the PDF method for studying particle size and shape is known [183] and is widely exploited in nanoparticle modeling where fine details of the nanoparticle crystallite morphology are not the target of the research. In this work, the goal was to determine whether reliable quantitative information about lognormal distribution parameters may be refined from the PDF, even when the LNSD model does not give a lower R_w than the MM. For this, the PSDs were obtained by measuring particle diameters from STEM images. STEM has the advantage of giving very direct information about nanoparticle sizes, but the disadvantage of being slow and tedious and not necessarily resulting in a representative sample average, since only a small part of the specimen is sampled. It is also very difficult to obtain information on structural changes occurring *in situ* with this technique. Getting this information directly from the PDF is thus very valuable. These two techniques, however, measure different quantities: STEM yields the particle size and the PDF the size of the domain of coherent structural order, or crystallite size. The two are the same only in structurally well ordered nanoparticles and in general the particle size is an upper bound on the crystallite size. Here we find excellent agreement between the STEM and the PDF, implying that the particles are single domain.

To compare reliably the histograms obtained by STEM and PDF, the LNSD obtained with the latter was normalized by the sphere volume (r^3) and then rescaled to obtain the number-weighted distribution. This normalization displaces the curve to lower size values. The resulting number-weighted distribution derived from the PDF agrees rather well with the STEM histograms. A comparison of the distributions refined from PDF and from TEM are compared

in Figure 7.4.

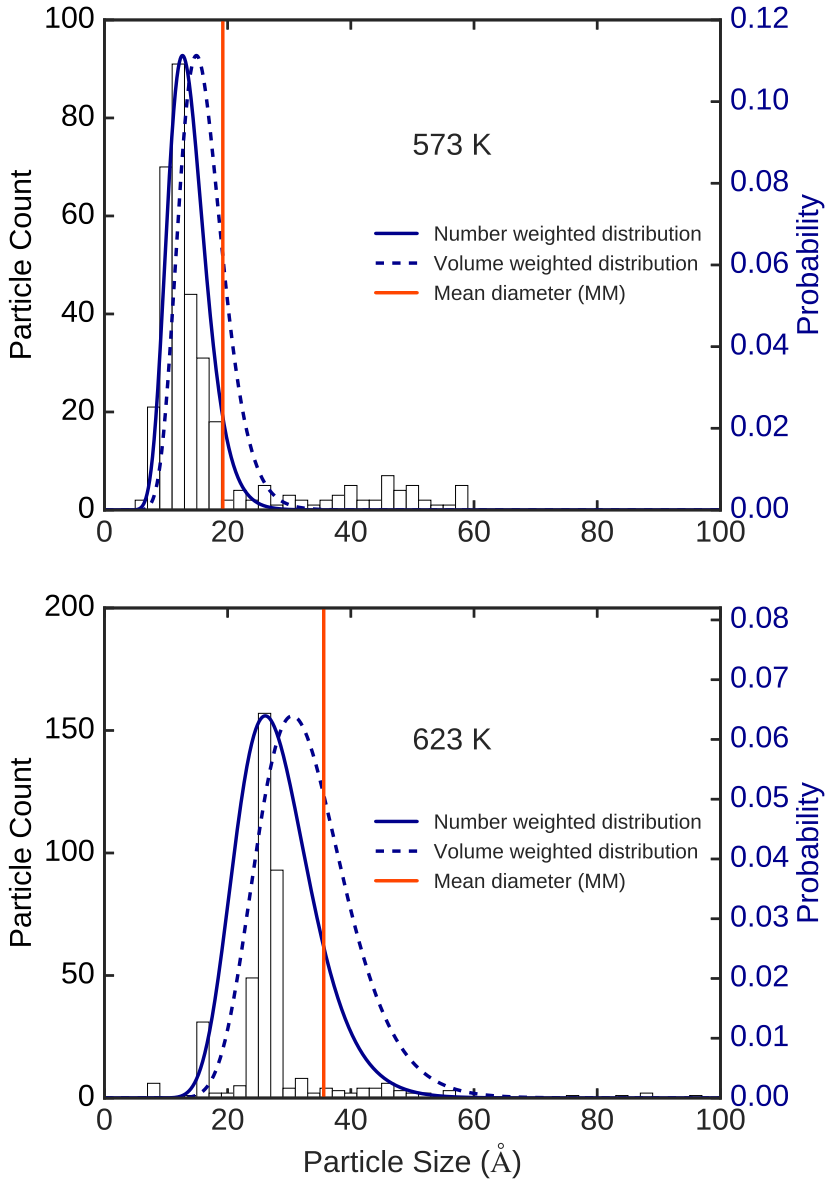

Figure 7.4: Histogram of the STEM results (bars), with the results of the lognormal size distribution (LNSD) and the mean diameter (D) obtained for the MM, for the samples reduced at (a) 573 and (b) 623 K.

Table 7.1 compares the mean particle sizes obtained by refinement of the PDF and the values obtained by fitting an LNSD to the primary distribution of the STEM results at 573 and 623 K.

Table 7.1: Comparison of the mean particle sizes obtained from refinement of the PDF from the MM (D), the volume-weighted LNSD P_{size}, and the number-weighted LNSD D_{NWLNSD} with the values obtained from STEM D_{STEM} for the samples reduced at 573 and 623 K.

Temp. (K)	D_{STEM} (nm)	D_{NWLNSD} (nm)	P_{size} (nm)	D (nm)
573	1.2	1.4	1.6	1.9
623	2.6	2.9	3.3	3.6

While the number-weighted LNSD obtained from the PDF overestimates the mean size, the error is within 0.3 nm. Considering that the goodness-of-fit parameter R_w was 0.302 at 573 K, the accuracy of the LNSD is encouraging. The mean values obtained from the PDF refinement could be skewed higher by the presence of larger particles not fitted by the monomodal distribution. This is an important result, as it suggests that this technique is reliable for studying the changes in average particle size of supported nanoparticles *in situ*, even when they are still very small (<5 nm). In comparing the crystallite size distributions obtained from the PDF and the PSD from STEM, the agreement suggests that the supported particles are monocrystalline and ordered in an fcc configuration at 573 and 623 K.

Assuming the same accuracy applies from 518 to 623 K where Pt fcc peaks are observed, Figure 7.5. shows the trend in the number-weighted LNSD obtained from the PDF. It shows, similarly to Figure 7.4, that the mean particle size increases with temperature with a distinct jump between 573 and 623 K; it also shows that the PSD broadens with temperature. This information is consistent with agglomerative sintering of the particles [184], where particles of different sizes coalesce with each other, yielding a wider distribution of particle sizes. The source of this sintering was discussed previously [185] but, in general, these results suggest that, if the reduction step were stopped at 573 K, the synthesis would produce small monodisperse ordered catalysts that are mainly contained within the pores of the support.

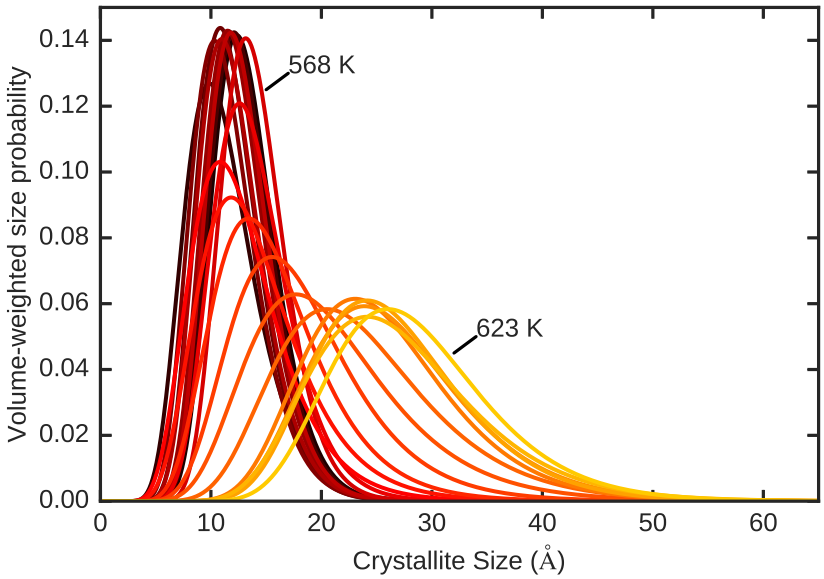

Figure 7.5: Number-weighted lognormal distributions obtained through refinement of PDFs from samples reduced from 518 to 623 K.

In general, one drawback observed in PDF PSD analysis is that it is not sensitive to different probability distributions, or to multimodal resolutions, owing to finite instrumental resolution [186, 187]. This could potentially be overcome in the future, by obtaining higher Q resolution data which would allow for size distribution analysis out to much higher distances.

7.7 Conclusions

This work describes a method to obtain particle size distributions of supported catalysts by refinement of their PDFs that can be compared directly to experimental distributions obtained by microscopy techniques. It shows that a number-weighted log-normal particle size distribution (LNSD) obtained from PDF is in good agreement with that obtained from STEM imaging for these Pt nanoparticles, extracted from a zeolite host support material. Since the

PDF actually measures crystallite size, which may be smaller than particle sizes, these results also show that these particles were well-ordered single-domain entities.

The three models studied (MM, volume weighted LNSD, and number weighted LNSD) described the same trends in particle growth with temperature in a semi-quantitative fashion. In the studied case this was true even when the goodness of fit was higher due to the presence of spurious peaks from imperfect subtraction of the support, suggesting that this technique is very sensitive to the particle size. The trend showed a jump in particle size between 573 K < T < 623 K that is consistent with agglomerative sintering. Sintering is ubiquitous in catalysts and information of the particle size distribution allows a better correlation between catalyst activity and their size.

More importantly, this work suggests that PDF is a reliable alternative to simultaneously observe how the PSDs and structure change with synthesis conditions which is a unique approach to design more active catalysts. Finally, this work shows the versatility of the DiffPy Complex Modeling Infrastructure (Diffpy-CMI) program to model deviations from an average model using PDF results to improve the accuracy of the results.

Chapter 8

Structure and loading in unconventional framework materials

This chapter further investigates aspects of host-guest interactions as in Chapter 7, but in this case for a very different type of system. In particular, the structure of a disorder MOF is solved, and the incorporation of ions into the structure is investigated. The samples synthesis and chemical characterization were performed by Rita Silbernagel and Abraham Clearfield. This work was published in the Inorganic Chemistry (2017) [188].

8.1 The structure of zirconium phosphonate-phosphate hybrid unconventional metal organic frameworks

The idea of unconventional metal organic frameworks (UMOFs) and their usefulness for ion exchange was introduced in Chapter 1. One variety are the hybrid zirconium(IV) phosphonate/phosphate UMOFs which exhibit strong affinity towards 3+ ions, while discriminating against ions with lower valences (*e.g.* 1+/2+) [189–191]. Therefore, they are good candidates

for separating lanthanide ions (L^{3+}) from actinide ions (A^{3+}), for example, in spent nuclear fuel rods [192], by first oxidizing the actinide ions to AO_2^+ then applying the UMOFs to take up L^{3+} which can be recycled using techniques such as chromatography. In order to understand the selectivity for 3+ ions, and further design for optimal performance, it is necessary to know the atomic structure of the material. This cannot be done crystallographically, because the materials are not crystalline and only show short-range order resulting in an intractable nanostructure problem [168, 193].

In this paper, hybrid phosphonate/phosphate compounds were investigated with the general formula $M(O_3PC_6H_4PO_3)_{1-(x/2)}(O_3POA)_x \cdot nH_2O$, where M = Zr and A = H or Na [194]. These materials consist of layers of zirconium phosphate type material, but they display no long range order and are resistant to crystallization. The basic inorganic motif in the structure is expected to be related to zirconium phosphate, whose structure has been solved crystallographically (α-ZrP) by Clearfield and Smith [195]. α-ZrP has a layered structure consisting of corner-shared ZrO_6 octahedra and PO_4 tetrahedra with water molecules intercalated between the layers, shown in Figure 8.1(a,b). It has a monoclinic structure (space group $P2_1/c$) with Zr, P, and O atoms sitting on general (x, y, z) positions. A similar structure to the α phase is reported for zirconium phenyl-phosphonate (ZrPP) [196], shown in Figure 8.1(c,d). The phenyl phase has a monoclinic structure with space group $C2/c$. Zr atoms sit at special positions (1/4,3/4,1/2) while P, O, and C atoms sit on general positions. Its inorganic layer has the same structural motif as found in α-ZrP, except that Zr atoms in ZrPP sit in the same atomic plane rather than slightly above and below the plane. An organic bilayer sits between the inorganic layers consisting of phenyl-phosphonate groups interdigitating between the opposing layers.

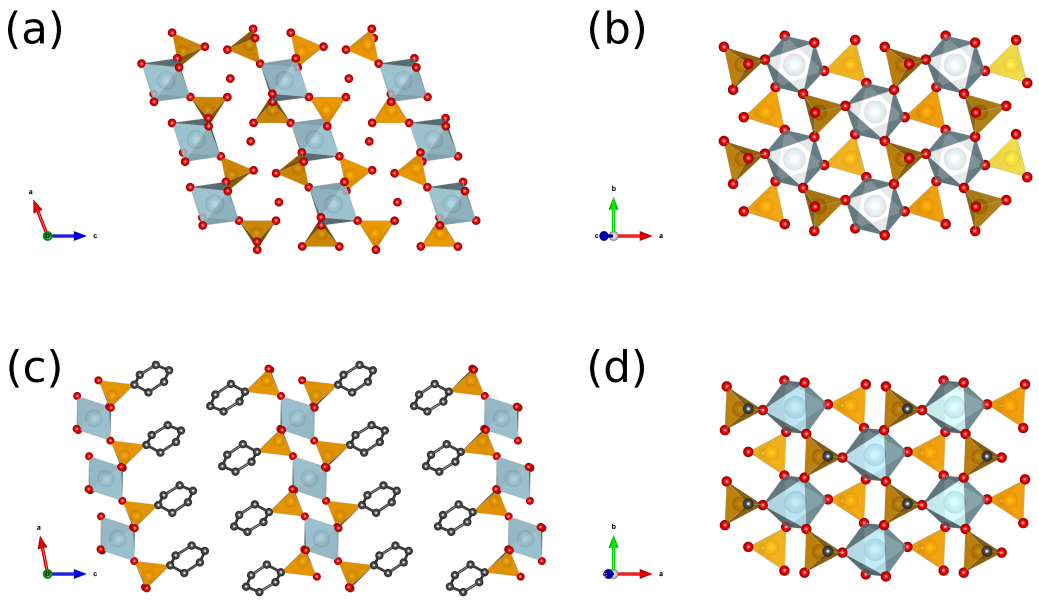

Figure 8.1: The structures of α-ZrP and ZrPP are shown along the layers (a) and (c) and perpendicular to the layers (b) and (d) respectively. Light blue spheres and octahedra represent zirconium, orange spheres and tetrahedra are phosphorus, red spheres are oxygen, and gray is carbon. The disconnected oxygens in ZrP are the intercalated water molecules.

In the hybrid structures here, the phosphorus atoms participate in either phosphate or phosphonate groups in a 1:2 ratio, where the phosphonates are terminated by a phenyl group which is thought to link between the layers. However, the challenge to determine the structure in more quantitative detail is illustrated in Figure 8.2, which shows the powder x-ray diffraction data from a conventional laboratory x-ray source. The signal is broad and diffuse and absent sharp Bragg peaks, which prevents a direct crystallographic analysis, in contrast to the crystalline α-ZrP diffraction pattern. Here, PDF analysis is used to determine the structures of two zirconium phosphonate/phosphate hybrid UMOFs, H–Zr and Na–Zr. In order to study the intercalation environment of a canonical 3+ ion, in this case terbium, additional samples of the H–Zr were measured with and without Tb ion loading in order to carry out a difference PDF (dPDF) analysis.

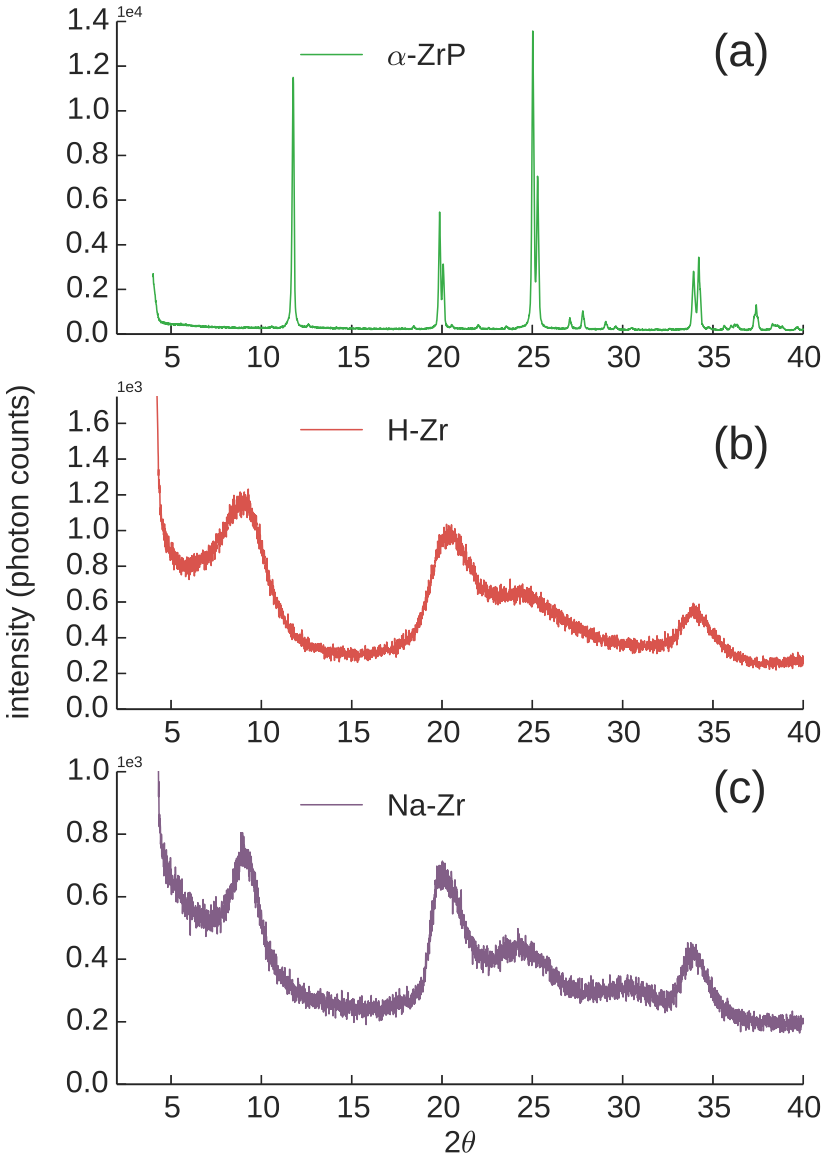

Figure 8.2: Laboratory XRD patterns for (a) bulk α-ZrP, (b) H–Zr hybrid, and (c) Na–Zr hybrid, respectively.

8.2 Materials

The chemical compositions of the two zirconium based hybrid samples are summarized in Table. 8.1. Zirconyl chloride octahydrate ($ZrOCl_2 \cdot 8H_2O$) was purchased from Aldrich. Inductively coupled plasma mass spectrometry (ICP-MS) metal-grade nitric acid was purchased from Fisher. Phosphoric acid (85%) was purchased from EMD. 1,4-Phenylenediphosophonic acid [$C_6H_4(PO_3H_2)_2$] was prepared by a modified Hirao palladium cross-coupling reaction [197]. The 120 mL Teflon digestion vessels used in the hydrothermal experiments were purchased from Savillex. Terbium chloride hexahydrate ($TbCl_3 \cdot 6H_2O$, 99.9%) was purchased from Strem Chemicals. All chemicals were used as received without further purification.

8.3 Synthesis

The compounds chosen for study were those for which the ratio of phosphonate to phosphate were 1:2. They were synthesized hydrothermally by a modification of the method reported by Burns *et al.* [192]. Samples were prepared by dissolving the phosphonate $C_6H_4(PO_3H_2)_2$ in 15.70 mL of H_2O, followed by the corresponding phosphate, phosphoric acid for H–Zr and trisodium phosphate for Na–Zr. Finally, an aliquot of a 0.5 M solution of $ZrOCl_2 \cdot 8H_2O$ (21.44 mL, 10.7175 mmol) was added dropwise to the solution. Upon addition of the metal

Table 8.1: Summary of hybrid ZrP nanoparticles and control samples.

Samples	Chemical formulas[1]
α-ZrP	$Zr(HPO_4)_2 \cdot 1H_2O$
ZrPP	$Zr(O_3PC_6H_5)_2$
H–Zr	$Zr(O_3PC_6H_4PO_3)_{0.34}(O_3POH)_1(OH)_{0.640} \cdot 1.63H_2O$
Na–Zr	$Zr(O_3PC_6H_4PO_3)_{0.38}(O_3PONa)_{0.89}(O_3POH)_{0.05}(OH)_{0.6} \cdot 1.45H_2O$

solution, precipitation occurred. The sample was heated hydrothermally in a Teflon pressure vessel at 120°C for 4 days. After cooling, the white solid was thoroughly washed with H_2O over vacuum filtration and dried in air at 60°C overnight. The resulting solid was ground into a fine, white powder. The Tb^{3+} loading was performed by titration of the H–Zr sample with 1×10^{-3} M Tb^{3+} completed with NaOH addition. Detailed information regarding composition determination and loading capacity for these compounds can be found in the recent publication by Silbernagel *et al.* [194].

8.4 Laboratory x-ray measurements

PXRD patterns were obtained using a Bruker D8 x-ray diffractometer using Cu–Kα radiation (λ=1.542 Å) at room temperature operated at 40 mA and 40 kV by the step-scan method (step 0.009°, time 0.1 s).

8.5 Total scattering measurements

Synchrotron x-ray total scattering experiments were conducted at beamline X17A at the National Synchrotron Light Source (NSLS) at Brookhaven National Laboratory (BNL). The samples were packed into 1 mm ID Kapton capillary tubes and measured at 100 K using a flowing nitrogen cryocooler. The rapid acquisition pair distribution function (RAPDF) technique [117] was used with an x-ray energy of 66.67 keV (λ=0.1860 Å). A large area 2D Perkin Elmer detector (2048×2048 pixels and 200×200 μm pixel size) was mounted orthogonal to the beam path with a sample-to-detector distance of 203.908 mm determined by calibrating

to a sample of known lattice parameter (Ni).

Total scattering measurements were also measured at beamline 28-ID-2 at the National Synchrotron Light Source II (NSLS-II) at BNL to measure the scattering of ZrPP and H–Zr over a smaller angle region. Measurements were performed at similar conditions as at X17A and also with a detector set farther away at 1735.597 mm giving a Q_{damp} =0.00743 Å^{-1} and Q_{broad} =0.0196 Å^{-1}

In order to determine the local environment of the Tb^{3+} ions, a difference PDF (dPDF) approach was adopted where PDFs of H–Zr sample with and without Tb^{3+} loading were measured, respectively. The synchrotron x-ray PDF experiment was carried out at beamline F2 at the Cornell High Energy Synchrotron Source (CHESS) at Cornell University. The experimental setup was similar to that previously described but with an incident x-ray energy of 61.332 keV (λ=0.20210 Å) and a sample-to-detector distance of 226.6842 mm which was calibrated using a nickel standard ($Q_{damp} = 0.0364$ Å^{-1} and $Q_{broad} = 0.0199$ Å^{-1}). The scattering intensities measured for H–Zr without Tb^{3+} loading were subtracted from the intensities from H–Zr with Tb^{3+} loaded, then the difference processed to obtain the dPDF. In this case, a Q_{max}=15.5 Å^{-1} was chosen to reduce the contributions from noise in the PDF.

8.6 Results and discussion

8.6.1 Intralayer structure

The diffraction patterns in Figure 8.2 show that crystalline α-ZrP has sharp Bragg peaks, while the hybrid structures have only broad, diffuse peaks indicating their nanocrystalline

nature. The low information content of this data is not sufficient to constrain a unique structure solution. There is much more information in the total scattering data obtained using synchrotron radiation. The resulting reduced structure functions, $F(Q)$, and the corresponding PDFs are shown in Figure 8.3(a-f). For reference, the laboratory x-ray data correspond

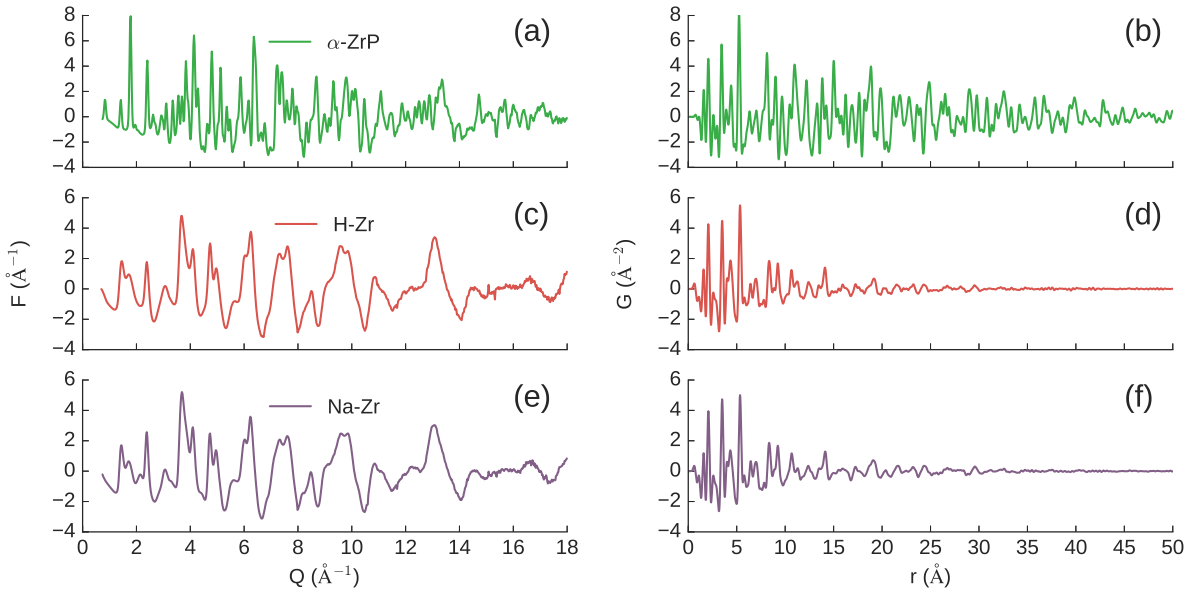

Figure 8.3: Reduced structure functions $F(Q)$ (a,c,e) processed from the x-ray scattering intensities collected from a synchrotron light source. It is clear that a significant amount of additional structure information is gained when considering the scattering at higher momentum transfers. The respective PDFs $G(r)$ (b,d,f) are shown on the right.

to just the first 2.79 Å^{-1} of these $F(Q)$ curves. The PDF, obtained by Fourier transforming $F(Q)$, of the α-ZrP control sample has sharp peaks present at all ranges of inter-atomic distance, r, signifying long range order in the crystalline sample. The PDFs of the hybrid samples also exhibit sharp peaks at low-r, indicating a well-defined local structure, but the peaks diminish in amplitude with increasing-r, disappearing by ∼40-50 Å, indicating an absence of long-range order consistent with the lab XRD data. By inspection, the PDFs from both hybrid samples are highly similar to each other, but substantially different from the crystalline structure after about 7.7 Å, approximately the thickness of a single layer.

Refinement of the known α-ZrP structure to the PDF of the control sample was performed using Eq. 2.9, refining lattice parameters a, b, c, β, Zr and P atomic sites by $P2_1/c$ symmetry, isotropic thermal parameters on Zr, P, and O, and a coherent domain size d_c giving a refined R_w of 0.251. The fit is shown in Figure 8.4(a) giving a measure of the quality of fit that can be expected for these materials when a known structure model is available.

As expected from the difference between the PDFs of the control sample and hybrid materials, the α-ZrP structure does not give a good fit to the H–Zr and Na–Zr structure. Other bulk zirconium phosphate structures including zirconium phenyl-phosphonate [196], γ-ZrP [198], and mixed phosphate/phosphonate [199, 200] models also do not give good fits.

For layered materials, significant disregistry in the stacking of the layers, *i.e.* turbostratic disorder, can lead to the loss of interlayer atomic correlations in the PDF. In such cases, it is possible to model the PDF with only a single or few layers [67, 201–204]. This method can also be used to determine stacking structures by constructing 3D models from the individual layers [205, 206]. As discussed later, the presence of multiple turbostratically disordered layers will have an effect on the PDF, but the sharp peaks are well fit by a model of a single layer, and this model yields the intra-layer structure with good accuracy. Eqs. 2.5 and 2.8 were used to generate the PDF for a single layer of the α-ZrP model with periodic boundary conditions in the x and y directions, and refinement was performed using the same parameters as for the crystalline sample. Phenyl linkers were left out of the final model. When included, the thermal parameters became extremely large, damping out any correlations from carbon, indicating that the phenyl rings are not orientationally ordered in the structure. Refinement of the layer structure to H–Zr and Na–Zr PDFs were performed using the same parameters as for the bulk structure. The fits are shown in Figure 8.4(b-c) and are of comparable quality to

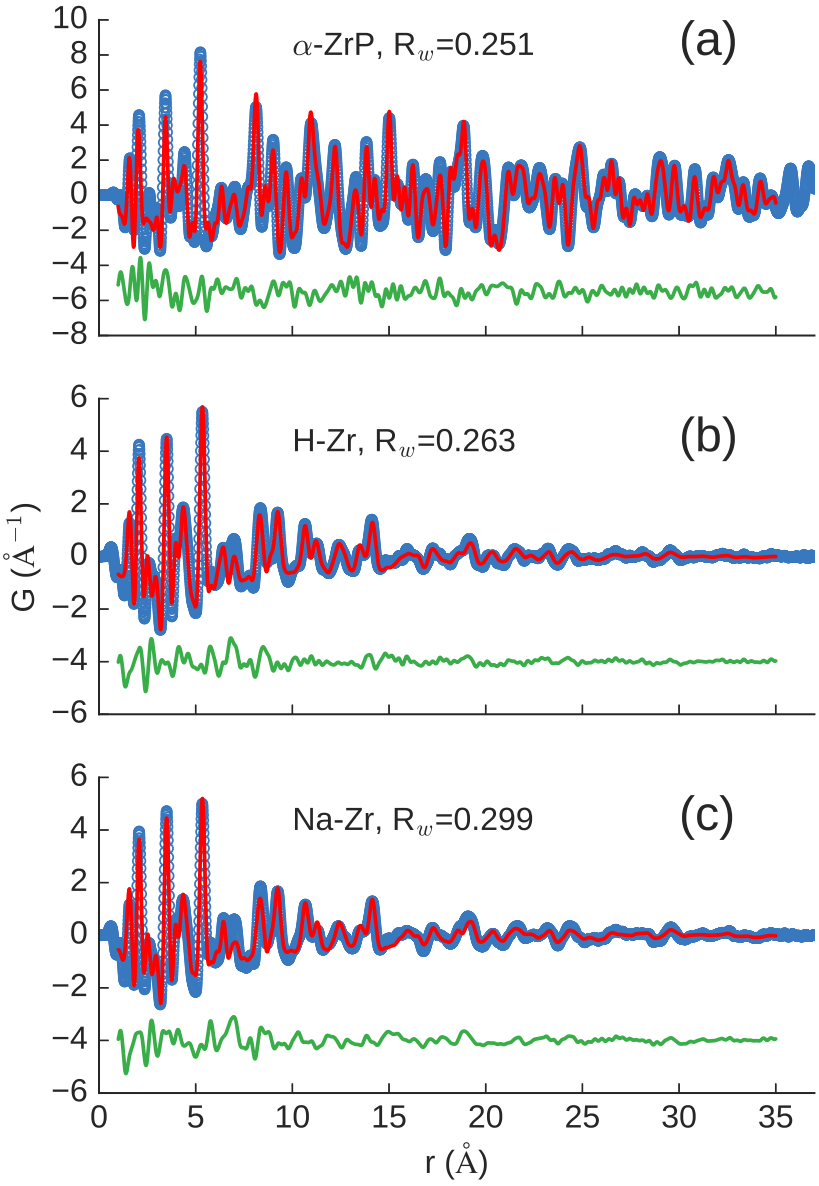

Figure 8.4: PDF fits (red) of the α-ZrP structure model to the measured data (blue): (a) fit of the bulk structure to the crystalline sample, and fit of the single layer model to (b) H–Zr and (c) Na–Zr. Difference curves (green) are offset for reference.

the bulk with R_w's of 0.263 and 0.299, indicating a satisfactory fit of these models.

It is expected that that ZrPP structure may be a better representation for the hybrid layer structure since they both contain phosphonate groups, even though there are not any significant correlations from the phenyl groups themselves observed. A second model was tested using a single layer of the ZrPP form and the same refinement parameters, this time with P atoms refined in $C2/c$ symmetry. Zr atoms were allowed to refine antisymmetrically in z off their special positions in the modified unit cell such that (1/4,3/4,z) and (3/4,1/4,z) become (1/4,3/4,$z+\delta$) and (3/4,1/4,$z-\delta$). This second set of fits for H–Zr and Na–Zr are shown in Figure 8.5(a-b). This results in refinements that are improved by $\sim$2 % for both samples, with

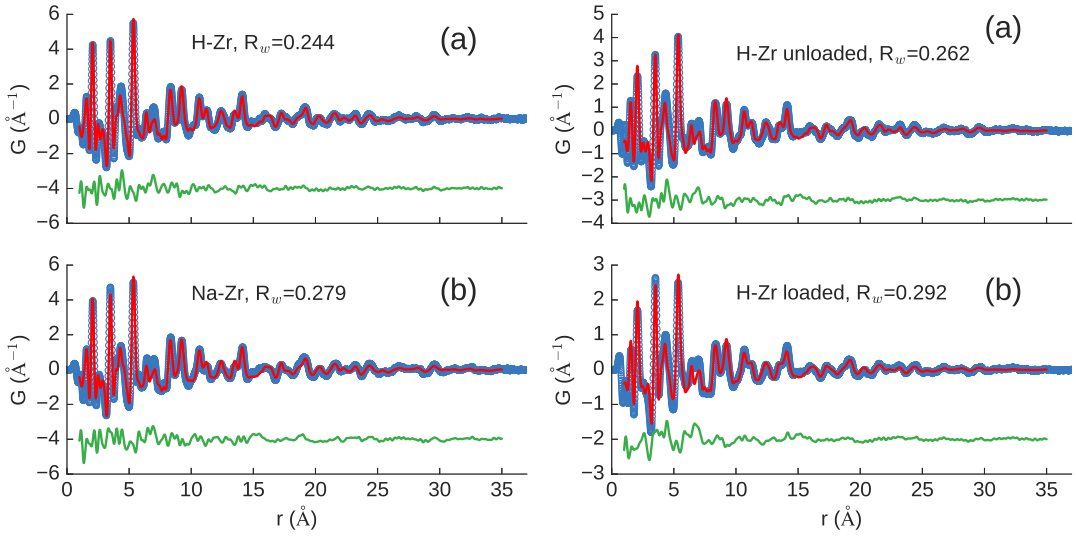

Figure 8.5: PDF fits (red) of the single layer ZrPP structure model to the measured data (blue): (left) (a) H–Zr and (b) Na–Zr and (right) (a) H–Zr unloaded and (b) H–Zr loaded. Difference curves (green) are offset for reference.

fewer parameters being refined (there is only one unique P site instead of three), suggesting that the positioning of the oxygens in our samples are better represented by the ZrPP structure than by α-ZrP, though the Zr atoms tend to move off the special positions as in the latter. The refined structural parameters are summarized in Table. 8.2.

Table 8.2: Refined models for the H-Zr and Na-Zr samples measured at X17A (NSLS), the H-Zr hybrid samples unloaded and loaded with Tb measured at F2 (CHESS), and the 1:0 phosphonate:phosphate H-Zr measured at 28-ID-2 (NSLS-II). Summary of PDF fit results using a single layer model. The c axis (originally 30.235 Å) was artificially modified to 400.0 Å to remove any interlayer correlations from the simulated PDF. The P atoms are refined in the original $C2/c$ symmetry, while Zr atoms are allowed to displace in z. Parameters for the previously reported bulk zirconium phenylphosphonate (ZrPP) structure are also listed for reference.

-	H–Zr (1:2)	Na–Zr (1:2)	H–Zr (unloaded) (1:2)	H–Zr (loaded) (1:2)	H–Zr (1:0)	ZrPP[1]
a (Å)	9.20	9.17	9.19	9.21	9.18	9.10
b (Å)	5.35	5.37	5.36	5.34	5.36	5.42
c (Å)	405.26	406.55	411.12	421.54	405.04	30.235
β (°)	101.57	102.23	100.24	100.42	101.56	101.23
z(Zr)	-0.00021	-0.00021	-0.00032	-0.00034	-0.00022	0.038
x(P)	0.948	0.948	0.944	0.948	0.949	0.938
y(P)	0.733	0.736	0.734	0.736	0.737	0.729
z(P)	-0.00011	-0.00011	-0.00016	-0.00019	-0.000085	0.042
d_c	45.9	54.6	48.3	42.4	36.3	-
U_{iso} (Zr) (Å^2)	0.0230	0.0215	0.0305	0.0370	0.0230	0.008
U_{iso} (P) (Å^2)	0.0042	0.0042	0.0022	0.0144	0.00160	0.011
U_{iso} (O) (Å^2)	0.0221	0.0296	0.0301	0.0161	0.0202	0.018[2]
R_w	0.244	0.279	0.262	0.292	0.281	-
r(Zr-O) (Å)	1.994	1.993	1.994	2.003	1.994	2.047×2
	2.042	2.041	2.008	2.018	2.037	2.065×2
	2.043	2.048	2.044	2.049	2.042	2.093×2
	2.101	2.100	2.161	2.191	2.104	-
	2.136	2.135	2.162	2.191	2.140	-
	2.145	2.151	2.192	2.216	2.144	-
r(P-O/C) (Å)	1.860	1.855	1.926	1.974	1.846	1.821
r(P-O) (Å)	1.452	1.461	1.467	1.442	1.450	1.493
	1.553	1.549	1.540	1.555	1.558	1.538
	1.567	1.567	1.546	1.567	1.578	1.550

[a]The structural parameters for zirconium phenylphosphonate are adapted from Poojary *et al.* [196].

[b]The average U_{iso} for O.

8.7 CIF coordinates for intralayer H-Zr model

The coordinates for the refined H-Zr structure are provided in CIF format below.

```
# Refined intralayer structure of H-Zr.
# Starting structure generated by increasing layer spacing of ZrPP structure [196].

data_3D
_audit_creation_date                    2016-07-20
_audit_creation_method                  P_cif.py

_symmetry_space_group_name_H-M          'P1'
_symmetry_Int_Tables_number             1
_symmetry_cell_setting                  triclinic

_cell_length_a                          9.20177
_cell_length_b                          5.34824
_cell_length_c                          405.263
_cell_angle_alpha                       90
_cell_angle_beta                        101.573
_cell_angle_gamma                       90

loop_
_atom_site_label
_atom_site_type_symbol
_atom_site_fract_x
_atom_site_fract_y
_atom_site_fract_z
_atom_site_U_iso_or_equiv
_atom_site_adp_type
_atom_site_occupancy
Zr1     Zr      0.250000    0.750000    0.037584    0.023330    Uani    1.0000
Zr2     Zr      0.750000    0.250000    0.038003    0.023330    Uani    1.0000
P1      P       0.947847    0.732500    0.041965    0.004010    Uani    1.0000
P2      P       0.052153    0.267500    0.033623    0.004010    Uani    1.0000
P3      P       0.447847    0.232500    0.041965    0.004010    Uani    1.0000
P4      P       0.552153    0.767500    0.033623    0.004010    Uani    1.0000
O1      O       0.065000    0.720000    0.040046    0.022491    Uani    1.0000
O2      O       0.935000    0.280000    0.035541    0.022491    Uani    1.0000
O3      O       0.565000    0.220000    0.040046    0.022491    Uani    1.0000
O4      O       0.435000    0.780000    0.035541    0.022491    Uani    1.0000
O5      O       0.838000    0.509000    0.041354    0.022491    Uani    1.0000
O6      O       0.162000    0.491000    0.034234    0.022491    Uani    1.0000
```

O7	O	0.338000	0.009000	0.041354	0.022491	Uani	1.0000
O8	O	0.662000	0.991000	0.034234	0.022491	Uani	1.0000
O9	O	0.847000	0.969000	0.041089	0.022491	Uani	1.0000
O10	O	0.153000	0.031000	0.034498	0.022491	Uani	1.0000
O11	O	0.347000	0.469000	0.041089	0.022491	Uani	1.0000
O12	O	0.653000	0.531000	0.034498	0.022491	Uani	1.0000
O13	O	0.029000	0.734000	0.046554	0.022491	Uani	1.0000
O14	O	0.971000	0.266000	0.029033	0.022491	Uani	1.0000
O15	O	0.529000	0.234000	0.046554	0.022491	Uani	1.0000
O16	O	0.471000	0.766000	0.029033	0.022491	Uani	1.0000

loop_
_atom_site_aniso_label
_atom_site_aniso_U_11
_atom_site_aniso_U_22
_atom_site_aniso_U_33
_atom_site_aniso_U_12
_atom_site_aniso_U_13
_atom_site_aniso_U_23

Zr1	0.022960	0.022960	0.022960	0.000000	0.000000	0.000000
Zr2	0.022960	0.022960	0.022960	0.000000	0.000000	0.000000
P1	0.004165	0.004165	0.004165	0.000000	0.000000	0.000000
P2	0.004165	0.004165	0.004165	0.000000	0.000000	0.000000
P3	0.004165	0.004165	0.004165	0.000000	0.000000	0.000000
P4	0.004165	0.004165	0.004165	0.000000	0.000000	0.000000
O1	0.022144	0.022144	0.022144	0.000000	0.000000	0.000000
O2	0.022144	0.022144	0.022144	0.000000	0.000000	0.000000
O3	0.022144	0.022144	0.022144	0.000000	0.000000	0.000000
O4	0.022144	0.022144	0.022144	0.000000	0.000000	0.000000
O5	0.022144	0.022144	0.022144	0.000000	0.000000	0.000000
O6	0.022144	0.022144	0.022144	0.000000	0.000000	0.000000
O7	0.022144	0.022144	0.022144	0.000000	0.000000	0.000000
O8	0.022144	0.022144	0.022144	0.000000	0.000000	0.000000
O9	0.022144	0.022144	0.022144	0.000000	0.000000	0.000000
O10	0.022144	0.022144	0.022144	0.000000	0.000000	0.000000
O11	0.022144	0.022144	0.022144	0.000000	0.000000	0.000000
O12	0.022144	0.022144	0.022144	0.000000	0.000000	0.000000
O13	0.022144	0.022144	0.022144	0.000000	0.000000	0.000000
O14	0.022144	0.022144	0.022144	0.000000	0.000000	0.000000
O15	0.022144	0.022144	0.022144	0.000000	0.000000	0.000000
O16	0.022144	0.022144	0.022144	0.000000	0.000000	0.000000

8.7.1 Interlayer structure

In the lab diffraction pattern, the (002) reflection for H–Zr was observed at approximately 0.645 Å^{-1}, corresponding to an average inter-layer spacing of ∼9.74 Å, which was estimated by fitting a Gaussian to the peak. The same procedure resulted in an average interlayer spacing of ∼9.69 Å for Na–Zr. These can be compared to the inorganic layer spacings of 14.83 Å for ZrPP and 7.55 Å for α-ZrP. These peaks are extremely broadened, indicating that the number of layers stacked together in a grain or particle is small and that there may be a distribution of interlayer distances. To understand how this affects the PDF, the case of crystalline ZrPP is first explored, whose layered structure is well known.

The layer structure is similar to α-ZrP as previously discussed, except in this case the presence of phenyl groups at the surface of the inorganic layers creates a larger interlayer spacing, shifting the (002) peak to lower scattering angle. The PDF for ZrPP is shown in Figure 8.6(a). This measurement was made at NSLS-II with the detector placed much further from the sample, allowing a lower Q_{min} to be accessed than the NSLS data. In this dataset, the (002) reflection is correctly measured. Due to the lower Q_{max}, the real space resolution of the PDF is much lower, resulting in slight broadening of the atom-pair correlations compared to those in the previous section. However, the increased Q-resolution of the measurement leads to less dampening of the PDF with increasing r so that layer-layer correlations can be observed to much higher distances. The measured PDF in Figure 8.6(a) is fit with both the crystal model for ZrPP, as well as an approximate model for the inorganic layer-layer correlations. This layer-layer model is generated by giving very large thermal displacements to the atoms in the a and b directions such that all intralayer correlations are removed. The

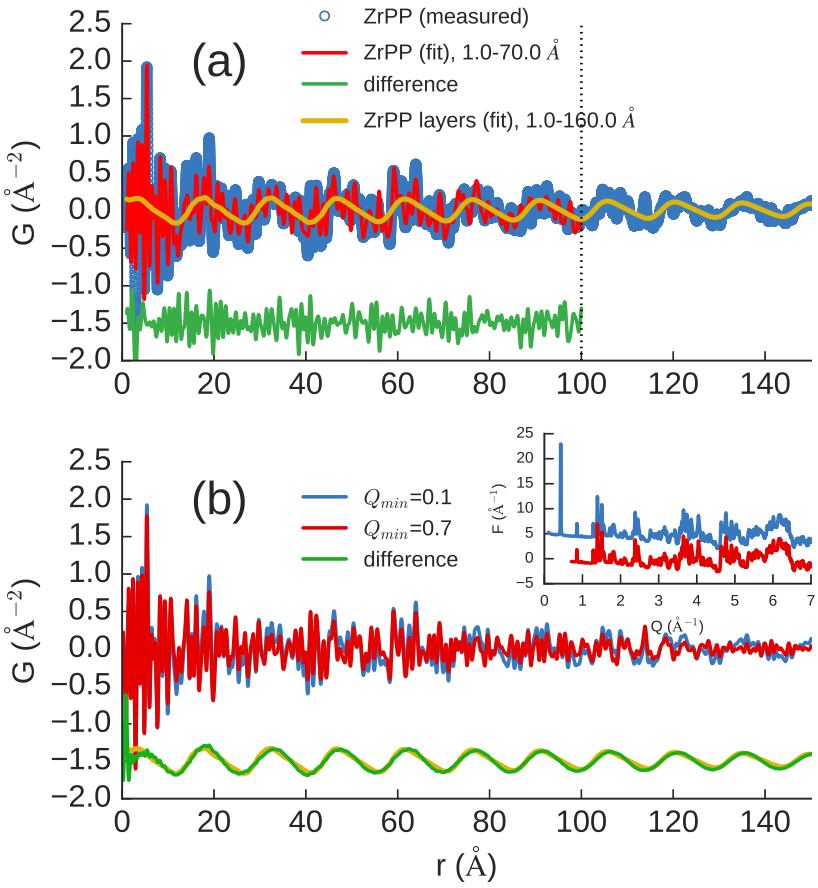

Figure 8.6: (a) The resulting PDF from the total scattering measurement of ZrPP over 0.1-7.0 Å^{-1} is shown with the resulting structural fit over 1–100 Å and difference offset below. A fit of the layer-layer stacking model is also shown to 150 Å. (b) The PDFs calculated from the reduced total scattering structure functions including the first Bragg peak Q_{min}=0.1, and omitting, Q_{min}=0.7, are overlaid. The difference is overlaid with the layer-layer model from (a) showing that the first Bragg peak in the diffraction data encodes this correlation in the PDF.

atoms are also given large thermal displacements in the c direction such that distinct atom-atom correlations between layers are removed, but not so large that electron density of the separate layer blurs together. Atoms in the organic layer are removed. This essentially gives us the PDF for stacked 2D sheets of homogeneous density with a thickness given by the inorganic $ZrPO_4$ layer. The result is a sawtooth pattern consisting of a periodic sequence of peaks with Warren line-shapes characteristic of 2D sheets of density stacked in a 1D array.

The wavelength of the sawtooth yields the spacing of the inorganic layers. In Figure 8.6(b), measured PDFs computed by including and omitting the (002) reflection, respectively, are compared. The difference shown below and overlaid with the layer-layer model from (a), shows that the first Bragg peak in the diffraction data encodes in the PDF this interlayer stacking information in these materials.

With this information in hand, the interlayer stacking can be considered, by comparing the PDF of H–Zr (including the (002) reflection) to the PDF analyzed in the previous section in Figure 8.7(a). In this case the increased Q-resolution of the measurement does not result in PDF peaks extending to higher-r. The loss of PDF peak intensity is therefore a sample-limited, not resolution-limited, phenomenon coming from the nanocrystallinity of the sample itself. The effect on the PDF of including, or not including, the first broad diffraction peak in the $F(Q)$ was also investigated, as shown in Figure 8.7(b). The difference curve shown is nearly, but not quite flat. It is shown magnified in in Figure 8.7(c), where it is clear that it is a damped oscillation which may be fit with a damped version of the previously described inorganic layer-layer model. This results in an average interlayer distance of 10.26 Å which is in reasonable agreement with the distance of 9.74 Å estimated from the XRD data. The PDF measurement reveals more information than a simple estimate of interlayer spacing from the inverse of the peak position. Fitting with a damped oscillating function yields an average spacing, but implies a distribution of spacings that result in the damping of the oscillation with increasing-r, with a complete loss of coherence after just 3-4 layer-spacings.

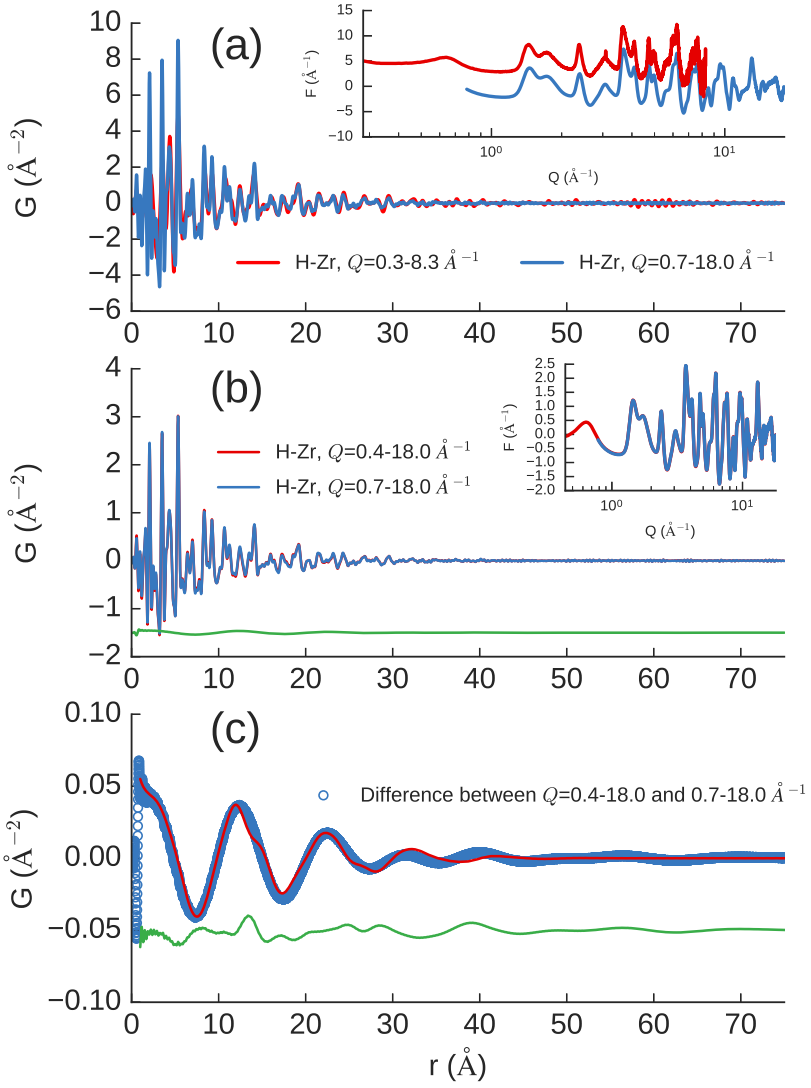

Figure 8.7: (a) The PDFs from the higher Q-resolution total scattering measurement and from the previous analysis overlaid for comparison. There are no obvious interlayer structure correlations in the H–Zr sample. (b) The PDFs obtained from the reduced total scattering structure functions including the first Bragg peak (Q_{min} = 0.4 Å^{-1}) and omitting it (Q_{min} = 0.7 Å^{-1}), are overlaid. (c) Zoomed plot of the difference to show that there is a small signal present. The interlayer model from ZrPP was fit to this signal to find that it gives a spacing of 10.26 Å which is close to the estimate from the Bragg position in the original lab XRD data.

8.7.2 Effects of the phosphonate:phosphate ratio

It was shown in a previous report [190], that even in the case of zero phosphate addition, the H–Zr materials still uptake 3+ ions with a preference over those of lower charge. It is therefore interesting to compare the structures of the hybrid H–Zr with both 1:2 and 1:0 phosphonate:phosphate. In Figure 8.8 the reduced structure functions and PDFs for a sample with a 1:0 phosphonate:phosphate ratio is compared to that of the 1:2 ratio as previously analyzed. For the 1:0 sample, the first Bragg peak is significantly sharpened and shifted to

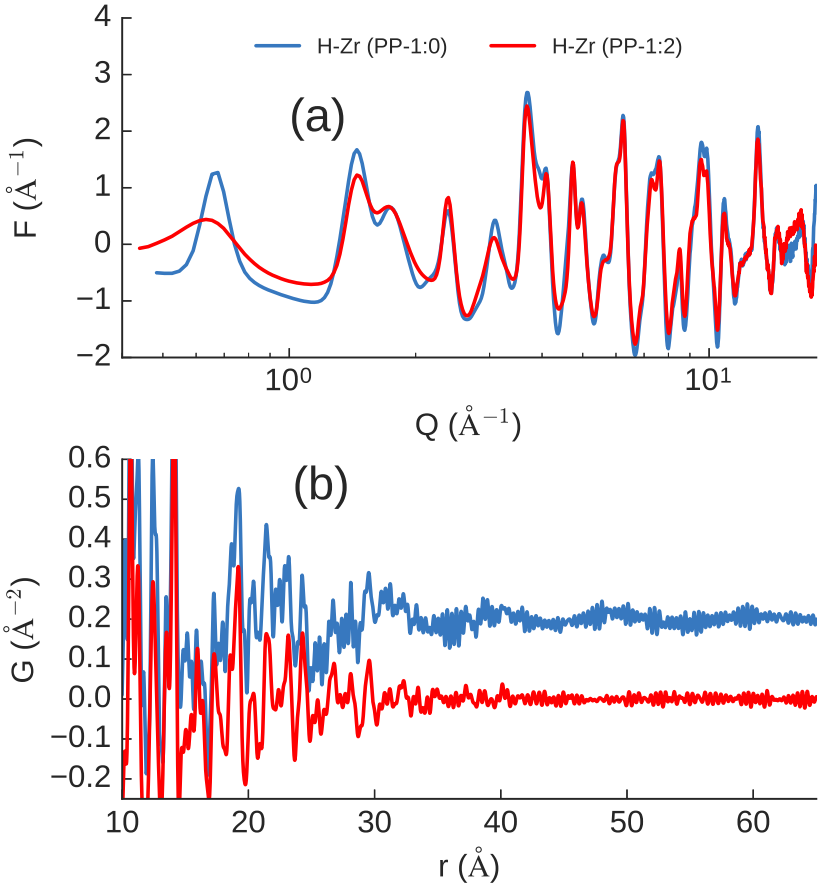

Figure 8.8: (a) The reduced total scattering structure functions $F(Q)$ for the 1:0 and 1:2 phosphonate:phosphate H–Zr materials are overlaid for comparison. (b) The high-r region of the resulting PDFs are offset and compared. Of particular note is the more pronounced oscillation in the 1:0 sample.

lower d-spacing. This indicates a more ordered stacking in the sample. In the PDFs, the sharp peaks are highly similar, indicating that the intralayer structure is the same for the 1:0 and 1:2 samples. A prominent difference does arise in the form of a pronounced long-wavelength oscillation extending to high-r. This arises from the ordered stacking in 1:0, and should be expected due to the higher degree of interlayer connectivity. In Figure 8.9, the intralayer and interlayer structure models are both refined to the 1:0 PDF, for comparison to the results from the previous sections. From the structure refinements, the presence of

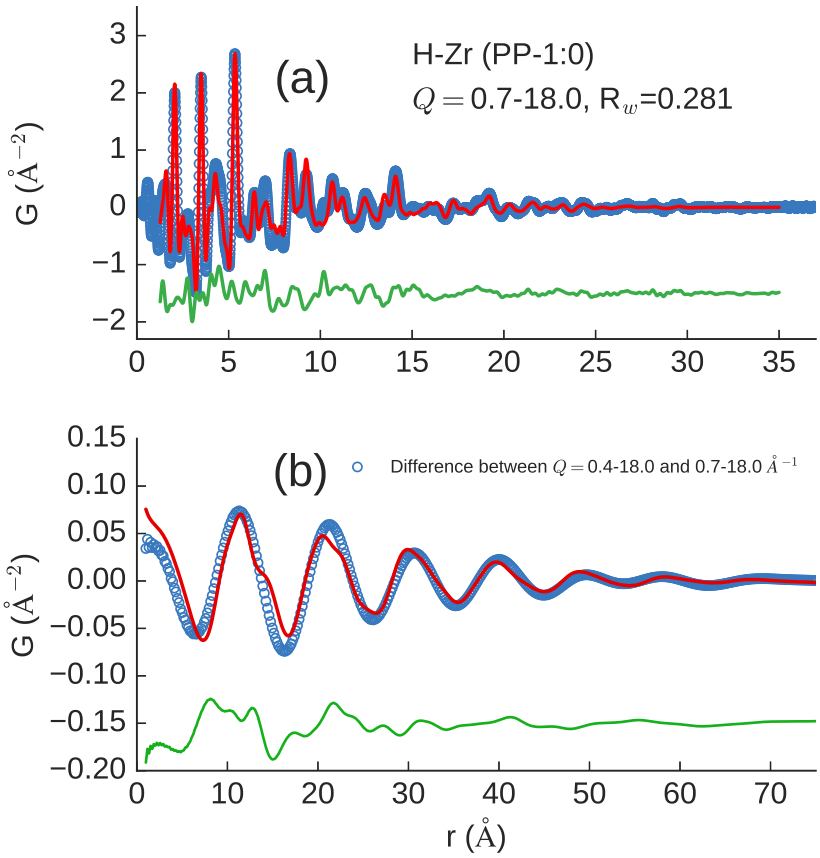

Figure 8.9: (a) PDF fit (red) of the α-ZrP structure model to the measured data (blue) with difference below (green). (b) As in Figure 8.7, a difference was taken between PDFs processed with and without the first Bragg peak in order to extract the interlayer structure PDF signal (blue). The PDF from fitting the ZrPP interlayer model (red) and difference (green) are also shown.

100% phosphonate sites does not significantly alter the layer structure. This is not surprising

since this same motif is also found in the ZrPP crystal structure. In comparison to the 1:2 H–Zr sample, the 1:0 has a shorter average interlayer distance of 9.625 Å and a much longer interlayer stacking coherence which is larger than the instrumental resolution in this case. However, it appears to have a slightly smaller intralayer coherence length of about 36.3 Å.

8.7.3 Local environment of Tb ions

With the parent structure well characterized, the local environment of Tb^{3+} ions intercalated into the layered structure can be investigated. Measurements of the H–Zr sample were carried out both as-is, and loaded with Tb^{3+} ions. Since the Tb^{3+} loading is low, it is a reasonable approximation that there is a negligible change in the intra-layer structure, supported by structural refinement for both of these measurements. As such, the measured as-is intensities were subtracted from the Tb^{3+} loaded intensities before transforming to the PDF. The resulting PDF contains the structural correlations that changed when the Tb^{3+} was intercalated, which to a reasonable approximation are the atomic correlations from the Tb^{3+} ions to atoms in its immediate environment. The loaded and unloaded H–Zr PDFs and the dPDF are shown in Figure 8.10(a). The Tb^{3+} dPDF is characterized by the appearance of two new sharp peaks at distances of $\sim$2.30 and 3.63 Å in addition to some broader structural correlations at higher distances. The PDF signal disappears beyond 10 to 15 Å. In order to identify the likely atom-pair contributions to the peaks in the dPDF, an investigation of a large number of Tb/phosphate based structures in the Inorganic Crystal Structure Database (ICSD) was carried out [207]. The structures investigated included those with the following ICSD database codes: '168755', '195925', '200591', '240703', '240931', '240972, '245065',

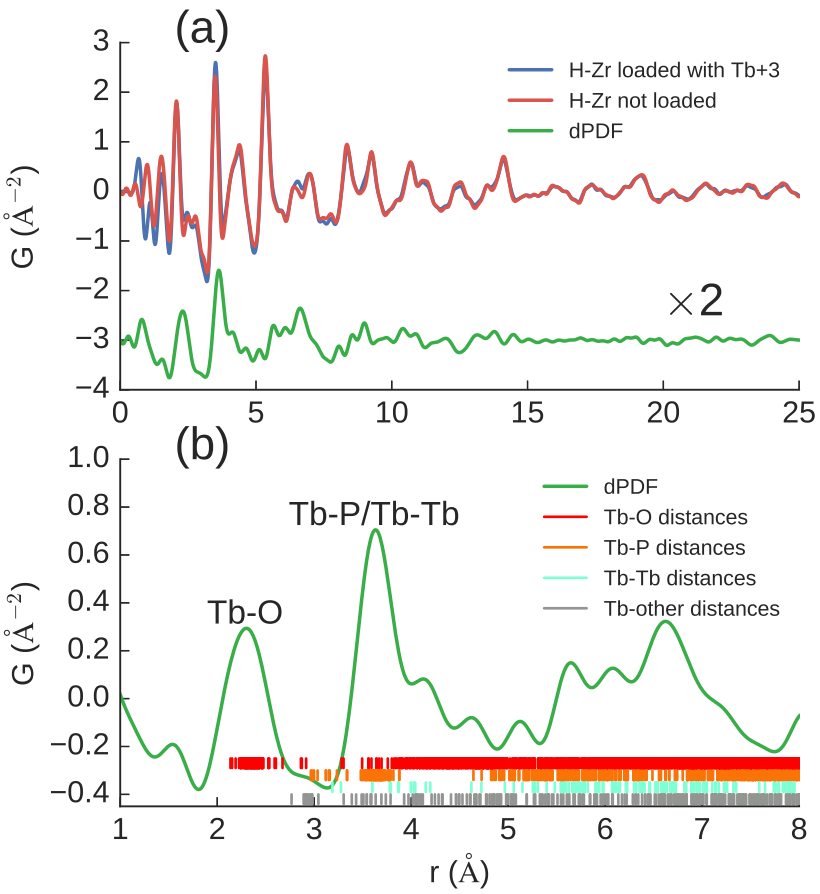

Figure 8.10: (a) Comparison of the PDFs measured from the H–Zr hybrid unloaded and loaded with Tb^{3+}. Qualitatively, the PDF traces are nearly identical. The dPDF is shown offset below (magnified $\times 2$), showing that entirely new structural correlations emerge related to the Tb^{3+} environment after subtracting away the scattering contributions from the zirconium phosphonate-phosphate layers. (b) The first few peaks of the dPDF shown compared to all atom-pair distances containing a terbium atom for Tb–phosphate based structures from the ICSD database.

'250437', '260730', '29316', '415322', '418979', '420118', '54085', '86282', '168754', '168756', '246392', '246394', '72145'. All pair distances which include a Tb atom were calculated for the various structures and the pair distance distribution is displayed for different atom types in Figure 8.10(b). There is a high density of Tb–O distances associated with the first peak in the dPDF. The positive Tb^{3+} ions are expected to prefer interaction with and therefore direct coordination by oxygen atoms. Thus, it is reasonable to assign the first peak as coming from

Tb–O correlations in the loaded hybrid sample. There is also a high density of Tb–P distances at the position of the second peak in the dPDF allowing us to tentatively assign it as coming from Tb–P correlations. This should be expected if P is the next nearest atom, also bonded to the nearest-neighbor O, which would be consistent with the Tb^{3+} ions interacting with the dangling O atoms of the phosphate groups. The literature structures also show some Tb–Tb and Tb–other-metal-ion distances near the position of the second PDF peak. The low concentration of Tb^{3+} suggests that it is unlikely that the peak in the measured PDF comes from Tb–Tb correlations, though this is not necessarily a requirement. These contributions could also reasonably correspond to distances between Tb and Zr atoms in the inorganic layer.

Refinements of the Tb–all (atoms) partial PDFs from all of the structures pulled from the database were carried out against the measured dPDF. Lattice parameters a, b, and c, a single isotropic thermal factor U_{iso}, scale factor, and coherence length d_c were allowed to refine. Despite most of the structures having similar Tb–O and Tb–P distances, many still performed very poorly during refinement, not fitting well to the intermediate-range structure. The four best refinements came from the following structures: (a) potassium terbium tetrakis (phosphate(V)) [208], (b) sodium terbium polytetraphosphate [209], (c) potassium terbium diphosphate(V) dihydrate [210], and (d) scheelite-type terbium phosphate [211]. The fits are displayed in Figure 8.11.

Overall, the four best-fit models perform similarly in describing the local structural environment of the Tb^{3+} ions. Tb atoms are consistently coordinated first by O, and then by P, and there are contributions to the second peak from Tb–(other-metal) pairs around 3.6 Å. In each structure, it is easy to find directions that locally resemble the stacking of metal phosphonate layers as in the Zr-phosphate structures. These directions are shown in Figure 8.11(e-h).

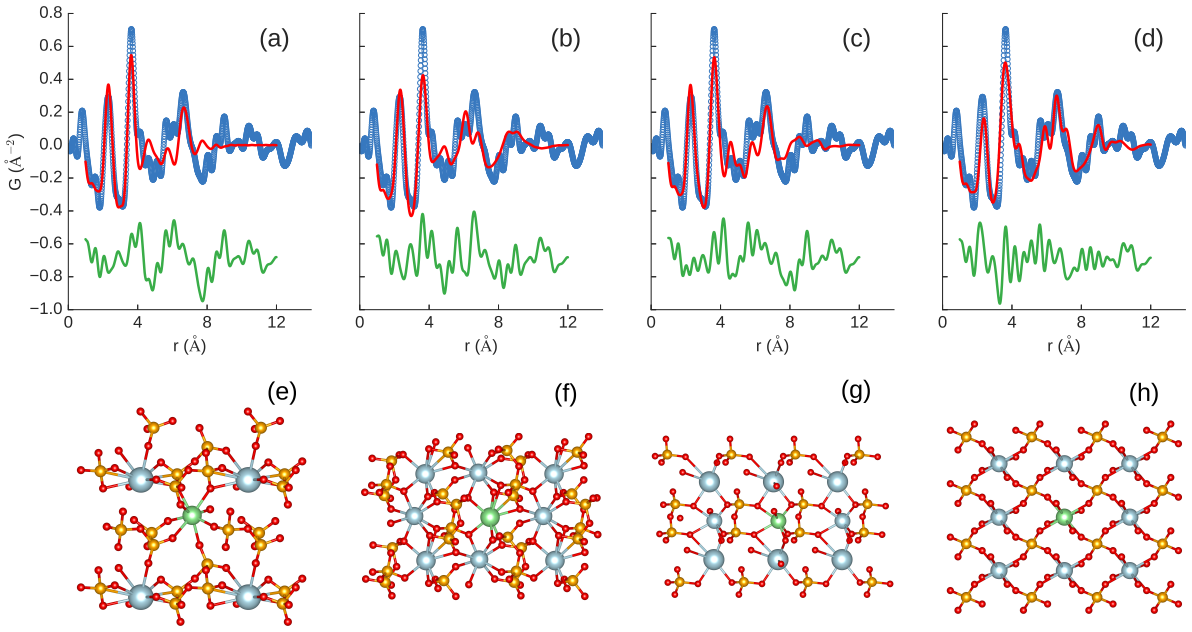

Figure 8.11: Fits of the Tb partial PDF for the best-fit Tb/phosphate based structures (red) to the measured H–Zr dPDF (blue). Difference curves (green) are offset for reference. Fits over a range of 1.0–12.0 Å are shown for the following structures (a) Potassium terbium tetrakis(phosphate(V)) (R_w=0.519), (b) Sodium terbium polytetraphosphate (R_w=0.517), (c) Potassium terbium diphosphate(V) dihydrate (R_w=0.471), and (d) scheelite-type terbium phosphate (R_w=0.449). Slices of the structures are shown respectively, viewed along the directions (e) [100], (f) [010], (g) [010], (h) [001]. The turquoise atom represents our origin Tb atom. O atoms are red, P atoms are orange, and all other Tb or other metal atoms are light blue.

Despite the similar overall R_w values, the scheelite model fits the intermediate range (4.0–12 Å) features better than the others. In fact, if the fits are instead performed over this higher range, the fit residuals become much worse for the first three (R_w= (a) 0.664, (b) 0.885, (c) 0.650), but remains approximately the same for scheelite (R_w= (d) 0.462), showing that some slightly distorted form of local structure of scheelite is the candidate that best describes the Tb environment in the UMOFs.

Looking again at the structure of scheelite, by choosing one center layer to be the interlayer space, and placing the origin at a Tb^{3+} there, it is shown how the intercalated ions

should be coordinated by dangling oxygens from the phosphate groups of the inorganic layers. Neighboring Tb atoms in the interlayer space have been removed for visual comparison. This bonding motif can be mapped directly onto the refined ZrPP structure of the hybrid samples. In Figure 8.12(a), the structure of two layers is viewed along the [112] direction for

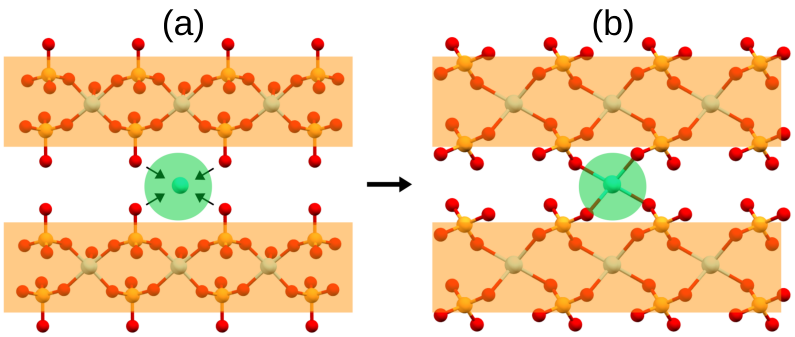

Figure 8.12: (a) A (112) slice from the ZrPP structure with the layers offset, shifted so phosphorus atoms sit directly atop one another, and a Tb atom placed between the layers, compared to (b) a slice from the (001) plane of the scheelite-type terbium phosphate structure with neighboring Tb atoms in the center layer removed.

the refined ZrPP structure, stacked at a distance of 10.26 Å and displaced in the x-y plane such that the P atoms sit directly over one another. Arbitrary shifting is reasonable since interlayer correlations are negligible, so it is reasonable to expect that neighboring layers could be related by an arbitrary shift or rotation. Having then placed a Tb atom in the center space, the result is a slice of material with a local Tb environment resembling that shown for the Scheelite structure. The bonding topology of the slices in (a) and (b) is identical, though the geometry is slightly distorted. It is reasonable to assume that the ZrPP layers could locally relax around the sites where Tb^{3+} ions sit in (a) to assume a structure more similar to that of (b). Therefore, on loading, the Tb ions intercalate between the disordered layers, and are essentially are taken up by the oxygens of the phosphate groups. Pair distance distributions from Tb–Zr correlations may manifest at shorter and longer distances if Tb ions also shift in

toward a Zr atom in either neighboring layer.

8.8 Conclusions

In designing materials for ion exchange, it is important to have a detailed understanding of the structure and the mechanism of loading in order to optimize performance. However, highly disordered structures do not lend ease to the process of structure determination by standard diffraction techniques. Here, we have determined the structure of two hybrid zirconium(IV) phosphonate-phosphate UMOFs, H–Zr and Na–Zr. They turn out to consist of modified nanocrystalline layers of the parent structure with an intralayer coherence length of approximately 4.59 nm and 5.46 nm respectively. The layers are stacked in a turbostratically disordered fashion, with weak ordering existing only between a few neighboring layers, although this stacking order drastically increases with higher phosphonate content. The local structural environment of Tb^{3+} ions loaded into the H–Zr sample was extracted by difference PDF methods. Among many alternative possibilities, the Tb environment is best described by the local environment of Tb in scheelite-type terbium phosphate structure. By orientationally mapping this local structure onto that of the refined structure for zirconium-phenylphosphonate, it is shown how the dangling oxygens of phosphate groups, might reorient to uptake the Tb^{3+} ions in between the inorganic layers.

An important question to be answered is why do these compounds prefer to take 3+ and 4+ ions in favor of ions of lower charge. It would be expected that there are many places within the ion exchanger that negatively charged species would cluster in groups of 3 or 4 to exert a high negative charge. This agrees well with our measurement and refinement of the

Tb ion coordination. Such groupings would then prefer the high charge of 3+ or 4+ ions in preference to the lower charged cations. It has also been shown that as the ratio of phosphate to phosphonate increases greater amounts of lower charged ions are taken up [194]. In the presence of higher levels of phosphate groups there may be a higher level of single cation species attractive to the lower charged cations. That is, the groupings of high charge fill up rapidly leaving HPO_4 groups to exchange H^+ for low charge ions.

Chapter 9

Nucleation of metal organic frameworks from solution

Stemming from the interesting behavior and structures observed through the work presented in Chapters 7 and 8, it made sense to further investigate how the frameworks of these microporous materials form, and further, how much information about the formation could be obtained using *in situ* PDF methods. I worked particularly with Debasis Banerjee from Pacific Northwest National Laboratory (PNNL) and Sanjit Ghose from Brookhaven National Laboratory (BNL) to perform experiments for this on the prototypical zeolitic imidazolate framework (ZIF-8). The results of my PDF analysis were supported by further experiments and fantastic efforts from a larger team at PNNL including Debasis Banerjee, Bharat Medasani, Anil Shukla, Benjamin A. Legg, Yufan Zhou, Zihua Zhu, Maria L. Sushko, Jim J. De Yoreo, Jun Liu, and Praveen Thallapally.

9.1 Room temperature solution synthesis of ZIF-8

Design and synthesis of new age materials [212] relies on a detailed understanding of nucleation and growth processes, especially for metal organic frameworks (MOFs) where structure

and morphology are highly tunable, for example by choice of the metal ions and ligands, additives, and/or synthesis conditions [213]. Among benchmark MOFs, ZIF-8 is a prototypical member of the zeolitic imidazolate framework (ZIF) family which consists of zinc metal centers tetrahedrally coordinated by 2-methylimidazolate (2-MeIm) linkers, in a 1:2 stoichiometry [61], shown in Figure 9.1. The secondary building units (SBUs) consist of $Zn(2\text{-MeIm})_4$

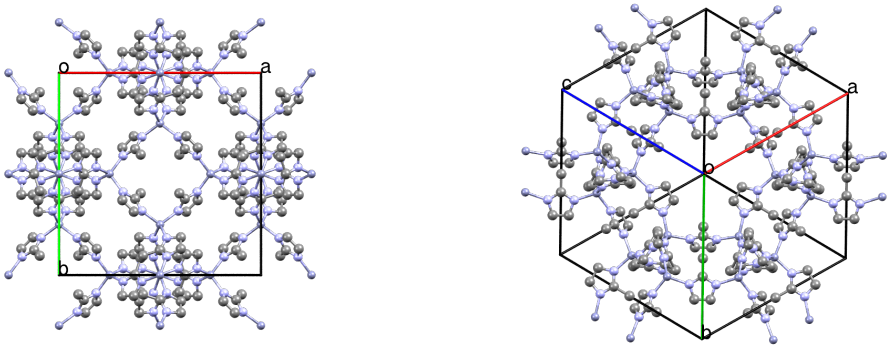

Figure 9.1: The crystal structure of ZIF-8 shown looking along the [001] direction (left) and along the [111] direction (right).

which connect to form a three-dimensional framework of sod topology [214].

The development of rapid, room temperature synthesis [215] in aqueous and/or mixed solvent has paved the way for studies involving *in situ* diffraction and microscopic techniques to elucidate the formation mechanism of the ZIF-8 structure. *In situ* liquid cell transmission electron microscopy (TEM) has been used to observe the late-stage growth of ZIF-8 particles [94], but lacks the image or time resolution to study atomistic mechanisms of formation, and is prone to inducing electron beam damage. Time-resolved static light scattering (TR-SLS) [216], *ex situ* [92], and *in situ* [90, 217] x-ray diffraction (XRD), and small-angle x-ray scattering (SAXS) [90], have been used to study solution-based synthesis, while solid state mechanochemical synthesis [69, 218] has been studied with *in situ* XRD. However, it is diffi-

cult to resolve atomistic details of disordered systems from traditional diffraction alone, and the reaction pathway and the atomic clusters which form during the development of ZIF-8 are not yet known. The PDF technique is a powerful technique for this purpose and has recently been used to observe nucleation and reaction pathways for inorganic nanoparticles during solvothermal synthesis [95–101]. It gives quantitative structural information about atomic clusters that are sub-nanometer, as well as over longer length scales, typically 1-10s of nm, and can distinctly separate information between crystalline and non-crystalline structures.

In this study, we have implemented an *in situ*, high energy, x-ray total scattering PDF experiment to probe the very local structures that form in solution as the precursors mix. Further, the brilliant light source allows for extremely high signal-to-noise, allowing even small concentrations of disordered, weakly scattering components to be detected [123, 128, 157]. Complimentary electrospray ionization mass spectrometry (ESI-MS) measurements were also performed to identify the most stable molecular species or mass fragments existing in solution, during the synthesis, by measuring the masses of their ionized counterparts [219]. This technique has been previously used to detect the presence of SBUs preceding network formation for a separate MOF system [89].

9.2 Experiments

9.2.1 Synthesis of ZIF-8

The synthesis was carried out by Debasis Banerjee using a previously reported procedure [220]. ZIF-8 formation occurred at room temperature using $Zn(NO_3)_2 \cdot 6H_2O$ as a metal

salt and 2-MeIm as linker at different molar ratio using water and methanol as the solvent respectively. In a typical scenario, approximately 50 mg of $Zn(NO_3)_2 \cdot 6H_2O$ (Sigma-Aldrich, 98%) was added to 10 ml of DI water, forming a clear solution. Similarly, approximately 87 mg of 2-MeIm (99%, Sigma-Aldrich) was added to 10 ml methanol. The solutions were then mixed with or without stirring to form ZIF-8, as confirmed by powder XRD. In the case of higher (or lower) molar ratio experiments, the concentration of $Zn(NO_3)_2 \cdot 6H_2O$ solution was kept constant, while changing the molar concentration of 2-MeIm.

For time dependent *ex situ* TEM studies, a $Zn(NO_3)_2$ to 2-MeIm molar ratio of 1:6 was used. The synthesis is as follows: 50 mg of $Zn(NO_3)_2$ in 10 ml water + 87 mg of 2-MeIm in 10 ml of methanol solution. For PDF experiments, the following calculation was performed: The conversion rate from reactants to ZIF-8 was assumed approximately 80%, followed by % weight calculation in a water/methanol (1:1 v/v) mixture (density: 0.86 g/ml). For example, for a 1 wt% ZIF-8 solution mixture (in-situ formation), we assumed that we need enough reactants to form at least 1.23 gram of ZIF-8 (100% conversion). 3 gram of $Zn(NO_3)_2 \cdot 6H_2O$ in 100 ml water and 1.64 gram of 2-MeIm in 100 ml methanol is needed to get a 1 wt% ZIF-8 solution with $Zn(NO_3)_2 \cdot 6H_2O$ to 2-MeIm ratio being 1:2. Similarly, for a 3 wt% ZIF-8 solution, 9 gram of $Zn(NO_3)_2 \cdot 6H_2O$ in 100 ml of water and 4.92 gram of 2-methyl 2-MeIm ml of water is needed. To go to even higher molar ratio for 2-MeIm (1:6), approximately 4.92 gram of 2-MeIm (for 1wt% ZIF-8) or 14.76 gram of 2-MeIm (for 3wt% ZIF-8 solution) is needed. As increases in concentration lead to faster formation of ZIF-8, the majority of the experiments were carried out at $Zn(NO_3)_2 \cdot 6H_2O$: 2-MeIm ratio of 1:2 with estimated ZIF-8 formation of 1wt%.

9.2.2 Total scattering measurements

Experiments were carried out using beamline 28-ID-2 at the National Synchrotron Light Source II (NSLS-II) at Brookhaven National Laboratory. The diffraction datasets were collected at room temperature, in rapid acquisition mode [117], using a 2D PerkinElmer amorphous silicon detector (2048×2048 pixels and 200×200 μm pixel size) with a sample-to-detector distance of 219.431 mm. The incident wavelength of the x-rays was λ = 0.1827 Å (67.86 keV). Calibration of the experimental setup was performed using a nickel standard sample. Standard liquid and powder samples were loaded into 1 mm ID Kapton capillaries and measured *ex situ* for comparison: crystalline ZIF-8, zinc dinitrate hexahydrate dissolved in water, 2-methylimidazole dissolved in methanol, and pure water, pure methanol, and empty Kapton for the respective backgrounds. For the *in situ* measurements, precursor solutions were mixed at a 1:1 ratio. Time dependent studies were performed in a static reaction cell or in the liquid flow cell with zero flow rate, both designed in house. Raw 2D data were corrected for geometrical effects, then azimuthally integrated to produce 1D scattering intensities versus the magnitude of the momentum transfer Q using the program Fit2D [118]. The program xPDFsuite with PDFgetX3 [107, 221] was used to perform the background subtraction, further corrections and normalization to obtain the reduced total scattering structure function $F(Q)$, and Fourier transformation to obtain the PDF, $G(r)$. The accessible Q_{min} was fixed by the beamstop, 0.45 Å^{-1}. PDFs were processed with both a Q_{max} =18.0 Å^{-1} for high resolution structural analysis, and a low value of 10.4 Å^{-1} for PDFs with sufficiently reduced noise to evaluate low-amplitude signals at high-r which come from ordered phases present at small concentrations.

9.2.3 Static reaction cell

In situ PDF measurements were initially performed in a static reaction cell, Figure 9.2, at Zn:2-MeIm ratios of 1:2 and 1:6. The precursor solutions were injected to the cell, and measurements started approximately 2 minutes after injection. For the 1:6 case, Bragg peaks were observed at the earliest times measured, approximately 2 minutes after injection, and the subsequent PDFs contained both high and low frequency terms at high-r, similar to the ZIF-8 standard, indicating the presence of crystalline ZIF-8 particles. Qualitatively, no changes were observed up to 104 minutes of measurement, indicating that reaction is rapidly completed, in agreement with TEM measurements. For the 1:2 case, distinct Bragg peaks were not observed, though a slight increase in structural ordering was evident in the PDF up to 224 minutes. However, in both cases, low Q-resolution and poor signal-to-noise in the resulting PDFs with this apparatus prevented reliable tracking of the extent of crystallization or crystallite size in either reciprocal or real space.

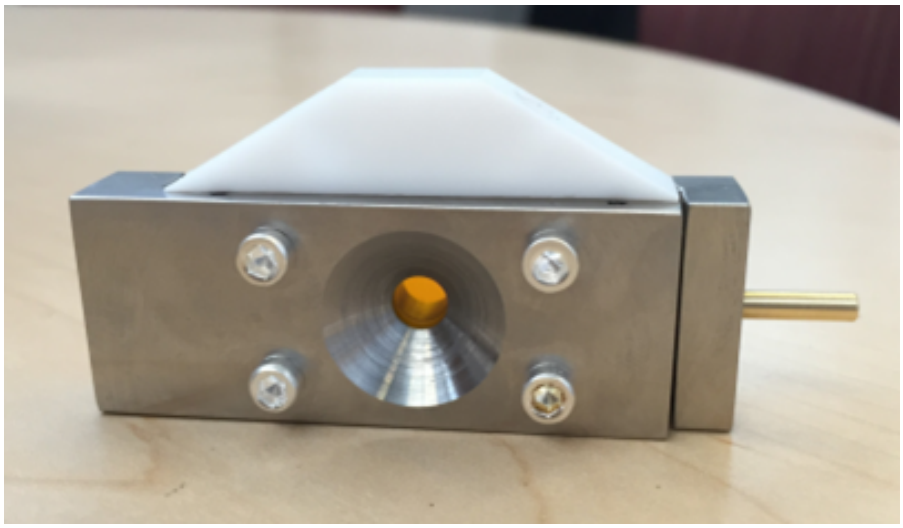

Figure 9.2: Static reaction cell. The pin on the right attaches to the goniometer to hold the cell in place. Precursor solutions are injected via syringe through the top ports, and x-rays penetrate the solution through the Kapton window in the center.

9.2.4 Flow cell

To try and investigate the early stages of the reaction, we loaded the precursors into syringes and injected them into a plug-flow reaction cell with a single outlet, allowing continuous flow of the product solution, such that the extent of reaction should remain constant in time at any given distance measured along the tube. The flow cell is shown in Figure 9.3. We sought

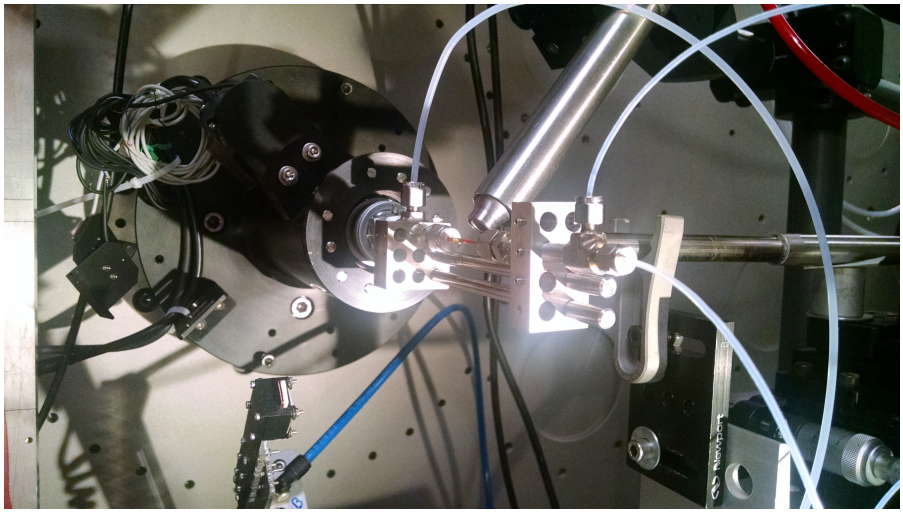

Figure 9.3: Flow cell used for *in situ* PDF measurements. Inlets mix (right side) then flow through an extended kapton capillary tube held in the beam path, before exiting the opposite end.

to slow down the reaction, without changing the temperature of the reagents, which was not possible in our setup. Two factors could be controlled to affect the extent of reaction in the measured signal:(a) measuring at different distances along the flow cell, and (b) changing the flow rate to change the residence time of the reactants. In our measurements, the beam could not be placed directly at the location where the inlets first mixed. We therefore tuned the flow rate of the inlets to change the relative extent of reaction at the same cell position. The pump rate was controlled using a Harvard Apparatus Pump 11 Elite. The cell consisted of a 2 mm ID Kapton to simultaneously increase the scattering statistics collected from a larger

scattering volume and decrease background scattering from the cell. The precursor solutions consisted of zinc nitrate in MeOH and 2-MeIm in H_2O prepared such that the molar ratio on mixing varied between 1:2, 1:4, and 1:6 (Zn:2-MeIm) with theoretical product yields of 1, 3, or 5 wt%. The background was measured by pumping methanol and water without the reactants at a 1:1 ratio.

9.2.5 Supplemental experiments and simulations

Time dependent *ex situ* TEM experiments were carried out by Benjamin Legg. The solutions were mixed and samples collected at different time interval. Samples were extracted at time intervals of 30 seconds, 10 minutes, and 1 hour. During sample preparation, a 2 μL droplet of the reacting solution was placed on a carbon film TEM grid (Ted Pella), blotted with filter paper, and allowed to air dry overnight. Samples were imaged using a 200 keV field-emission FEI Technai in TEM mode.

Time dependent *ex situ* TEM studies were performed by Benjamin Legg at PNNL. A $Zn(NO_3)_2$ to 2-MeIm molar ratio of 1:6 was used. The synthesis is as follows: 50 mg of Zn(NO3)2 in 10 ml water + 87 mg of 2-MeIm in 10 ml of methanol solution. The solutions were mixed and samples collected at different time interval. Samples were extracted at time intervals of 30 seconds, 10 minutes, and 1 hour. During sample preparation, a 2 μL droplet of the reacting solution was placed on a carbon film 10TEM grid (Ted Pella), blotted with filter paper, and allowed to air dry overnight. Samples were imaged using a 200 keV field-emission FEI Technai in TEM mode.

Electrospray ionization mass spectrometry was performed at PNNL. Mass spectrometry

analysis of the mixed solutions of varying concentrations of zinc nitrate with 2-MeIm were carried out by ionizing the mixed solution by electrospray (ESI) process and recording the resulting mass spectra using an Exactive Orbitrap mass spectrometer (Thermo Fisher Scientific, Bremen, Germany). A syringe pump was used to deliver the mixed solution to a 150 μm OD and 20 μm ID chemically etched silica capillary emitter held at 2.2 kV using a flow rate of 1 μL/min. The ESI tip was placed at a distance of 3 mm from a 360 μm ID heated capillary interface to the mass spectrometer. The heated capillary interface temperature was maintained at a temperature of 100°C as varying the temperature between 50°C and 100°C for the desolvation process had no significant effect on the intensity and masses of the resulting ions. Mass spectra were recorded at a mass resolution of 100,000 (at m/z 400) in the positive ion mode, covering the m/z range from 100-2,000 or in the mass range suitable for analysis. Mass spectra of the mixed solutions of different molar ratios were recorded at different time intervals from approximately 2 minutes to 2 hours or longer to explore the kinetics of the complex formation process. Mass spectra were accumulated for some period of time for signal averaging to get better quality spectra. Some spectra were recorded on a LTQ Orbitrap Velos mass spectrometer from Thermo Fisher Scientific under similar experimental conditions.

DFT was performed by Maria Sushko at PNNL to optimize the structure of Zn(2-MeIm)$_x$. Calculations were performed with NWCHEM code using PBE0 exchange- correlation functional and Dunning's correlation consistent polarized basis sets augmented with diffuse functions at the level of aug-cc-pVDZ as supplied in NWCHEM. Grimme's DFT-D3 12dispersion was accounted for when computing the energetics.

9.3 Results and discussion

An *ex situ*, time dependent TEM study was carried out by collaborators, Debasis Banerjee and Benjamin Legg, to understand how the particle morphology evolves over time. The reaction is extremely fast; large particles up to approximately 100 nm in diameter are observed after just 30 seconds of reaction, Figure 9.4. Little change in particle size or morphology is

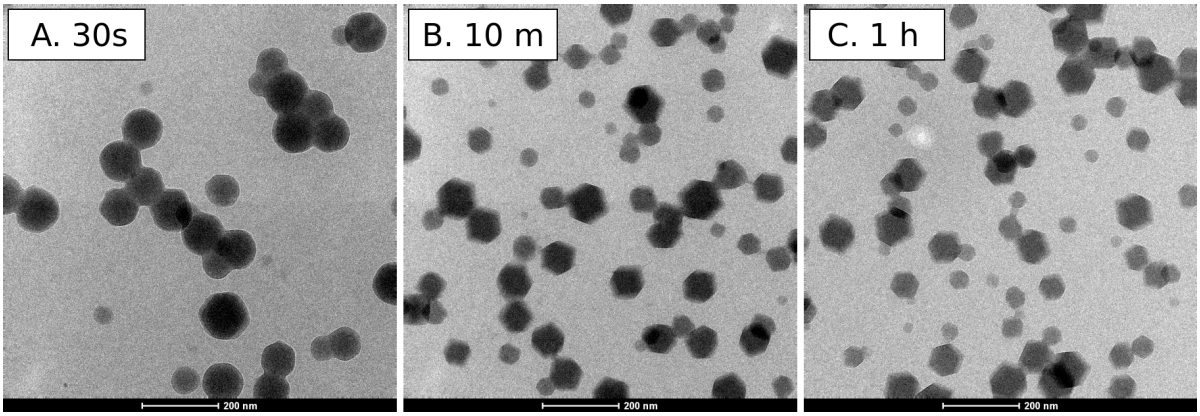

Figure 9.4: Time dependent *ex situ* transmission electron microscopy (TEM) data of ZIF-8 (a) 30 seconds (b) 10 minute (c) 1 hour.

observed over time. Although the particles extracted at 30 seconds do show distinct signs of faceting, indicating a crystalline nature, the crystalline cores appear to be enveloped in a thin coating that causes them to appear more spherical. It is not clear whether this coating is an inherent property of the particle in solution, or whether it is formed from unreacted precursors during the drying process. After 10 minutes of aging, this coating is no longer apparent, and the particles display distinct, rhombic dodecahedral morphology. Because this reaction approaches completion after just 30 seconds, attempts were made to slow the reaction and capture earlier stages of crystal growth. The reaction was repeated using concentrations of 15 mg $Zn(NO_3)_2$ (0.047 mmol) in 10 mL water with 25 mg 2-MeIm (0.30 mmol) in 10 mL methanol, and conducting the reaction at 0°C using an ice-water bath. These reaction con-

ditions ultimately lead to the formation of significantly larger particles, with particle widths exceeding 250 nm after just 30 minutes of reaction. However, we were able to capture significantly smaller early-stage particles using this method, with typical widths ranging from 30 to 60 nm. The early-stage particles extracted from solution after 20 seconds have much less well developed crystalline facets than observed at later times and display extensive aggregation. We obtained high-resolution TEM images of these samples and confirmed that despite the poorly developed surface faceting, the particles contain a well-defined crystalline core that is consistent with the ZIF-8 crystal structure. However, this crystallinity does not consistently extend to the particle surface, and there often appear to be amorphous regions bridging the gap between two distinct crystalline domains, suggesting that an aggregation-based growth process may be active.

PDF measurements were then carried out to investigate the reaction. *Ex situ* measurements of the reagent solutions, $Zn(NO_3)_2 \cdot 6H_2O$ dissolved in water and 2-MeIm in methanol, and pre-synthesized crystalline ZIF-8 standard, helping to build some intuition about the features in the PDFs of these materials and what will be seen in the *in situ* measurements. Total scattering measurements were taken of the reagent molecules dissolved in solvent. The solvent scattering was measured separately and subtracted, such that Fourier transformation of the resulting structure function results in a difference PDF (dPDF) with peaks corresponding only to atom-pair distances within the precursor molecules, and any coherent interactions between the precursors and neighboring solvent molecules [123, 222]. The measured PDFs of 2-MeIm, $Zn(NO_3)_2$, and ZIF-8 are compared with PDFs from structural models for these species, and the primary atom-pair contributions to the signal are indexed in Figure 9.5(a-c). The first and second peaks in the PDF of aqueous $Zn(NO_3)_2$ [Figure 9.5(a)

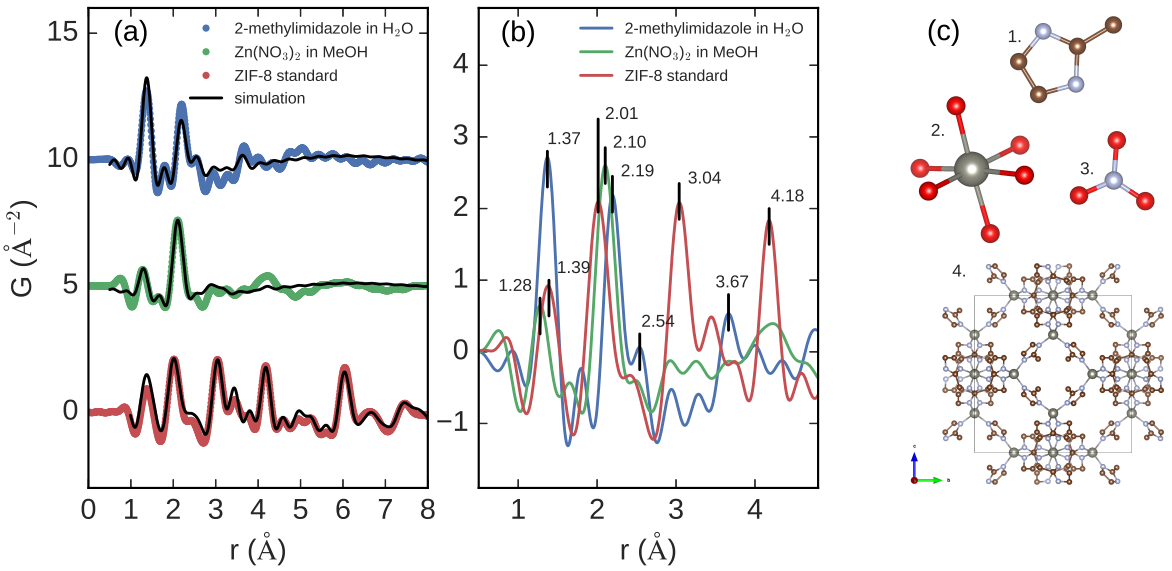

Figure 9.5: (a) Low-r region of the PDFs measured for aqueous 2-MeIm, methanolic $Zn(NO_3)_2$ and crystalline ZIF-8. PDFs simulated from refined molecular or crystal (in the case of ZIF-8) structures are superimposed in black. (b) The experimental PDFs are then superimposed for direct comparison of the atom-pair distances associated with the respective molecular structures. The models used for the refinements in (a) are shown in (c): 1. 2-MeIm, 2. oxygen-coordinated zinc, 3. NO_3^-, 4. ZIF-8 crystal. The corresponding elements are carbon (brown), nitrogen (blue), zinc (silver), oxygen (red).

green curve] correspond respectively to the nitrate N-O bond (1.28 Å) and the coordination of Zn^{2+} ions by water oxygens: a Zn-O bond at 2.10 Å. For methanolic 2-MeIm [Figure 9.5(a) blue curve], the first and second peaks correspond to the average nearest-neighbor distance, C-C/C-N (1.37 Å), and average second-nearest-neighbor (2.17 Å). ESI-MS was also carried out on the separate reagent solutions. The mass spectra of the Zn precursor showed the presence of $ZnNO_3$+ (m/z 128). Several mass fragments of general formula $Zn(NO_3)_x{\cdot}(H_2O)_y^+$ ($0 \leq x, y \leq 2$) were observed due to either incomplete dehydration in the gas-phase or the solvation of the $ZnNO_3^+$ ion, for example peaks around 145.9, 161.9, and 179.9 are due to $ZnNO_3{\cdot}H_2O^+$, $ZnNO_3{\cdot}(H_2O)_2^+$, and $ZnNO_3{\cdot}(H_2O)_3^+$ respectively. In the second solution, 2-MeIm was found to be present as mainly 2-$MeImH^+$ (m/z 83) and (2-MeIm)$\cdot 2H^+$ (m/z 165).

In the PDF of pre-synthesized crystalline ZIF-8 [Figure 9.5(a) red curve], the first peak (1.39 Å) is still comprised of the nearest neighbor contributions from 2-MeIm. The second peak shifts lower (2.01 Å) as it is now dominated by the Zn-N pairs, though also still containing the second-nearest-neighbors from 2-MeIm. Coordination of the Zn^{2+} ion is most easily observed from the appearance of strong contributions of the Zn center with second nearest neighbor C at 3.04 Åand with third nearest neighbor C(N) at 4.18 Å, each of which have a high pair multiplicity of 8, and therefore are strong features in the PDF (in the case of a full tetrahedral coordination as here). The linkage of the SBUs with one another is apparent in the ZIF-8 product (red curve) by the observation of Zn-Zn pairs, each bonded to opposing N atoms on the same 2-MeIm ring, contributing the sharp peak at 6.03 Å.

The high-r region of the PDF for crystalline ZIF-8 is shown in Figure 9.6. Long range

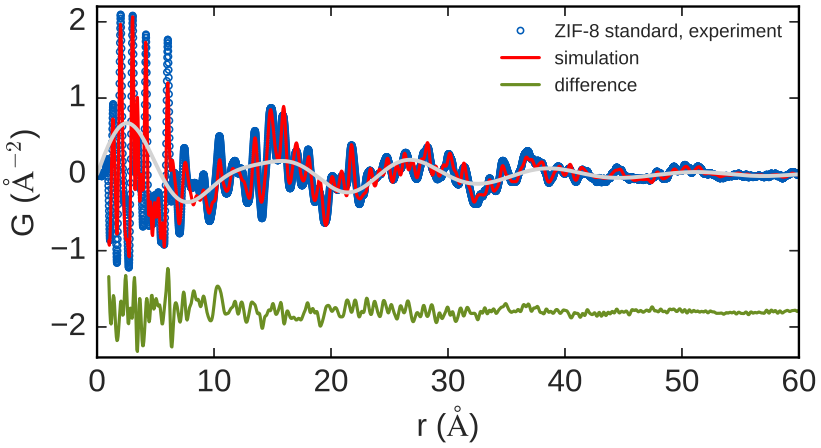

Figure 9.6: The PDF of the crystalline ZIF-8 standard (blue) is compared to that simulated from a refined structural model (red), with the difference curve plotted below (green). The long wavelength modulations are highlighted by the gray line, an approximate model of the density distribution between pore and framework, calculated as the Fourier transform of the first two Bragg reflections in a simulated powder pattern and damped by a Gaussian envelope corresponding to the experimental resolution.

crystalline order is evident by the persistence of sharp peaks over a wide range of r. In fact,

the damping of the features at high-r is limited by the Q-resolution of the measurement, indicating a highly crystalline material, as expected for this standard. A low-frequency oscillatory component in the measured PDF also persists to high distances and is characteristic of the presence of a well-ordered arrangement of pores. These oscillations are modulations in the electron density between framework and empty space; the wavelength corresponds to the diameter of the pores, 11.87 Å here, or roughly 2π/FSDP (FSDP $\equiv$ first sharp diffraction peak). The observation of such long-wavelength oscillations in the PDF baseline can show the presence of a porous structure even when no long-range crystal structure is known for the material.

In situ PDF measurements were performed on mixing aqueous $Zn(NO_3)_2$ and methanolic 2-MeIm in the liquid flow cell (molar ratio 1:n, n = 2, 4, 6 for 2-MeIm) to capture the structural state of all the components in the reaction system as a function of time after mixing. The rate of reaction increases with n, so variable concentrations were tested for their effects on the synthesis of ZIF-8. The theoretical product wt% was increased to improve signal-to-noise, and flow rate was varied such that the point of measurement corresponded to reaction times ranging between 0.05-2.0 s.

Comparing the high-r region of the PDFs for pre-synthesized crystalline ZIF-8 to those of the just-mixed systems, shows that even after fractions of a second, the reaction has already nucleated crystalline ZIF-8 particles Figure 9.7(a). The particle diameters were estimated on the order of 10 nm by fitting the crystalline standard PDF to the *in situ* PDF, rescaled, and modulated by a spherical envelope function which simulates the effects of a finite spherical domain. However, there is still a strong signal left over in the difference curve, Figure 9.7(b), indicating either unreacted precursors or a non-crystallized, short-range ordered product in

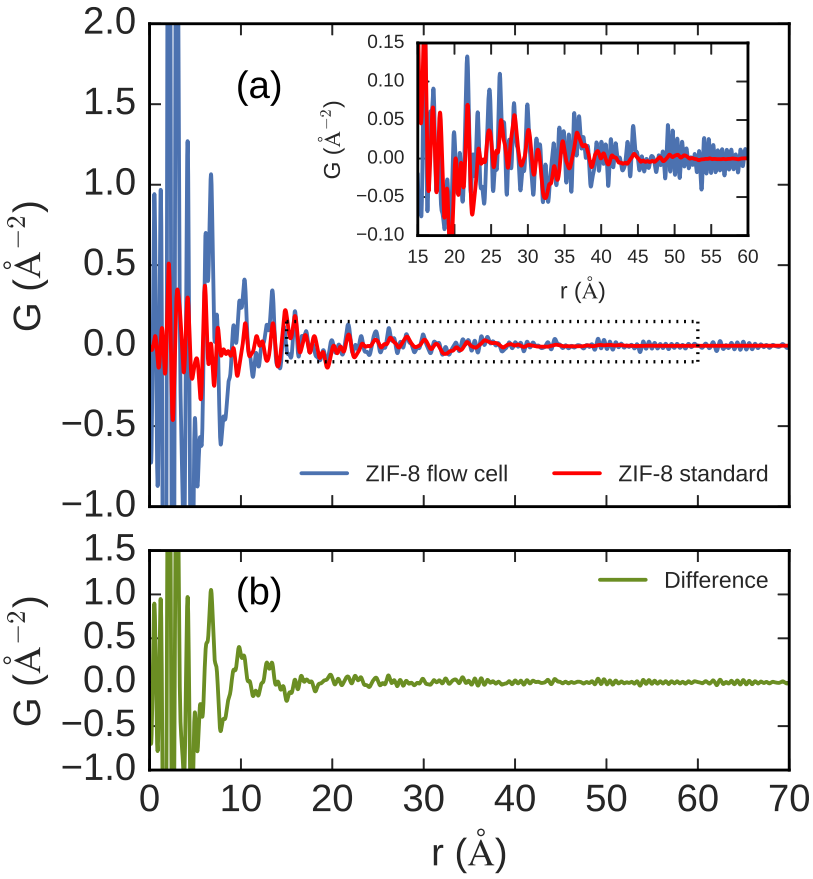

Figure 9.7: (a) High-r comparison of the PDFs from the ZIF-8 standard and the product after nucleation. The standard is rescaled to fit the high-r signal in the nucleated product, showing that some long-range ordered crystalline phase has already formed. A zoomed plot of the region boxed by dotted lines is shown in the inset. (b) The difference between the product PDF and the rescaled standard shows that a significant signal persists, principally in the low-r region, which is substantially different from the final product.

addition to the nanocrystalline ZIF-8 product. In this short-range ordered component (SROC) there are sharp peaks at low-r and a broad signal at intermediate-r that disappears by ~15-20 Å. Inspection over the first few Å [Figure 9.8(a)] shows that the first two peaks are shifted from the respective positions in the ZIF-8 standard: the first peak shifted to a shorter distance of 1.26 Å and the second peak shifted to a higher distance of 2.10 Å. This is consistent with the persistence of unreacted, aqueous $Zn(NO_3)_2{\cdot}6H_2O$ precursor [For example, see Figure 9.8(b)] which can be explained by the presence of $Zn(NO_3)_x{\cdot}(H_2O)_y^+$ type species as observed by

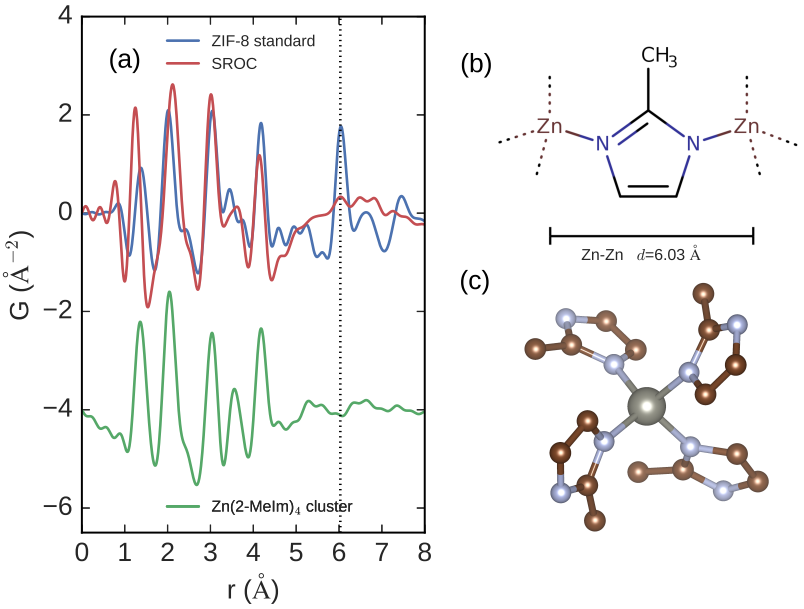

Figure 9.8: (a) Low-r comparison of PDFs from the ZIF-8 standard (blue) and the ZIF-8 product directly after nucleation in MeOH:H2O (red). A PDF simulated from a single Zn(2-MeIm)$_4$ cluster (green) is offset below. Of particular note is the absence of a sharp peak at the Zn-Zn pair distance shown diagrammatically in (b) and indicated by the vertical dotted line in the Figure. This suggests the presence of a significant amount of Zn and 2-MeIm in the form of Zn(2-MeIm)$_4$ shown in (c), which does not have a distinct Zn-Zn pair contribution

ESI-MS of the unmixed precursor. Despite the high ratio of 2-MeIm to Zn^{2+}, this suggests that unreacted Zn^{2+} ions exist, which have not yet formed full complexes with 2-MeIm. However, we cannot rule out the formation of Zn(2-MeIm)$_x$ (x = 1, 2, 3) species with partial oxygen coordination and bond-lengths differing from those of the fully coordinated cluster. Sharp peaks at 3.04 and 4.18 Å have also appeared, but there is no strong peak at 6.03 Å. These peaks do not come from the crystalline product because their amplitudes far exceed that expected from the minority crystalline component, and furthermore there are no sharp peaks at higher-r. The absence of a sharp peak at the Zn-Zn distance suggests that a high concentration of Zn(2-MeIm)$_4$ clusters have formed, but not yet organized into an ordered network.

The signal from the SROC does not vary significantly with time during the synthesis indicating that Zn(2-MeIm)$_4$ clusters form rapidly and persist (at least several hours) during the reaction under all conditions tested. Similar behavior has been observed for other MOF species [88, 89]. The coexistence of nanocrystals and persistent SBUs also agrees well with previous observations of comparatively slow nucleation but fast particle growth [216].

ESI-MS was used to corroborate these observations. The reagents were mixed using the same molar ratios tested with PDF, though at a much lower reagent to solvent ratio, and injected as a function of time. Mass spectra obtained from 5 minutes to 240 minutes do not show any significant differences, agreeing that the reaction is almost instantaneous, even in solution with a much lower total theoretical yield than that measured with PDF. For a 1:2 (slowest expected reaction rate) and 1:4 molar ratios, Figure 9.9(a,b), there are four main peaks in the spectrum at m/z 165.11, 290.02, 327.09 and 372.08 which correspond to (2-MeIm)·2H$^+$, ZnNO$_3$·(2-MeIm)$_2^+$, Zn(2-MeIm)$_2$·(2-MeIm-H)·H$_2$O$^+$ and ZnNO$_3$·(2-MeIm)$_3^+$, respectively, with the ZnNO$_3$·(2-MeIm)$_3^+$ ions found to be the most abundant. The significant presence of clusters still coordinated by nitrate groups or H$_2$O agrees with the observed shifts in the PDF peaks at low-r. For the 1:4 molar ratio, the relative abundance of the ZnNO$_3$·(2-MeIm)$_2^+$ component increase substantially, which may correspond with a higher driving force for zinc/2-MeIm interaction. The mass spectrum for the 1:6 molar ratio solution is shown in Figure 9.9(c). An additional peak at m/z 391.13 is now observed that corresponds to Zn(2-MeIm)$_3$·(2-MeIm-H)$^+$ ion which is the second most abundant ion in the spectrum, besides the (2-MeIm)$_2$·H$^+$ (m/z 165.11), likely due to the excess 2-MeIm driving the formation of Zn(2-MeIm)$_x$(NO$_3$)$_y$ (x $>>$ y) species. Higher order (Zn)$_x$(2-MeIm)$_y$ complexes were also observed. Further increase in 2-MeIm concentration [Zn(NO$_3$)$_2$: 2-MeIm = 1:8(12)] did not

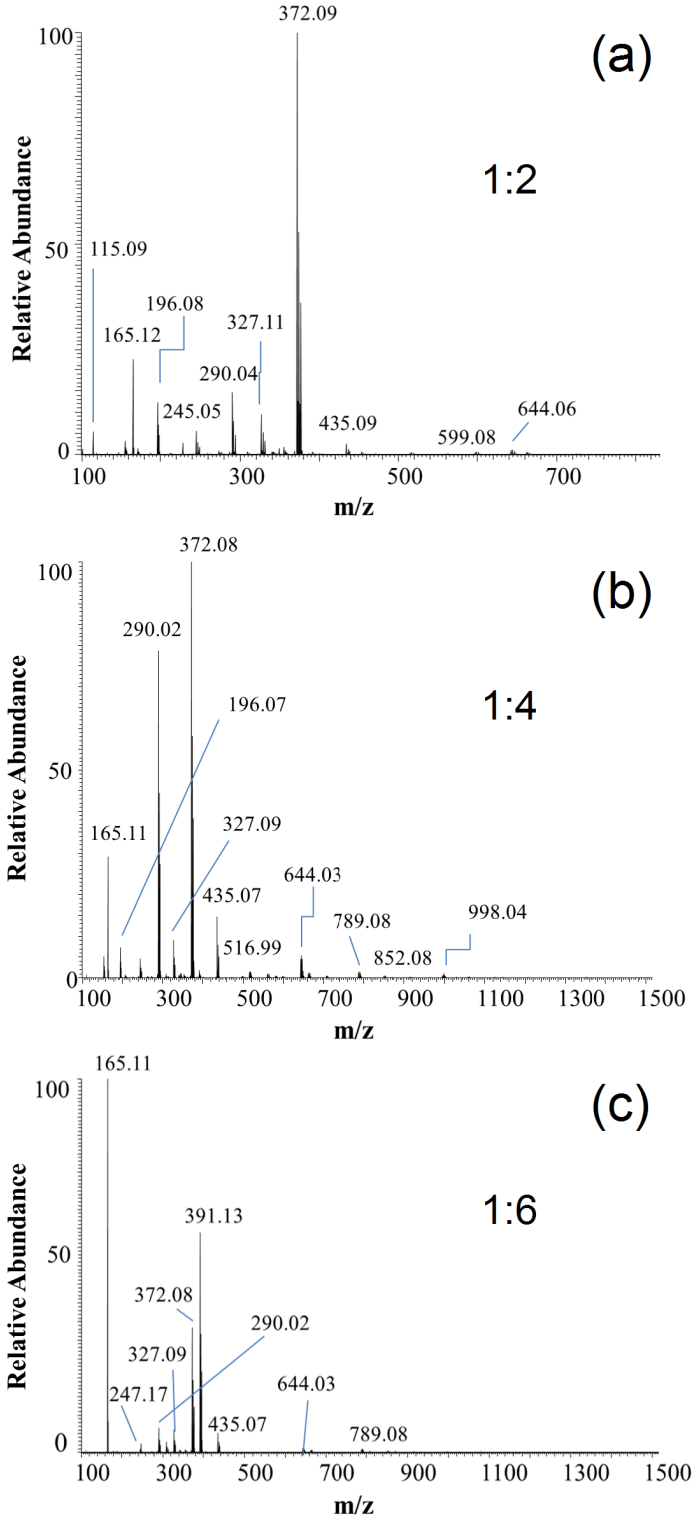

Figure 9.9: ESI-MS spectra of mixtures 2-MeIm in methanol solution showing the presence of imidazole clusters in the solution (b) spectra depicting $Zn(NO_3)_2$ and 2-MeIm in 1:6 molar ratio.

make any significant difference to the mass spectrum. Taking the PDF and ESI-MS results together, the observation of Zn(2-MeIm)$_3$·(2-MeIm-H)$^+$ as the major product in the mass spectra, corresponding to the Zn(2-MeIm)$_4$ seen in the PDF in the solution phase, suggests that the Zn(2-MeIm)$_4$ is the basic building unit of ZIF-8 in solution.

The energies of various species in the gaseous phase were calculated using density functional theory (DFT) [223]. DFT calculations on Zn(2-MeIm)x were performed with NWCHEM code using PBE0 exchange-correlation functional and Dunning's correlation consistent polarized basis sets augmented with diffuse functions at the level of aug-cc-pVDZ as supplied in NWCHEM. Grimme's DFT-D3 dispersion was accounted for when computing the energetics. More details about simulations, and resulting structures, can be found in SI Section VII. Starting with multiple Zn(2-MeIm)$_x$ configurations for $x = 3$ and 4 and Zn charge states of 0, 1+, and 2+, we identified the most stable Zn(2-MeIm)$_x$ structure. The results agreed with previous theoretical simulations for Zn–imidazole complexes [224], and the most energetically favorable stoichiometry of Zn-2-MeIm coordination complexes corresponds to those with Zn^{2+} and $x = 4$. Calculations were converged to get binding energies for different possible configurations ranging from linear chain 2-MeIm-2-MeIm-Zn-2-MeIm-2-MeIm, to tetrahedral Zn(2-MeIm)4 configuration. The tetrahedral configuration is the most energetically favorable. The low energy of the tetrahedrally coordinated Zn(2-MeIm)$_4$ from the DFT calculations supports the abundance of this cluster in the ESI-MS data and its observation in the PDF, adding further support to the idea that it is a basic building unit for ZIF-8. The difference in binding energies for this configuration and for other configurations studied is larger than 17.6 kcal/mol. The analysis of the distribution of the electron density of these fragments demonstrates that the optimum configuration is defined by the balance of Zn^{2+} -

N coordination bonding, 2-MeIm-2-MeIm hydrogen bonding, and steric repulsion between 2-MeIm linkers. The configurations tested are shown in Figure 9.10

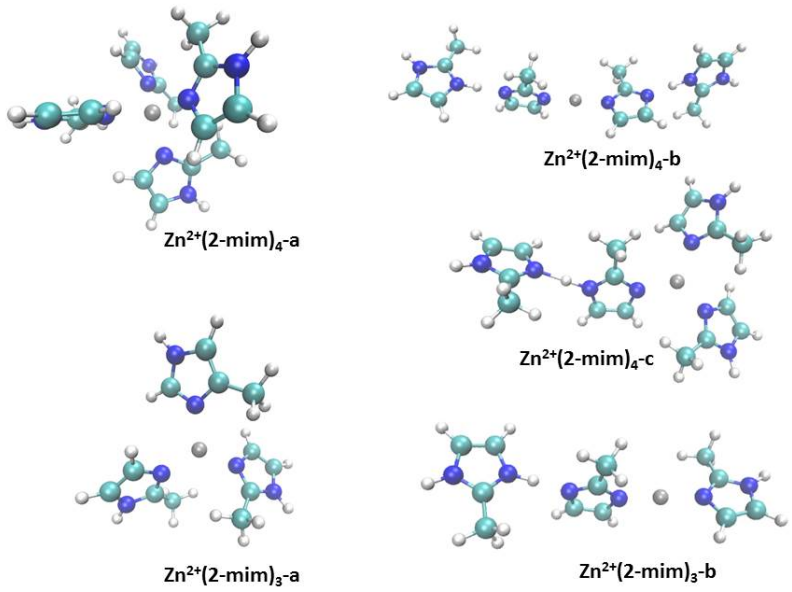

Figure 9.10: Different configurations of Zn(2-MeIm)$_4$ optimized by DFT.

This simple picture of stable SBUs present in solution still does not explain the broader features existing in the PDF up to ~20 Å, that suggest the presence of larger objects that are, nonetheless, disordered. There are some higher order cluster ions present in the ESI-MS spectrum but at much lower intensities. This implicates aggregations of SBUs (possibly other components, *i.e.* (2-MeIm)$_n$), or higher order complexes as observed by ESI-MS. Amorphous ZIFs have been reported through thermal and mechanical degradation of the crystalline parent phase [70, 71, 225, 226], and as an intermediate during *in situ* mechanochemical syntheses [69]. For solution syntheses, the formation of medium-range ordered intermediates has been hypothesized [92], and early formation of clusters ~2 nm in diameter has been shown using SAXS [90], and these are consistent with our PDF observations. In the case of the SAXS

study [90], the disappearance of the clusters suggested that clusters either act as seeds to the crystalline particles, or dissolve and redeposit onto larger particles as in Ostwald ripening. In the present study, however, we do not observe a change in this component with time, likely a factor of the different synthesis or experimental conditions. Interestingly, differences in the SROC are observed in different measurements, even at similar reaction conditions. However, the differences are not necessarily monotonic with any of the primary synthetic variables: time, flow rate, ratio, weight percent, so it is unclear whether these differences are a result of different conditions, extent of reaction, or simply random. It is possible that a future control for solution mixing in our apparatus may result in better consistency.

The atomic structure of the SROC was analyzed to see if there was any structural pre-organization related to ZIF-8. There are no long wavelength oscillations present, so any significant porous nature to this component can be ruled out. Attenuation of the signal to zero allows us to estimate a finite structural coherence of the intermediate of ~1.5-2.0 nm, in agreement with Cravillon *et al.* [90]. Without the constraint of framework connectivity, 2-MeIm groups connected over several SBU linkages will have rotational degrees of freedom, which we hypothesize could result in weak structural correlation between the 2-MeIm groups and therefore little contribution to the PDF signal at higher distances. The cluster signal should then be dominated by Zn-Zn pairs. The extracted intermediate PDF signal is compared to a Zn-Zn partial PDF, simulated from the ZIF-8 structure in Figure 9.11. This simple model suggests that the approx. 2 nm diameter SROC is actually a disordered seed of connected SBU's where the connections are disordered and possibly confused (have connection errors) that do not allow them to become crystalline and long-range ordered. The slight differences in the SROCs observed across different experiments then appear to be higher or

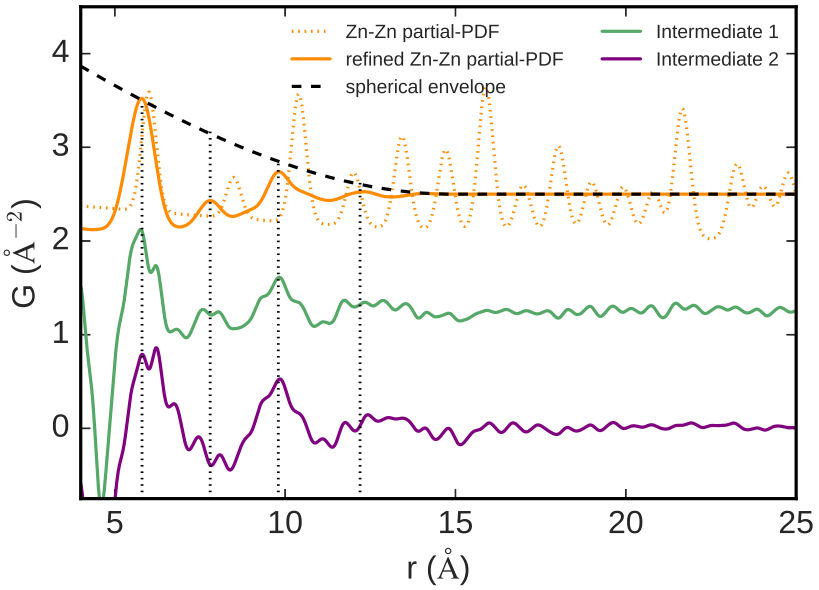

Figure 9.11: Examples of the different amorphous intermediate SROCs measured under similar reaction conditions (1:2 Zn:2-MeIm) are shown in green and purple, extracted from the measured data by fitting and subtracting the crystalline signal at high-r. The simulated Zn-Zn partial PDF from the ZIF-8 structure is given above for reference, and the partial PDF after fitting to intermediate 1 is shown. The black dashed line represents the spherical envelope applied to adjust the partial PDF for finite structural coherence of approximately ~15 Å. Additional dotted lines are given as reference markers for the approximate broad peak positions observed in the SROC and in the model.

lower degrees of order in the intermediate, with a limit approaching highest similarity to the Zn-Zn partial PDF of ZIF-8 crystal structure. This suggests, then, that the SROC does show some possible pre-organization resembling the final structure, and may contribute to framework development.

9.4 Conclusions

In conclusion, we have shown that, despite nearly instantaneous formation of ZIF-8 nanocrystals, stable clusters Zn(2-MeIm)$_4$ form in solution as the basic building unit and persist over longer time scales during the reaction, up to at least several hours as measured

in our experiments. We also observe the formation of higher order clusters Zn_x(2-MeIm)$_y$ and an amorphous intermediate with a structural coherence of approximately 2 nm in diameter, which also persists in solution. The intermediate phase appears to correlate with the Zn-Zn partial structure of ZIF-8, indicating that the organization of the intermediate may be related to the final ZIF-8 product, but contains considerable disorder and may be structurally confused with incorrect connectivity, preventing long-range crystalline order. Further experiments and modeling are needed to better understand the interplay of the various structural components, though in general, we expect application of *in situ* PDF for studying the initial stages of MOF nucleation opens up a new powerful approach to elucidate the mechanism of formation of hybrid materials of diverse architecture and synthesis conditions.

Chapter 10

Concluding thoughts

This thesis has presented the investigations of atomic structure on a variety of organic, soft, and nanoporous materials. These studies have been tied together primarily by the use of the PDF technique, and determining in which areas and to what extent it can be incorporated to provide useful, complimentary, or necessary information. Use of the PDF method over the past couple of decades has been primarily focused on studying inorganic materials. While there are a handful of studies which have looked at organic and nanoporous materials, I feel they are still underrepresented, and that the adoption of this technique by these communities has not been proportional to the relative simplification of the experimental and data analysis tools available.

Major hurdles in the technological application of the materials presented center around the ability to detect small quantities of phases or components in materials, and track how they change under various synthetic or post-process based conditions. To rationally design successful pharmaceutical solid dosage forms, a more intimate understanding of how atomic structure and phase composition effects the function and stability of the formulations. The PDF technique is highly sensitive to both of these aspects, and I have shown how it can

dramatically improve, by nearly an order of magnitude, upon the currently accepted detection limits for active pharmaceutical ingredients in the final product form. I further showed that this analysis can be applied to quantifying ordered and disordered phases in both sugar-based excipients and in thermoplastic polymers, and that the phase fraction could be tracked to study the kinetics of differently processed samples. I think that the true advantage in these cases is that the kinetics can be tracked even prior to the formation of any significant crystalline phases, and that short-range-ordered or nanocrystalline phases can be directly identified. Absent any predetermined crystallographic structure model, these nanocrystalline structures can even be determined. There are many powerful DFT and MD codes for searching the energy landscape and finding theoretically possible forms of molecular polymorphs. The PDF was significantly advantageous for fingerprinting and validating both MD and crystallographic models for the nanocrystalline hard segments in thermoplastic polyurethanes, and I believe this simple combination of techniques can be widely effective in addressing similar problems.

The area of nano- or microporous materials faces similar issues. As I previously noted, it is often the case that amorphous MOFs will be put aside in preference toward crystalline ones, however it is not always the case that they do not possess desirable properties. In the case of Unconventional MOFs, there is still significant porosity which can selectively incorporate species making them valuable ion exchange materials. But again, there must be robust methods for determining the structure of these nanocrystalline materials, and I have shown that the PDF can provide structural information on all levels of guest structure, guest-host interaction, domain or layer structures, and even weak interactions between turbostratically stacked layers.

Finally, there is much work to be done in determining the mechanisms of nucleation and growth in regards to both pharmaceutical stability and toward understanding the formation of MOFs. we have shown that the adoption of experimental methods from the inorganic nanoparticle synthesis community can already provide valuable information about the initial secondary building unit species which form during the synthesis of ZIF-8, and that this is highly complimentary to other available techniques. I think that much more work is needed in this area, in particular to design reactors which are better tailored to the reactants, their kinetics, and the data collection demands for these *weakly scattering* systems. Overall, I hope that I have provided a set of rational approaches to extracting useful structural information in organic and nanoporous systems, and that these can provide encouragement to those synthesizing these materials and trying to understand how they work. In the meantime, I am grateful for the opportunities presented thus far, and look forward to continuing on with this endeavor.

Bibliography

1. United Nations. International years, web page URL: http://www.un.org/en/sections/observances/international-years/index.html.

2. IUCr. Nobel prize winners associated with crystallography, web page URL: https://www.iucr.org/people/nobel-prize.

3. Nobelprize.org. Nobel prize in chemistry 2016, web page URL: https://www.nobelprize.org/nobel_prizes/chemistry/laureates/2016/.

4. Egami, T. & Billinge, S. J. L. *Underneath the Bragg peaks: structural analysis of complex materials* 2nd (Elsevier, Amsterdam, 2012).

5. Young, C. A. & Goodwin, A. L. Applications of pair distribution function methods to contemporary problems in materials chemistry. *J. Mater. Chem.* **21**, 6464–6476 (2011).

6. Kitaigorodsky, A. I. *Molecular crystals and molecules* (Academic Press, New York, 1973).

7. Proffen, T. *et al.* Atomic pair distribution function analysis of materials containing crystalline and amorphous phases. *Z. Kristallogr.* **220**, 1002–1008 (2005).

8. Peterson, J. *et al.* Quantifying amorphous and crystalline phase content with the atomic pair distribution function. *J. Appl. Crystallogr.* **46**, 332–336 (2013).

9. Shah, B., Kakumanu, V. K. & Bansal, A. K. Analytical techniques for quantification of amorphous/crystalline phases in pharmaceutical solids. *J. Pharm. Sci.* **95**, 1641–1665 (2006).

10. World Health Organization. WHO model list of essential medicines, 2017, web page URL: http://www.who.int/medicines/publications/essentialmedicines/20th_EML2017.pdf.

11. Biopharmaceutical research industry profile, 2016, web page URL: http://phrma-docs.phrma.org/sites/default/files/pdf/biopharmaceutical-industry-profile.pdf.

12. Thayer, A. M. Finding solutions. *Chemical & Engineering News* **88**, 13–18 (2010).

13. Savjani, K. T., Gajjar, A. K. & Savjani, J. K. Drug solubility: importance and enhancement techniques. *ISRN Pharm.* **2012**, 1–10 (2012).

14. Billinge, S. J. L. *et al.* Characterisation of amorphous and nanocrystalline molecular materials by total scattering. *CrystEngComm* **12**, 1366–1368 (2010).

15. Sheth, A. R., Bates, S., Muller, F. X. & Grant, D. J. W. Polymorphism in piroxicam. *Cryst. Growth Des.* **4**, 1091–1098 (2004).

16. Bates, S. *et al.* Assessment of defects and amorphous structure produced in raffinose pentahydrate upon dehydration. *J. Pharm. Sci.* **96**, 1418–1433 (2007).

17. Moore, M. D., Steinbach, A. M., Buckner, I. S. & Wildfong, P. L. A structural investigation into the compaction behavior of pharmaceutical composites using powder x-ray diffraction and total scattering analysis. *Pharmaceut. Res.* **26**, 2429–2437 (2009).

18. Boetker, J. P., Koradia, V., Rades, T., Rantanen, J. & Savolainen, M. Atomic pairwise distribution function analysis of the amorphous phase prepared by different manufacturing routes. *Pharmaceutics* **4**, 93–103 (2012).

19. Dykhne, T., Taylor, R., Florence, A. & Billinge, S. J. L. Data requirements for the reliable use of atomic pair distribution functions in amorphous pharmaceutical fingerprinting. *Pharmaceut. Res.* **28**, 1041–1048 (2011).

20. Gohel, M. C. & Jogani, P. D. A review of co-processed directly compressible excipients. *J. Pharm. Pharm. Sci.* **8**, 76–93 (2005).

21. Davis, T., Johnson, M. & Billinge, S. J. L. Towards phase quantification at the nanoscale using the total scattering pair distribution function (TSPDF) method: recrystallization of cryomilled sulfamerazine. *Cryst. Growth Des.* **13**, 4239–4244 (2013).

22. Lehto, V. *et al.* The comparison of seven different methods to quantify the amorphous content of spray dried lactose. *Powder Tech.* **167**, 85–93 (2006).

23. Newman, A. *et al.* Characterization of amorphous API: polymer mixtures using x-ray powder diffraction. *J. Pharm. Sci.* **97**, 4840–4856 (2008).

24. Ivanisevic, I., Bates, S. & Chen, P. Novel methods for the assessment of miscibility of amorphous drug-polymer dispersions. *J. Pharm. Sci.* **98**, 3373–3386 (2009).

25. Nollenberger, K. *et al.* Pair distribution function X-ray analysis explains dissolution characteristics of felodipine melt extrusion products. *J. Pharm. Sci.* **98**, 1476–1486 (2009).

26. Rumondor, A. C. F., Ivanisevic, I., Bates, S., Alonzo, D. E. & Taylor, L. S. Evaluation of drug-polymer miscibility in amorphous solid dispersion systems. *Pharmaceut. Res.* **26**, 2523–2534 (2009).

27. Engers, D. *et al.* A Solid-State Approach to Enable Early Development Compounds: Selection and Animal Bioavailability Studies of an Itraconazole Amorphous Solid Dispersion. *J. Pharm. Sci.* **99**, 3901–3922 (2010).

28. Padilla, A. M. *et al.* The study of phase separation in amorphous freeze-dried systems. Part I: raman mapping and computational analysis of XRPD data in model polymer systems. *J. Pharm. Sci.* **100**, 206–222 (2010).

29. Moore, M. D., Shi, Z. & Wildfong, P. L. D. Structural interpretation in composite systems using powder x-ray diffraction: applications of error propagation to the pair distribution function. *Pharmaceut. Res.* **27**, 2624–2632 (2010).

30. Moore, M. D. & Wildfong, P. L. D. Informatics calibration of a molecular descriptors database to predict solid dispersion potential of small molecule organic solids. *Int. J. Pharm.* **418**, 217–226 (2011).

31. Chieng, N. *et al.* Detecting phase separation of freeze-dried binary amorphous systems using pair-wise distribution function and multivariate data analysis. *Int. J. Pharm.* **454**, 167–173 (2013).

32. Benmore, C. J. in *Discovering and developing molecules with optimal drug-like properties* (eds Templeton, A. C., Byrn, S. R., Haskell, R. J. & Prisinzano, T. E.) 15, 263–283 (Springer New York, 2015).

33. Chen, S., Sheikh, A. Y. & Ho, R. Evaluation of effects of pharmaceutical processing on structural disorders of active pharmaceutical ingredient crystals using nanoindentation and high-resolution total scattering pair distribution function analysis. *J. Pharm. Sci.* **103**, 3879–3890 (2014).

34. Atassi, F., Mao, C., Masdeh, A. S. & Byrn, S. R. Solid-state characterization of amorphous and mesomorphous calcium ketoprofen. *J. Pharm. Sci.* **99**, 3684–3697 (2009).

35. Bordet, P. *et al.* Solid state amorphization of β-trehalose: a structural investigation using synchrotron powder diffraction and PDF analysis. *Cryst. Growth Des.* **16**, 4547–4558 (2016).

36. Thi, Y. N., Rademannb, K. & Emmerling, F. Direct evidence of polyamorphism in paracetamol. *CrystEngComm* **17**, 9029–9036 (2015).

37. American Chemistry Council. Polyurethane applications, web page URL: http://polyurethane.americanchemistry.com/Introduction-to-Polyurethanes/Applications.

38. Bonart, R., Morbitzer, L. & Hentze, G. X-ray investigations concerning the physical structure of cross-linking in urethane elastomers. II. Butanediol as chain extender. *J. Macromol. Sci. Phys.* **3**, 337–356 (June 1969).

39. Bonart, R. X-ray investigations concerning the physical structure of cross-linking in segmented urethane elastomers. *J. Macromol. Sci. Phys.* **2**, 115–138 (Mar. 1968).

40. Noriega, R. *et al.* A general relationship between disorder, aggregation and charge transport in conjugated polymers. *Nature Mater.* **12**, 1038–1044 (2013).

41. Armes, S. P., Aldissi, M., Hawley, M., Beery, J. G. & Gottesfeld, S. Morphology and structure of conducting polymers. *Langmuir* **7**, 1447–1452 (1991).

42. Boeva, Z. A. & Sergeyev, V. G. Polyaniline: synthesis, properties, and application. *Polym. Sci. Ser. C* **56**, 144–153 (2014).

43. Anderson, M. R., Mattes, B. R., Reiss, H. & Kaner, R. B. Conjugated polymer films for gas separations. *Science* **252**, 1412–1415 (1991).

44. Macdiarmid, A. G., Chiang, J. C., Richter, A. F. & Epstein, A. J. Polyaniline: a new concept in conducting polymers. *Synthetic Metals* **18**, 285–290 (1987).

45. Annis, B. K., Narten, A. H., Macdiarmid, A. G. & Richter, A. F. A covalent bond to bromine in HBr-treated polyaniline from X-ray diffraction. *Synthetic Metals* **22**, 191–199 (1988).

46. Winokur, M. J. & Mattes, B. R. Differential anomalous scattering studies of amorphous HBr-doped polyaniline. *Synthetic Metals* **84**, 725–728 (1997).

47. Laridjani, M. *et al.* Amorphography - the relationship between amorphous and crystalline order. 1. The structural origin of memory effects in polyaniline. *Macromolecules* **25**, 4106–4113 (1992).

48. Maron, J., Winokur, M. J. & Mattes, B. R. Processing-induced changes in the local structure of amorphous polyaniline by radial distribution function analysis of X-ray scattering data. *Macromolecules* **28**, 4475–4486 (1995).

49. Winokur, M. J. & Mattes, B. R. Determination of the local molecular structure in amorphous polyaniline. *Phys. Rev. B* **54**, 12637–12640 (1996).

50. Murugavel, R., Walawalkar, M. G., Dan, M., Roesky, H. W. & Rao, C. N. R. Transformations of molecules and secondary building units to materials: a bottom-up approach. *Acc. of Chem. Res.* **37**, 763–774 (2004).

51. J. Tranchemontagne, D., L. Mendoza-Cortés, J., O'Keeffe, M. & M. Yaghi, O. Secondary building units, nets and bonding in the chemistry of metal–organic frameworks. *Chem. Soc. Rev.* **38**, 1257–1283 (2009).

52. Martínez-Inesta, M. M. & Lobo, R. F. Investigation of the negative thermal expansion mechanism of zeolite chabazite using the pair distribution function method. *J. Phys. Chem. B* **109**, 9389–9396 (2005).

53. Chapman, K. W., Chupas, P. J. & Kepert, C. J. Selective recovery of dynamic guest structure, in a nanoporous Prussian Blue through in situ X-ray diffraction: A differential pair distribution function analysis. *J. Am. Chem. Soc.* **127**, 11232–11233 (2005).

54. Baerlocher, C. & McCusker, L. Database of zeolite structures. http://www.iza-structure.org/databases/ (2017).

55. Higgins, J. B. *et al.* The framework topology of zeolite beta. *Zeolites* **8**, 446–452 (1988).

56. Martínez-Inesta, M. M., Peral, I., Proffen, T. & Lobo, R. F. A pair distribution function analysis of zeolite beta. *Micropor. Mesopor. Mat.* **77**, 55–66 (2005).

57. E. White, C., L. Provis, J., Proffen, T., P. Riley, D. & van Deventer, J. S. J. Combining density functional theory (DFT) and pair distribution function (PDF) analysis to solve the structure of metastable materials: the case of metakaolin. *Phys. Chem. Chem. Phys.* **12**, 3239–3245 (2010).

58. Smeets, S. & McCusker, L. B. in *Structure and bonding* 1–31 (Springer Berlin Heidelberg, Berlin, Heidelberg, 2017).

59. Petkov, V., Billinge, S. J. L., Vogt, T., Ichimura, A. S. & Dye, J. L. Structure of intercalated Cs in zeolite ITQ-4: an array of metal ions and electrons confined in a pseudo-1D nanoporous host. *Phys. Rev. Lett.* **89**, 075502 (2002).

60. Shatnawi, M. *et al.* Structures of alkali metals in silica gel nanopores: new materials for chemical reductions and hydrogen production. *J. Am. Chem. Soc.* **129**, 1386–1392 (2007).

61. Park, K. S. *et al.* Exceptional chemical and thermal stability of zeolitic imidazolate frameworks. *Proc. Natl. Acad. Sci. USA* **103**, 10186–10191 (2006).

62. Frameworks for commercial success. *Nat. Chem.* **8**, 987 (2016).

63. Hughes, J. T. & Navrotsky, A. MOF-5: enthalpy of formation and energy landscape of porous materials. *J. Am. Chem. Soc.* **133**, 9184–9187 (2011).

64. Howarth, A. J. *et al.* Chemical, thermal and mechanical stabilities of metal–organic frameworks. *Nat. Rev. Mater.* **1**, 1–15 (2016).

65. Goodwin, A. L. *et al.* Nanoporous structure and medium-range order in synthetic amorphous calcium carbonate. *Chem. Mater.* **22**, 3197–3205 (2010).

66. Collings, I. E., Tucker, M. G., Keen, D. A. & Goodwin, A. L. Static disorder and local structure in zinc(II) isonicotinate, a quartzlike metal–organic framework. *Z. Kristallogr.* **227**, 313–320 (2012).

67. Funnell, N. P. *et al.* Structural characterisation of a layered double hydroxide nanosheet. *Nanoscale* **6**, 8032–8036 (2014).

68. Mohideen, M. I., Allan, P. K., Chapman, K. W., Hriljac, J. A. & Morris, R. E. Ultrasound-driven preparation and pair distribution function-assisted structure solution of a copper-based layered coordination polymer. *Dalton T.* **43**, 10438–10442 (June 2014).

69. Katsenis, A. D. *et al.* In situ X-ray diffraction monitoring of a mechanochemical reaction reveals a unique topology metal-organic framework. *Nat. Commun.* **6**, 1–8 (2015).

70. Bennett, T. D. *et al.* Structure and properties of an amorphous metal-organic framework. *Phys. Rev. Lett.* **104**, 115503 (2010).

71. Cao, S., D. Bennett, T., A. Keen, D., L. Goodwin, A. & K. Cheetham, A. Amorphization of the prototypical zeolitic imidazolate framework ZIF-8 by ball-milling. *Chem. Commun.* **48**, 7805–7807 (2012).

72. F. Baxter, E. *et al.* A comparison of the amorphization of zeolitic imidazolate frameworks (ZIFs) and aluminosilicate zeolites by ball-milling. *Dalton T.* **45**, 4258–4268 (2016).

73. Mulfort, K., Farha, O., Malliakas, C., Kanatzidis, M. & Hupp, J. An interpenetrated framework material with hysteretic CO2 uptake. *Chem.-Eur. J.* **16**, 276–281 (Jan. 2010).

74. K. Allan, P. *et al.* Pair distribution function-derived mechanism of a single-crystal to disordered to single-crystal transformation in a hemilabile metal–organic framework. *Chem. Sci.* **3**, 2559–2564 (2012).

75. Platero-Prats, A. E. *et al.* Structural transitions of the metal-oxide nodes within metal-organic frameworks: on the local structures of NU-1000 and UiO-66. *J. Am. Chem. Soc.* **138**, 4178–4185 (2016).

76. Eckert, J., Nicol, J. M., Howard, J. & Trouw, F. R. Adsorption of hydrogen in Ca-exchanged Na-A zeolites probed by inelastic neutron scattering spectroscopy. *J. Phys. Chem. C* **100**, 10646–10651 (1996).

77. Rosi, N. L. *et al.* Hydrogen storage in microporous metal-organic frameworks. *Science* **300**, 1127–1129 (2003).

78. Rowsell, J. L. C., Spencer, E. C., Eckert, J., Howard, J. A. K. & Yaghi, O. M. Gas adsorption sites in a large-pore metal-organic framework. *Science* **309**, 1350–1354 (2005).

79. Chapman, K. W., Chupas, P. J., Maxey, E. R. & Richardson, J. W. Direct observation of adsorbed H_2-framework interactions in the Prussian Blue analogue Mn-3(II)[Co-III$(CN)_6]_2$: The relative importance of accessible coordination sites and van der Waals interactions. *Chem. Commun.* 4013–4015 (2006).

80. Sava, D. F. *et al.* Capture of volatile iodine, a gaseous fission product, by zeolitic imidazolate framework-8. *J. Am. Chem. Soc.* **133**, 12398–12401 (2011).

81. Abney, C. W., Gilhula, J. C., Lu, K. & Lin, W. Metal-organic framework templated inorganic sorbents for rapid and efficient extraction of heavy metals. *Adv. Mater.* **26**, 7993–7997 (2014).

82. Clearfield, A. Unconventional metal organic frameworks: porous cross-linked phosphonates. *Dalton Trans.* 6089–6103 (2008).

83. De Moor, P.-P. E. A., Beelen, T. P. M. & van Santen, R. A. In situ observation of nucleation and crystal growth in zeolite synthesis. a small-angle X-ray scattering investigation on Si-TPA-MFI. *J. Phys. Chem. B* **103**, 1639–1650 (1999).

84. Pelster, S. A., Kalamajka, R., Schrader, W. & Schuth, F. Monitoring the nucleation of zeolites by mass spectrometry. *Angew. Chem.* **46**, 2299–2302 (2007).

85. Wakihara, T. *et al.* A new approach to the determination of atomic-architecture of amorphous zeolite precursors by high-energy X-ray diffraction technique. *Phys. Chem. Chem. Phys.* **8**, 224–227 (2006).

86. Sankar, G., Thomas, J. M. & Catlow, C. R. A. Combining X-ray absorption with X-ray diffraction for the structural elucidation of catalysts. *Top. Catal.* **10**, 255–264 (2000).

87. Cundy, C. S. & Cox, P. A. The hydrothermal synthesis of zeolites: precursors, intermediates and reaction mechanism. *Micropor. Mesopor. Mat.* **82**, 1–78 (2005).

88. Surble, S., Millange, F., Serre, C., Férey, G. & I. Walton, R. An EXAFS study of the formation of a nanoporous metal–organic framework: evidence for the retention of secondary building units during synthesis. *Chem. Commun.* 1518–1520 (2006).

89. Rood, J. A., Boggess, W. C., Noll, B. C. & Henderson, K. W. Assembly of a homochiral, body-centered cubic network composed of vertex-shared Mg12 cages: use of electrospray ionization mass spectrometry to monitor metal carboxylate nucleation. *J. Am. Chem. Soc.* **129**, 13675–13682 (2007).

90. Cravillon, J. *et al.* Fast nucleation and growth of ZIF-8 nanocrystals monitored by time-resolved in situ small-angle and wide-angle X-ray scattering. *Angew. Chem.* **123**, 8217–8221 (2011).

91. Shoaee, M., Anderson, M. W. & Attfield, M. P. Crystal growth of the nanoporous metal–organic framework HKUST-1 revealed by in situ atomic force microscopy. *Angew. Chem.* **120**, 8653–8656 (2008).

92. Venna, S. R., Jasinski, J. B. & Carreon, M. A. Structural evolution of zeolitic imidazolate framework-8. *J. Am. Chem. Soc.* **132**, 18030–18033 (2010).

93. Mintova, S., Olson, N. H. & Bein, T. Electron microscopy reveals the nucleation mechanism of zeolite Y from precursor colloids. *Angew. Chem.* **38**, 3201–3204 (1999).

94. Patterson, J. P. *et al.* Observing the growth of metal–organic frameworks by in situ liquid cell transmission electron microscopy. *J. Am. Chem. Soc.* **137**, 7322–7328 (2015).

95. Bøjesen, E. D. & Iversen, B. B. The chemistry of nucleation. *CrystEngComm* **18**, 8332–8353 (2016).

96. Dippel, A.-C. *et al.* Towards atomistic understanding of polymorphism in solvothermal synthesis of ZrO_2 nanoparticles. *Acta Crystallogr. A* **72**, 645–650 (2016).

97. Jensen, K. M. O. *et al.* Mechanisms for iron oxide formation under hydrothermal conditions: an in situ total scattering study. *ACS Nano* **8**, 10704–10714 (2014).

98. Jensen, K. M. Ø. *et al.* Revealing the mechanisms behind SnO_2 nanoparticle formation and growth during hydrothermal synthesis: an in situ total scattering study. *J. Am. Chem. Soc.* **134**, 6785 –6792 (2012).

99. Saha, D. *et al.* In situ total X-ray scattering study of WO_3 nanoparticle formation under hydrothermal conditions. *Angew. Chem. Int. Ed.* **53**, 3667–3670 (2014).

100. Tyrsted, C. *et al.* Understanding the formation and evolution of ceria nanoparticles under hydrothermal conditions. *Angew. Chem. Int. Edit.* **51**, 9030–9033 (2012).

101. Tyrsted, C. *et al.* Evolution of atomic structure during nanoparticle synthesis. *IUCrJ.* **1**, 165–171 (2014).

102. Cullity, B. D. & Stock, S. R. *Elements of X-Ray Diffraction* 3rd (Prentice Hall, 2001).

103. Guinier, A. *X-ray Diffraction in Crystals, Imperfect Crystals, and Amorphous Bodies.* (W.H. Freeman, San Francisco, 1963).

104. Warren, B. E. *X-ray Diffraction* (Dover, New York, 1990).

105. Farrow, C. L. & Billinge, S. J. L. Relationship between the atomic pair distribution function and small angle scattering: implications for modeling of nanoparticles. *Acta Crystallogr. A* **65**, 232–239 (2009).

106. Billinge, S. J. L. & Farrow, C. L. Towards a robust *ad-hoc* data correction approach that yields reliable atomic pair distribution functions from powder diffraction data. *J. Phys: Condens. Mat.* **25**, 454202 (2013).

107. Juhás, P., Davis, T., Farrow, C. L. & Billinge, S. J. L. PDFgetX3: A rapid and highly automatable program for processing powder diffraction data into total scattering pair distribution functions. *J. Appl. Crystallogr.* **46**, 560–566 (2013).

108. Farrow, C. L. *et al.* PDFfit2 and PDFgui: Computer programs for studying nanostructure in crystals. *J. Phys: Condens. Mat.* **19**, 335219 (2007).

109. Juhás, P., Farrow, C. L., Yang, X., Knox, K. R. & Billinge, S. J. L. Complex Modeling: a strategy and software program for combining multiple information sources to solve ill-posed structure and nanostructure inverse problems. *Acta Crystallogr. A* **71**, 562–568 (2015).

110. Rietveld, H. M. A profile refinement method for nuclear and magnetic structures. *J. Appl. Crystallogr.* **2**, 65–71 (1969).

111. Jeong, I., Proffen, T., Mohiuddin-Jacobs, F. & Billinge, S. J. L. Measuring correlated atomic motion using X-ray diffraction. *J. Phys. Chem. A* **103**, 921–924 (1999).

112. Rademacher, N., Daemen, L. L., Chronister, E. L. & Proffen, T. Pair distribution function analysis of molecular compounds: significance and modeling approach discussed using the example of p-terphenyl. *J. Appl. Crystallogr.* **45**, 482–488 (2012).

113. Prill, D., Juhás, P., Schmidt, M. U. & Billinge, S. J. L. Modeling pair distribution functions (PDF) of organic compounds: describing both intra- and intermolecular correlation functions in calculated PDFs. *J. Appl. Crystallogr.* **48**, 171–178 (2015).

114. Kodama, K., Iikubo, S., Taguchi, T. & Shamoto, S. Finite size effects of nanoparticles on the atomic pair distribution functions. *Acta Crystallogr. A* **62**, 444–453 (2006).

115. Guinier, A., Fournet, G., Walker, C. & Yudowitch, K. *Small-angle scattering of x-rays* (John Wiley & Sons, Inc., New York, 1955).

116. Myers, J. L. & Well, A. D. *Research Design and Statistical Analysis* 3rd ed. (Hillsdale: Lawrence Erlbaum Associates, 2010).

117. Chupas, P. J. *et al.* Rapid acquisition pair distribution function analysis (RA-PDF). *J. Appl. Crystallogr.* **36**, 1342–1347 (2003).

118. Hammersley, A. P., Svenson, S. O., Hanfland, M. & Hauserman, D. Two-dimensional detector software: from real detector to idealised image or two-theta scan. *High Pressure Res.* **14**, 235–248 (1996).

119. Wright, C. J. & Zhou, X.-D. Computer-assisted area detector masking. *J. Synchrotron Radiat.* **24**, 506–508 (2017).

120. Skinner, L. B., Benmore, C. J. & Parise, J. B. Nuclear instruments and methods in physics research section A: accelerators, spectrometers, detectors and associated equipment. *Nucl. Instrum. Meth. A* **662**, 61–70 (2012).

121. Skinner, L. B., Benmore, C. J. & Parise, J. B. Comment on 'Molecular arrangement in water: random but not quite'. *J. Phys.: Condens. Mat.* **24**, 155102 (2012).

122. Qiu, X., Thompson, J. W. & Billinge, S. J. L. PDFgetX2: a GUI driven program to obtain the pair distribution function from X-ray powder diffraction data. *J. Appl. Crystallogr.* **37**, 678 (2004).

123. Terban, M. W., Johnson, M., DiMichiel, M. & Billinge, S. J. L. Detection and characterization of nanoparticles in suspension at low concentrations using the x-ray total scattering pair distribution function technique. *Nanoscale* **7**, 5480–5487 (2015).

124. ICH. Validation of analytical procedures: Text and methodology Q2(R1). 2005.

125. Newton, M. A., Chapman, K. W., Thompsett, D. & Chupas, P. J. Chasing Changing Nanoparticles with Time-Resolved Pair Distribution Function Methods. *J. Am. Chem. Soc.* **134**, 5036–5039 (2012).

126. Gagin, A., Allen, A. J. & Levin, I. Combined fitting of small- and wide-angle X-ray total scattering data from nanoparticles: benefits and issues. *J. Appl. Crystallogr.* **47**, 619–629 (2014).

127. Granlund, L., Billinge, S. J. L. & Duxbury, P. M. Algorithm for systematic peak extraction from atomic pair distribution functions. *Acta Crystallogr. A* **71**, 392–409 (2015).

128. Terban, M. W., Cheung, E. Y., Krolikowski, P. & Billinge, S. J. L. Recrystallization, phase composition, and local structure of amorphous lactose from the total scattering pair distribution function. *Cryst. Growth Des.* **16**, 210–220 (2015).

129. Fox, P. F. & McSweeney, P. L. H. *Dairy chemistry and biochemistry* ISBN: 0-412-72000-0 (Kluwer Academic/Plenum Publishers, New York, 1998).

130. Angberg, M. Lactose and thermal-analysis with special emphasis on microcalorimetry. *Thermochim. Acta* **248**, 161–167 (1995).

131. Schmitt, E. A., Law, D. & Zhang, G. G. Z. Nucleation and crystallization kinetics of hydrated amorphous lactose above the glass transition temperature. *J. Pharm. Sci.* **88**, 291–296 (1999).

132. Roos, Y. & Karel, M. Crystallization of amorphous lactose. *J. Food Sci.* **57**, 775–777 (1992).

133. Jouppila, K., Kansikas, J. & Roos, Y. H. Crystallization and X-ray diffraction of crystals formed in water-plasticized amorphous lactose. *Biotechnol. Progr.* **14**, 347–350 (1998).

134. Newell, H. E., Buckton, G., Butler, D. A., Thielmann, F. & Williams, D. R. The use of inverse phase gas chromatography to study the change of surface energy of amorphous lactose as a function of relative humidity and the processes of collapse and crystallisation. *Int. J. Pharm.* **217**, 45–56 (2001).

135. Buckton, G. & Darcy, P. Water mobility in amorphous lactose below and close to the glass transition temperature. *Int. J. Pharm.* **136**, 141–146 (1996).

136. Kirk, J. H., Dann, S. E. & Blatchford, C. G. Lactose: A definitive guide to polymorph determination. *Int. J. Pharm.* **334**, 103–114 (2007).

137. Fries, D. C., Rao, S. T. & Sundaralingam, M. Structural chemistry of carbohydrates. III. crystal and molecular structure of 4-O-β-D-galactopyranosyl-α-D-glucopyranose monohydrate (α-lactose monohydrate). *Acta Crystallogr. B* **27**, 994–1005 (1971).

138. Platteau, C., Lefebvre, J., Affouard, F. & Derollez, P. Ab initio structure determination of the hygroscopic anhydrous form of α-lactose by powder X-ray diffraction. *Acta Crystallogr. B* **60**, 453–460 (2004).

139. Platteau, C. *et al.* Structure determination of the stable anhydrous phase of α-lactose from X-ray powder diffraction. *Acta Crystallogr. B* **61**, 185–191 (2005).

140. Garnier, S., Petit, S. & Coquerel, G. Dehydration mechanism and crystallisation behaviour of lactose. *J. Thermal Anal. Calorimetry* **68**, 489–502 (2002).

141. Olano, A., Bernhard, R. A. & Nickerson, T. A. Alteration in the ratio of α– to β–lactose co-crystallized from organic solvents. *J. Food Sci.* **42**, 1066–1068 (1977).

142. Drapier-Beche, N., Fanni, J. & Parmentier, M. Kinetics of the synthesis of lactose molecular compounds. *J. Dairy Sci.* **81**, 2826–2832 (1998).

143. Lefebvre, J. *et al.* Structure determination of the 1/1 α/β mixed lactose by X-ray powder diffraction. *Cryst. Growth Des.* **61**, 455–463 (2005).

144. Willart, J. F. *et al.* Athermal character of the solid state amorphization of lactose induced by ball milling. *Solid State Commun.* **132**, 693–696 (2004).

145. Islam, M. I. U. & Langrish, T. A. G. An investigation into lactose crystallization under high temperature conditions during spray drying. *Food Res. Int.* **43**, 46–56 (2010).

146. Burnett, D. J., Thielmann, F. & Booth, J. Determining the critical relative humidity for moisture-induced phase transitions. *Int. J. Pharm.* **287**, 123–133 (2004).

147. Vollenbroek, J., Hebbink, G. A., Ziffels, S. & Steckel, H. Determination of low levels of amorphous content in inhalation grade lactose by moisture sorption isotherms. *Int. J. Pharm.* **395**, 62–70 (2010).

148. Gustafssona, C., Lennholmb, H., Iversenc, T. & Nystroma, C. Comparison of solid-state NMR and isothermal microcalorimetry in the assessment of the amorphous component of lactose. *Int. J. Pharm.* **174**, 243–252 (1998).

149. Lubach, J. W., Xu, D., Segmuller, B. E. & Munson, E. J. Investigation of the effects of pharmaceutical processing upon solid-state NMR relaxation times and implications to solid-state formulation stability. *Int. J. Pharm.* **96**, 777–787 (2007).

150. Listiohadi, Y. D., Hourigan, J. A., Sleigh, R. W. & Steele, R. J. Properties of lactose and its caking behaviour. *Aust. J. Dairy Tech.* **60**, 33–52 (2005).

151. Jawad, R. *et al.* The measurement of the β/α anomer composition within amorphous lactose prepared by spray and freeze drying using a simple ^{1}H-NMR method. *Pharmaceut. Res.* **29**, 511–524 (2012).

152. Guiry, K. P., Coles, S. J., Moynihan, H. A. & Lawrence, S. E. Effect of 1-deoxy-D-lactose upon the crystallization of D-lactose. *Cryst. Growth Des.* **8**, 3927–3934 (2008).

153. Toby, B. H. & Von Dreele, R. B. GSAS-II: the genesis of a modern open-source all purpose crystallography software package. *J. Appl. Crystallogr.* **46**, 544–549 (2013).

154. Hancock, B. C. & Zografi, G. The relationship between the glass transition temperature and water content of amorphous and partially amorphous pharmaceutical solids. *Pharmaceut. Res.* **11**, 471–477 (1994).

155. Walstra, P., Geurts, T. J., Noomen, A., Jellema, A. & van Boekel, M. A. J. S. *Dairy technology: principles of milk properties and processes* ISBN: 0-8247-0228-X (Marcel Dekker, New York, 1999).

156. Barham, A. S. & Hodnett, B. K. In situ X-ray diffraction study of the crystallization of spray-dried lactose. *Cryst. Growth Des.* **5**, 1965–1970 (2005).

157. Terban, M. W., Dabbous, R., Debellis, A. D., Pöselt, E. & Billinge, S. J. L. Structures of hard phases in thermoplastic polyurethanes. *Macromolecules* **49**, 7350–7358 (2016).

158. Blackwell, J. & Gardner, K. H. Structure of the hard segments in polyurethane elastomers. *Polymer* **20**, 13–17 (1979).

159. Blackwell, J. & Nagarajan, M. Conformational analysis of poly(MDI-butandiol) hard segment in polyurethane elastomers. *Polymer* **22**, 202–208 (1981).

160. Blackwell, J. & Lee, C. D. Hard-segment domain sizes in MDI/diol polyurethane elastomers. *J. Polym. Sci. Pol. Phys.* **21**, 2169–2180 (1983).

161. Briber, R. M. & Thomas, E. L. Investigation of two crystal forms in MDI/BDO-based polyurethanes. *J. Macromol. Sci. Phys.* **22**, 509–528 (1983).

162. Briber, R. M. & Thomas, E. L. The structure of MDI/BDO-Based polyurethanes: diffraction studies on model compounds and oriented thin films. *J. Polym. Sci. Pol. Phys.* **23**, 1915–1932 (1985).

163. Brunette, C. M., Hsu, S. L. & MacKnight, W. J. Hydrogen-bonding properties of hard-segment model compounds in polyurethane block copolymers. *Macromolecules* **15**, 71–77 (1982).

164. Zhang, C., Hu, J., Chen, S. & Ji, F. Theoretical study of hydrogen bonding interactions on MDI-based polyurethane. eng. *J. Mol. Model* **16**, 1391–1399 (2010).

165. Quay, J. R., Sun, Z., Blackwell, J., Briber, R. M. & Thomas, E. L. The hard segment unit cell for MDI-BDO-based polyurethane elastomers. *Polymer* **31**, 1003–1008 (1990).

166. Born, L., Crone, J., Hespe, H., Müller, E. H. & Wolf, K. H. On the structure of polyurethane hard segments based on MDI and butanediol-1,4: X-ray diffraction analysis of oriented elastomers and of single crystals of a model compound. *J. Polym. Sci. Pol. Phys.* **22**, 163–173 (1984).

167. Sun, Z. *X-ray analysis of structures of polyurethanes and copolyesters* Electronic Thesis (Case Western Reserve University, Cleveland, OH, 1990).

168. Billinge, S. J. L. & Levin, I. The problem with determining atomic structure at the nanoscale. *Science* **316**, 561–565 (2007).

169. Randall, D. & Lee, S. *The Polyurethanes Book* (Wiley, New York, 2003).

170. Wilson, R. B., Chen, Y. S., Paul, I. C. & Curtin, D. Y. Crystal structure and solid-state reactivity of 4,4'-methylenediphenyl isocyanate (MDI). *J. Am. Chem. Soc.* **105**, 1672–1674 (1983).

171. Cesari, M., Perego, G. & Mazzei, A. The crystal structure of polytetrahydrofuran. *Makromol. Chem.* **83**, 196–206 (1965).

172. Forcier, P. G. & Blackwell, J. The structure of bis(4-hydroxybutyl) 4,4'-methylenebis(phenylcarbamate): a model compound for diol-linked MDI units in polyurethane elastomers. *Acta Crystallogr. B* **37**, 286–289 (1981).

173. Gardner, K. H. & Blackwell, J. Structure of dimethyl 4,4'-methylenebis(phenylcarbamate): a model for MDI units in polyurethane hard segments. *Acta Crystallogr. B* **36**, 1972–1975 (1980).

174. Born, L., Hocker, J., Paulus, H. & Wolfel, E. The stable modification (modification-2) of (Methylene-di-4,1-phenylene)biscarbamic acid dimethylester C17H18N2O4. *Acta Crystallogr. C* **10**, 187–190 (1981).

175. Mayo, S. L., Olafson, B. D. & Goddard, W. A. DREIDING: a generic force field for molecular simulations. *J. Phys. Chem.* **94**, 8897–8909 (1990).

176. Rappe, A. K. & Goddard, W. A. Charge equilibration for molecular dynamics simulations. *J. Phys. Chem.* **95**, 3358–3363 (1991).

177. Koberstein, J. T. & Stein, R. S. Small-angle X-ray scattering studies of microdomain structure in segmented polyurethane elastomers. *J. Polym. Sci. Pol. Phys.* **21**, 1439–1472 (1983).

178. Leung, L. M. & Koberstein, J. T. Small-angle scattering analysis of hard-microdomain structure and microphase mixing in polyurethane elastomers. *J. Polym. Sci. Pol. Phys.* **23**, 1883–1913 (1985).

179. Szalewicz, K. Determination of structure and properties of molecular crystals from first principles. *Acc. of Chem. Res.* **47**, 3266–3274 (2014).

180. Li, C. & Strachan, A. Molecular Scale Simulations on Thermoset Polymers: A Review. *J. Polym. Sci. Pol. Phys.* **53**, 103–122 (2015).

181. Gamez, L., Terban, M. W., Billinge, S. J. L. & Martinez-Inesta, M. Modelling and validation of particle size distributions of supported nanoparticles using the pair distribution function technique. *J. Appl. Crystallogr.* **50**, 741–748 (2017).

182. Choi, M., Wu, Z. & Iglesia, E. Mercaptosilane-assisted synthesis of metal clusters within zeolites and catalytic consequences of encapsulation. *J. Am. Chem. Soc.* **132**, 9129–9137 (2010).

183. Farrow, C. L., Shi, C., Juhás, P., Peng, X. & Billinge, S. J. L. Robust structure and morphology parameters for CdS nanoparticles by combining small angle X-ray scattering and atomic pair distribution function data in a complex modeling framework. *J. Appl. Crystallogr.* **47**, 561–565 (2014).

184. Bayram, E. *et al.* Agglomerative sintering of an atomically dispersed Ir_1/Zeolite Y catalyst: compelling evidence against ostwald ripening but for bimolecular and autocatalytic agglomeration catalyst sintering steps. *ACS Catal.* **5**, 3514–3527 (2015).

185. Gamez-Mendoza, L., Resto, O. & Martinez-Inesta, M. Effect of using polyimide capillaries during thermal experiments on the particle size distribution of supported Pt nanoparticles. *J. Appl. Crystallogr.* **48**, 1599–1603 (2015).

186. Toby, B. H. & Egami, T. Accuracy of pair distribution function analysis applied to crystalline and noncrystalline materials. *Acta Crystallogr. A* **48**, 336–46 (1992).

187. Qiu, X., Božin, E. S., Juhás, P., Proffen, T. & Billinge, S. J. L. Reciprocal space instrumental effects on the real space neutron atomic pair distribution function. *J. Appl. Crystallogr.* **37**, 110–116 (2004).

188. Terban, M. W., Shi, C., Silbernagel, R., Clearfield, A. & Billinge, S. J. L. Local environment of terbium(III) ions in layered nanocrystalline zirconium(IV) phosphonate–phosphate ion exchange materials. *Inorg. Chem.* **56**, 8837–8846 (2017).

189. Veliscek-Carolan, J., Hanley, T. L. & Luca, V. Zirconium organophosphonates as high capacity, selective lanthanide sorbents. *Sep. Purif. Technol.* **129**, 150–148 (2014).

190. Silbernagel, R., Shehee, T. C., Martin, C. H., Hobbs, D. T. & Clearfield, A. Zr/Sn(IV) phosphonates as radiolytically stable ion-exchange materials. *Chem. Mater.* **28**, 2254–2259 (2016).

191. Veliscek-Carolana, J., Rawalb, A., Lucac, V. & Hanley, T. L. Zirconium phosphonate sorbents with tunable structure and function. *Micropor. Mesopor. Mat.* **252**, 90–104 (2017).

192. Burns, J. D., Clearfield, A., Borkowski, M. & Reed, D. T. Pillared metal(IV) phosphate-phosphonate extraction of actinides. *Radiochim. Acta* **100**, 381–387 (2012).

193. Billinge, S. J. L. The nanostructure problem. *Physics* **3**, 25 (2010).

194. Silbernagel, R., Martin, C. H. & Clearfield, A. Zirconium(IV) Phosphonate–Phosphates as Efficient Ion-Exchange Materials. *Inorg. Chem.* **55**, 1651–1656 (2016).

195. Clearfield, A. & Smith, G. D. The crystallography and structure of α-zirconium bis(monohydrogen orthophosphate) monohydrate. *Inorg. Chem.* **8**, 431–436 (1969).

196. Poojary, M. D., Hu, H. L., Campbell, F. L. & Clearfield, A. Determination of crystal structures from limited powder data sets: crystal structure of zirconium phenylphosphonate. *Acta Crystallogr. B* **49**, 996–1001 (1993).

197. Hirao, T., Masunaga, T., Yamada, N., Ohshiro, Y. & Agawa, T. Palladium-catalyzed new carbon-phosphorus bond formation. *Bull. Chem. Soc. Jpn.* **55**, 909–913 (1982).

198. Poojary, D. M., Shpeizer, B. & Clearfield, A. X-ray powder structure and Rietveld refinement of γ-zirconium phosphate, $Zr(PO_4)(H_2PO_4).2H_2O$. *J. Chem. Soc. Dalton Trans.* 111–113 (1995).

199. Byrd, H., Clearfield, A., Poojary, D., Reis, K. P. & Thompson, M. E. Crystal structure of a porous zirconium phosphate/phosphonate compound and photocatalytic hydrogen production from related materials. *Chem. Mater.* **8**, 2239–2246 (1996).

200. Poojary, D. M., Zhang, B. & Clearfield, A. Structure of a mixed phosphate/phosphonate layered zirconium compound from synchrotron X-ray powder diffraction data. *Angew. Chem. Int. Ed.* **33**, 2324–2326 (1994).

201. Petkov, V., DiFrancesco, R. G., Billinge, S. J. L., Acharya, M. & Foley, H. C. Local structure of nanoporous carbons. *Philos. Mag. B* **79**, 1519 (1999).

202. Petkov, V. *et al.* Structure of $V_2O_5.nH_2O$ xerogel solved by the atomic pair distribution function technique. *J. Am. Chem. Soc.* **124**, 10157 (2002).

203. Anasori, B. *et al.* Control of electronic properties of 2D carbides (MXenes) by manipulating their transition metal layers. *Nanoscale Horiz.* **1**, 227–234 (2016).

204. Farrow, C. L., Bediako, D. K., Surendranath, Y., Nocera, D. G. & Billinge, S. J. L. Intermediate-range structure of self-assembled cobalt-based oxygen evolving catalysts. *J. Am. Chem. Soc.* **135**, 6403–6406 (2013).

205. Petkov, V., Billinge, S. J. L., Heising, J. & Kanatzidis, M. G. Application of atomic pair distribution function analysis to materials with intrinsic disorder. Three-dimensional structure of exfoliated-restacked WS_2: not just a random turbostratic assembly of layers. *J. Am. Chem. Soc.* **122**, 11571 (2000).

206. Shi, C. *et al.* Structure of nanocrystalline Ti_3C_2 MXene using atomic pair distribution function. *Phys. Rev. Lett.* **112**, 125501 (2014).

207. Hellenbrandt, M. The inorganic crystal structure database (ICSD)—present and future. *Crystallogr. Rev.* **10**, 17–22 (2004).

208. Xing, Y., Hu, N., Zhou, Q., Hong, G. & Yue, S. Crystal structure of potassium terbium metaphosphate. *Acta Phys-Chim Sin* **3** (1987).

209. Oudahmane, A., Daoud, M., Tanouti, B., Avignant, D. & Zambon, D. Sodium terbium(III) polyphosphate. *Acta Crystallogr. E* **66**, i28–i29 (2010).

210. Tahiri, A. A., El, B. B., Lachkar, M., Piniella, J. F. & Capitelli, F. Crystal structure of new lanthanide diphosphates $KLnP_2O_7{\cdot}2H_2O$ (Ln = Gd, Tb, Yb). *Z. Kristallogr.* **221**, 173–177 (2009).

211. López-Solano, J. *et al.* Theoretical and experimental study of the structural stability of $TbPO_4$ at high pressures. *Phys. Rev. B* **81**, 144126 (2010).

212. Yaghi, O. M. *et al.* Reticular synthesis and the design of new materials. *Nature* **423**, 705–714 (2003).

213. Stock, N. & Biswas, S. Synthesis of metal-organic frameworks (MOFs): routes to various MOF topologies, morphologies, and composites. *Chem. Rev.* **112**, 933–969 (2011).

214. Huang, X.-C., Lin, Y.-Y., Zhang, J.-P. & Chen, X.-M. Ligand-directed strategy for zeolite-type metal–organic frameworks: zinc(II) imidazolates with unusual zeolitic topologies. *Angew. Chem.* **118**, 1587–1589 (2006).

215. Pan, Y., Liu, Y., Zeng, G., Zhao, L. & Lai, Z. Rapid synthesis of zeolitic imidazolate framework-8 (ZIF-8) nanocrystals in an aqueous system. *Chem. Commun.* **47**, 2071–2073 (2010).

216. Cravillon, J. *et al.* Rapid room-temperature synthesis and characterization of nanocrystals of a prototypical zeolitic imidazolate framework. *Chem. Mater.* **21**, 1410–1412 (2009).

217. Polyzoidis, A., Etter, M., Herrmann, M., Loebbecke, S. & Dinnebier, R. E. Revealing the initial reaction behavior in the continuous synthesis of metal–organic frameworks using real-time synchrotron X-ray analysis. *Inorg. Chem.* **56**, 5489–5492 (2017).

218. Friscic, T. *et al.* Real-time and in situ monitoring of mechanochemical milling reactions. *Nat. Chem.* **5**, 66–73 (2013).

219. Yamashita, M. & Fenn, J. B. Electrospray ion source. Another variation on the free-jet theme. *J. Phys. Chem.* **88**, 4451–4459 (1984).

220. Nune, S. K. *et al.* Synthesis and properties of nano zeolitic imidazolate frameworks. *Chem. Commun.* **46**, 4878–4880 (2010).

221. Yang, X., Juhás, P., Farrow, C. & Billinge, S. J. L. xPDFsuite: an end-to-end software solution for high throughput pair distribution function transformation, visualization and analysis. *arXiv.* 1402.3163. <http://arxiv.org/abs/1402.3163> (2015).

222. Zobel, M., Neder, R. B. & Kimber, S. A. J. Universal solvent restructuring induced by colloidal nanoparticles. *Science* **347**, 292–294 (2015).

223. Kohn, W. & Sham, L. J. Self-consistent equations including exchange and correlation effects. *Phys. Rev.* **140** (1965).

224. Boussouf, K. *et al.* Structure, spectroscopy, and bonding within the Zn^{q+}-imidazole$_n$ (q=0, 1, 2; n=1-4) clusters and implications for zeolitic imidazolate frameworks and Zn-enzymes. *J. Phys. Chem. A* **119**, 11928–11940 (2015).

225. Bennett, T. D. *et al.* Thermal amorphization of zeolitic imidazolate frameworks. *Angew. Chem. Int. Ed.* **50**, 3067–3071 (2011).

226. Bennett, T. D. & Cheetham, A. K. Amorphous metal-organic frameworks. *Acc. of Chem. Res.* **47**, 1555–1562 (2014).